Dissertation

submitted to the

Combined Faculties of the Natural Sciences and Mathematics

of the Ruperto-Carola-University of Heidelberg. Germany

for the degree of

Doctor of Natural Sciences

Put forward by

Anne Christin Wegmann

born in: Rheine

Oral examination: 18. 01. 2017

Characterization of the liquid argon veto of the GERDA experiment and its application for the measurement of the ^{76}Ge half-life

Referees:

Prof. Dr. Manfred Lindner

Prof. Dr. Norbert Herrmann

The search for neutrinoless double-beta decay ($0\nu\beta\beta$) is one of the most active fields in modern particle physics as the observation of this process would prove lepton number violation and imply new physics beyond the Standard Model of particle physics. The GERDA experiment searches for this decay by operating bare Germanium detectors, enriched in the $\beta\beta$ isotope ^{76}Ge, in liquid argon. For the first time, a $\beta\beta$-experiment combines the excellent properties of semiconductor Germanium detectors with an active background suppression technique based on the simultaneous detection of liquid argon scintillation light by photomultiplier tubes and silicon photomultipliers coupled to scintillating fibers (LAr veto). The LAr veto has been successfully operated during the first six months of Phase II of the experiment and yielded – in combination with a Germanium detector pulse shape discrimination technique – a background index of $(0.7^{+1.1}_{-0.5}) \cdot 10^{-3}\,(\frac{\text{cts}}{\text{kg}\cdot\text{keV}\cdot\text{yr}})$. With an ultimate exposure of $100\,\text{kg}\cdot\text{yr}$ this will allow for a $0\nu\beta\beta$-decay half-life sensitivity of the GERDA Phase II experiment of $10^{26}\,\text{yr}$.

Double-beta decay under the emission of two neutrinos ($2\nu\beta\beta$) is a second-order process but which is allowed by the Standard Model. The excellent background reduction of the LAr veto results in an unprecedented signal-to-background ratio of 30:1 in the energy region dominated by $2\nu\beta\beta$-decay of ^{76}Ge. The remaining background after LAr veto is estimated using the suppression factor from calibration source measurements and results in a measurement of $\text{T}^{2\nu}_{1/2} = (1.98 \pm 0.02\ (\text{stat}) \pm 0.05\ (\text{syst})) \cdot 10^{21}\,\text{yr}$ and $\text{T}^{2\nu}_{1/2} = (1.92 \pm 0.02\ (\text{stat}) \pm 0.11\ (\text{syst})) \cdot 10^{21}\,\text{yr}$ based on two different detector designs and given uncertainties on the detector parameters but both with improved systematic uncertainties in comparison to earlier measurements.

Ein Argon Szintillationsveto für die Phase II des GERDA Experiments
Die Suche nach dem neutrinolosen Doppelbetazerfall ($0\nu\beta\beta$) stellt eines der aktivsten Forschungsfelder der modernen Teilchenphysik dar. Die Entdeckung dieses Leptonenzahl verletzenden Zerfalls würde eine Erweiterung des Standardmodells der Teilchenphysik erfordern. Das GERDA Experiment sucht nach diesem Zerfall, indem es Germaniumdetektoren direkt in Argon betreibt. In Phase II des Experiments werden erstmals die exzellenten Eigenschaften von Halbleiterdetektoren mit einem aktiven Veto kombiniert, welches auf der simultanen Detektion von Argon Szintillationslicht – mithilfe von PMTs und an Szintillationsfasern gekoppelten SiPMs – basiert. Dieses Veto wurde während der ersten sechs Monate der zweiten Experimentphase erfolgreich betrieben und ergab in Kombination mit einer Pulsformanalyse der Germaniumdetektorsignale einen Untergrundindex von $(0.7^{+1.1}_{-0.5}) \cdot 10^{-3}\,(\frac{\text{Ereignisse}}{\text{kg}\cdot\text{keV}\cdot\text{yr}})$, welcher mit einer Exposition von $100\,\text{kg}\cdot\text{yr}$ eine Sensitivität auf die $0\nu\beta\beta$-Halbwertszeit von $10^{26}\,\text{yr}$ ermöglicht.

Der neutrinobehaftete Doppelbetazerfall ($2\nu\beta\beta$) ist ein Prozess zweiter Ordnung, welcher vom Standardmodell erlaubt ist. Die exzellente Untergrundunterdrückung des Szintillationsvetos führt in dem Energiebereich, der von dem $2\nu\beta\beta$-Zerfall dominiert wird, zu einem bislang unerreichten Verhältnis von Signal zu Untergrundereignissen von 30:1. Der nach der Anwendung des Szintillationsvetos verbleibende Untergrund wird mithilfe der gemessenen Untergrundunterdrückung von Kalibrationsmessungen abgeschätzt. Ausgehend davon wird für zwei unterschiedliche Detektordesigns mit vorgegebenen Unsicherheiten der Detektorparameter eine Halbwertszeit von $\text{T}^{2\nu}_{1/2} = (1.98 \pm 0.02\ (\text{stat}) \pm 0.05\ (\text{syst})) \cdot 10^{21}\,\text{yr}$ und $\text{T}^{2\nu}_{1/2} = (1.92 \pm 0.02\ (\text{stat}) \pm 0.11\ (\text{syst})) \cdot 10^{21}\,\text{yr}$ bestimmt. Dies stellt im Vergleich zu vorausgegangenen Messungen eine Verbesserung der systematischen Unsicherheiten dar.

in Erinnerung an meine liebe Oma
Maria Jörgens

CONTENTS

LIST OF TABLES

LIST OF FIGURES

CHAPTER 1

INTRODUCTION

Neutrinoless double beta decay ($0\nu\beta\beta$) is a hypothetical second order nuclear process which violates lepton number by two units. The observation of this process would prove that neutrinos have at least a tiny Majorana mass component. This is in contradiction to their properties in the Standard Model (SM) of particle physics and requires extensions to the Standard Model. Assuming that the exchange of a light Majorana neutrino is the dominant mechanism of the process allows to extract information on the absolute mass scale of neutrinos and the neutrino mass ordering.

In Sec. 1.1 the basics of neutrino physics, in particular the physics of double-beta decays and its implications for neutrino physics are presented. The experimental aspects and challenges, together with an overview of the current limits of the different experiments, are discussed in Sec. 1.2.

1.1 Neutrino physics

The history of neutrino physics starts in 1930 with an open letter by W. Pauli, in which he postulates an electrically neutral particle with spin 1/2 and a small but not necessarily vanishing rest mass in order to rescue the conservation of energy and momentum in β-decays[1] [115]. Due to the small cross section of the neutrino 26 years had passed before the neutrino was first discovered experimentally in 1956. F. Reines and C. Cowan used the inverse β-decay to detect reactor antineutrinos from the Savannah River reactor [58]. Moreover, it has been shown in the Wu [139] and the Goldhaber [75] experiment that neutrinos exist predominantly as particles of left helicity (left handed) and antineutrinos as particles of right helicity (right handed), confirming the parity violating nature of the weak interaction.

The neutrinos and antineutrinos are embedded in the Standard Model of particle physics (see Tab. 1.1) as distinct particles with lepton number $+1$ (ν) and -1 ($\bar{\nu}$). There are three lepton families in the Standard Model: electron (e), muon (μ), tau (τ)[2] [27], each of which contains a left-handed doublet composed of a charged lepton and a

[1] Up to that point β-decay was assumed to be a two-body-decay and the continuous electron energy spectrum measured by Chadwick seemed to violate the laws of energy and momentum conservation.

[2] confirmed by the analysis of the decay width of the Z^0 boson for light, active neutrinos with $m_\nu < M_Z/2$ and M_Z the mass of the Z boson.

	flavor 1	2	3	charge	color	spin
quarks	u	c	t	$+2/3$	r,g,b	1/2
	d	s	b	$-1/3$		
leptons	e	μ	τ	-1	-	1/2
	ν_e	ν_μ	ν_τ	0		

Table 1.1: Overview of the elementary particles in the Standard Model: quarks and leptons together with their electric charge, color and spin. Not shown are the corresponding antiparticles and the exchange particles of the interactions.

massless and electrically neutral Dirac neutrino and is accompanied by a right-handed singlet l_R of the charged lepton. The lepton number is conserved in all interactions of the Standard Model.

The first hint for the incompleteness of the Standard Model came up with the observations of the Homestake experiment [61] which was aiming to measure the solar neutrino flux predicted by the Solar Standard Model (SSM) [40] using a radiochemical detection technique. Instead of confirming the predictions, the experiment found a clear deficit by a factor three [62] – known as the *solar neutrino problem*.

$$\text{Homestake} : 2.56 \pm 0.22\,\text{SNU} \tag{1.1}$$

$$\text{SSM} : 9.3 \pm 1.3\,\text{SNU}. \tag{1.2}$$

Several experiments like the water-Cherenkov experiment Kamiokande [87] and the gallium radiochemical experiments SAGE [4] and Gallex [32] confirmed this deficit in the following years. The concept of *neutrino oscillations* has been established to solve the solar neutrino problem. Nonetheless, it was only in 1998 that the Super-Kamiokande experiment could finally prove the existence of neutrino oscillations by atmospheric neutrino measurements [72]. Subsequently, the SNO experiment was able to distinguish between electron neutrinos and the μ and τ-neutrino flux. They all add up to the predicted solar neutrino flux [23].

1.1.1 Neutrino oscillations and masses

Neutrino oscillations were originally proposed by B. Pontecorvo in 1957 as a conversion between ν and $\bar{\nu}$. They require neutrino flavor mixing, which is based on the fact that the weakly interacting flavor eigenstates $|\nu_\alpha\rangle$ ($\alpha = e, \mu, \tau$) are not identical to the three neutrino mass eigenstates $|\nu_i\rangle$ ($i = 1, 2, 3$) with mass m_i but can be written as linear combinations of the mass eigenstates:

$$|\nu_\alpha\rangle = \sum_i U^*_{\alpha i} \, |\nu_i\rangle \, . \tag{1.3}$$

The relation between the flavor eigenstates and the mass eigenstates is given by the unitary mixing matrix U_{PMNS} [106] (named after Pontecorvo, Maki, Nakagawa and Sakata). The PMNS matrix can be parametrized in analogy to the CKM matrix in the quark sector [112]. In case neutrinos are Majorana particles ($\nu_\alpha = \overline{\nu_\alpha}$), the PMNS matrix contains two more physical phases—the so-called Majorana phases α_1 and α_2.

The matrix can then be parametrized in the form:

$$U_{\text{PMNS}} = \begin{pmatrix} 1 & 0 & 0 \\ 0 & c_{23} & s_{23} \\ 0 & -s_{23} & c_{23} \end{pmatrix} \times \begin{pmatrix} c_{13} & 0 & s_{13}e^{-i\delta_{CP}} \\ 0 & 1 & 0 \\ -s_{13}e^{i\delta_{CP}} & 0 & c_{13} \end{pmatrix} \times \begin{pmatrix} c_{12} & s_{12} & 0 \\ -s_{12} & c_{12} & 0 \\ 0 & 0 & 1 \end{pmatrix} \times diag(1, e^{i\alpha_1/2}, e^{i\alpha_2/2}) \tag{1.4}$$

where

s_{ij}	$\equiv sin\theta_{ij}$,
c_{ij}	$\equiv cos\theta_{ij}$,
θ_{ij}	the mixing angles,
δ_{CP}	CP violating Dirac phase,
$\alpha_{1,2}$	CP violating Majorana phases.

The time evolution of a neutrino created in the flavor eigenstate ν_α is obtained by solving the Schrödinger equation for Eq. 1.3. A neutrino of flavor α with energy E at the neutrino source evolves to

$$|\nu_\alpha, x = L\rangle = \sum_j U^*_{\alpha j} e^{-im_j^2 L/2E} |\nu_j\rangle \tag{1.5}$$

at a distance $L = ct$ from the detector. The probability to find the neutrino in a flavor eigenstate ν_β after it has traveled the distance L from a source to a detector in the absence of matter can then be written as

$$\begin{aligned} \mathcal{P}(\nu_\alpha \to \nu_\beta) &= \left| \sum_i U_{\beta i} e^{-im_i^2 L/2E} U^*_{\alpha i} \right|^2 \\ &= \delta_{\alpha\beta} - 4 \sum_{i>j} \Re(U^*_{\alpha i} U_{\beta i} U_{\alpha j} U^*_{\beta j}) sin^2(\Delta m^2_{ij} L/4E) \\ &\quad + 2 \sum_{i>j} \Im(U^*_{\alpha i} U_{\beta i} U_{\alpha j} U^*_{\beta j}) sin(\Delta m^2_{ij} L/2E) \end{aligned} \tag{1.6}$$

with $\Delta m^2_{ij} = m^2_i - m^2_j$ [120]. Note that flavor oscillations can only occur if $\Delta m^2_{ij} \neq 0$, i.e. if $m_i \neq m_j$ and at least one mass eigenstate fulfills $m_i \neq 0$. Neutrino oscillation experiments are only sensitive to the mass squared differences Δm^2_{ij}, the three mixing angles θ_{ij} and the CP violating Dirac phase δ_{CP}. They are neither sensitive to the absolute mass scale nor to the Majorana phases $\alpha_{1,2}$, i.e. no conclusion can be drawn about the Majorana or Dirac nature of the neutrinos.

Note that the described formalism holds only for neutrino oscillations in vacuum. When neutrinos propagate through matter, the electron neutrinos undergo elastic scattering processes via the charged current. This effect is known as the *Mikheyev-Smirnov-Wolfenstein (MSW) effect* [110, 138] and is required to fully explain the large reduction of the solar electron neutrino flux. Solar neutrino oscillations and long-baseline reactor neutrino oscillations allow to measure Δm^2_{21} and θ_{12}, as done by the SNO experiment [23] and the KamLAND experiment [68]. Atmospheric neutrino oscillations give access to Δm^2_{32} and θ_{23}. The first measurement was performed by the Super-Kamiokande experiment [72] examining the disappearance of $\overline{\nu_\mu}$. With short baseline reactor neutrino oscillations and long-baseline $\nu_\mu \to \nu_e$ oscillations Δm^2_{31} and θ_{13} are determined. θ_{13} was only measured within the last years by the reactor $\overline{\nu_e}$ disappearance experiments

Double Chooz [5], DayaBay [30] and Reno [24] $\theta_{13} = 9.6 \pm {}^{\circ}$ and allows to extract information on the CP violating phase δ_{CP} by means of global fits to the oscillation data. While the sign of Δm^2_{32} is not known, the MSW effect for the solar neutrinos revealed $m_2 > m_1$, leaving the following possibilities for the neutrino mass ordering.

normal ordering (NH)	$m_1 < m_2 < m_3$,
inverted ordering (IH)	$m_3 < m_1 < m_2$,
quasi-degeneracy (QD)	$m_3 \cong m_1 \cong m_2$,

In Tab. 1.2 a compilation of the oscillation parameters derived from a global fit to the oscillation data for the normal hierarchy and the case of the inverted hierarchy is given.

parameter	best fit	
	normal hierachy	inverted hierachy
$sin^2\theta_{12}(\theta_{12}[^\circ])$	0.323 ± 0.016 (34.6 ± 1.0)	
$sin^2\theta_{23}(\theta_{23}[^\circ])$	$0.567^{+0.032}_{-0.124}$ $(48.9^{+1.8}_{-7.2})$	$0.573^{+0.025}_{-0.039}$ $(49.2^{+1.5}_{-2.3})$
$sin^2\theta_{13}(\theta_{13}[^\circ])$	0.0226 ± 0.0012 $(8.6^{+0.3}_{-0.2})$	0.0229 ± 0.0012 (8.7 ± 0.2)
Δm^2_{21} $[10^{-5}\,\mathrm{eV}^2]$	$7.60^{+0.19}_{-0.18}$	
Δm^2_{31} $[10^{-3}\,\mathrm{eV}^2]$	$2.48^{+0.05}_{-0.07}$	$-2.38^{+0.05}_{-0.06}$
δ_{CP} $[\pi]$	$1.41^{+0.55}_{-0.40}$	1.48 ± 0.31

Table 1.2: Mass and mixing parameters for 3ν oscillations derived from a global fit to the current oscillation data for the normal hierarchy and the inverted hierarchy [70]. The uncertainties are given for the 1σ range of the best fit result.

1.1.2 The neutrino mass scale and the Standard Model

The observation of neutrino oscillations requires an extension of the Standard Model (SM) allowing for non-vanishing neutrino masses. We present a short overview of the theoretical framework following the discussion in [74].

In the SM particle masses are created by Yukawa couplings to the Higgs field. The Dirac mass term for the neutrino in the Lagrangian is written as

$$\mathcal{L}^D = -\overline{\nu_R} m_D \nu_L + \text{h.c.}, \tag{1.7}$$

with $m_D = v h_\nu$, where v is the vacuum expectation value of the Higgs field, h_v the neutrino Yukawa coupling constant and ν_R and ν_L the right- and left-handed components of the neutrino field. Here the only addition to the SM is the right-handed component of the neutrino field, because they do not participate in the weak interaction. Additionally, the Lorentz invariant Majorana mass terms for ν_L

$$\mathcal{L}^L = \frac{1}{2}\overline{\nu^c_L} m_L \nu_L + \text{h.c.}, \tag{1.8}$$

and ν_R

$$\mathcal{L}^R = \frac{1}{2}\overline{\nu_R^c} m_R \nu_R + \text{h.c.}, \tag{1.9}$$

have to be considered in the Lagrangian. Therefore, the neutrino mass Lagrangian in its most general form becomes

$$\mathcal{L}^{D+M} = \mathcal{L}^D + \mathcal{L}^L + \mathcal{L}^R = \begin{pmatrix} \overline{\nu_L^c} & \overline{\nu_R} \end{pmatrix} \begin{pmatrix} m_L & m_D \\ m_D & m_R \end{pmatrix} \begin{pmatrix} \nu_L \\ \nu_R^c \end{pmatrix} + \text{h.c.}\,. \tag{1.10}$$

As the Majorana mass term for left-handed neutrinos in Eq. 1.8 is not invariant under SM gauge transformations, $m_L = 0$ is required to assure gauge invariance in the SM. In case physics beyond the Standard Model is considered, $\mathcal{L}^L$ with $m_L \neq 0$ can be retained. A direct consequence of the Majorana mass term in the Lagrangian is that neutrinos are their own anti-particles, ($\nu = \overline{\nu}$).

Nevertheless, the smallness of the neutrino masses compared to the mass of the other fermions is a mystery. It is natural to assume that the phenomenon is related to a new fundamental mass scale. The see-saw mechanism is capable to provide such a natural explanation [111]. When adding three right-handed (RH) neutrinos[3] to the Lagrangian the Higgs field acquires a non-zero vacuum expectation value v. v breaks the electroweak symmetry and leads to the Dirac mass matrix $m_D = v \cdot h$. Adding a right-handed Majorana mass term means that the neutrino masses would be the result of an interplay of the Dirac and Majorana mass terms

$$m_\nu = -m_D \frac{1}{m_R} m_D^T. \tag{1.11}$$

Assuming $m_D \sim 100\,\text{GeV}$ of the order of the electroweak scale the observed neutrino mass is reproduced for $m_R \sim 10^{14-15}\,\text{GeV}$ close to the GUT scale $M_{GUT} \sim 10^{15-16}\,\text{GeV}$. Note that in this scenario the measured neutrino mass scale is not fundamental but a by-product of two other fundamental scales.

Information on the absolute mass scale of neutrinos can be acquired using cosmological constraints, Kurie-Plot experiments like the KATRIN experiment and its predecessors, and neutrinoless double-beta decay experiments, see Sec. 1.1.3.

Today's large-scale structure of the Universe is determined by density fluctuations present in the early Universe. These fluctuations were partly washed out by light neutrinos being able to escape from overdense regions. The imprint on the large-scale structure left by this washout depends on the neutrino masses. In 2013, the Planck experiment released a constraint on the summed neutrino mass, using the Sachs-Wolfe effect in the CMB power spectrum with constraints[4] from other astrophysical experiments [10]:

$$\sum m_i < 0.23\,\text{eV}, \qquad \text{at } 95\%\text{ C.L.}. \tag{1.12}$$

This result depends on the assumed cosmological model, namely the ΛCDM model.

The only model-independent access to the neutrino mass is given by Kurie-plot experiments. They measure the kinematics of a single β-spectrum with high accuracy.

[3] This is the most attractive case where we have one RH neutrino for each generation in the SM and it is predicted by several SO(10) GUT models. Current data can be explained with only two RH neutrinos.

[4] Namely the WMAP polarization low-multipole likelihood (*WP*), the high-resolution CMB experiments (*high L*) and baryon acoustic oscillations (*BAO*)

The *effective electron neutrino mass*, defined as $m_{\nu_e} = \sqrt{\sum_i |U_{ei}^2| m_i^2}$, can be extracted from the shift of the endpoint due to the non-vanishing neutrino mass. To date the best limit comes from the Troitsk experiment measuring the endpoint of the Tritium β-spectrum [104]

$$m_{\nu_e} < 2.05\,\text{eV}. \tag{1.13}$$

The KATRIN experiment is currently in its commissioning phase and has an aspired sensitivity of 0.2 eV with a discovery potential of 0.35 eV at 5σ significance [90].

1.1.3 Neutrinoless double-beta decay

The neutrinoless and the two-neutrino double beta decay ($\beta^-\beta^-$) can occur for some even-even nuclei for which the single beta decay (β^-) is energetically forbidden, as illustrated in Fig. 1.1. The Q-value of the decay is defined as the mass difference between the parent and the daughter nucleus. Thirty-five isotopes are known for which the decay is hypothetically possible.

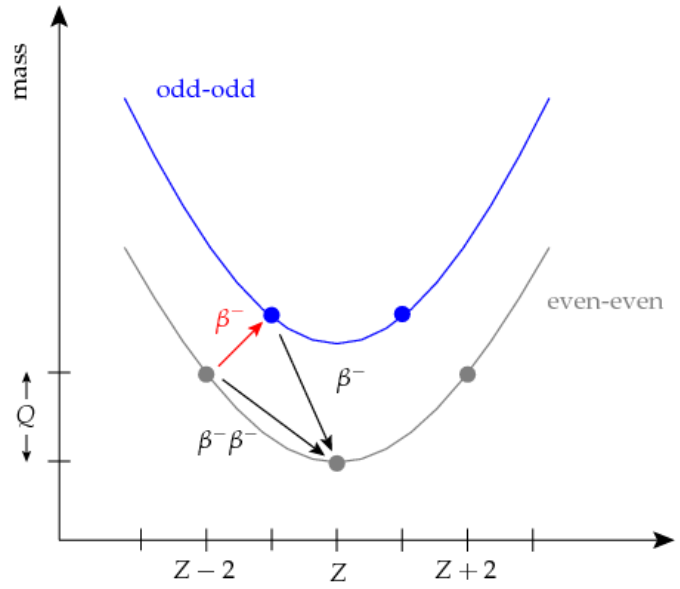

Figure 1.1: Mass parabola for even-even (gray) and odd-odd (blue) nuclei. For some nuclei the single beta decay (denoted β^- in the figure) is energetically forbidden because of a larger mass of the daughter nucleus. In case of even-even nuclei second order double beta decay (denoted $\beta^-\beta^-$) can occur. The Q-value is defined as the mass difference between the mother and daughter nucleus. The figure is taken from [67].

In **Two-neutrino double-beta decay ($2\nu\beta\beta$)**, an initial nucleus (Z,A) with proton number Z and total nucleon number A decays to (Z+2,A), emitting two electrons and two electron antineutrinos, i.e.

$$(Z, A) \rightarrow (Z + 2, A) + 2e^- + 2\overline{\nu_e}. \tag{1.14}$$

The half-life is inversely proportional to the decay rate $\Gamma^{2\nu}$ and is given as the product of the Phase space factor $G^{2\nu}(Q_{\beta\beta}, Z)$ and the squared matrix element $M^{2\nu}$,

$$\left[T_{1/2}^{2\nu}\right]^{-1} = \Gamma^{2\nu}/\log 2 = G^{2\nu}(Q_{\beta\beta}, Z) \cdot \left|M^{2\nu}\right|^2. \tag{1.15}$$

Neutrinoless double-beta decay ($0\nu\beta\beta$): An initial nucleus (Z,A), with proton number Z and total nucleon number A decays to (Z+2,A), only emitting two electrons in the process, i.e.

$$(Z, A) \rightarrow (Z + 2, A) + 2e^-. \tag{1.16}$$

This decay is forbidden by the Standard Model as is violates lepton number by two units ($\Delta L = 2$). Nevertheless, lepton number violation is required by various models beyond the Standard Model, e.g. Leptogenesis and Baryogenesis, explaining the baryon asymmetry in the Universe. The observation of neutrinoless double-beta decay would reveal the nature of neutrinos, being a *Majorana* particle. According to the black box

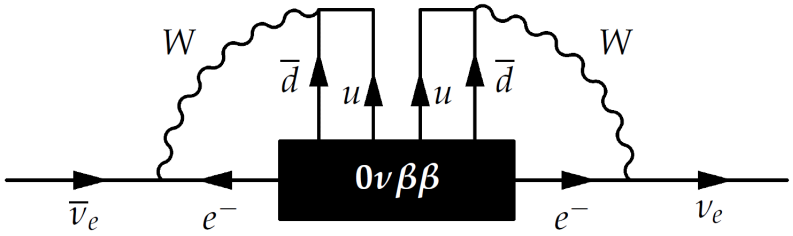

Figure 1.2: Schechter-Valle or black box theorem. Figure taken from [122].

or Schechter-Valle theorem, sketched in Fig. 1.2, all possible realizations of $0\nu\beta\beta$-decay involve the existence of a Majorana neutrino mass [122]. However, this radiative mass component is too small to explain neutrino masses by orders of magnitude [66].

The standard mechanism mediating neutrinoless double beta decay is the exchange of a light Majorana neutrino within the nucleus. On the one hand, it is the simplest theoretical model, on the other hand it is presumably the best motivated one. Examples for other $0\nu\beta\beta$ mechanisms are the exchange of particles associated to heavy Majorana neutrinos or Higgs triplets in left-right symmetric theories, R-parity violating SUSY or leptoquarks [113], or decay modes with an extended number of particles in the final states, like modes with Majoron emission [19]. In this thesis we only discuss the standard mechanism.

The Feynman diagram for neutrinoless double-beta decay through the exchange of a light Majorana neutrino is depicted in Fig. 1.3.

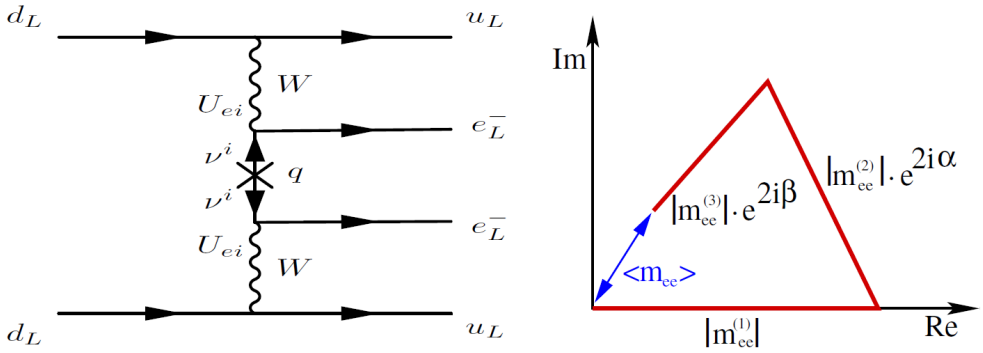

Figure 1.3: Left: quark level 'lobster' diagram for neutrinoless double-beta decay in case of light Majorana neutrino exchange. Right: geometrical visualization of the effective mass (α, β are defined as $\alpha = 2\alpha_1$ and $\beta = \alpha_2 - \delta_{CP}$ with α_1, α_2 and δ_{CP} the phases from the U_{PMNS} matrix. Figure taken from [121].

The half-life of the $0\nu\beta\beta$-decay is directly related to the so-called *effective neutrino mass* m_{ee} by

$$\left[T_{1/2}^{0\nu}\right]^{-1} = \Gamma^{0\nu} / \log 2 = G^{0\nu}(Q_{\beta\beta}, Z) \cdot |M^{0\nu}|^2 \cdot \langle m_{ee} \rangle, \tag{1.17}$$

with Phase space integral $G^{0\nu}$ and nuclear matrix element $M^{0\nu}$. The effective neutrino mass is defined as

$$\langle m_{ee} \rangle = \left| \sum_{i=1}^{3} m_i U_{ei}^2 \right| = \left| |m_{ee}^{(1)}| + |m_{ee}^{(2)}| e^{2i\alpha} + |m_{ee}^{(3)}| e^{2i\beta} \right|, \tag{1.18}$$

a geometrical visualization of which is shown on the right side of Fig. 1.3 as sum of three complex vectors $m_{ee}^{(1,2,3)}$ defined as $m_{ee}^{(i)} = m_i U_{ei}^2$.

While the phase space integral can be calculated with rather good accuracy, the nuclear matrix elements cannot be measured and are difficult to be computed theoretically. There exist a variety of models to calculate nuclear matrix elements, making different assumption to simplify the many-body-problem, namely the *Interacting Shell Model (ISM)* [108, 109], the *Interacting Boson Model (IBM-2)* [42], the *Quasiparticle Random-Phase Approximation model (QRPA)* [130, 125], the *Energy Density Functional Method (EDF)* [133] and the *projected Hartree-Fock-Bogoliubov method (pHFB)* [119]. The nuclear matrix elements calculated with the different methods for the most common isotopes are shown in Fig. 1.4.

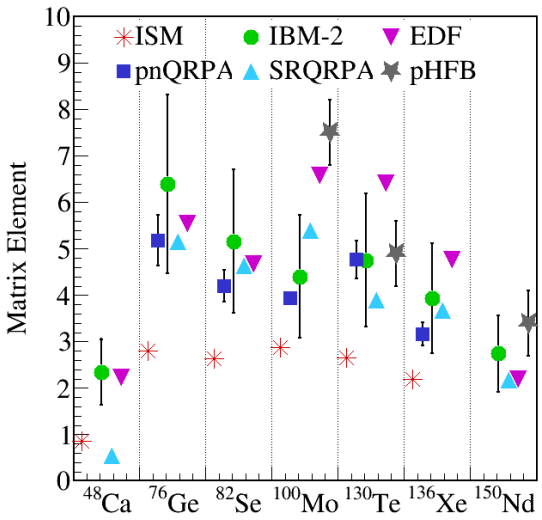

Figure 1.4: Nuclear matrix element calculations in case of light Majorana neutrino exchange for the most common $0\nu\beta\beta$-isotopes. Considered are the *Interacting Shell Model (ISM)* [108, 109], the *Interacting Boson Model (IBM-2)* [42], the *proton-neutron Quasiparticle Random-Phase Approximation model (pnQRPA)* [130], the *Self-consistent Renormalized Quasiparticle Random-Phase Approximation model (SRQRPA)* [125], the *Energy Density Functional Method (EDF)* [133] and the *projected Hartree-Fock-Bogoliubov method (pHFB)* [119].

Fig. 1.5 shows the effective neutrino mass versus the smallest neutrino mass in case of the normal (left) and the inverted (right) hierarchy. On top the 3σ range for the neutrino oscillation parameters have been used, indicated by the green and red areas. At the bottom these parameters were fixed to the best fit values. The blue shaded areas can only be realized for non-trivial CP-phases. For the normal hierarchy, the effective neutrino mass can vanish due to cancellations in Eq. 1.18. Note that the picture changes completely in the presence of light sterile neutrinos as discussed in [113]. The straight dashed black lines show different limits on the sum of the neutrino masses ($\sum m_i$) obtained from cosmology. Red lines indicate constraints set by Kurie-plot experiments (m_β), and limits on the effective neutrino mass ($\langle m_{ee} \rangle$) attained from neutrinoless double-beta decay experiments. The complementarity of the approaches facilitates conclusions on whether the normal or the inverted neutrino mass hierarchy is realized in nature.

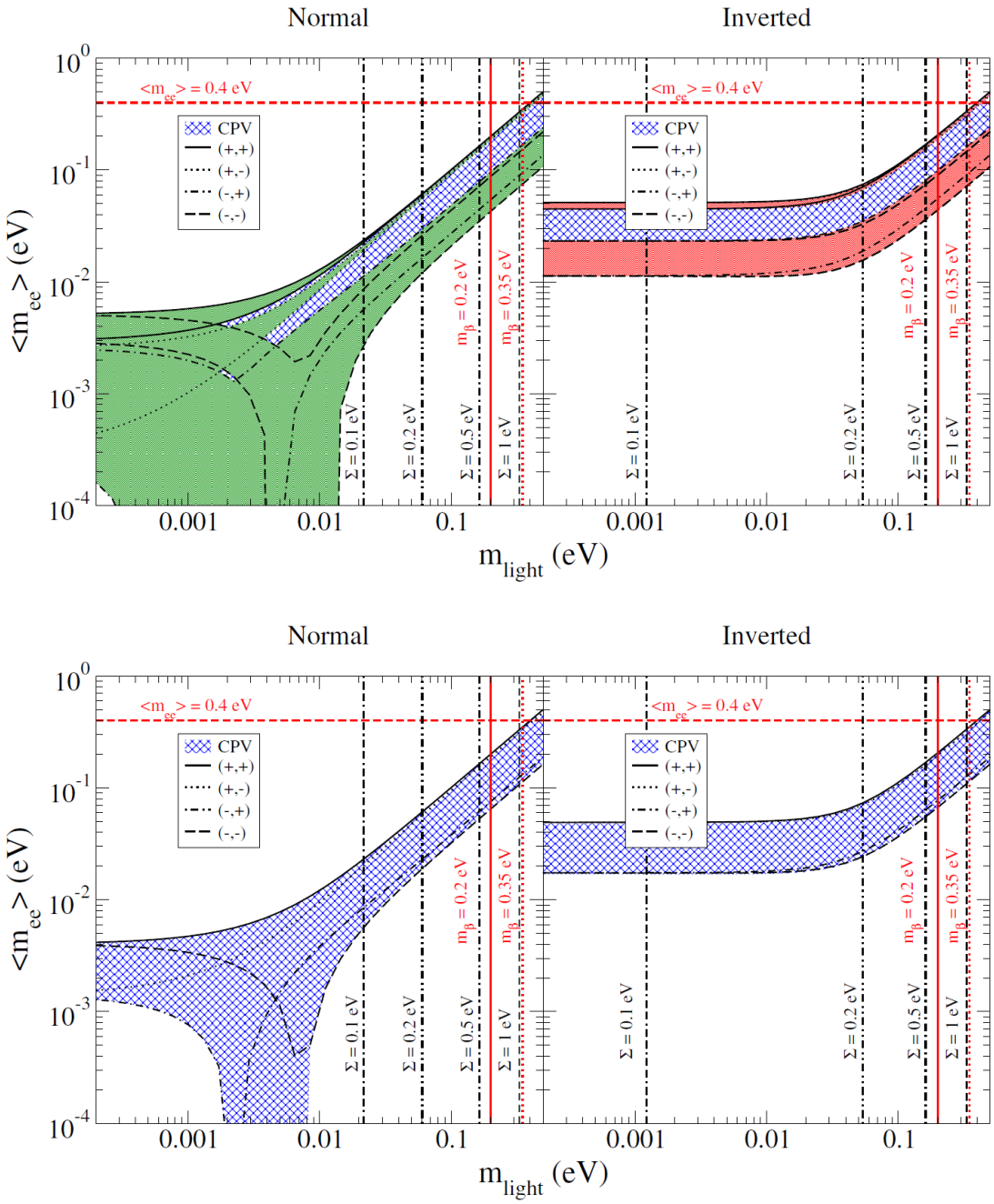

Figure 1.5: Effective neutrino mass as function of the smallest neutrino mass in case of the normal (left) and the inverted (right) hierarchy. On top the 3σ range of the neutrino oscillation parameters has been used, limited by the green and red colored areas. At the bottom these parameters were fixed to the best fit values. The blue shaded areas can only be realized for non-trivial CP-phases. Expected limits from cosmology ($\sum m_i$), Kurie-plot experiments (m_β) and $0\nu\beta\beta$-decay ($\langle m_{ee} \rangle$) are shown. Figure taken from [121].

1.2 Experimental aspects of $0\nu\beta\beta$-decay search

Several considerations have to be taken into account for $0\nu\beta\beta$-experiments, the most important one being in general the sensitivity to the $0\nu\beta\beta$-half-life. Out of thirty-five candidate isotopes for neutrinoless double-beta decay eleven possess Q-values above 2 MeV. These are typically considered for experimental $0\nu\beta\beta$-searches. However, none of these isotopes optimally comprises all the experimental parameters. This section portrays the experimental challenges in $0\nu\beta\beta$-decay searches and highlights the specific properties of commonly used double-beta isotopes.

1.2.1 $0\nu\beta\beta$-decay detection and experimental constraints

Every $0\nu\beta\beta$-experiment measures the electron energy spectrum assigned to double-beta decays, as illustrated in Fig. 1.6. Neutrinos that are emitted in $2\nu\beta\beta$-decays do not interact in the detector volume and their energy remains undetected. Consequently, the blue continuous spectrum arises from two-neutrino double-beta decays. The end-point of the spectrum is at the Q-value of the decay, and the maximum is reached at $\sim Q_{\beta\beta}/3$. The signature of neutrinoless double-beta decay would be a peak at the Q-value as drawn in red in Fig. 1.6 (the peak amplitude was increased for visibility).

The sensitivity to detect this peak depends on the signal to background ratio at $Q_{\beta\beta}$. The number of background counts in the *Region Of Interest* (ROI) can be written as

$$N_{bkg} = M_{det} \cdot t \cdot BI \cdot \Delta E \tag{1.19}$$

with the detector mass M_{det}, the measurement time t, the background index BI and the energy resolution ΔE of the detector. The product $M_{det} \cdot t$ is referred to as exposure. The number of signal counts in the same energy window is given by

$$N_{sig} = \epsilon \cdot f \cdot \frac{M_{det} \cdot N_A}{m_A} \cdot \frac{t \cdot \log 2}{T_{1/2}} \qquad t \ll T_{1/2} \tag{1.20}$$

with the signal efficiency ϵ, the isotopic abundance f and the molar mass m_A of the detector and the half-life $T_{1/2}$.

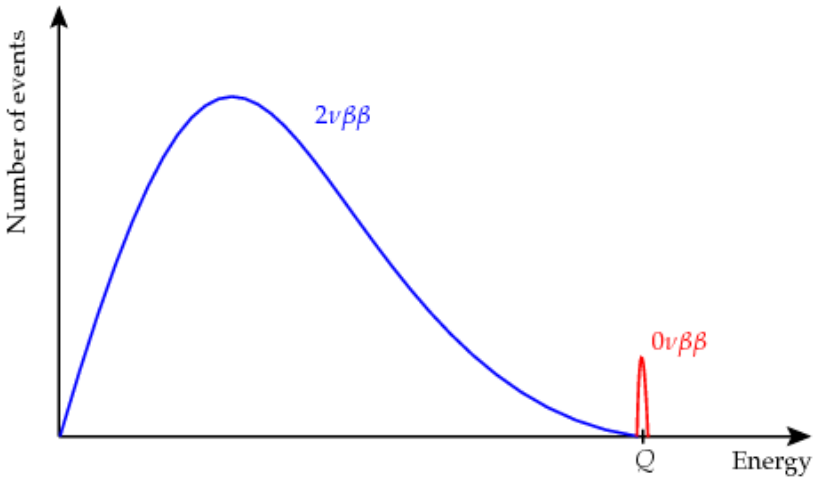

Figure 1.6: Illustration of the electron energy spectrum assigned to double-beta decays. The figure is taken from [67].

For the $0\nu\beta\beta$-sensitivity we distinguish two cases:

1. $N_{bkg} \ll 1$: the 90% confidence limit on the $0\nu\beta\beta$-decay half-life is proportional to the exposure

$$T^{0\nu}_{1/2}(90\%\text{C.L.}) \propto \epsilon_{det} \cdot f \cdot M_{det} \cdot t \qquad (N_{bkg} \ll 1). \tag{1.21}$$

2. $N_{bkg} \gg 1$: the 90% confidence limit on the $0\nu\beta\beta$-decay half-life is proportional to the square root of the exposure normalized to the background in the region of interest and the energy resolution

$$T^{0\nu}_{1/2}(90\%\text{C.L.}) \propto \epsilon_{det} \cdot f \cdot \sqrt{\frac{M_{det} \cdot t}{BI \cdot \Delta E}} \qquad (N_{bkg} \gg 1). \tag{1.22}$$

Eq. 1.22 shows that the sensitivity to the half-life depends on the detection efficiency ϵ, the energy resolution ΔE of the detector, the total source material mass and therewith the isotopic abundance and the background index BI at $Q_{\beta\beta}$. The experimental parameters are distinct for every isotope under consideration, although some of them depend strongly on the detector technique. They are elucidated in more detail in the following to explain the requirements and experimental limitations.

Detection efficiency ϵ: Due to the rareness of double beta decays an as high as possible detection efficiency is desired.

Isotopic abundance f: The natural isotopic abundance of the double beta isotopes under consideration vary between 0.187% and 34.5% (see Tab. 1.3). This necessitates an isotopic enrichment for materials of low natural abundance. For example, the Germanium diodes used in the first phase of the GERDA experiment were enriched in ^{76}Ge from 7.8% to an average isotopic abundance of $\sim$ 86% [16].

Energy resolution ΔE: The energy resolution is an important parameter to maximize the signal to background ratio at $Q_{\beta\beta}$, as it directly impacts the number of $2\nu\beta\beta$-decays in this energy window. It also helps to model background contributions and identify signal and background lines. The best energy resolution is achieved with Germanium

isotope	$Q_{\beta\beta}$[keV]	nat. ab. f [%]	$G^{0\nu}$ [$10^{-14} yr^{-1}$]
^{48}Ca	4273.7	0.187	6.35
^{76}Ge	2039.1	7.8	0.623
^{82}Se	2995.5	9.2	2.70
^{96}Zr	3347.7	2.8	5.63
^{100}Mo	3035.0	9.6	4.36
^{110}Pd	2004.0	11.8	1.40
^{116}Cd	2809.1	7.6	4.62
^{124}Sn	2287.7	5.6	2.55
^{130}Te	2530.3	34.5	4.09
^{136}Xe	2461.9	8.9	4.31
^{150}Nd	3367.3	5.6	19.2

Table 1.3: Q-value, isotopic abundance f and phase-space factor $G^{0\nu}$ (scaled to $g_A = 1.25$) for the known double-beta decay isotopes. Values are taken from [120].

detectors (0.1%), which allow to assume flat background in the ROI. The worst energy resolution is obtained by liquid scintillator experiments such as KamLAND-Zen and SNO+, where the distinction between signal and background is more complex.

Source material mass M_{det}: The source material mass for currently running or planned experiments is in the range of $10 - 400\,\text{kg}$. While parameters like the signal efficiency, the isotopic abundance and the energy resolution are mostly given by the choice of the source material and detector technology, the mass of the source material can be scaled. However, future ton-scale experiments are facing enormous technological and financial challenges.

Background index BI: It is greatly beneficial for a $0\nu\beta\beta$-decay experiment to stay in the quasi background-free regime as long as possible, since in this case the sensitivity (see Eq. 1.21) scales linearly with the exposure. Beyond that regime, the background index plays a crucial role since the sensitivity scales with $1/\sqrt{BI}$.

α, β and γ emitters with endpoint energies above the Q-value of the isotope under scrutiny create background events in the *region of interest (ROI)*. The higher the Q-value of the double-beta decay isotope, the less background sources can contribute to the background events in the ROI. Typically, only isotopes with Q-values above 2 MeV are taken into account for experimental searches (leaving eleven out of 35 isotopes).

In most experiments an important contribution comes from the *natural decay chains* of ^{238}U and ^{228}Th which are present to some extent in all surrounding materials. The highest gamma energies are 2204 keV (^{238}U chain) and 2615 keV (^{228}Th chain).

Another background is coming from *Radon gas* that emanates from the surrounding materials. It diffuses through the setup and creates background events via the 2204 keV γ from ^{214}Bi. Furthermore, charged decay products can stick to the detector and induce background via high energy alphas and betas. Nowadays, the experiments, as for instance the GERDA experiment, do not only perform gamma screening but also radon emanation measurements to reduce and quantify the background from radon gas.

Due to their short stopping length *alpha and beta emitters* are only a relevant background source if they are extremely close to the detectors, for instance on the detector surfaces or in the detector itself.

Furthermore, high energy *cosmic rays* are a potential background for all low-background experiments. The cosmic rays interact in the atmosphere of the earth and produce showers of secondary particles, composed of a hadronic component ($K^{\pm}, p, n$), an electromagnetic component (e^{+}, γ) and a muonic component ($\mu^{\pm}, \nu_{\mu}, \bar{\nu_{\mu}}$). Due to its long life-time of $\tau_{\mu} = 2.2\,\mu\text{s}$ [47] the muons can travel several tens of kilometers before they are stopped. To minimize the muon flux all double beta decay experiments are placed underground. In addition to the direct background component, the experiments have to fight against the indirect muon background created by the spallation products and neutrons using low A radiopure shielding, such as water.

In general, there exist two experimental strategies for a source-detector setup to investigate double-beta decay:

Detector and source are identical: The double-beta decay isotope is embedded into the detector material. This can either be realized by naturally occurring isotopes, such as ^{76}Ge in Germanium detectors or ^{136}Xe in liquid Xenon scintillation detectors, or by

admixtures of double-beta decay isotopes into a liquid scintillator or solids. Since it is likely that the energy of the two electrons emitted in double-beta decay gets completely absorbed in the detector material the detection efficiency is high for this approach. The choice of the calorimetric energy measurement technique – either by means of charge, phonons, scintillation light or a combination of them – defines the energy resolution of the experiment. Measuring charge or phonons in solid state detectors results in a good energy resolution because almost the entire information is collected. In contrast, the energy resolution of scintillating detectors measuring only light is inferior due to photon losses.

Detector is distinct from source: The double-beta decay isotope is embedded in thin detector foils which are placed in between two detectors. This allows to track the electrons of the decay and to determine their angular correlation, resulting in a very high background suppression. In return, these experiments have poor energy resolution and low source masses. Another advantage of this detector type is that with only one experiment many different isotopes my be deployed.

1.2.2 Experimental status of $0\nu\beta\beta$-decay searches

Since about fifty years experimental physicists are searching for neutrinoless double-beta decay, pursuing a variety of different experimental techniques.

A compilation of the to-date best results is given in Tab. 1.4 for the most used double-beta decay isotopes. Quoted are the half-life for two-neutrino double-beta decay, the most stringent half-life limits for neutrinoless double-beta decay along with the name of the experiment and the utilized detection method. Some of the experiments

isotope	$T^{2\nu}_{1/2}$ [10^{19} yr]	$T^{0\nu}_{1/2}$ [yr]	Experiment	detection method
^{48}Ca	6.4 ± 1.4	$> 5.8 \cdot 10^{22}$ [132, 37]	CANDLES	scint. crystal
^{76}Ge	193 ± 9	$> 5.2 \cdot 10^{25}$ [22, 19]	GERDA	semicond. det.
^{82}Se	9.2 ± 0.7	$> 3.6 \cdot 10^{23}$ [41]	NEMO-3	tracking
^{96}Zr	2.3 ± 0.2	$> 9.2 \cdot 10^{21}$ [38]	NEMO-3	tracking
^{100}Mo	0.693 ± 0.004	$> 1.1 \cdot 10^{24}$ [35]	NEMO-3	tracking
^{116}Cd	2.62 ± 0.14	$> 1.9 \cdot 10^{23}$ [60]	AURORA	scint. crystal
^{130}Te	82 ± 6	$> 4.0 \cdot 10^{24}$ [28, 26]	CUORE-0	bolometer
^{136}Xe	217 ± 6	$> 1.1 \cdot 10^{25}$ [25]	EXO-200	liquid TPC
	221 ± 7	$> 1.1 \cdot 10^{26}$ [73]	KamLAND-Zen	liquid scint.
^{150}Nd	0.93 ± 0.07	$> 2.0 \cdot 10^{22}$ [36]	NEMO-3	calo-tracko

Table 1.4: Overview on properties of $\beta\beta$-isotopes with $Q_{\beta\beta} > 2\,\text{MeV}$ as measured by the leading experiments. Given are the half-life for the $2\nu\beta\beta$-decay, the most stringent half-life limits for the $0\nu\beta\beta$-decay at 90% C.L., along with the name of the experiment and the utilized detection method.

are already concluded, others are still running and will provide stronger limits within the next years.

The strongest limits are obtained with liquid scintillator experiments using ^{136}Xe, such as EXO-200 [25] and KamLAND-Zen [39], and semiconductor germanium detectors such as GERDA (see Ch. 2 and references therein).

The Enriched Xenon Observatory (*EXO-200*) experiment utilizes a time projection chamber (TPC) of 40 cm diameter and 44 cm length, filled with 175 kg of liquid Xenon enriched to 80.6 % in ^{136}Xe. Since ionization and scintillation light signals are measured simultaneously, their anti-correlation allowed to reach an energy resolution (FWHM) of 4% at 2.5 MeV, the Q-value of ^{136}Xe. Based on 100 kg $\cdot$ yr exposure a lower limit to the $0\nu\beta\beta$ decay half-life of $T^{0\nu}_{1/2} > 1.1 \cdot 10^{25}$ yr at 90% C.L. was published in 2014 [25].

The *KamLAND-Zen* experiment operates an inner balloon ($R = 1.54$ m) made from 25 μm thick Nylon and filled with 13 tons of Xe-loaded liquid scintillator (383 kg of the $\beta\beta$ decay isotope ^{136}Xe). The inner balloon is surrounded by 1 kton of purified liquid scintillator ($R = 6.5$ m) which serves as shield against external radiation and as detector for internal radiation from the inner balloon and Xe-loaded liquid scintillator. The energy (FWHM $\approx$ 10% at 2.5 MeV) and position (resolution $\approx 15\,\mathrm{cm}/\sqrt{E(MeV)}$) of events are reconstructed by detecting the scintillation light with surrounding photomultiplier tubes. The combination of phase-1 (213.4 days of measurement) and phase-2 data allows with 534.5 days to extract a lower limit to the $0\nu\beta\beta$ decay half-life of $T^{0\nu}_{1/2} > 1.07 \cdot 10^{26}$ yr at 90% C.L. while exhibiting a sensitivity of only $5.6 \cdot 10^{25}$ yr [73].

In addition, there exist a variety of experiments that are currently under preparation, such as Majorana, SNO+, SuperNEMO, NEXT. They are planning to use masses in the range of several tens to a few hundred kg of source material and aim to explore $0\nu\beta\beta$-decay half-lifes up to 10^{26} yr. However, the ultimate goal of all ton-scale next-generation double-beta decay experiments, such as nEXO and a ton-scale Germanium detector experiment, is the exploration of the inverted hierarchy, requiring sensitivities in the range of $T^{0\nu}_{1/2} \sim 10^{26} - 10^{27}$ yr. For a more detailed overview on this topic the reader is referred to [76, 59].

CHAPTER 2

THE GERMANIUM DETECTOR ARRAY EXPERIMENT

For more than a decade the best lower limits on the $0\nu\beta\beta$-decay half-life came from the Heidelberg-Moscow (HdM) collaboration and the International Germanium Experiment (IGEX) using enriched Germanium detectors. Both of them published a lower limit of $T_{1/2}^{0\nu} < 1.9 \cdot 10^{25}\,\mathrm{yr}$ (HdM) [99] and $T_{1/2}^{0\nu} < 1.6 \cdot 10^{25}\,\mathrm{yr}$ (IGEX) [1], [2]. In 2004, a subgroup of the HdM collaboration claimed to have observed the $0\nu\beta\beta$-decay with a half-life of $T_{1/2}^{0\nu} = 1.19 \cdot 10^{25}\,\mathrm{yr}$ at 4σ significance [100]. This claim is later refuted (see Sec. 2.4.2). Another claim of 2006 [101] is known to be based on a false analysis [124].

Present experiments searching for neutrinoless double-beta decay of ^{76}Ge are the Majorana experiment [3] and the GERDA experiment [9]. The latter is described in this chapter.

2.1 Concept

In contrast to other experiments searching for $0\nu\beta\beta$ decay of ^{76}Ge, the GERDA experiment pursues a novel concept of operating bare Germanium detectors in cryogenic liquid, as suggested by G. Heusser [86] in 1995. Surrounding liquid Argon (LAr) allows to significantly reduce the mass of nearby detector components and at the same time serves as passive shielding against external radiation and as a cooling medium for the detectors.

The GERDA experiment deploys Germanium detectors which are isotopically enriched in ^{76}Ge to $\approx 86\%$. Since the source and the detector of the decay are equal the signal efficiency is high compared to other technologies. These detectors provide an excellent energy resolution of about 0.2% at $Q_{\beta\beta}$. The conditions during crystal growing can be well controlled leading to extremely good radiopurity of the Germanium crystals.

The GERDA experiment is operated in two phases. The first phase aimed to refute the claim by part of the HdM collaboration in 2004 [100]. It started in November 2011 and was completed in September 2013. In total an exposure of $21.6\,\mathrm{kg \cdot yr}$ was collected, the background level being $1 \cdot 10^{-2}\,(\mathrm{cts/keV \cdot kg \cdot yr})$ in the region of interest after pulse shape discrimination. No peak at $Q_{\beta\beta}$ was found and a lower limit of $T_{1/2}^{0\nu} > 2.1 \cdot 10^{25}\,\mathrm{yr}$ could be extracted at 90% C.L. [16]. Therewith, the claim was refuted with 99% probability [16]. During Phase II of the experiment an exposure

of $100\,\mathrm{kg}\cdot\mathrm{yr}$ with a background level of $10^{-3}\,(\mathrm{cts/keV}\cdot\mathrm{kg}\cdot\mathrm{yr})$ shall be collected in order to stay in the background-free regime (see Eq. 1.21). Therewith, GERDA aims to probe half-lives in the range of $10^{26}\,\mathrm{yr}$, corresponding to effective neutrino masses below $100\,\mathrm{eV}$. To reach this challenging objective several upgrades have been implemented. Of major importance are active background suppression techniques such as pulse shape analysis and the implementation of a LAr veto system.

2.2 Design

The experiment is located underground in the Hall C of the INFN **L**aboratori **N**azionale del **G**ran **S**asso (LNGS) in Italy. On average 3500 m w.e. of rock overburden reduce the muon flux by a factor 10^6 to $\approx 1\,\mathrm{muon}/(\mathrm{m}^2\cdot\mathrm{h})$.

An schematic of the experiment is depicted in Fig. 2.1. The Germanium detector array is put in a cryostat filled with $64\,\mathrm{m}^3$ of LAr. The cryostat is made of low activity stainless steel and for further shielding the inner walls are lined with radiopure copper. The whole LAr cryostat is placed inside a water tank filled with ultra-pure water. This water tank has a diameter of 10 m and a height of 9 m, leaving 3 m distance to the LAr cryostat on each side. On the one hand, the water serves as passive shielding for spallation neutrons and γ-rays from the surrounding rock. On the other hand,

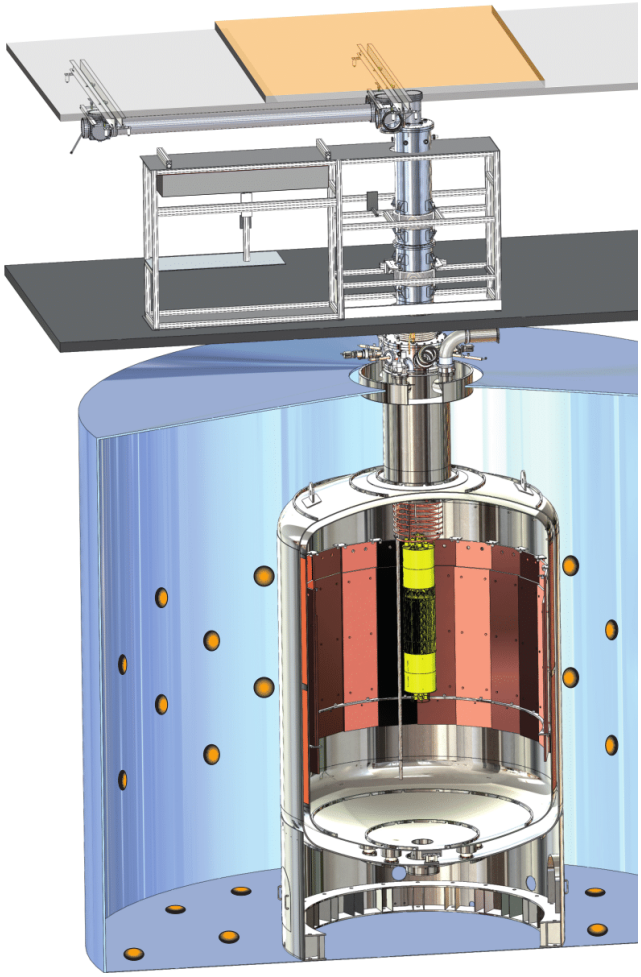

Figure 2.1: **Schematic drawing of the GERDA experiment.** The germanium detector array is surrounded by the LAr light instrumentation of Phase II and inserted in a LAr cryostat. Around the cryostat a huge water tank is installed as passive shiedl and active μ-veto. The germanium detector array can be installed through the lock system on top of the cryostat which is placed inside glove box and clean room. On top of the clean room, scintillator plates are installed as μ-veto.

it serves as an active muon veto. For this purpose the tank is equipped with 66 8“ photomultiplier tubes (PMTs) and lined with reflective mirror foil to detect Cherenkov light of the remaining muons.

The Germanium diodes are inserted in the cryogenic liquid through a lock system on top of the cryostat. The lock system is surrounded by a class 100 glove box and is placed inside a class 10.000 clean room. An additional muon veto system comprised of plastic scintillator panels is installed on top of the clean room. A detailed description of the GERDA setup can be found in [9].

2.3 Germanium detectors

2.3.1 Detection principle of Germanium semiconductors

Materials are classified as metal, semiconductor or insulator according to the *band gap* between valence and conduction band. In an ideal Germanium semiconductor crystal at 0 K the valence band is completely filled with charge carriers and the conduction band is empty. In case of Germanium the band gap between valence and conduction band is 0.67 keV at room temperature. The following description is based on [102].

The energy to lift an electron from the valence band to the conduction band can be attained by thermal excitation or by energy from interactions of ionizing radiation. An *electron-hole pair* is created by this process. An electron is lifted to the conduction band and a net positively charged vacancy is left in the valence band, referred to as hole. The electrons in the conduction band and the holes in the valence band are called *charge carriers*. Since a fraction of the energy of passing particles goes into the excitation of phonons, the energy needed to create an electron-hole pair E_{pair} is higher than the band gap. In Germanium the pair energy E_{pair} is 2.95 keV at 80 K.

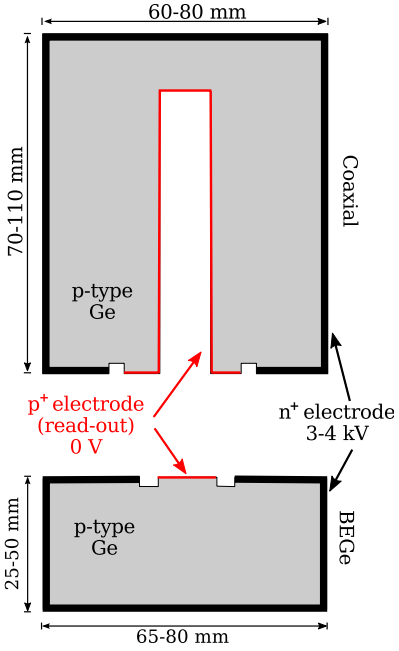

Figure 2.2: Cross section through a semi-coaxial and a BEGe detector.

Dotation: Semiconductor materials like Germanium form covalent bonds with the four nearest neighboring atoms.

In completely pure semiconductors, so-called *intrinsic semiconductors*, each electron that is excited to the conduction band leaves a hole in the valence band. By adding impurities to the material, referred to as *dotation*, additional energy levels are created which help to increase the conductivity of the material. In case Germanium is doped with an atom with one additional valence electron like Lithium it is called *n-type*. These extra electrons are only weakly bound and occupy the *donor level* slightly below the conduction band, thus only little energy is needed to raise them to the conduction band.

The material is called *p-type* if it is doped with atoms that have one valence electron less. Hence, there exist atoms that are missing one covalent bond and result in the formation of the *acceptor level* slightly above the valence band. If electrons are lifted to this level a vacancy (hole) remains in the valence band which cor-

responds to the main charge carrier in p-type semiconductors.

p-n junction To build up a semiconductor radiation detector a junction between n- and p-type semiconductor material is required. In the n-type region the density of conduction electrons is much higher than in p-type. As the density of conduction electrons sharply varies a net diffusion of conduction electrons into the p-type material takes place where they quickly recombine with holes. As a consequence, immobile positive space charges in form of ionized donor impurities build up in n-type material. The same arguments hold for holes diffusing into n-type material. These space charges (positive immobile charges in n-type material and negative charges in p-type material) create an electric field which prevents further diffusion of free charge carriers establishing a so-called *depletion layer*.

Electron-hole pairs that are created in this depletion layer by energy deposition of ionizing radiation drift along the electric field lines in the depleted region.

Depletion of HPGe detectors: A cross-section through a semi-coaxial and a BEGe Germanium detector is shown in Fig. 2.2. The bulk material is composed of p-type germanium, as well as the p^+ readout electrode (drawn in red), while the remaining outer surface is composed of an n^+ electrode. The electrodes are separated by an isolating groove.

If germanium detectors are reversely biased the created electrons and holes can be collected on the corresponding electrodes. With increasing bias voltage and depending on the impurity concentration the region between the electrodes becomes completely depleted, and thus sensitive to ionizing radiation. The voltage for which the entire detector volume is depleted is defined as the *full depletion voltage* and the region is referred to as the *active volume* of the detector. Charge carriers drifting in the electric field induce a mirror charge on the readout electrode. The induced signal is normally read-out with charge sensitive preamplifiers. Typical impurity concentrations of *High Purity Germanium* (HPGE) diodes are about 10^{10} atoms/cm^3 and bias voltages around $3 - 4\,\mathrm{kV}$.

Particle interactions in germanium: When particles pass through the active volume of a p-n-junction they deposit energy which is subsequently converted into electron-hole pairs. Since the interaction mechanism is different depending on the particle type and incident energy a brief overview is given for photons (γ-rays), electrons and positrons, and α-particles.

Photons that are emitted in radioactive decays exhibit energies in the range of a few keV to several MeV. The mean free path of a 1 MeV photon in germanium is about 3 cm. The interaction of photons with matter is dominated by three processes in this energy range:

1. Up to a few hundred keV the *photoelectric absorption* process is dominant. An incident γ transfers its entire energy to an orbital electron of the detector material which gets ejected from the shell. The kinetic energy of the photo-electron is given by
$$E_e = h \cdot \nu - E_b, \tag{2.1}$$
where $h \cdot \nu$ is the energy of the incident photon and E_b is the binding energy. The vacancy in the electron shell is filled with electrons from outer shells. The

remaining energy is released in form of Auger electrons or characteristic X-rays. If the entire energy of the incident photon is absorbed in the detector, it manifests in the energy spectrum of the detector as a *Full Energy Peak* (FEP).

2. *Compton scattering* is the dominant process in intermediate energy regions. The incident photon scatters off an electron of the detector material while simultaneously transferring part of its energy to the so-called *recoil electron*. Since all scattering angles θ are possible the transferred energy varies. When exploiting the conservation of energy and momentum the energy of the scattered γ-ray photon can be written as

$$E'_\gamma = \frac{E_\gamma}{1 + \frac{E_\gamma}{m_0 c^2}(1 - cos\theta)}, \tag{2.2}$$

where m_0c^2 is the rest mass energy of the electron. From Eq. 2.2 can be deduced that the transferred energy is maximal for $\theta = \pi$, but a small fraction of energy is still carried away by the scattered Compton gamma. This effect manifests in the *Compton Edge* below the FEP.

3. The process of *pair production*, in which the incident photon is converted into an electron-positron pair, is energetically possible if the incident photon energy exceeds 1.02 MeV. As the positron is not stable, it annihilates with another electron creating two annihilation γ's of 511 keV. If both annihilation γ's are absorbed in the detector the event contributes to the full energy peak. If one γ escapes from the detector volume without further interacting, the event shows up in the *single escape peak* (SEP) located 511 keV below the FEP. Furthermore, the *double escape peak* (DEP), 1.02 MeV below the FEP, arises due to events for which both annihilation γ's escape the detector volume.

Electrons created by either of the photon interaction processes or in β-decays of radioactive isotopes loose their energy within a much shorter range in the germanium. For example, 1 MeV electrons and positrons have a range of only 1 mm in Germanium. Electrons and positrons loose their energy through *Bremsstrahlung*, or excitation of atoms and *ionization*, as described by the Bethe-Bloch-Formula [102].

Alpha particles are much heavier. Therefore the Bremsstrahlung is negligible and the energy is predominantly deposited via ionization. The average range of 1 MeV alpha particles in germanium is 2 μm.

2.3.2 Semi-coaxial detectors

A semi-coaxial Germanium detector is a cylindrical semiconductor diode with a n-type contact on the outer surface, and a p-type contact on the surface of an axial well as illustrated in Fig. 2.2 and Fig. 2.3. Positive bias voltage is applied to the n^+ contact while the p^+ electrode is used as signal readout. During GERDA Phase I eight refurbished detectors formerly owned by the HdM [99] and IGEX [1] collaborations were deployed. These detectors are p-type semi-coaxial high-purity Germanium detectors, enriched to 86% in ^{76}Ge.

Seven semi-coaxial detectors that have been used for Phase I analysis are also inserted in Phase II of the experiment.

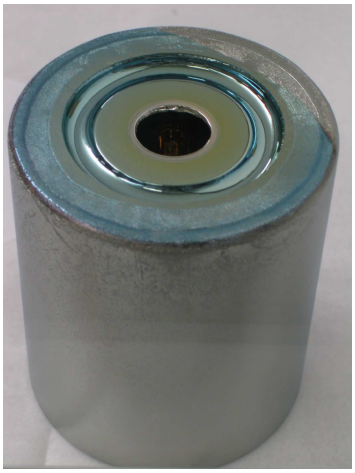

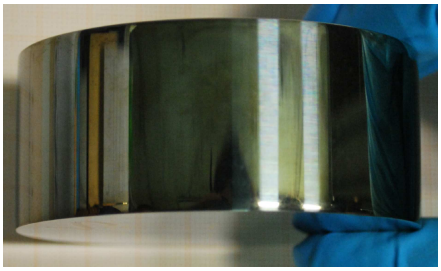

Figure 2.3: Left: Picture of an enriched semi-coaxial HPGe detector. Right: Picture of an enriched BEGe detector with passivated surface.

2.3.3 BEGe detectors

Another type of Germanium detector are *B*road-*E*nergy *Ge*rmanium detectors (BEGe). In contrast to semi-coaxial Germanium detectors, BEGe detectors have a small-sized p^+ readout electrode on one of the flat cylinder surfaces. Like for semi-coaxial detectors it is separated from the n^+ electrode by a circular insulating groove (Canberra design [54]).

This detector type has been chosen for the new Phase II detectors due to its higher background rejection by pulse shape analysis and an improved energy resolution compared to semi-coaxial detectors. Thirty BEGe detectors with a total mass of 20.0 kg have been produced for Phase II.

In December 2015, all BEGe detectors, seven semi-coaxial enriched HPGe detectors together with three natural Germanium detectors were installed in the GERDA setup. Therewith physics data taking of Phase II started in December 2015.

2.3.4 Pulse shape discrimination

By analyzing the time structure of recorded pulses the background level in $0\nu\beta\beta$-decay searches can further be reduced. Event topologies of $0\nu\beta\beta$ signals and background events can differ significantly. Different event classes of background contributions and their interactions with a BEGe detector and a potential $0\nu\beta\beta$-decay are depicted in In Fig. 2.4.

Assuming little energy loss by bremsstrahlung the $0\nu\beta\beta$ events deposit their energy mainly localized within a few mm^3 of the detector volume. This event topology is called *single site event* (SSE).

In contrast, background events which deposit their energy at well separated locations in the detector are referred to as *multi-site events*, such as multiple Compton scattered γ-rays. Other background events are coming from α or β decays close to the electrode surfaces, also referred to as *surface events*.

Pulse shape analysis for BEGe detectors using A/E: In BEGe detectors the gradient of the weighting potential is largest close to the readout electrode. As free

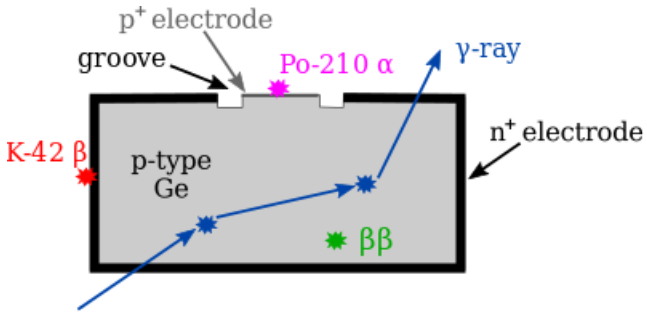

Figure 2.4: Schematic examples of different event classes of background contributions interacting with a BEGe detector. Blue: multi-site event, such as a Compton scattered γ-ray, Red: β decay on n^+ surface, Purple: α decay on p^+ surface. Furthermore, a localized energy deposition (single site event) arising from $0\nu\beta\beta$ decay is depicted in green.

charge carriers drift along their paths through this region the highest current signal is induced. In p-type germanium these are predominantly holes. Therefore, the maximum amplitude (A) of the current pulse is almost the same for all localized events of the same energy (E), independent of the position where the energy deposition happened. This characteristic of the current pulse can be utilized to effectively classify various event types.

The induced charge and current signals[1] of the different event types are depicted in Fig. 2.5:

1. Since *multi-site events* (MSE) are events with more than one energy deposition in the detector bulk volume, the individual hole clusters have different drift times until they reach the region of the strong weighting potential close to the p^+ electrode. This leads to several maxima of the current pulse separated in time. The amplitudes of the individual maxima are lower than the maximum of a single

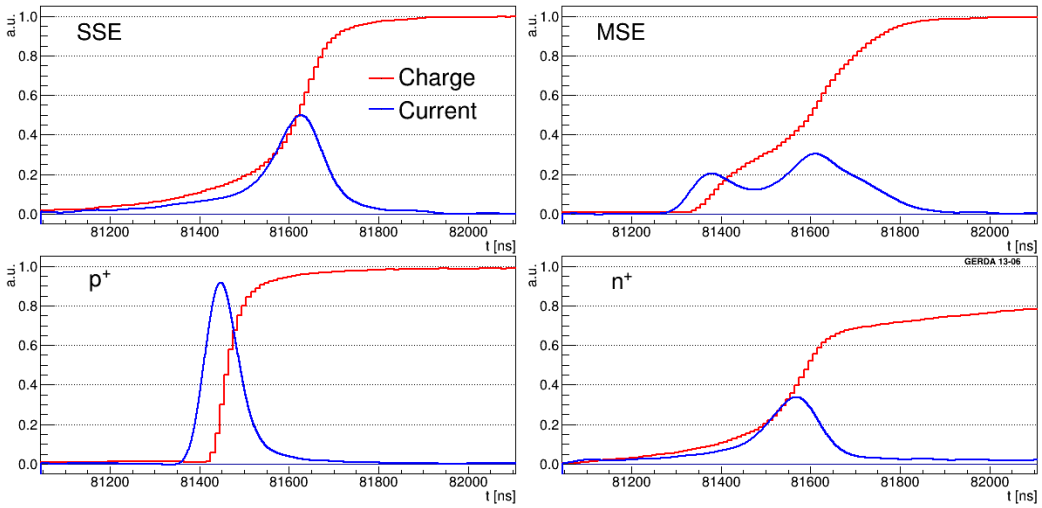

Figure 2.5: Characteristic charge and current signals of single site events (SSE), multi site events (MSE), events on the p^+ surface and on the n^+ surface in a BEGe detector. The figure has been taken from [17].

[1] In GERDA the charge signal is readout and the current signals are obtained by differentiation.

localized deposition of the same energy.

2. p^+ *surface events* exhibit larger current pulse amplitudes compared to single site events in the bulk for the reason that in this case only electrons contribute to the signal creation. Moreover, the drift velocity of electrons is larger which results in a higher maximum of the current pulse.

3. n^+ *surface events* are also called slow pulses. The dead layer and the active volume of the detector are separated by a transition layer in which the electric field is zero but the detector is not completely insensitive to particle interactions. Charge carriers in this region are not drifting towards the read out electrode but diffuse slowly. This results in longer signal rise times and charge losses.

4. *single site events* (SSE) have a constant ratio of current pulse amplitude (A) and the energy (E). The double escape peak (DEP) of the 2.6 MeV γ-ray from ^{208}Tl consists predominantly of single site events and is often used as a proxy for signal events in pulse shape discrimination studies. Another example would be events which arise from $2\nu\beta\beta$-decays in the active volume of the Germanium detectors.

The characteristic ratio of maximum amplitude (A) and energy (E) „A/E“ can be taken advantage of by using it to distinguish background events (MSE and surface) from signal like events (SSE). Henceforth, this parameter has been established during Phase I of the experiment to provide an effective pulse shape discrimination cut [17].

Pulse shape analysis for semi-coaxial detectors using a neural network: Due to their geometry and the resulting more homogeneous weighting potential the pulse shape discrimination capability of semi-coaxial Germanium detectors is inferior compared to BEGe detectors. For this detector type holes and electrons both contribute to the signal and A/E is not a suitable discrimination parameter any longer.

In Phase I the pulse shape for the semi-coaxial detectors was performed using a neural network technique. The input parameters are risetimes of the amplitude reaching between 1% and 99% of full height of the charge pulse in increments of 2%. The time at 50% is used as a reference.

The training of the neural network was carried out using ^{228}Th calibration data. The background in the region of interest could be reduced by about 45%, while keeping 90% of the signal-like DEP events [17]. As the semi-coaxial detectors make up half of the detector mass in Phase II the pulse shape discrimination of these detectors is still an important parameter for the outcome of Phase II. Nevertheless, the measurements from the integration and commissioning of Phase II that are presented in this thesis focus on BEGe data. More details about the pulse shape discrimination with semi-coaxial detectors are provided in [98, 17].

2.4 Phase I result

GERDA Phase I collected data from November 2011 until September 2013. Eight enriched Germanium detectors of the former IGEX and HdM experiment were installed since the beginning, amounting to a total mass of 17.6 kg. In July 2012, five additional enriched BEGe detectors with a mass of 3.6 kg were deployed.

2.4.1 $2\nu\beta\beta$ analysis

The to-date best published value for the half-life of two-neutrino double-beta decay ($2\nu\beta\beta$) of ^{76}Ge was extracted from the golden data-set of GERDA Phase I, amounting to an exposure of 17.9 kg · yr (see Tab. 2.1). It was determined to be

$$T_{1/2}^{2\nu} = (1.926 \pm 0.094)\, 10^{21}\,\text{yr} \qquad (90\%\ \text{C.L.}). \tag{2.3}$$

A global fit with the minimal background model has been used to extract the number of events $N_{2\nu}^{fit}$ in the $2\nu\beta\beta$ spectrum in the fit window of 570 − 7500 keV [19].

Since the background level in Phase I of the GERDA experiment is lower by a one order of magnitude compared to predecessor ^{76}Ge experiments it was possible to measure the $2\nu\beta\beta$ spectrum with a signal-to-background ratio of 3:1 in the 570 − 2039 keV energy interval. Therewith, the GERDA experiment extracted $T_{1/2}^{2\nu}$ with unexcelled precision [19]. For comparison, the first measurement of the $2\nu\beta\beta$-decay half-life based on the energy spectra obtained after the LAr veto cut after the first six months of Phase II, yielded an even better signal-to-background ratio of 30:1 and is presented in Ch. 8.

2.4.2 $0\nu\beta\beta$ analysis

The total exposure of the $0\nu\beta\beta$-analysis amounts to 21.6 kg · yr. The data was split in three data sets: "golden" and "silver" refer to data from semi-coaxial detectors before and after insertion of the BEGe string, and a distinct BEGe data set. The corresponding numbers are given in Tab. 2.1.

For the first time in this field a blinded analysis was performed. A region of 40 keV around $Q_{\beta\beta}$= 2039 keV has been blinded during data taking. After development of the background model, fixation of selection cuts for candidate signal events and the pulse shape discrimination cuts the blinded region was opened in June 2013.

The unblinded spectrum around $Q_{\beta\beta}$ is depicted in Fig. 2.6. The open (filled) histogram shows the energy spectrum after selection cuts and before (after) pulse shape discrimination. In $Q_{\beta\beta} \pm 5$ keV seven events are observed, out of which three are accepted by pulse shape discrimination.

A profile likelihood fit of the three data sets has been performed using a constant term to account for the flat background and a Gaussian peak for the signal with mean

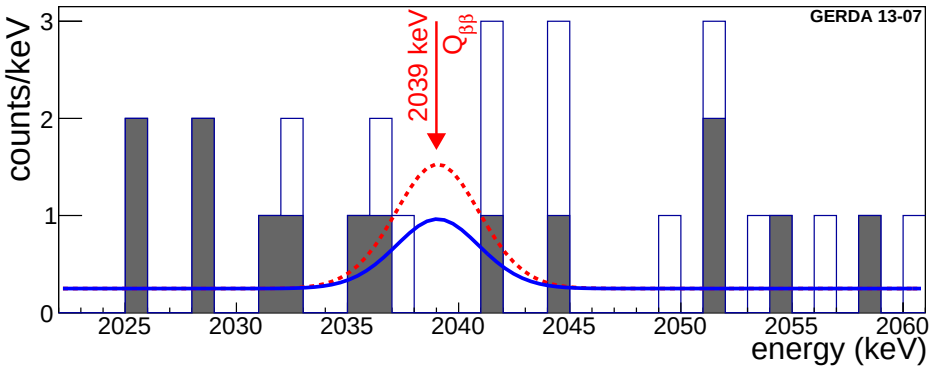

Figure 2.6: **Phase I energy spectrum at** $Q_{\beta\beta}$= 2039 keV. The open (filled) histogram shows the energy spectrum after selection cuts and before (after) pulse shape discrimination. In blue the profile likelihood fit corresponding to the derived limit on the half-life with $N^{0\nu} < 3.5$ signal counts is illustrated. In red the expectation using the central value from [100] is shown.

set	exposure $(kg \cdot yr)$	events in ROI (cts)	BI $(\frac{10^{-3} cts}{keV \cdot kg \cdot yr})$	ΔE (keV)	efficiency ϵ	counts
without PSD						
golden	17.9	76	18 ± 2	4.8	0.688 ± 0.031	5
silver	1.3	19	63^{+16}_{-14}	4.8	0.688 ± 0.031	1
BEGe	2.4	23	42^{+10}_{-8}	3.2	0.720 ± 0.018	1
with PSD						
golden	17.9	45	11 ± 2	4.8	$0.619^{+0.044}_{-0.070}$	2
silver	1.3	9	30^{+11}_{-9}	4.8	$0.619^{+0.044}_{-0.070}$	1
BEGe	2.4	3	5^{+4}_{-3}	3.2	0.663 ± 0.022	0

Table 2.1: Phase I data sets. Data taken from [16].

at $Q_{\beta\beta}$ and width σ_E. The best fit value is obtained for zero signal strength, $N^{0\nu} = 0$. Subsequently, a lower limit on the half-life

$$T^{0\nu}_{1/2} > 2.1 \cdot 10^{25}\,\text{yr} \qquad (90\%\ \text{C.L.}) \tag{2.4}$$

has been derived, corresponding to $N^{0\nu} < 3.5$ signal counts (indicated by the blue peak in Fig. 2.6).

No indication for a peak at $Q_{\beta\beta}$ has been found. Hence, the GERDA Phase I result strongly disfavors the claim for the observation of $0\nu\beta\beta$ decay by a subgroup of the HdM collaboration [100] with $> 99\%$ probability. For visual comparison, the expectation based on the central value in [100] is plotted in red color in Fig. 2.6.

Combining the GERDA data with the former HdM [99] and IGEX [1] experiments, yields an even stronger limit on the half-life of $T^{0\nu}_{1/2} > 3.0 \cdot 10^{25}\,\text{yr}$ at 90% C.L. This corresponds to a limit on the effective electron neutrino Majorana mass of $0.2 - 0.4\,\text{eV}$, depending on the utilized calculation of nuclear matrix elements.

The description of further analyses, such as the search for neutrinoless double beta decay with Majoron emission [19] and neutrinoless double beta decay to excited states [20], is beyond the scope of this thesis.

2.4.3 Backgrounds in GERDA Phase I

To identify and mitigate critical background contributions in Phase II we have to understand the critical background components in Phase I. Fig. 2.7 shows energy spectra of the semi-coaxial detectors and the BEGe detectors in this phase. The green shaded band indicates the region of interest from which the BI is determined and the red band indicates the blinded region at $Q_{\beta\beta} \pm 5\,\text{keV}$.

Several background components can be identified in both spectra distributed over a large energy range:

1. The energy region below 565 keV is dominated by the β-decay of ^{39}Ar. It is cosmogenically produced and homogeneously distributed in the LAr. Due to different detector geometries and different n^+ dead layer thickness the spectral shape is different in the dataset from the coaxial detectors and the BEGe detectors.

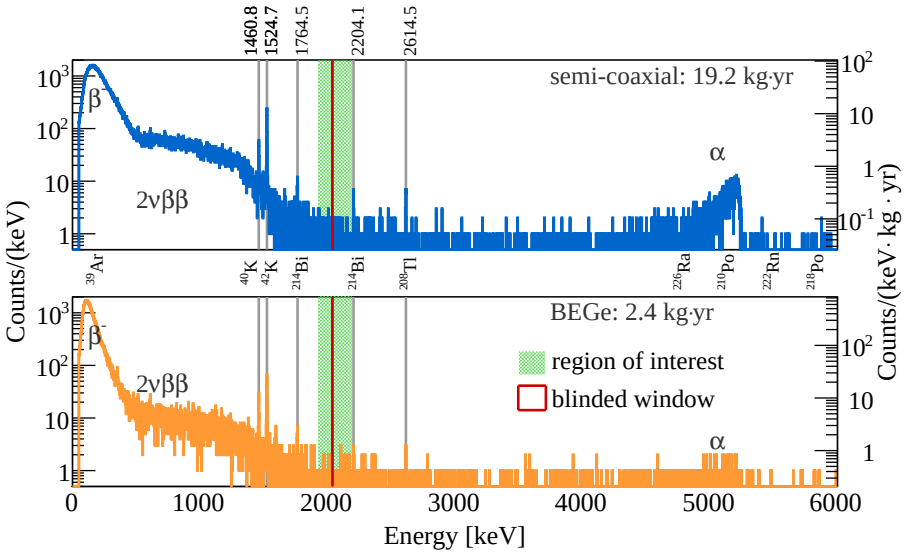

Figure 2.7: GERDA **Phase I energy spectra** with all enriched semi-coaxial (top) and BEGe (bottom) detectors. They correspond to a total exposure of 19.2 kg · yr or 2.4 kg · yr, respectively. The green band indicates the ROI from which the BI is determined and the red band indicates the blinded region at $Q_{\beta\beta} \pm 5$ keV. Prominent gamma lines are marked with gray lines.

2. The energy region between 600 keV and 1500 keV is dominated by the continuous spectrum of two-neutrino double-beta decay. The $2\nu\beta\beta$ spectrum is an intrinsic background to the $0\nu\beta\beta$ peak and best dealt with via a good energy resolution.

3. γ-ray peaks from ^{40}K and ^{42}K are visible in both energy spectra. In the spectrum of the enriched coaxial detectors also γ-ray peaks from ^{60}Co, ^{208}Tl, ^{214}Bi, ^{214}Pb and ^{228}Ac can be identified (γ-line energies are indicated in the figure canvas).

4. One prominent peak structure is visible around 5.3 MeV in the enriched coaxial detector spectrum and in the BEGe energy spectrum. It can be attributed to alpha decays from ^{210}Po on the p^+ detector surfaces. Equivalently, further peak-like structures at 4.7 MeV, 5.4 MeV and 5.9 MeV are due to ^{226}Ra, ^{222}Rn and ^{210}Po decays.

A thorough background model has been developed based on 18.5 kg · yr exposure [18]. Starting from known contaminations and visible γ-lines, background sources at different locations have been simulated and fitted to the measured energy spectra in the range of 570 − 7500 keV. The spectra coincide within the statistical uncertainty. For each of the simulated background sources the radioactive isotope, location, decay mode and its contribution to the background index (BI) is listed in Tab. 2.2.

According to the background model one third of the background of the semi-coaxial detectors in the ROI is related to ^{42}K-decays close to the detectors and another third is induced by ^{214}Bi and subsequent ^{214}Pb-decays in various locations. The remaining contributions are due to α-decays, ^{228}Th related background and cosmogenic ^{60}Co-decays in the Germanium detectors. In case of the BEGe detectors ^{42}K-decays account for more than half of the background level. This can be explained by a thinner dead layer of the BEGe detectors compared to the semi-coaxial detectors.

isotope	decay mode	location	BI $[10^{-3} cts/(keV \cdot kg \cdot yr)]$ coaxial	BEGe
^{76}Ge	$2\nu\beta\beta$	detector volume		
^{210}Po	α	p+ surface		
^{226}Ra chain	α	p+ surface	2.4	1.5
^{222}Rn chain	α	LAr in borehole		
^{42}K	β	homogenous in LAr	2.6	2.0
		n+ surface	0.2	20.8
		p+ surface	4.6	-
^{214}Bi & ^{214}Pb	β,γ	detector assembly,	2.2	5.1
		radon shroud	0.7	-
		p+ surface	1.3	0.7
		LAr close to p+ surface	3.1	-
^{40}K	β, γ	detector assembly	-	-
^{208}Tl & ^{212}Bi	γ	detector assembly	1.6	4.2
		radon shroud	1.7	-
		heat exchanger	-	-
^{60}Co	γ	detector volume	0.6	1.0
		detector assembly	0.9	-
^{228}Ac	γ	detector assembly	-	-
		radon shroud	-	-
sum			21.9	38.1

Table 2.2: Phase I background contributions for semi-coaxial and BEGe detectors as determined by the background model. The decay mode, location and background index is quoted for each simulated background source which contributes to the BI in the ROI. Values are taken from [18].

In the upper canvas of Fig. 2.8 the measured counts in the ROI are shown in gray. Note that $Q_{\beta\beta} \pm 5\,\text{keV}$ is blinded in this figure. In addition, the full model (black) along with the fitted individual background sources (colored) are superimposed. At the bottom, the background spectrum obtained from the background model (black) has been fitted with a constant (red). Apart from visible gamma lines both spectra coincide. Since HPGe diodes have excellent energy resolution $2\nu\beta\beta$-decays do not contribute significantly to background at $Q_{\beta\beta}$ and hence, a flat background at $Q_{\beta\beta}$ could be assumed.

A background level of $18.5 \cdot 10^{-3}\,(\text{cts/keV} \cdot \text{kg} \cdot \text{yr})$ is predicted by the background model. This is in agreement with the measured BI of the golden data set of $(18 \pm 2)\,10^{-3}\,(\text{cts/keV} \cdot \text{kg} \cdot \text{yr})$ (see Tab. 2.1). Further details are described in [18].

2.5 Phase II

The goal of Phase II of the GERDA experiment is an increase in sensitivity to the half-life of $0\nu\beta\beta$ decay by a factor of more than five compared to Phase I, and reach half-lives of $T^{0\nu}_{1/2} > 10^{26}\,\text{yr}$. Eq. 1.22 shows that the sensitivity in presence of background is proportional to the square root of exposure and inversely proportional to the square root of background index and energy resolution. To reach the aspired sensitivity, $100\,\text{kg} \cdot \text{yr}$ exposure at a background index of $10^{-3}\,(\text{cts/kg} \cdot \text{keV} \cdot \text{yr})$ has to be acquired. This

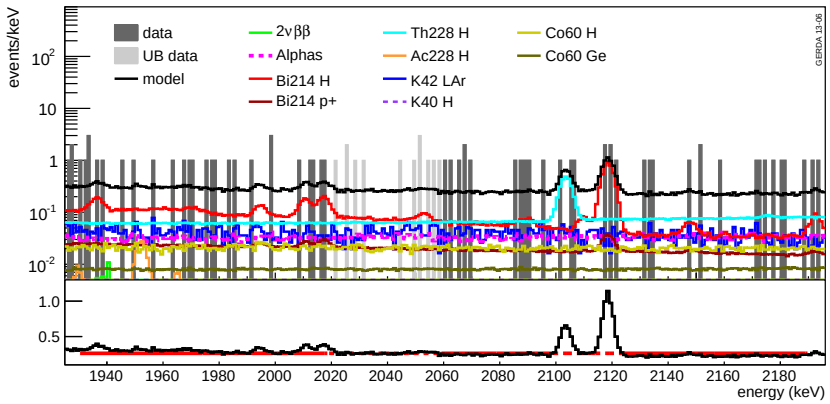

Figure 2.8: **Measured energy spectrum and background model**. In the upper part the measured counts in the ROI are shown in gray. Superimposed are the full background model (black) along with the fitted individual background sources (colored). Contaminations in the detector holders are denoted *H*, contaminations in the Germanium detector volume *Ge*, radioactive background sources in the LAr close to the detectors are labeled *LAr* and background sources close to the readout electrodes are denoted p^+. At the bottom, the background spectrum obtained from the background model (black) has been fitted with a constant (red) representing a flat background.

requires several upgrades of the Phase I detector system.

In preparation of Phase II, 20 kg of Germanium have been purchased and subsequently 30 BEGe Germanium detectors, enriched to 87% of ^{76}Ge in average, were produced (see Sec. 2.3.3). Operating them together with the detectors from Phase I allows to collect an exposure of 100 kg · yr within three years of data taking. The lock system of the GERDA cryostat had to be enlarged and modified in order to accommodate a total of approximately 40 Germanium detectors in seven detector strings.

To meet the challenging background requirements a manifold strategy is pursued. *Material selection and reduction* of components close to the detectors: of major importance are the new low mass detector holders, consisting of crystalline silicon plates, three copper rods and small interconnecting parts. The detector holder mass per detector is reduced by a factor eight compared to Phase I detector holders.[2] Along with the new holder goes a contacting scheme using low mass bonding wires and new cables.

Active background reduction techniques: Most of the Phase II detectors are of BEGe type. This detector type exhibits an enhanced pulse shape discrimination efficiency compared to semi-coaxial HPGe detectors and allows to significantly suppress background from multi-site events, n^+ and p^+ contact events. The technique based on *A/E* is described in Sec. 2.3.4. Additionally, these detectors exhibit a better energy resolution due to a smaller capacitance of the read-out contact.

As the Germanium detectors in the GERDA experiment are operated bare in LAr, for the first time in a $0\nu\beta\beta$-decay searching experiment of ^{76}Ge, the installation of a *LAr veto* for active background suppression is possible. The detection of scintillation light that is created in coincidence with an energy deposition in Germanium detectors constitutes an effective possibility to discriminate between background and potential signal from $0\nu\beta\beta$ decay. The LAr veto plays an important role to reach the aspired

[2] Phase I holders: 80 g copper, 10 g PTFE, 1 g silicon.

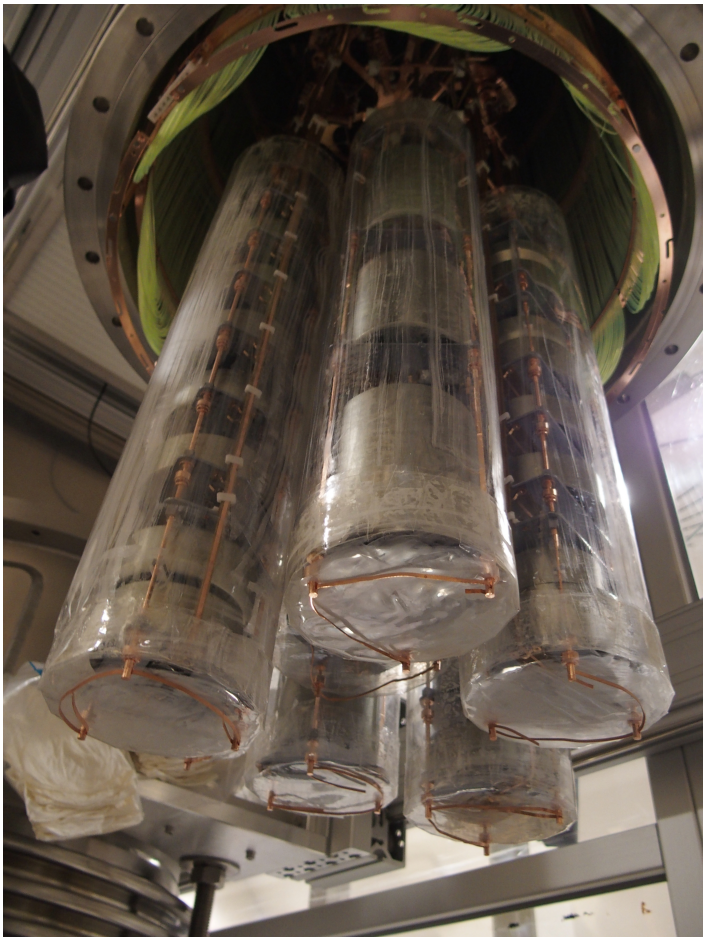

Figure 2.9: **Picture of the complete Phase II detector array**. The individual detector strings are surrounded by Nylon mini-shrouds. At the top, part of the light instrumentation is visible. See Ch. 6 for further explanations.

background level in Phase II, as discussed for the first six month of Phase II data taking in Sec. 7.5.4.

CHAPTER 3

INTRODUCTION TO THE LIGHT INSTRUMENTATION CONCEPT FOR THE GERDA EXPERIMENT

Liquid argon (LAr) scintillates upon energy deposition through ionizing radiation. By detecting this scintillation light in coincidence with germanium detector signals it is possible to discriminate between background events producing multiple interactions and a potential signal from neutrinoless double-beta decay. This chapter describes the scintillation mechanism of liquid argon along with the principle of a LAr scintillation veto, in the following referred to as *LAr veto*. In addition, it briefly summarizes the background discrimination power of such a light readout as it has been obtained by the LArGe experiment. Finally, the requirements for a light instrumentation in the GERDA experiment are discussed.

3.1 Scintillation mechanism of liquid argon

As other noble gases argon scintillates upon energy deposition. The passage of ionizing radiation through liquid argon ionizes and excites argon atoms. These ionized or excited atoms form strong bonds with neutral argon atoms, leading to ionized dimers Ar_2^+ or excited dimers (so-called excimers) Ar_2^* [29]. Ionized dimers recombine with free electrons and decay into the ground state by creating two neutral argon atoms and

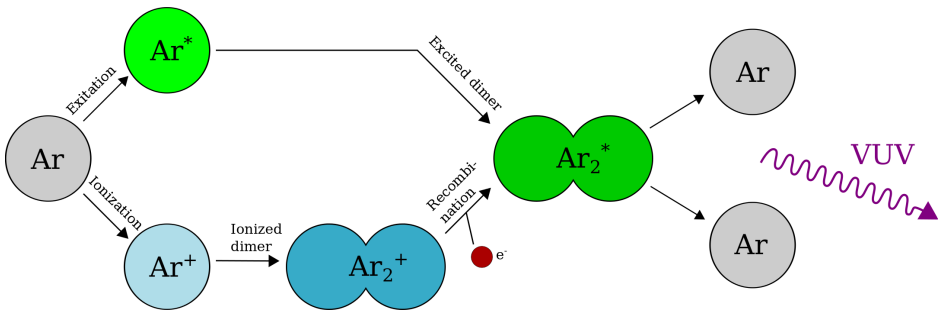

Figure 3.1: **Scintillation mechanism** of liquid (or gaseous) argon via two different excimer formation processes and subsequent decay in two neutral argon atoms and emission of 127 nm scintillation light [29].

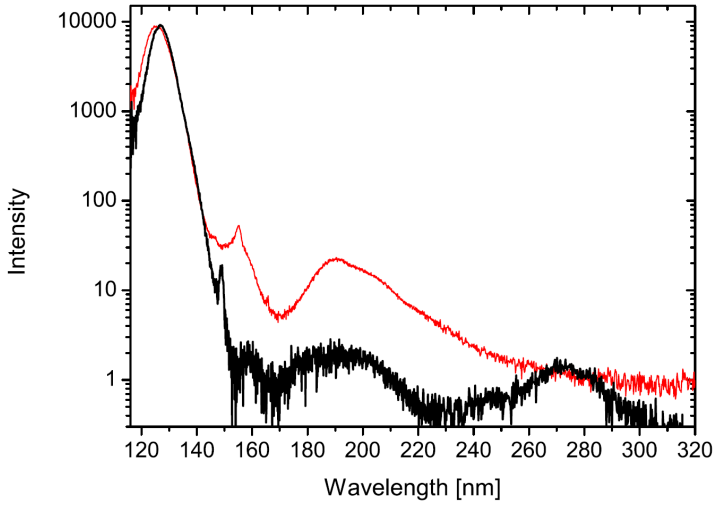

Figure 3.2: **Scintillation light emission spectrum** of liquid (black) and gaseous (red) argon, induced by an electron beam. Both spectra are dominated by the second excimer continuum at 126.8 nm. Figure taken from [81].

emitting ultraviolet scintillation light. The ratio of excitation and ionization strongly depends on the temperature and density of the argon, as well as on the incident particle type. In gaseous argon excitation is the dominant process, whereas ionization dominates in liquid argon [131, 55].

Fig. 3.2 shows the light emission spectrum in liquid (black) and gaseous (red) argon. The peak at 126.8 nm wavelength – the so-called *second excimer continuum* – dominates the light emission and is due to the radiative decay of the lowest-lying molecular states $^1\Sigma$ and $^3\Sigma$ in the gas phase. Additionally, liquid argon has some rather strong emission features in the near infrared [81].

The excimer occurs in two distinct states: a singlet state $^1\Sigma_u$ and a triplet state $^3\Sigma_u$. Due to overlapping rotational energy levels the emission peaks from the singlet and triplet excimer decay are not resolved and only one broad peak with 7.8 nm FWHM at 126.8 nm is observed [81]. The decay of the singlet state is allowed, while the decay of the triplet state is forbidden by angular momentum conservation. This manifests in the characteristic lifetimes of the decay: The decay of the singlet state with $\tau = (6 \pm 2)$ ns is called fast component and the decay of the triplet state with $\tau = (1590 \pm 100)$ ns in liquid argon is called slow component [88]. The ratio R of dimers in the singlet N_s and triplet N_t state

$$R = \frac{N_s}{N_t} \tag{3.1}$$

depends on the linear energy transfer dE/dx (LET) of the incident radiation. The more energy is dissipated per unit track length the more excimers are created in the singlet state and the bigger R becomes. R has been measured to be 0.3, 1.3, 3.0 for photons, α-particles and fission fragments, respectively [88].

In ultra-pure liquid argon, the scintillation light yield of both components together is 40 photons per keV energy deposition [63]. However, several photon reducing processes can take place in liquid argon which detoriate the scintillation light yield. These are: biexcitonic quenching, escaping electrons, charge carrier trapping, alpha quenching and electronic energy transfer to impurity atoms [63, 64, 89]. The later presumably depopulates mainly the triplet state due to collisional excitation energy transfers to impurity atoms, such as nitrogen or oxygen. They relax non-radiatively and therefore quench the scintillation light and reduce the triplet lifetime. The dependence of the

triplet lifetime with the nitrogen and oxygen contamination has been studied in [6, 7]. Based on their results, it can be concluded that the triplet lifetime provides a good measure of the impurity concentration in liquid argon, independent of the incident radiation.

3.2 Principle of active background suppression using LAr scintillation

Scintillation light is created by energy deposition in LAr through ionizing radiation, arising from e.g. muons, radioactive isotopes in argon (^{39}Ar or ^{42}Ar), cosmogenically produced radioactive isotopes in the germanium detectors and radio-impurities in solids near the detectors. Detecting this scintillation light in coincidence with germanium detector signals allows to discriminate between $0\nu\beta\beta$ decay signal events and background events. Since $0\nu\beta\beta$ decays deposit their energy within a few millimeters in a germanium detector they do not create scintillation light in LAr (see illustration in light green in Fig. 3.3). In contrast, ionizing radiation created by radioactive backgrounds can deposit part of their energy in germanium detectors and the remaining energy in liquid argon. Of special interest are background events with energy depositions in the germanium at the Q-value of double-beta decay. The remaining energy is then referred to as *excess energy* E_{excess}

$$E_{excess} = E - Q_{\beta\beta}, \tag{3.2}$$

with E the energy released in the decay and $Q_{\beta\beta}$ the Q-value of double-beta decay.

A system which is installed to detect LAr scintillation light in coincidence with germanium detector signals and to provide a veto information is called LAr scintillation light anti-coincidence veto (LAr veto) (see Sec. 6.1). Background rejection efficiency

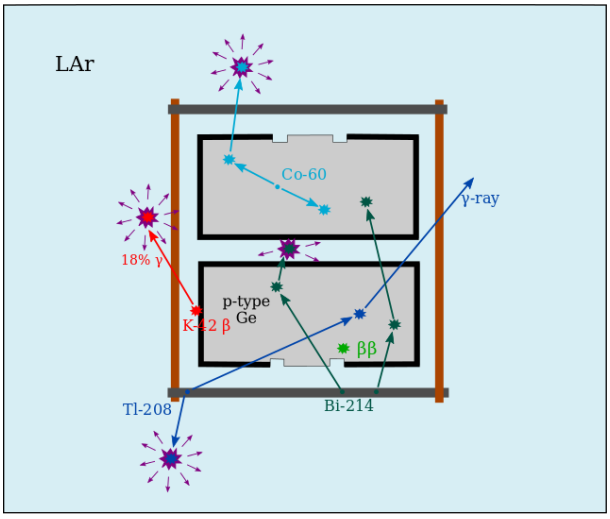

Figure 3.3: **Schematic of different classes of background contributions to the region of interest interacting with a BEGe pair and LAr.** Event topologies from five different classes are illustrated: $0\nu\beta\beta$ decays as signal class (light green). Radioactive isotopes in argon, represented by a ^{42}K (red). Radio-impurities in near-by solids which are represented by ^{208}Tl (dark blue) and ^{214}Bi (dark green) in the detector holders. Decays from cosmogenically produced isotopes in the detectors such as ^{60}Co in a BEGe (light blue).

using such a LAr veto depends on excess energy of the radioactive decay and energy threshold of the light detection system In the following discussion, no energy threshold is considered which would be caused by impurities and geometrical shadowing.

In Fig. 3.3 different classes of background contributions and their interactions with a BEGe pair and LAr are depicted along with a $0\nu\beta\beta$-decay signature:

1. *Muons*: Muons that reach the LNGS underground laboratory have an average energy of $\approx 270\,\mathrm{GeV}$. If they reach the GERDA detector array it is most likely that they deposit energy in more than one germanium detector. In addition, they deposit $2\,\mathrm{MeV}/(\mathrm{g/cm^2})$ energy in the water tank and in LAr and create therewith an enormous amount of Cherenkov and scintillation light, respectively. This event class is not illustrated in Fig. 3.3.

2. *Radioactive isotopes in LAr / on the detector surface*: In this case, energy depositions in LAr from β-particles and γ's can create scintillation light and thus contribute to background suppression efficiency. Most important background sources from this category are isotopes are ^{42}K and ^{214}Bi on detector surfaces and in LAr.

   This event class is represented by a ^{42}K decay on the detector surface (red). The β^- decay of ^{42}K has an endpoint of 3525 keV and is accompanied with 17.64% probability by a γ-ray of 1525 keV, depicted in Fig. C.4.
   The β decay happens on the n^+ surface of the bottom BEGe detector and deposits part of the energy inside the detector. The γ-ray deposits its energy inside the LAr and creates scintillation light.

3. *Cosmogenically produced radioactive isotopes in germanium detectors*: Due to short absorption length of β-particles in germanium only γ-rays can create scintillation light in LAr in case of intrinsic contaminations. Consequently, the veto efficiency depends on the energy of γ-rays that leave the germanium detector.

   The event class is represented by a ^{60}Co decay in a BEGe. The isotope decays via a β^- decay as illustrated in Fig. C.5. Two γ-rays with 1173 keV and 1332 keV are emitted coincidently. A typical topology of a ^{60}Co decay within a BEGe detector is shown in light blue. One of the γ-rays is absorbed in the detector volume via a photoelectric effect and the other does a Compton scattering in the detector and deposits the remaining energy in LAr under emission of scintillation light.

4. *Radioactive contaminations in near-by solids*: Energy of β-particles is mostly absorbed in the contaminated solid itself and is not considered in this discussion. Consequently, γ's have to deposit energy in the germanium detectors and at the same time in LAr to trigger the LAr veto. In case the focus is set on background suppression in the ROI, only isotopes with high energetic γ-rays are important.

   (a) One important radioactive isotope which belongs to this category is ^{208}Tl which arises from the ^{232}Th decay chain. It decays via a β^- decay under emission of a 583 keV γ-ray which is followed 16.7 ps later by a 2615 keV γ-ray [69] as illustrated in Fig. C.1.
   A ^{208}Tl decay is illustrated in dark blue showing a Compton scattering of the 2615 keV γ-ray in a BEGe detector and then leaving the volume. In addition, the coincident 583 keV γ-ray deposits all its energy in LAr and creates scintillation light.

(b) Another important isotope is ^{214}Bi which is contained in the natural decay chain of ^{238}U (see Fig. B.2) and decays via β^- decay with emission of several single γ-rays. The decay scheme is shown in [Fig. C.6, C.7, C.8]. The γ-ray which is mainly responsible for background in the ROI of the GERDA experiment has an energy of 2204 keV. Two distinct decay topologies from ^{214}Bi contaminations in the detector holder are illustrated in dark green.

i. First, the γ-ray on the left deposits energy via a Compton scattering in the BEGe detector and then its remaining energy in the LAr under emission of scintillation light in between the detector pairs.

ii. The γ-ray created by the second decay (right) undergoes a Compton scattering in the bottom BEGe detector and is afterwards absorbed via a photoelectric effect in the top BEGe detector without the creation of scintillation light.

The following paragraph discusses in more detail the expected background suppression by the LAr veto in the case of γ-ray induced background in germanium detectors. Therefore, the difference between single and coincident γ-lines has to be defined. *Single γ-lines* are emitted independently for which it is sufficient if the next γ is emitted after a time difference larger than the time resolution of the detector. In contrast, *coincident γ-lines* are emitted within time resolution of the germanium detectors.

Compton background in ROI: Suppression of Compton scattered background depends on the total energy that is released in form of γ-rays in the decay. The excess energy which remains after an energy deposition in the region of interest of $0\nu\beta\beta$ decay, can be deposited in LAr and creates scintillation photons. This energy is highest for ^{208}Tl decays for which the 2615 keV γ-ray is in coincidence with the 583 keV γ-ray (84.5%) and amounts to 1158 keV. In case of ^{60}Co, an energy of 466 keV remains to trigger a LAr veto system. In ^{214}Bi-decays only 165 keV excess energy is available.

Single γ-lines: If the full energy of single γ-line (FEP) is deposited in the germanium detector no energy is left to trigger the LAr veto.. These lines can only be vetoed by *random coincidences* (see Sec. 6.3.4). In the case of a single escape peak (SEP) and a double escape peak (DEP) (see Sec. 2.3.1) 511 keV and 1022 keV are available to create scintillation light in LAr, respectively, and hence, a significant suppression is expected.

Coincident γ-lines: In the case that one γ-ray is completely absorbed in a germanium detector and the other γ-ray does not interact within the germanium detector, the suppression depends on the energy of the γ-ray which is not absorbed in germanium and on the amount of energy it deposits in LAr. The same arguments as for single γ-lines hold for the summation peak of two coincident γ-rays.

Based on the Phase I background model, strong background contributions are expected from ^{42}K in LAr and on the detector surface and contaminations in solids which are placed close to the germanium detectors, such as the detector holders and high-voltage and signal cables (see Sec. 2.4.3). Following the explanations above, a strong background rejection is expected for ^{228}Th and to less extent for ^{226}Ra induced backgrounds. The background rejection for ^{42}K depends on the exact location since the β has to deposit energy in LAr in order that scintillation light might be created. The background model revealed in addition a significant contributions from α decays on the detector surface. Since no suppression by the LAr veto this event class was omitted in the discussion.

3.3 Proof of the background reduction by the LArGe experiment

The Liquid argon Germanium Detector (LArGe) experiment is a GERDA low background test facility. It is located in GDL (**G**ermanium **D**etector **L**aboratory), in the interferometer tunnel next to Hall A at LNGS. Its purpose was to test novel background reduction techniques for the GERDA experiment, in particular the background reduction in the germanium detectors with the help of LAr scintillation light detection in a low background environment. The experimental setup has been build during the PhD thesis of M. Heisel [82] and the measurements to determine the veto performance have also been carried out at this time. At this point only a short summary of the setup and the main results is given with respect to the application of such a LAr veto in the GERDA experiment.

As shown in Fig. 3.4 it consists of a vacuum isolated copper cryostat with an inner diameter of 90 cm and a height of 205 cm which is filled with 1.4 t of LAr. The cryostat can hold up to nine germanium detectors which are deployed through the lock system on top of the cryostat. The cryostat is equipped with nine 8" ETL photomultiplier tubes (PMTs) mounted on a copper plate in the way that the photocathodes are immersed in the LAr. Additionally, the inner surface of the cryostat is lined with VM2000 reflector foil. Both the reflector foil and the photocathodes are coated with a wavelength shifter (WLS) composed of Tetraphenyl-butadiene (TPB) and polystyrene in order to shift the UV scintillation light into the sensitive range of the PMTs [116]. Around the cryostat a graded shielding consisting of copper, lead, steel and polyethelene is installed. It is designed to attenuate an external γ-ray from the 2615 keV line of ^{208}Tl to $5 \cdot 10^{-8}$ of

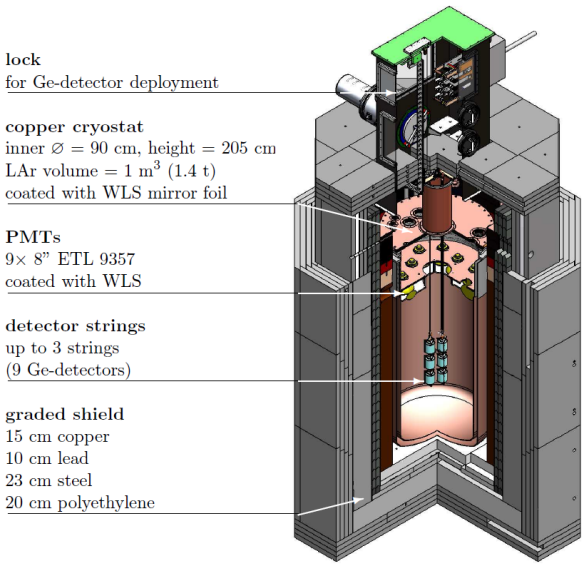

Figure 3.4: **Cutaway view inside the LArGe setup**. The main component is a copper cryostat lined with wavelength-shifting VM2000 reflector foil and filled with 1.4 t of LAr. The cryostat can hold up to 9 germanium detectors. At the top of the cryostat a copper plate with nine 8" ETL PMTs coated with wavelength-shifter is mounted. Around the cryostat a graded shielding consisting of copper, lead, steel and polyethelene is installed. At top of the setup is the lock system for detector deployment. Figure taken from [82].

the initial flux and to reach a background index of $< 10^{-2}$ cts/(keV · kg · yr) [82].

Suppression factors with various calibration sources

Several measurements have been performed using different radioactive sources (^{228}Th, ^{226}Ra, ^{60}Co) that represent some of the main background components of the GERDA experiment [18]. On the one hand, these are internal radioactive calibration sources which serve as a proxy for sources close to the detectors. On the other hand, the suppression has been measured for external ^{228}Th and ^{226}Ra sources which emulate contaminations in the cryostat and in the PMTs which are 90 cm far away. The measurements have been carried out with a natural p-type BEGe of 878 g produced by Canberra Semiconductors, N.V. Olen/Belgium [54] at a triplet lifetime value of ≈ 600 ns.

In addition to the scintillation light anti-coincidence veto, a pulse shape analysis using the A/E parameter has been applied. The method has been shortly introduced in Sec. 2.3.4. The PSD cut value is calibrated to accept 90% of the double escape peak of the 2615 keV γ-ray of ^{208}Tl. Since the peak is mainly populated by single site events, it serves as a good proxy for $0\nu\beta\beta$ events. The obtained survival probabilities of the PSD analysis, the LAr veto and their combination are listed in Tab. 3.1.

source	position	acceptance ϵ_{acc} [%]	SF in ROI LAr veto	SF in ROI PSD	SF in ROI total
^{60}Co	int	96.6	27 ± 2	76 ± 9	3900 ± 1300
^{226}Ra	ext	78.7	3.2 ± 0.2	4.4 ± 0.4	18 ± 3
	int	94.2	4.6 ± 0.2	4.1 ± 0.2	45 ± 5
^{228}Th	ext	78.3	25 ± 1	2.8 ± 0.1	129 ± 15
	int	95.7	1180 ± 250	2.4 ± 0.1	5200 ± 1300

Table 3.1: Suppression factors in the ROI ($Q_{\beta\beta}$) for various radioactive sources in the LArGe experiment using the LAr veto, the PSD and the combination of both methods to suppress the background. Furthermore the veto acceptance is quoted. The values are taken from [82].

^{228}*Th*: It is expected that ^{228}Th accounts for a significant part of the gamma background in the GERDA experiment. As example for close-by contaminations one has to name the detector holder and the front-end electronics, as external contaminations the neck of the cryostat and the heat exchanger. Therefore, it was important to determine the suppression capability of the LAr veto and the PSD for this kind of background. In Tab. 3.1 it is shown that the LAr veto suppresses an internal ^{228}Th background by a factor 1180 ± 250, the PSD analysis gives a factor 2.4 ± 0.1 and in combination the spectrum in the ROI is suppressed by a factor 5200 ± 1300. The full energy spectrum of this measurement including the differently suppressed spectra are depicted in the top part of Fig. 3.5. The suppression by the LAr scintillation light veto by three orders of magnitude can be explained because the events in the ROI are dominated by Compton background of the 2615 keV γ-ray which is emitted coincidently with the 583 keV γ-ray and more than 1 MeV excess energy is left to trigger the scintillation light veto. In case of an external ^{228}Th source the background at $Q_{\beta\beta}$ is also dominated by the Compton continuum of the 2615 keV γ-ray but it is much more likely that the 583 keV γ-ray is absorbed in the outer surrounding of the cryostat and does not contribute to the suppression of events in the ROI. Suppression factors of 25 ± 1 (LAr veto), 2.8 ± 0.1 (PSD)

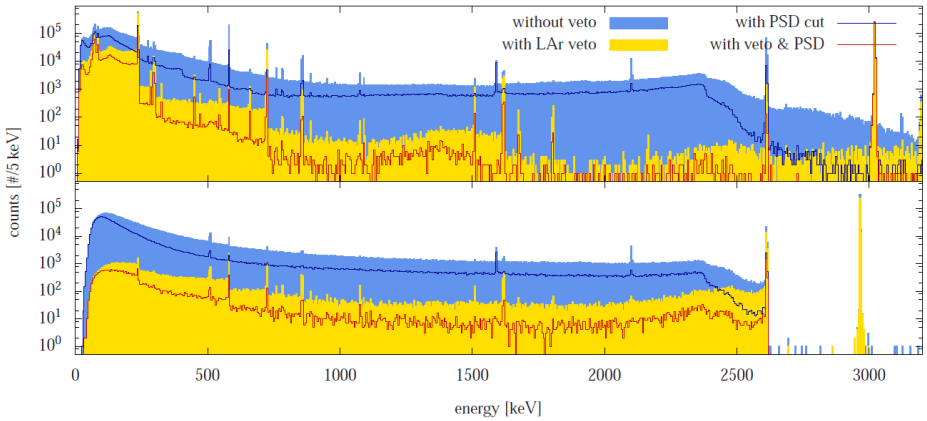

Figure 3.5: **Energy spectra for an internal and external ^{228}Th calibration source.** Top) Internal ^{228}Th spectrum. Bottom) External ^{228}Th spectrum. In both measurements the pulser is set to 3 MeV. Figure taken from [21].

and in combination 129 ± 15 are reached in this measurement [82] and the corresponding energy spectra are shown in the bottom part of Fig. 3.5. In the spectrum of the internal ^{228}Th source more γ-peaks are visible in the low energy part of the spectrum which are already absorbed outside the germanium detector in the case of an external source. In both spectra, it is visible that single γ-lines are barely suppressed by the LAr veto. The marginal suppression is due to random coincidences. Therefore these lines can be used to determine the acceptance of the veto, similar to pulser events (see Sec. 6.2). In Tab. 3.1 the veto acceptance is listed in addition to the suppression factors.

^{226}Ra: In addition, the suppression of an internal and and external ^{226}Ra source have been measured with this setup. The Compton continuum of the 2204 keV gamma of the ^{214}Bi decay to ^{214}Po dominates the region around $Q_{\beta\beta}$. Since this is a single gamma only a small amount of energy is left to be deposited in LAr. External ^{226}Ra is suppressed by a factor 3.2 ± 0.2 (LAr veto), 4.4 ± 0.4 (PSD) and the combination gives

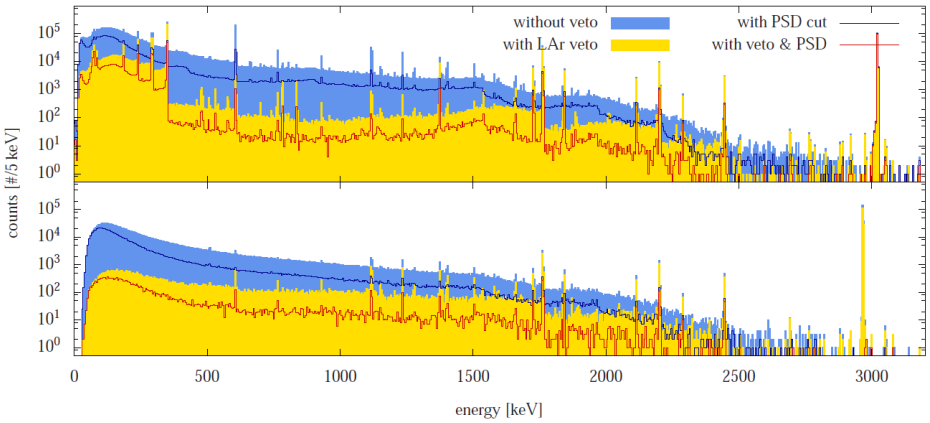

Figure 3.6: **Energy spectra for an internal and external ^{226}Ra calibration source.** Top) Internal ^{226}Ra spectrum. Bottom) External ^{226}Ra spectrum. In both measurements the pulser is set to 3 MeV. Figure taken from [21].

a factor 18 ± 3. An internal source is only slightly better suppressed by the LAr veto, SF$= 4.6 \pm 0.2$, the PSD gives approximately the same suppression, SF $= 4.1 \pm 0.2$, and the combined suppression amounts to a factor 45 ± 5.

^{60}Co: Another background contribution in GERDA is expected from ^{60}Co that is produced cosmogenically. To determine the suppression capability for this background source approximately an internal ^{60}Co source has been utilized. The following suppression factors were reached: 27 ± 2 (LAr veto), 76 ± 9 (PSD) and combined 3900 ± 1300. The high suppression factors for this source are explained by the decay structure. Events that exhibit an energy deposition in the ROI in the germanium detector are exclusively multi-site because they can only originate from the summation of the two coincident gammas and furthermore, it is most likely that the remaining energy is deposited in the immediate vicinity of the detector i.e. in the LAr.

These measurements showed that it is possible to obtain excellent suppression factors within the LArGe setup. However, it was found in later simulations that part of the suppression is due to β-particles escaping from the source holder and entering the LAr [103]. This is not expected for the same contaminations in other materials. It was found that it is possible to trigger on one single photo-electron to set a veto flag. The draw-back of such a low trigger threshold could be a bad veto acceptance due to random coincidences. The veto acceptance obtained during the calibration source measurements (see Tab. 3.1) do not represent the veto acceptance during a background measurement. Because of high source activities radioactive decays from the source that do not create a signal in the germanium detectors can be coincident with pulser events.

The orthogonality factor for the combined suppression of LAr veto and PSD (see Eq. 7.1) is 1.83 ± 0.90 in the case of the internal ^{228}Th calibration source measurement [82]. In Sec. 7.4 Monte Carlo simulations which include both the classification of events as single- or multi-site and the rejection by a scintillation light veto are presented and give a possible explaination of this feature.

Background measurement

A background measurement in LArGe has been performed utilizing a natural semi-coaxial germanium detector (GTF44) which has a mass of 2465 g. In total, an exposure of $116\,\mathrm{kg} \cdot \mathrm{d}$ was collected.

In the acquired energy spectrum background contributions from ^{208}Tl, ^{214}Bi, ^{40}K and ^{42}K can be identified together with the $2\nu\beta\beta$-decay spectrum. In a 300 keV window around $Q_{\beta\beta}$ 40 events are detected in the germanium detector. Out of these events only one survives the LAr veto cut [21]. The background is suppressed by at least one order of magnitude. The corresponding BI is $0.12 - 4.6 \cdot 10^{-2}\,\mathrm{cts}/(\mathrm{keV} \cdot \mathrm{kg} \cdot \mathrm{yr})$ (confidence intervals are given with 90%).

This background measurement could prove the high potential of a LAr scintillation light readout in the GERDA experiment. The dead time during this measurement was $< 3\%$ [82] and meets the requirements for a LAr veto using cryogenic PMTs in the GERDA setup. The LArGe setup reached the aspired background index, even though the graded shielding was not finished at the time of the measurement.

Lessons for a light instrumentation in GERDA

Some of the results of LArGe can be transferred to a LAr veto in GERDA other aspects will change. It is expected that a similar veto acceptance can be reached in GERDA if cryogenic PMT are utilized. Although, the suppression factors for comparable radioactive sources will be different due to differences in the geometry of the setup. LArGe is a relatively simple setup with only one germanium detector in the middle of the argon volume whereas an entire array of germanium detectors grouped in seven strings will be operated during Phase II of the GERDA experiment. The effect of light that is absorbed in between the detectors or in near-by solids is expected to be much more pronounced in this geometry. Since veto performance is strongly dependent on the background decomposition it is obvious that the ultimate suppression in GERDA will be different from the one in LArGe.

Some experimental teachings are obtained from the LArGe experiment: During the measurements it was not possible to operate all PMTs because either their dark rate was very unstable or the PMT was shut down by the high voltage power supply. The most likely reason for the *flashing* of the photomultiplier tubes was that the voltage dividers were operated in the gas phase of the argon and sparks were created in between pins of different high voltage. In GERDA this issue should not pose a problem since the PMTs including the voltage dividers are operated in liquid argon.

A relatively low triplet lifetime of $< 500\,\mathrm{ns}$ was measured in LArGe at the time of the background measurements [82]. The lesson for the GERDA experiment could be that it is possible to reach a good veto performance as long as the average number of detected photoelectrons is $\gg 1$ and the veto threshold is set to one photoelectron. However, the light yield of liquid argon will be strongly affected. Since the light instrumentation and germanium detector array is more complex in the GERDA experiment a reduced triplet lifetime might in the end significantly lower the background rejection by the LAr veto.

The utilized wavelength shifting reflector foil in LArGe was composed of VM2000 coated with a matrix of TPB and polystyrene. Over the operation time of LArGe part of the wavelength shifter coating was detached. Therefore, this combination of reflector foil and coating is not considered as option for the operation in the GERDA experiment.

3.4 Requirements for light instrumentation in GERDA

The light instrumentation setup for Phase II of the GERDA experiment has to meet several requirements of mechanical and of functional nature.

The quality of the scintillator, in this case liquid argon, plays a fundamental role for the veto performance. Impurities decrease light yield and attenuation length and therewith the probability to detect scintillation light in a given distance of the germanium detectors. The triplet lifetime of the scintillation is an indicator for the quality of liquid argon [82]. In 2012, the triplet lifetime of the LAr in the GERDA cryostat has been measured to be $(922 \pm 31)\,\mathrm{ns}$, as described in Sec. 5.1.2. As this seems sufficient for an effective LAr veto, based on the experience with the LArGe setup, the GERDA collaboration decided to not replace the LAr for Phase II.

As a consequence, the light instrumentation has to be inserted as a ready-build entity into a filled cryostat through the lock system, instead of being assembled in the cryostat. This decision allows to replace or work on the light detectors during operation.

The instrumentation setup has to accommodate seven germanium detector strings

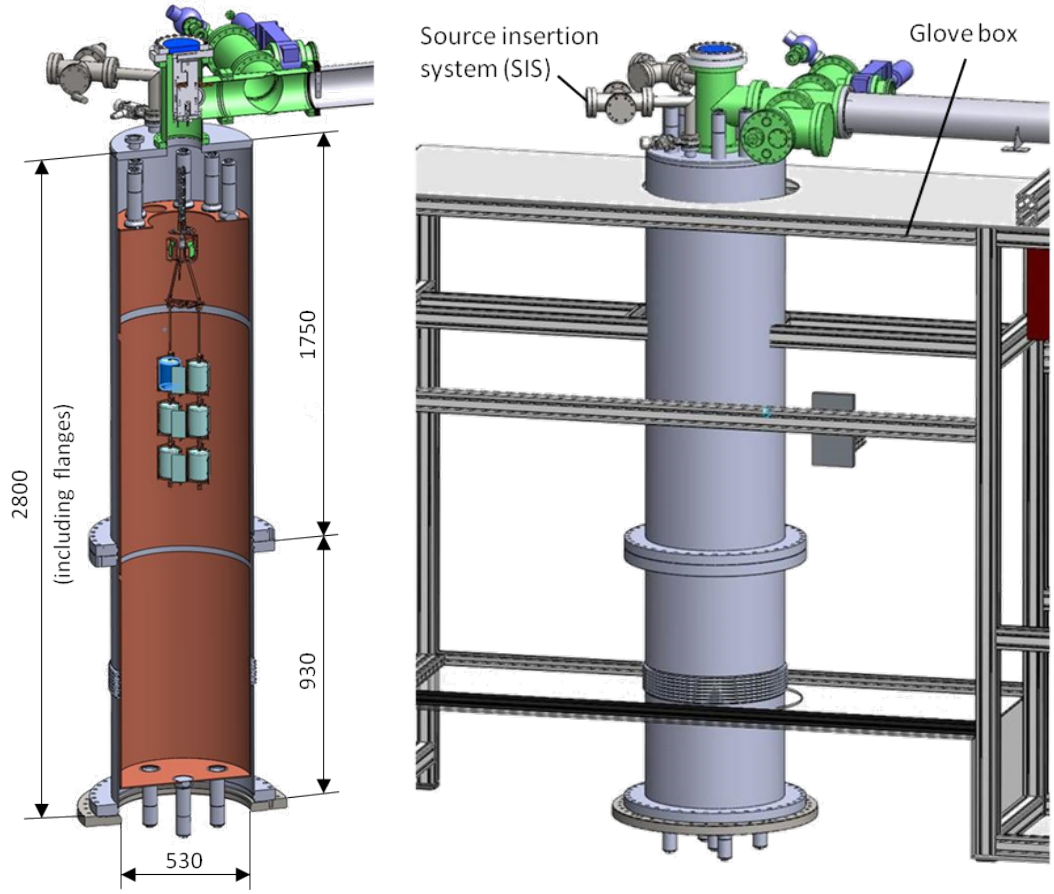

Figure 3.7: **Schematic drawing of the Phase II lock system** of the LAr cryostat. a)

with up to eight detectors each. Due to the clean room height, the maximal height inside the lock which could be realized is 2800 mm and the diameter is 530 mm. One part of the lock system is composed of a movable tube of 930 mm height. This tube has to be connected to the rest of the lock by closing flanges at the top and bottom. If the total height of the lock should be used for the light instrumentation system a part of the light instrumentation setup has to be stored inside this tube and then connected to the rest prior to the closure of the lock. The maximal outer diameter of the setup should be ≤ 500 mm which allows for several millimeters tolerance at each side.

The setup should provide permanent access to the germanium detectors. To ease practical handling it should be possible to work on the germanium detectors without dismounting the whole fiber cylinder including the cabling. This requires that germanium detectors with their support can be moved independently from the light instrumentation setup. In addition, the radioactive calibration sources have to be lowered inside the light instrumentation down to the height of the germanium detectors.

The deployed light detectors should perform stable over the whole measurement time of Phase II of the experiment. In conclusion, the GERDA collaboration decided in the beginning of the design process to explore two different light readouts, namely scintillating fibers read-out by silicon photomultipliers (SiPMs) and cryogenic photo-

multipliers. The fibers seemed promising since it was assumed they can be put much closer to the germanium detectors due to their low internal radioactivity and the high expected self-vetoing. Additionally a fiber shroud would not be optically closed to the volume outside the shroud. The LArGe facility had proven in the past that impressive suppression factors can be reached with cryogenic photomultipliers and they were considered as reliable technique. However, it was clear that the ETL 8" PMTs which were used in the LArGe experiment would be too radioactive to be operated in the GERDA cryostat and even new types of cryogenic PMTs with lower internal radioactivity would have to be placed at a distance $\geq 50\,\mathrm{cm}$. The task of testing cryogenic PMTs with respect to their long-term stability has been undertaken by the group of Prof. Lindner at Max-Planck Institut für Kernphysik (the PMT assessment is described in Ch. 4). The group of Prof. Schönert at TU Munich decided to investigate the light detection using scintillating fibers connected to SiPMs. However, since both light read-outs had not been operated in LAr for such a long time period the idea of using both simultaneously came up soon.

Another important component of a scintillation light veto system are wavelength shifting reflector foils and coatings for fibers and PMTs. As liquid argon emits scintillation light at a wavelength of 128 nm it is not directly detectable by most light detectors. The common strategy is to shift the UV light to visible light using fluorescent chemicals, such as Tetraphenyl-butadiene, with good conversion efficiencies. The foil together with the wavelength shifter should be radiopure and mechanically stable at cryogenic temperature during Phase II of the experiment. In addition, the reflector foil should be highly reflective for visible light. As described in Sec. 3.3, a VM2000 mirror foil coated with a matrix of TPB in polystyrene was used in the LArGe experiment. Due to a lack in long-term stability it is not sufficient for the use in the GERDA experiment and a new foil is developed for the light instrumentation setup in GERDA (see Sec. 6.1).

In Phase I of the experiment so-called mini-shrouds made off copper were installed around each detector string in order to minimize background from ^{42}K. These mini-shrouds have to be replaced by transparent mini-shrouds in order to allow detection of scintillation light that is created inside the mini-shroud volume[1]. A short description is given in Sec. 6.1.

During physics data taking with germanium detectors it is favorable to operate problematic germanium detectors in anti-coincidence mode. Detectors that are completely switched of count as *dead volume* as the energy depositions inside these germanium diodes are not detected. This undetected energy cannot be deposited in LAr and thus the veto efficiency of the light readout is artificially decreased. In contrast, the reduction of the energy threshold for the germanium detector-detector anti-coincidence improves the veto efficiency of a light instrumentation in GERDA in the same manner.

In Ch. 5 the expectations from Monte Carlo simulations concerning a light instrumentation for the GERDA experiment are presented and in Sec. 7.3 a comparison between the LAr veto commissioning test results using radioactive calibration sources and the corresponding Monte Carlo results is made. The final design which takes into account both the mechanical and functional requirements and the results of the Monte Carlo simulation based optimization campaign is described in Sec. 6.1.

[1] An alternative option would be to still use copper mini-shrouds but equip them with a light read-out inside the mini-shroud volume. In [103] a discussion of this option is given.

CHAPTER 4
PHOTOMULTIPLIER TUBE ASSESSMENT

For the LAr veto of the GERDA experiment eighteen 3" photomultiplier tubes of type R11065-10/20 from Hamamatsu Photonics K.K. [77] are used. These photomultiplier tubes are specified to have low radioactivity ($\sim$ mBq level) and to work at cryogenic temperature.

This chapter explains briefly the functional principle of photomultiplier tubes (PMTs) along with important parameters. Afterwards, the R11065 photomultiplier type, together with the test stands at MPIK, and the in-house developed voltage divider production optimized for low radioactivity and pulse shape are described. Sec. 4.4 focuses on the long-term tests of the PMTs and the determination of important PMT characteristics. In particular, the issue of light emission of several PMTs during the operation in a cryogenic liquid and the countermeasures undertaken by the manufacturer are explained in detail.

4.1 Photomultipliers as light detectors

The functional principle of a photomultiplier tube is as follows: an incoming photon hits the photocathode of a PMT and is absorbed. Subsequently, an electron – a so-called *photoelectron* – is emitted with a certain probability via the external photoelectric effect if the energy of the incident photon is high enough. The interior of the PMT is kept under vacuum to avoid photoelectrons to collide with atoms or molecules in gas. The produced photoelectron is accelerated towards the first dynode which is at a slightly more positive voltage than the photocathode. To improve the collection of electrons a focusing electrode is placed in between. When the first dynode is hit, several electrons are knocked out, resulting in a multiplication of electrons. The second dynode is on an even more positive high voltage and the process of multiplication is repeated, leading to a growing cascade of emitted electrons. Eventually, all emitted photons are accelerated towards an anode. The electrons on the anode create a measurable electric current which is directly proportional to the number of electrons emitted from the photocathode.

Since amplification factors of approximately 10^6 can be reached, it is possible to detect single photons with PMTs and to reach a good separation of signal and noise. Voltage divider bases are necessary to provide each dynode with the appropriate voltage

and to ensure linear response of the PMT.

The following PMT parameters are important for the successful operation in the low background experiment GERDA.

- **Total detection efficiency**: is given as the product of quantum efficiency and collection efficiency of the PMT. The total detection efficiency should be as high as possible to be able to detect single photons.

  The quantum efficiency (Q.E.) is a measure for the probability that an incident photon creates a photoelectron. Nowadays, by means of a better understanding of the creation process of bi-alkali photocathodes, quantum efficiencies of $\approx 35\%$ at 420 nm are reached [78]. Collection efficiency is a measure for the probability that an electron emitted from the photocathode is accelerated towards the first dynode and detected. It depends on the geometry inside the PMT, especially on the structure of the focusing electrodes and first dynode. In case of the R11065 PMTs it is 95% [43].

- **Gain**: is the factor by which a single photoelectron emitted from the photocathode is amplified by the manifold dynode structure. It is defined as

$$g = \frac{Q_{spe}}{e} \tag{4.1}$$

  with Q_{spe} the charge from a single photoelectron and e the elementary charge. A high gain is preferable to discriminate between charge created by photoelectrons and charge created by noise signals. It allows to reduce the number of additional amplification stages by external electronics which itself induce noise.

- **Dark count rate**: arises mainly from thermal emission from the photocathode. Thermal emission of electrons is randomly distributed in time. The signals created by thermal electrons exhibit the same structure and characteristics as a real signal. Henceforth, they cannot be distinguished from a real signal. However, when operating the PMTs at cryogenic temperature this contribution is negligable. The remaining dark count rate may be due to internal radioctivity. It is important for any experiment to understand the rate of fake signals caused by such dark counts at the specific operation conditions.

- **Afterpulses**: are caused by photoelectrons that ionize rest gas molecules before reaching the first dynode. The ion drifts back to the photocathode and in turn generates a photoelectron. Afterpulses are registered at the anode with a time delay of typically 200 ns to a few μs, thus in the same time window as the slow component of the LAr scintillation light. Consequently, they contribute to the random coincidence rate.

- **Linearity of PMT response**: defines in which energy range the relation between the number of incident photons and the detected photoelectrons is linear. It strongly depends on the design of the voltage divider base.

- **Radioactivity**: A low intrinsic radioactivity of the PMT of a few mBq is necessary to minimize the induced background level by the PMTs.

- **Thermal robustness**: The PMTs have to stand multiple thermal cycles staying tight. Moreover, the PMTs have to perform stable at cryogenic temperature and should keep or even improve performance parameters such as gain, dark rate and linearity.

4.2 R11065-10/20 3" photomultiplier tubes

The R11065 photomultiplier tube by Hamamatsu Photonics [77] has a 3-inch circular silica window. Thereof 64 mm are covered by the bi-alkali photocathode. The PMT is designed to be operated at cryogenic temperature, such as in liquid argon, in low background experiments.

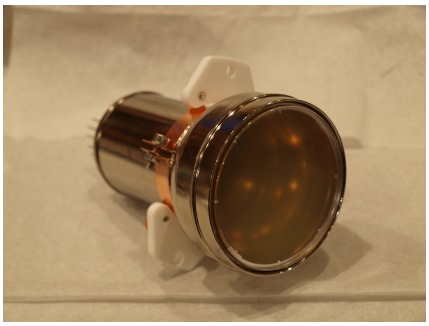

Figure 4.1: Picture of a Hamamatsu Photonics R11065 photomultiplier tube.

Hamamatsu Photonics quotes radioactivity levels of 1 mBq/PMT and 6 mBq/PMT in ^{228}Th and ^{226}Ra, respectively [91]. Based on screening measurements of the individual components of R11065-10 PMTs a contamination of < 1.94 mBq/PMT in ^{228}Th and < 1.70 mBq/PMT in ^{226}Ra, respectively, was calculated [83] and later utilized to estimate the PMT induced background index in the GERDA experiment (see Sec. 5.3.2).

This type of PMT yields a high quantum efficiency (Q.E.) above 30% at 420 nm and almost negligable at 127 nm, the wavelength of LAr scintillation light. Hence, the scintillation light has to be shifted into the visible range by using a wavelength shifting coating (see Sec. 4.2.3). To improve the stability of the coating on the silica window, the window of each PMT has been sandblasted by Hamamatsu Photonics prior to delivery.

Hamamatsu quotes a maximal cool-down rate of 2 K/min. When filling the cryogenic test stand with LAr (see Sec. 4.3) this rate can neither be controlled nor guaranteed. However, special care is taken to slowly flush and cool down the cryostat by adjusting the valve to the LAr cryostat. In the GERDA setup, the light instrumentation setup is kept for some minutes above the LAr level and then also at the positions where the photocathodes enter the LAr.

4.2.1 Generations & modifications

There exist three different models of the PMT: R11065-10, R11065-20 and R11065-20 MOD. Seven batches of PMTs have been delivered to Max-Planck-Institut für Kernphysik (MPIK) in the course of time. The first one of type R11065-10, the second one of type R11065-20 and the others of type R11065-20 MOD featuring several modifications in comparison to the baseline R11065-20 version.

Subsequently, the modifications are presented in correlation to the results of the qualification tests at MPIK (see Tab. 4.3 for the final classification of the PMTs).

1. R11065-10: This was the *original* PMT design with Q.E. $\approx 30\%$ at 420 nm.

   Apart from one PMT (BB0012) for which no acceptable gain could be reached in a cryogenic liquid, four PMTs exhibited light production during the test measure-

ments of the first batch. An investigation campaign started to exclude problems generated by the way the PMTs are operated in the cryogenic test stand, including (1) potting the cable feedthroughs, (2) gluing the voltage divider bases with resin, (3) isolating the PMT leads by PTFE tubes and resin on the intersection to the ceramic stem, (4) isolating the metal body of the PMT from the copper PMT holding structure and (5) using positive bias voltage such that the PMT body is at 0 V. In general, it was found that the probability of light flashing is reduced when operating the PMTs at lower bias voltages.

2. R11065-20: The distance of the leads to the metal body of the PMT was changed from 1 mm to 2.3 mm. The main difference in comparison to model R11065-10 was an improvement in the evaporation process of the photocathode coating which led to higher quantum efficiency (Q.E. $\approx 35\%$ at 420 nm).

   The problems with operating the PMTs in a cryogenic liquid increased strongly for the second batch of PMTs. No PMT of this batch could be operated stable in LAr, although all the aforementioned modifications to the test stand were kept. An additional test run was performed in liquid nitrogen to unambiguously exclude spike discharges outside the PMT. It was found that PMTs of this batch yield similar instabilities in liquid nitrogen. Some PMTs could not even be re-ramped once they emitted light at cryogenic temperature.

   The producer was informed about these issues and also about the fact that a time delay of the PMT response was observed (see Sec. 4.4.4). The suspicion was that the electrical conductivity of the photocathode is significantly lower in cryogenic temperature than at room temperature leading to the build-up of space charges and finally to the emission of light by electrical discharges.

   Moreover, the DarkSide experiment which operates R11065-10 PMTs in the current phase of their experiment as light detectors in a liquid argon time projection chamber, confirmed light emission of their PMTs [11] and reported it as well to Hamamatsu Photonics. They confirmed a clear dependence of the light emission issues with the applied voltage and decided to operate the PMTs at a low voltage by amplifying the PMT signal by a cryogenic pre-amplifier which is mounted directly on the voltage divider base [12].

3. R11065-20 Mod: As a result, Hamamatsu Photonics confirmed, for the first time, by own measurements light emission at the ceramic stem between two pins but inside the PMT.

   (a) By changing the pin placement of the getter stripe, they reduced the maximal voltage gap between two pins from 1176 V to 324 V. This modification will be referred to as *getter stripe placement* [91].

   (b) It was assumed that the instabilities are connected to the higher Q.E. of type R11065-20 which means more bi-alkali material inside the photomultiplier tubes. The bi-alkali which is to a certain extent also deposited on the ceramic stem could lead to an electron charge-up on the ceramic stem. It was tried to reduce the surface resistance by a *metal layer* on the ceramic stem.

batch	#	Model Nr	S/N	modifications	gain at 1500 V [10^6]	Q.E. @ 420 nm
1	1	R11065-10	BB0008	-	-	28.54
	2	R11065-10	BB0009	-	-	27.14
	3	R11065-10	BB0010	-	-	30.02
	4	R11065-10	BB0012	-	-	29.25
	5	R11065-10	BB0013	-	-	28.11
	6	R11065-10	BB0015	-	-	30.21
	7	R11065-10	BB0016	-	-	30.89
	8	R11065-10	BB0017	-	-	30.77
	9	R11065-10	BB0018	-	-	32.28
	10	R11065-10	BB0019	-	-	32.40
2	11	R11065-20	BC0005	improved Q.E.	4.92	35.16
	12	R11065-20	BC0006	improved Q.E.	3.34	36.39
	13	R11065-20	BC0007	improved Q.E.	3.75	36.15
	14	R11065-20	BC0009	improved Q.E.	4.43	35.01
	15	R11065-20	BC0011	improved Q.E.	3.01	35.26
	16	R11065-20	BC0016	improved Q.E.	3.17	34.43
	17	R11065-20	BC0018	improved Q.E.	4.84	35.80
	18	R11065-20	BC0020	improved Q.E.	5.16	35.96
	19	R11065-20	BC0021	improved Q.E.	-	34.70
3	20	R11065-20 MOD	ZK6853	getter placement	5.51	31.42
	21	R11065-20 MOD	BC0084	getter placement	3.50	35.80
	22	R11065-20 MOD	BC0086	metal coating	3.21	32.45
	23	R11065-20 MOD	BC0088	metal coating	3.29	34.82
	24	R11065-20 MOD	BC0089	wing attachment	9.24	33.82
	25	R11065-20 MOD	BC0090	wing attachment	6.95	34.08
	26	R11065-20 MOD	BC0091	wing attachment	8.38	33.41
	27	R11065-20 MOD	BC0092	wing attachment	8.99	34.14
	28	R11065-20 MOD	BC0093	wing attachment	6.55	34.17
	29	R11065-20 MOD	BC0094	wing attachment	7.39	33.50
4	30	R11065-20 MOD	ZK6904	fillet stem	4.02	25.05
	31	R11065-20 MOD	ZK6905	fillet stem	6.92	24.52
	32	R11065-20 MOD	BC0117	quartz plate	4.82	34.72
	33	R11065-20 MOD	BC0118	quartz plate	2.55	34.22
	34	R11065-20 MOD	BC0120	quartz plate	4.58	28.75
	35	R11065-20 MOD	BC0121	quartz plate	6.13	34.98
	36	R11065-20 MOD	BC0122	quartz plate	5.79	31.62
5	37	R11065-20 MOD	BC0141	quartz plate	4.15	34.32
	38	R11065-20 MOD	BC0142	quartz plate	4.35	34.11
	39	R11065-20 MOD	BC0147	quartz plate	2.91	30.06
	40	R11065-20 MOD	BC0155	quartz plate	2.71	28.59
	41	R11065-20 MOD	BC0157	quartz plate	2.16	32.07
	42	R11065-20 MOD	BC0158	quartz plate	2.15	28.29
6	43	R11065-20 MOD	BC0139	quartz plate	5.32	34.44
7	44	R11065-20 MOD	ZK7716	metal stem	6.01	30.92
	45	R11065-20 MOD	ZK7717	metal stem	6.25	30.62
	46	R11065-20 MOD	ZK7718	metal stem	4.49	30.34
	47	R11065-20 MOD	ZK7720	metal stem	6.10	27.62

Table 4.1: **Main characteristics of all PMT batches as provided by Hamamatsu Photonics.** Listed are model number, serial number (S/N), the gain at 1500 V and Q.E. at 420 nm measured by the producer along with the modifications that have been adopted for the specific PMT. See text for a discussion of these modifications.

(c) As a second option, Hamamatsu Photonics tried to use a *wing attachment* in order to trap escaped electrons from the shield while keeping the getter placement.

Ten PMTs for which these three options were adopted were sent to MPIK as batch 3. Since four PMTs from this batch did not pass the long-term tests (see Sec. 4.4.3 for a detailed discussion of light emission features of this PMT batch) and because of in-house tests at Hamamatsu Photonics, two new options were tried for the next batch of PMTs.

(d) A fillet was added at the ceramic stem to enlarge the distance between the pins – a so-called *fillet stem*.

(e) Another trial was made by putting a *quartz plate* on the ceramic stem to prevent electron charge-up on the ceramic stem.

In total, two PMTs with fillet stem and eleven with quartz plate were delivered in batch 4 and 5 to MPIK. Of the latter, three were discarded by our long-term tests.

(f) For the last PMTs delivered to MPIK, the ceramic stem was replaced by a *metal stem*.

Because of the late arrival, these PMTs could not be tested in the cryogenic test stand at MPIK but were directly mounted in the light instrumentation of the GERDA experiment.

4.2.2 Voltage divider bases

The R11065 PMTs are operated with negative high voltage bias, using custom-made voltage divider bases. The voltage divider bases (VD) are designed to provide linearity over a wide range, while lowering the heat dissipation to $P = 27.17\,\mathrm{mW}$ at $-1750\,\mathrm{V}$ (similar design as the one used in the LArGe experiment [82], see Fig. D.1 for the electronic circuit).

Special attention was paid to the low background restrictions of the GERDA experiment. The printed-circuit board (PCB) is fabricated on low radioactivity Cuflon and PEN capacitors are used. Based on the screening measurements of the PEN capacitors,

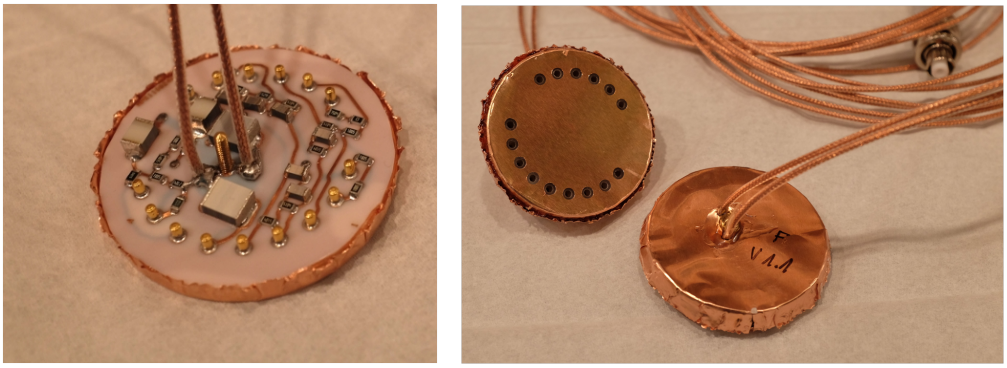

Figure 4.2: Pictures of custom-made voltage divider bases for R11065 photomultiplier tubes. Left: top of PCB. Right: Voltage divider bases from top and bottom after casting.

the activity of one voltage divider base has been derived as $< 0.5\,\mathrm{mBq/VD}$ in ^{228}Th and $< 1.14\,\mathrm{mBq/VD}$ in ^{226}Ra [83].

In the beginning of the stability test measurements (see Sec. 4.4.3) it was not yet confirmed that the light emission issues were caused by the PMT itself. In order to exclude discharges in LAr between electrical components at different potentials it was decided to cast the voltage divider base by a cylinder made out of copper and filled with resin. In this way, the PCB has no direct contact to LAr and is shielded by the copper surrounding. A voltage divider base during the casting process is depicted at the left of Fig. 4.2 and the completely casted voltage divider base from top and bottom is shown at the right. The cables are coaxial cables (SAMI RG178), fabricated without colors in the dielectric shield to ensure low radioactivity at the level of μBq/m.

4.2.3 Wavelength shifting coating

The photocathodes of the PMTs are coated with wavelength shifter (WLS) consisting of tetraphenyl-butadiene (TPB) and polystyrene dissolved in toluene. The wavelength shifter solution has been produced following the recipe developed at the Mini-LArGe and the LArGe setups [82, 116].

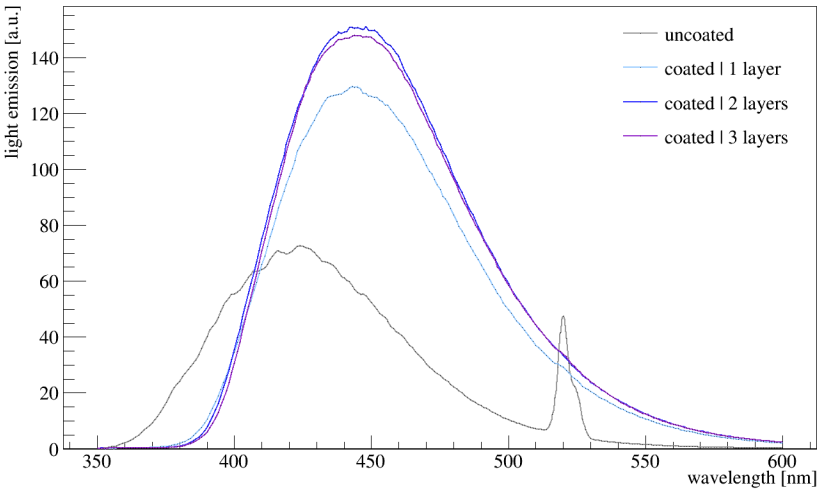

Figure 4.3: **Emission spectrum of VM2000 coated with WLS.**

The quality of the wavelength shifter solution and the optimal thickness have been checked with fluorimeter measurements at an excitation wavelength of 200 nm (Cary Eclipse, Fluorescence spectrophotometer). Fig. 4.3 shows the emission spectrum of VM2000 samples which are uncoated (gray), coated with one (light blue), two (dark blue) and three (violet) layers of wavelength shifting (WLS) solution, respectively. The emission spectra obtained with the coated VM2000 foils are shifted to higher wavelengths, the maximum being at 450 nm compared to the spectrum of the uncoated foil (maximum at 420 nm). In addition, the maximum of the emission spectrum is doubled.

Since the emission intensity is comparable for two and three layers of WLS solution painted with a brush, it was decided to coat the VM2000 foil surrounding the active volume of the test stand and the PMT photocathodes with two layers of WLS solution.

4.3 PMT test stands

4.3.1 Cryogenic test stand

A cryogenic test stand has been build up in the low level laboratory at MPIK for the qualification tests of the R11065 photomultiplier tubes. The left part of Fig. 4.4 shows a schematic drawing of the test stand. It can operate up to ten 3-inch PMTs

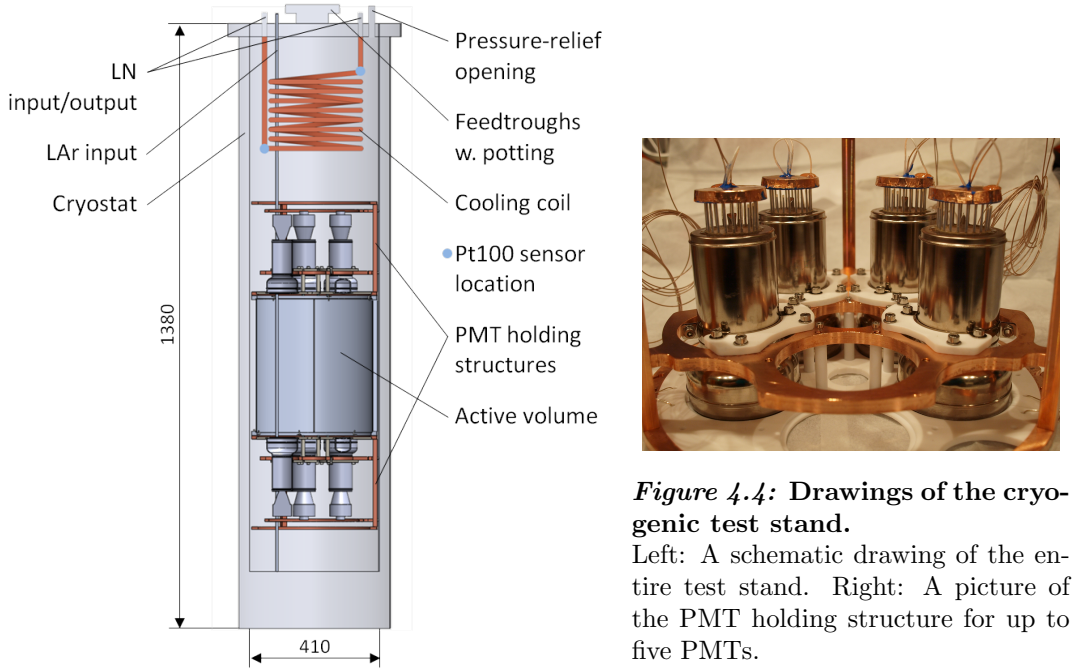

Figure 4.4: **Drawings of the cryogenic test stand.**
Left: A schematic drawing of the entire test stand. Right: A picture of the PMT holding structure for up to five PMTs.

mounted in two PMT holding structures, as depicted at the right of Fig. 4.4. Each five PMTs are facing each other with an active volume of 20 l liquid argon in between. The volume is surrounded by a reflector foil coated with wavelength shifter (see Sec. 4.2.3) to maximize the scintillation light that reaches the PMT photocathodes. At the top of the cryostat, a small flange holds 22 potted cable feedthroughs for signal and high voltage cables of the PMTs.

The threefold readout scheme of the PMTs is depicted in Fig. 4.5. The bias voltage of the PMTs is supplied by ISEG HV modules. The signal output of the PMTs is fed into custom made shapers which amplify and stretch the signal. To determine the signal rate of the PMTs, the signal is further amplified by a linear 10x amplifier and signals above the threshold of the discriminator (set to 1/3 PE) are counted by the scaler. A PC saves the rate to file. The second option shown in Fig. 4.5 allows to

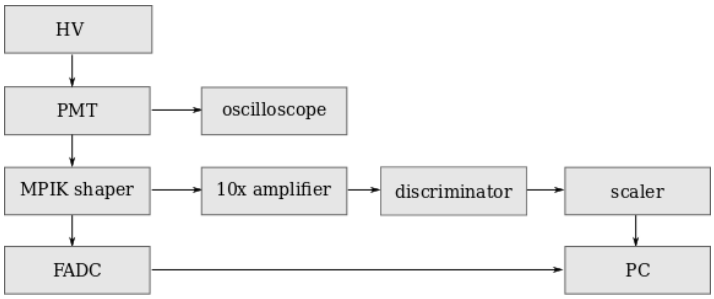

Figure 4.5: Scheme of the electronics in the cryogenic test stand.

digitize waveforms and save SPE spectra by feeding the output signal of the shaper into a 14-bit fast-analog-to-digital-converter (FADC) and saving them to file on a PC. In case an absolute gain calibration should be performed, the signal waveforms are recorded by a FADC or digital oscilloscope.

4.3.2 Dark room test stand

In addition to the cryogenic PMT test stand, a setup for room temperature measurements with low noise conditions is available at MPIK. This setup is a light-tight room which is surrounded by metal walls to shield against electromagnetic fields. Therefore, the setup is in the following referred to as *Faraday test stand*. Twelve PMT slots are available in the setup, each of them equipped with a light guide transferring light from a LED to the photocathode of the PMTs. The LED emits light of 380 nm [44].

In the test stand, a data acquisition system is installed, allowing to measure e.g. gain, dark rates and afterpulses of the PMTs. The output signal of each PMT is handled by a separate channel. First, the signals are amplified by a linear 10x amplifier and then split by a fan out module. The first output signal is further amplified (10x) and then sent through a discriminator with adjustable threshold (normally set to $\approx 1/3$ PE). The logical signal is (1) counted by a scaler and (2) sent to a time-to-digital-converter (TDC) which measures the time difference between two incoming signals. The second output signal of the fan out module is fed into a charge-to-digital-converter (QDC), integrating the signal charge in a 200 ns wide window. Scaler, TDC and QDC signals are saved by a computer. The computer controls a trigger board, sending logical signals to the QDC (starts integration window), TDC (start signal) and LEDs (trigger). A complete description of the electronic readout and data acquisition system is given in [44].

4.4 Measurements

Since the main purpose of the PMTs in GERDA is to provide a veto information in coincidence with germanium detector signals, one of the most important criteria is that the long-term performance of the PMTs is stable.

4.4.1 Test procedure in cryogenic test stand

The following procedure is typically adopted for the measurements in liquid argon in the PMT test stand:

1. mounting of up to ten PMTs in two holder modules and their insertion into the cryogenic test stand,
2. test of electric connections and subsequent closure of cryostat,
3. operation of PMTs in gaseous nitrogen (GN) atmosphere for > 1 h to assure their general performance,
4. fill liquid nitrogen (LN) and test the stability of the PMTs in LN for > 5 h,
5. cleaning cryostat from rest gas contaminations, such as oxygen, until the residual gas concentration is $< 10^{-3}$ prior to filling with liquid argon:

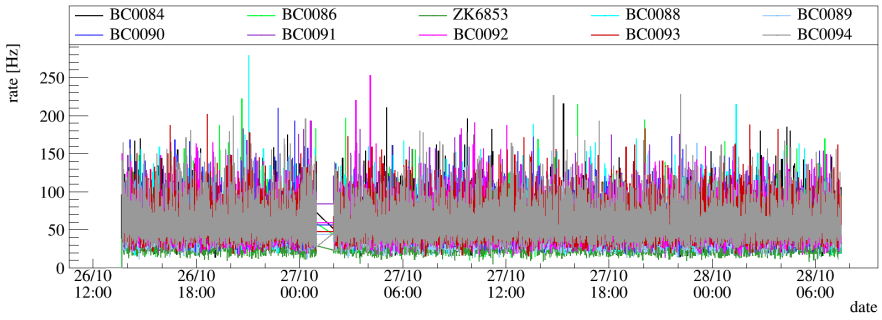

Figure 4.6: **Long-term stability of third batch of PMTs in LN.**

- pumping down to 100 mbar
- flushing with gaseous argon up to 1100 mbar
- repeated 5 times,

6. adjust PMTs to operational HV and monitor their rates over six weeks.

4.4.2 Dark rate measurement in liquid nitrogen

Testing the PMTs for a short time period in liquid nitrogen allows to verify fundamental requirements for stable operation in a cryogenic liquid, such as the mechanical stability and tightness of the photomultiplier tubes. In contrast to liquid argon, the dielectric strength of liquid nitrogen is higher. Thereby spark discharges on the voltage divider base are excluded as possible origin of unstable behavior of the PMTs. In Fig. 4.6 the rate of ten PMTs from the third batch recorded in LN during 18 h of operation are depicted. The average rates of these ten PMTs vary between 34 Hz and 59 Hz (see Tab. 4.2). The average rate amounts to 53.0 ± 8.0.

Since LN is a non scintillating medium, these rates correspond to the intrinsic dark noise rate of the R11065 PMT at cryogenic temperature. The dark noise rate of PMTs contribute to the random coincidence rate in the GERDA experiment and thus lower the acceptance of an installed veto system. In the GERDA experiment, 16 PMTs with a dark noise rate of 53 Hz and a 5 μs coincidence time window lower the veto acceptance by 0.4%.

SN	HV [-V]	dark rate [Hz]
BC0084	1514	53.4
BC0086	1528	49.5
ZK6853	1319	33.7
BC0088	1409	57.9
BC0089	1240	45.9
BC0090	1282	58.8
ZK6901	1255	58.0
BC0092	1242	55.0
BC0093	1294	58.6
BC0094	1272	59.0

Table 4.2: Dark rates in LN.

4.4.3 Long-term stability

The long-term stability has been tested by operating each PMT for at least six weeks in the cryogenic test stand at its operational voltage. The operational voltage was chosen as low as possible (gain $\approx 2 \cdot 10^6$) since we observe that the light emission problems decrease at lower voltage.

This section elucidates the phenomena discovered in different PMTs during the long-term tests. It is based on the test of the third batch of PMTs since only with

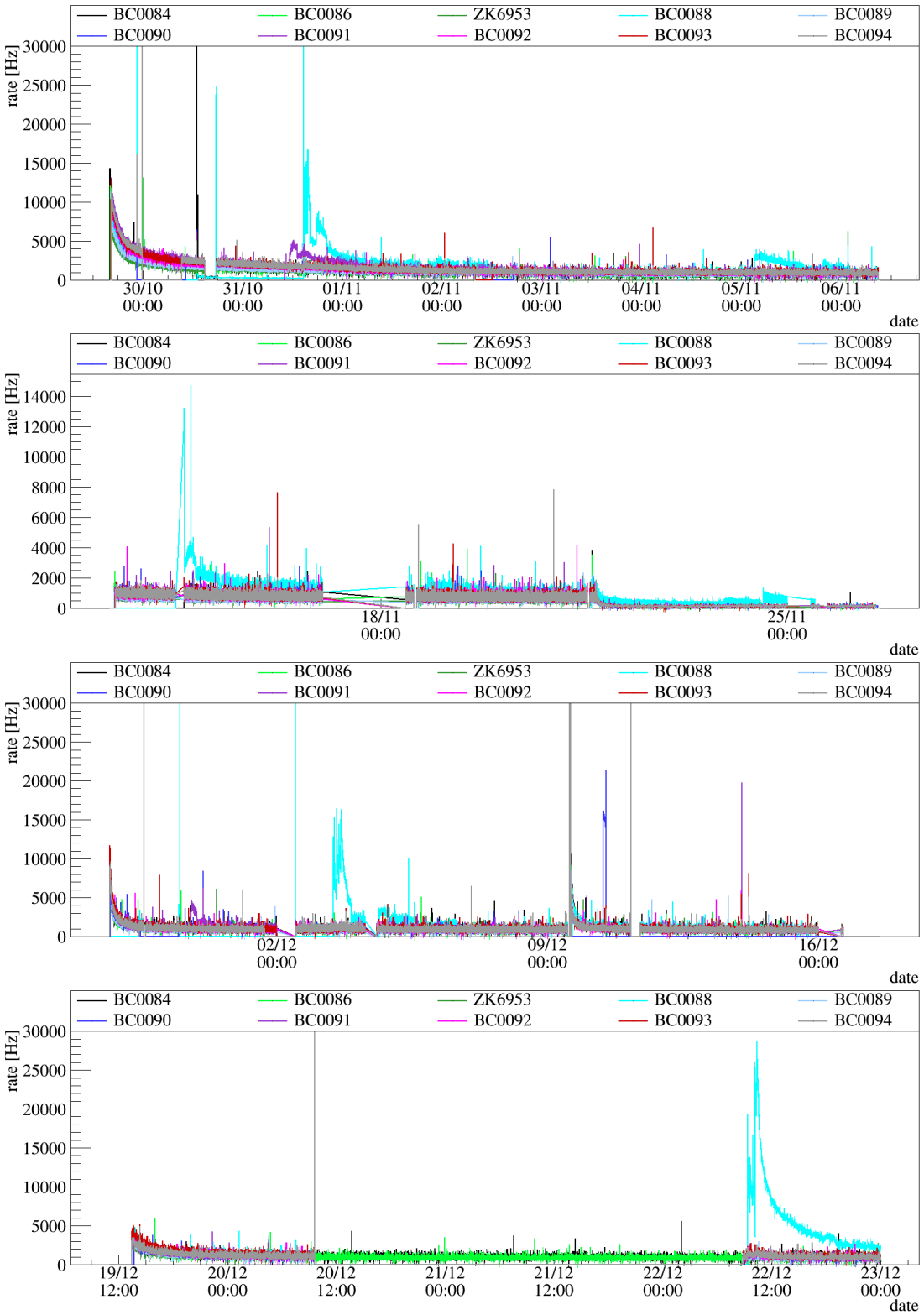

Figure 4.7: Long-term stability of third batch of PMTs measured in LAr. See text for a discussion of the observed features.

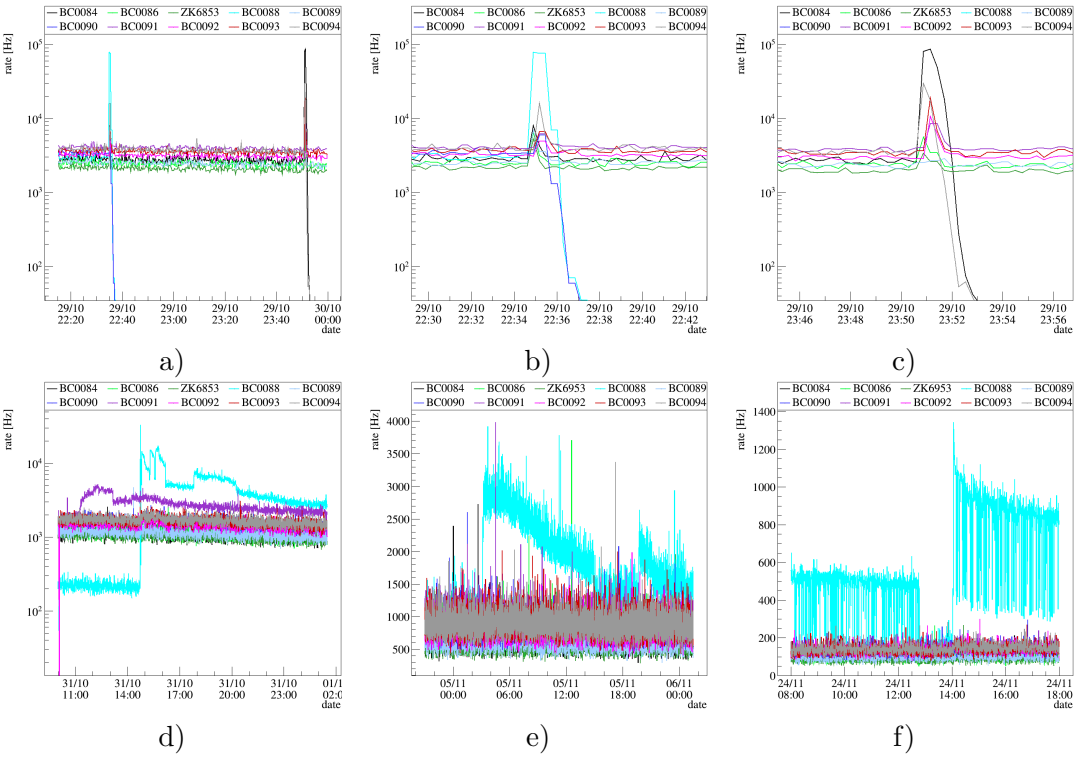

Figure 4.8: **Close-up of different instabilities in LAr in various PMTs of the third batch.** a) - c) instant flashes. d) & e) constant flashing. f) oscillating flashing.

their delivery the problems diminished to an extent that allowed long-term tests of the PMTs.

All PMTs are connected to a slow control which continuously monitors signal rates and divider currents during the long-term tests. The PMTs are automatically ramped down in case a rate threshold of 20 kHz and/or a divider current of 0.1 mA is exceeded.[1]

In Fig. 4.7 the signal rates of all PMTs belonging to the third batch are shown during the complete long-term test period (29/10/2013 to 23/12/2013). After cooling down and turning on the PMTs they need to be operated for several hours until the rate is stabilized since they were exposed to light during the installation process. In LAr this rate is typically around 1000 to 1500 Hz. Only if the LAr is contaminated with impurities, such as nitrogen and oxygen, and the triplet lifetime is significantly reduced the rate may be significantly lower. An example can be identified on the 22/11 when the active cooling was too strong such that the cryostat was at a slight underpressure and the LAr was contaminated with air. As a consequence, the signal rates went down from 1000 Hz to 200 Hz. In these rate plots several features can be identified:

Instant flashing: The most prominent feature produces huge and instant light flashes, as illustrated in the close-up in Fig. 4.8 a), b) and c). Two sparks are visible Fig. 4.8 a). A zoom into the first one is shown in Fig. 4.8 b) and reveals that PMT BC0088 (cyan) started to emit light. It was automatically ramped down as soon as the monitoring system detected a rate above the threshold (maximum rate reached $\approx$ 80 kHz). Other PMTs, such as BC0090 (dark-blue) which was mounted on the

[1] During some time the rate threshold was increased to 30 kHz such that a flashing PMT does not evoke other PMTs which only detect the light to be ramped down.

opposite side of the LAr volume, detected the light emitted by BC0088 and was also ramped down because it exceeded the rate threshold. All the other PMTs detected also the light produced by BC0088 but did not exceed the rate threshold. 100 minutes later BC0084 (black) produced also such an instant light spark (see Fig. 4.8 c)). Again, one PMT (BC0094 gray) was ramped down together with the light emitting PMT while the others exhibited only an increased rate. In other cases, the PMT shut-down was even due to the surpassing of the trip current in the high-voltage module.

The assumption is that these instant flashes are caused by electrical discharges on the ceramic stem of the PMT. They may occur because space charges can be build up if part of the bi-alkali of the photocathode is deposited on the isolating ceramic stem. The manufacturer confirmed light emission at the ceramic stem at cryogenic temperatures [91] by own tests.

Constant flashing: The feature of constant light production is illustrated in Fig. 4.8 d) and e) by PMT BC0091 (purple) and BC0088 (cyan). BC0091 reaches at maximum a rate of 5 kHz and even returns to the same level as the stable PMTs after several hours. This time, the other PMTs do not detect the light emitted by the flashing PMT. Several times during the long-term test BC0088 produced continuously light but in contrast to BC0091 the rate was much higher (up to 30 kHz. Fig. 4.8 d) illustrates the rate evolution of PMT BC0088 when trying to ramp it up after it instantly flashed. The voltage was increased to a level of $\approx$ 15 kHz signal rate, kept constant until the rate decreased to a level of below 8 kHz and then increased again. The sudden jumps at 4 p.m and 6 p.m are intrinsic to the PMT behavior and not caused by voltage changes. A slight increase of the signal rate of the other PMTs is observed. The rate course proves that even for a PMT which flashes regularly it is possible to ramp them slowly up to nominal voltage and to have them running stable for some time. However, this was never considered as an option for the operation of a PMT inside the GERDA light instrumentation. To conclude, all PMTs which showed this behavior during the long-term tests were returned to Hamamatsu and marked in red in Tab. 4.3.

In contrast to the instant flashed, there are indications that the constant flashing is caused by micro-discharges on the last dynodes of the PMT [77]. Similar to the discharges on the ceramic stem they are related to a deposition of bi-alkali.

Oscillating flashing: This feature was only observed with PMT BC0088 (see Fig. 4.8 d)). With a frequency of < 10 mHz the rate jumps down by $(400 - 600)$ Hz. While possible mechanism have been explained that may lead to instant and constant flashing, no possible explanation is found yet for the oscillating flashing of PMT BC0088.

A final classification of all delivered PMTs is given in table Tab. 4.3. The color coding indicates the status after the long-term tests at MPIK and in the GERDA light instrumentation setup (see Sec. 4.5). In total, 42 PMTs had to be tested in order to find 18 PMTs which are qualified for the operation in the GERDA light instrumentation setup.

batch	#	SN	op. HV [-V]	test time [d]	classification MPIK	classification GERDA	comment
1	1	BB0008	-	-			
	2	BB0009	-	-			
	3	BB0010	-	> 39			
	4	BB0012	-	-			low gain
	5	BB0013	-	-			
	6	BB0015	-	-			
	7	BB0016	-	> 39			
	8	BB0017	-	> 39			
	9	BB0018	-	> 39			
	10	BB0019	-	-			
2	11	BC0005	-	-			
	12	BC0006	-	-			
	13	BC0007	-	-			
	14	BC0009	-	-			
	15	BC0011	-	-			
	16	BC0016	-	-			
	17	BC0018	-	-			
	18	BC0020	-	-			
	19	BC0021	-	-			
3	20	ZK6853	1494	> 51			
	21	BC0084	-	> 104			flashed once
	22	BC0086	1538	> 51			
	23	BC0088	-	-			
	24	BC0089	1322	> 51			
	25	BC0090	1382	> 129			
	26	BC0091	1338	> 104			continuous flashing
	27	BC0092	1335	> 51			
	28	BC0093	1379	> 51			
	29	BC0094	1347	> 51			
4	30	ZK6904	1421	> 90			
	31	ZK6905	1339	> 53			afterpulses
	32	BC0117	1453	> 53			
	33	BC0118	1535	> 93			
	34	BC0120	1626	> 90			
	35	BC0121	-	-			
	36	BC0122	1393	> 53			
5	37	BC0141	1445	> 40			
	38	BC0142	1429	> 40			
	39	BC0147	1559	> 40			
	40	BC0155	1542	> 40			afterpulses
	41	BC0157	1612	> 40			continuous flashing
	42	BC0158	1577	> 40			
6	43	BC0139	-	-			
7	44	ZK7716	-	-			
	45	ZK7717	-	-			
	46	ZK7718	-	-			
	47	ZK7720	-	-			

Table 4.3: **Final classification of all PMTs after testing**. The operational bias voltage and test time are quoted for the long-term tests at MPIK. In addition to the classification after the long-term tests at MPIK the performance in the GERDA setup is given as of 2016/11/01.

4.4.4 Investigation of the delayed PMT response

During PMT tests in the test stand it was found that some PMTs exhibit a significant time delay between reaching operational voltage and building up the final signal rate in LAr. A dedicated series of measurements have been performed to study this phenomenon in more detail as described in [85]. Therefore, only one PMT was ramped up each time to nominal voltage in $(20 - 30)$ sec while the others were kept turned off. The signal rate was continuously monitored and SPE spectra were acquired in time intervals of $(10 - 60)$ sec by the FADC (see Sec. 4.3).

First, these measurements have been performed in gaseous nitrogen at room temperature. No time delay between reaching signal rate and gain, respectively, and nominal voltage was observed.

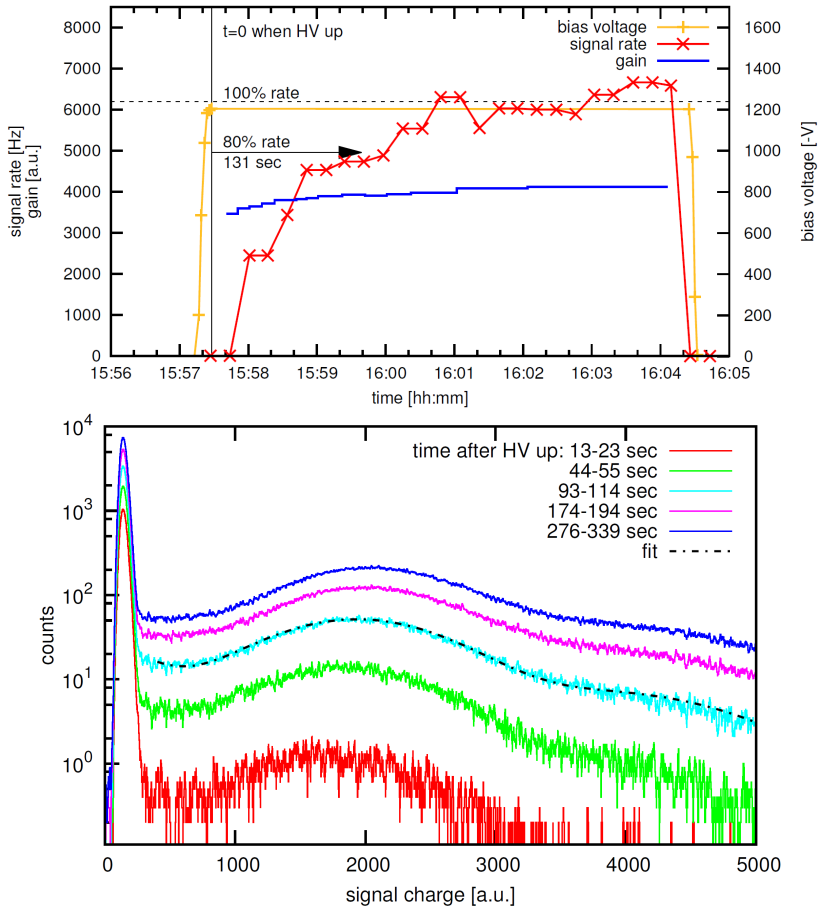

Figure 4.9: **Delayed signal rate of PMT BB0016.** Left: Bias voltage, signal rate and gain versus time. Right: SPE spectra acquired in short time intervals after ramping up the PMT to nominal voltage. Figures are taken from [85].

Second, the PMTs were submersed in LAr. After thermalizing the same measurement series were performed at cryogenic temperature. In Fig. 4.9 the results for one typical PMT (BB0016) are illustrated. At the left, the bias voltage (yellow) is plotted together with the signal rate in Hz (red) and the gain in arbitrary units (blue). The time delay between reaching nominal voltage and 80% of the final signal rate is 131 sec while the gain changes only by $\approx$ 20% (illustrated by SPE spectra acquired in the

individual time interval at the right of Fig. 4.9). Out of ten PMTs seven exhibited a significant time delay of up to 211 sec. The mean value of all PMTs was 76.6 sec.

This observation of a time delayed signal rate indicates a deterioration of the collection efficiency caused by a low electric conductivity of the photocathode at cryogenic temperature. It is known from literature that an inhomogeneous potential of the photocathode strongly affects the collection efficiency. Furthermore, a reduced potential at the photocathode reduces the amplification factor between cathode and first dynode and thus the gain of the PMT [79].

4.4.5 Gain

The following subsections describe measurements which were performed in the Faraday test stand.

The gain of a PMT is measured by determining the charge of a single photoelectron and dividing it by the elementary charge e. Typically, the charge spectrum is collected by illuminating the PMT by a LED triggered at single photon intensity[2] and measuring the charge by a QDC.[3] The charge spectrum in Fig. 4.10 contains several components: (1) the pedestal (green) being populated by events for which no pulse was detected in the integration window but only the baseline noise is integrated. The pedestal peak is centered a μ_0 since the signal baseline is adjusted to a non-zero value. (2) The Gaussians attributed to one, two, three,... photoelectrons (blue). The Gaussian peak of a pulse which contains i PE is centered at $i \cdot (\mu_1 - \mu_0) + \mu_0$, with μ_1 the mean of the single photoelectron peak (SPE peak).

The mean values of the charge spectrum are extracted by fitting the functions $f_1(x)$ (pedestal) and $f_2(x)$ (PE Gaussians) to the spectrum [80], with

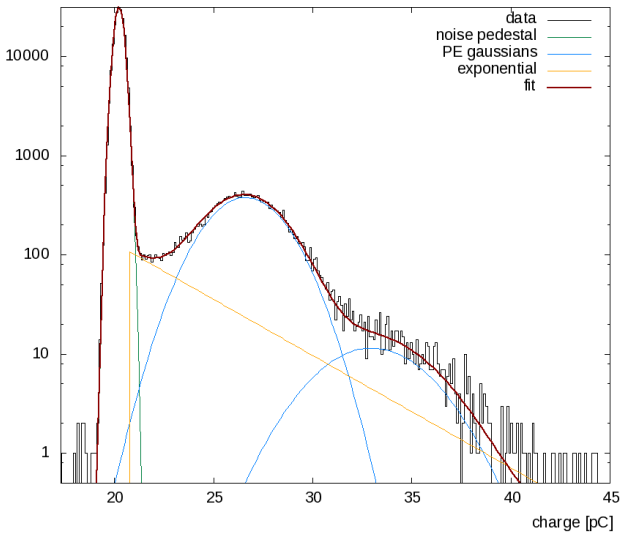

Figure 4.10: Single photoelectron spectrum and its components.

[2] Intensity at which, on average, every 10th pulse or less is detected by the PMT.

[3] If no absolute gain calibration is needed the same spectrum can be acquired using a FADC (see Sec. 6.3.3)

$$f_1(x) = A_0 \cdot \exp\left[\frac{-(x-\mu_0)^2}{2\sigma_0^2}\right], \text{ and} \tag{4.2}$$

$$f_2(x) = \sum_{i=1}^{4} A_i \exp\left[\frac{-(x - i(\mu_1 - \mu_0) + \mu_0)^2}{2i\sigma_1^2}\right] + B\exp(-x\tau). \tag{4.3}$$

The exponential function in $f_2(x)$ is added for phenomenological reasons, probably accounting for under-amplified pulses. Consequently, the gain is given as

$$g = \frac{\mu_1 - \mu_0}{10e}, \tag{4.4}$$

with the factor ten accounting for the 10x amplifier of the PMT signals placed before the QDC.

Hamamatsu Photonics specified for most of the delivered PMTs, in addition to the quantum efficiency, the gain that they have measured at 1500 V (Tab. 4.1). Fig. 4.11 shows the comparison of their measured gain to the gain measured in the Faraday test stand (left) and the relative difference between the values (right). At the left a red line is drawn indicating 100% correlation of the measured gains. The relative differences vary between −40% and +38%. However, no instable behavior has been seen for the two PMTs with the highest gain difference and no PMT was returned because of this deviation.

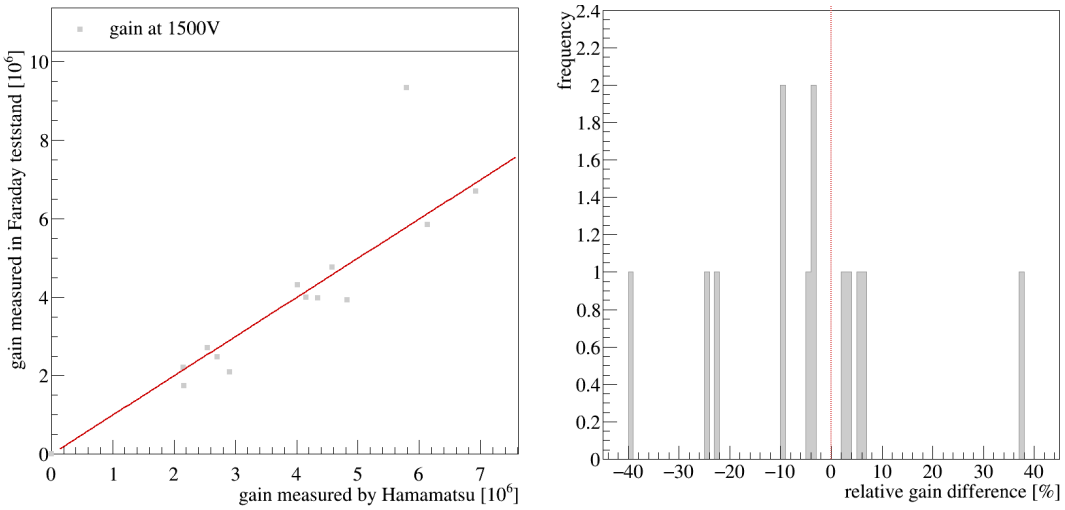

Figure 4.11: **Comparison of gain at -1500 V to the value provided by the manufacturer.** Left: Illustration of gain determined in Faraday test stand vs the gain at -1500 V provided by Hamamatsu. Right: Relative gain difference between the two values.

4.4.6 Peak to valley and resolution

The peak-to-valley (P/V) of a PMT is defined as the ratio of the SPE peak's maximum and the valley which is given by the minimum between the noise pedestal and the SPE peak. Hence, it is a measure for the signal-to-noise separation of the PMT signals.

The mean of the SPE peak shifts to higher charges and thus gain when increasing the bias voltage of the PMTs.[4] In this special low noise conditions, the peak-to-valley

[4]The gain and the bias voltage are related by a power law since the number of electrons emitted at

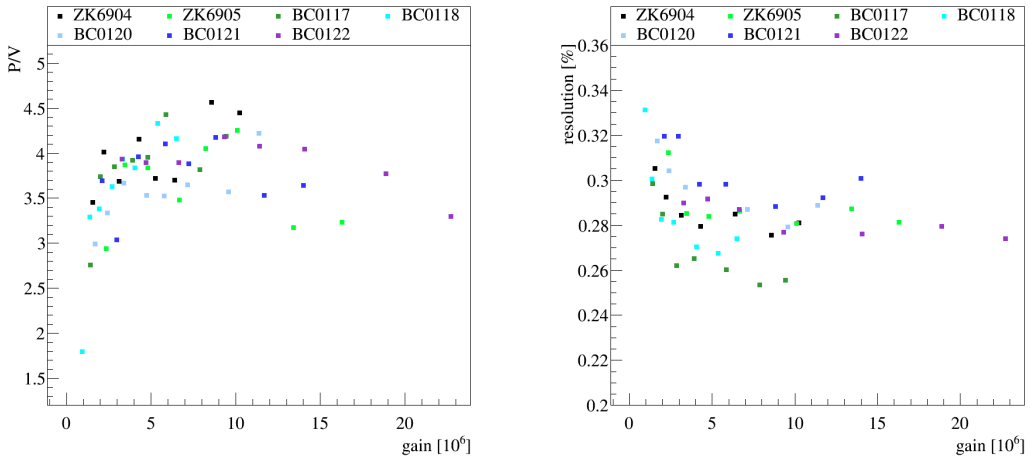

Figure 4.12: Left: P/V as function of the gain. Right: SPE resolution vs gain. Measurements were taken at room temperature in the Faraday test stand.

starts to saturate at values between 3.5 and 4 and a gain of $(2-3)\cdot 10^6$ as illustrated in Fig. 4.12 (left) for a subset of the measured PMTs.

Furthermore, the relative resolution of the SPE peak can be quoted to quantify the separation of baseline noise and a single photoelectron signal of the PMT. It is defined as the resolution of the SPE Gaussian divided by the baseline subtracted mean of the SPE peak. Similar to the P/V, the relative resolution stabilizes at a value of $\approx 0.3\%$ at a gain of $(2-3)\cdot 10^6$ (see the plot at the right of Fig. 4.12).

4.4.7 Afterpulse probability

Afterpulses are time delayed pulses belonging to a first main pulse. Their time structure is the same as for real signals. Since they reduce the veto acceptance (see Sec. 6.3.4), PMTs which exhibit afterpulse probabilities above 10% are discarded from the final selection to be operated in the GERDA experiment.

Photoelectrons which are created at the photocathode of a PMT may ionize residual gas molecules on their way to the first dynode. Due to the electrical field, the positive ion is drifted backwards to the photocathode generating an afterpulse. Since the drift times of the positive ions depend on their mass to charge ratio, the time difference between the main pulse and an afterpulse gives insight into the residual gas composition inside the PMT vacuum [43].

The top of Fig. 4.13 shows the normalized afterpulse spectra of all operational PMTs of the first batch after more than five cool-down cycles. For every PMT a continuous exponentially decreasing component is visible. The huge component with short time delays is probably generated by secondary electrons scattering off the first dynode and hit it again. The pulses with time delays up to several μs is caused by dark pulses and single photoelectrons of unclear origin [43]. Moreover, several peaks can be identified on top of the continuous spectrum. The most prominent one is at $\approx$ 1000 ns time difference. As proven by electric field simulations including the transport of electrons, this peak can be attributed to CH_4^+ molecules [43].[5] The peak around 300 ns is most

one dynode depends on the energy of the incoming electron which is in turn proportional to the high voltage [57]

[5]The paper is about PMTs for the XENON1T experiment, but the discussion holds also for the

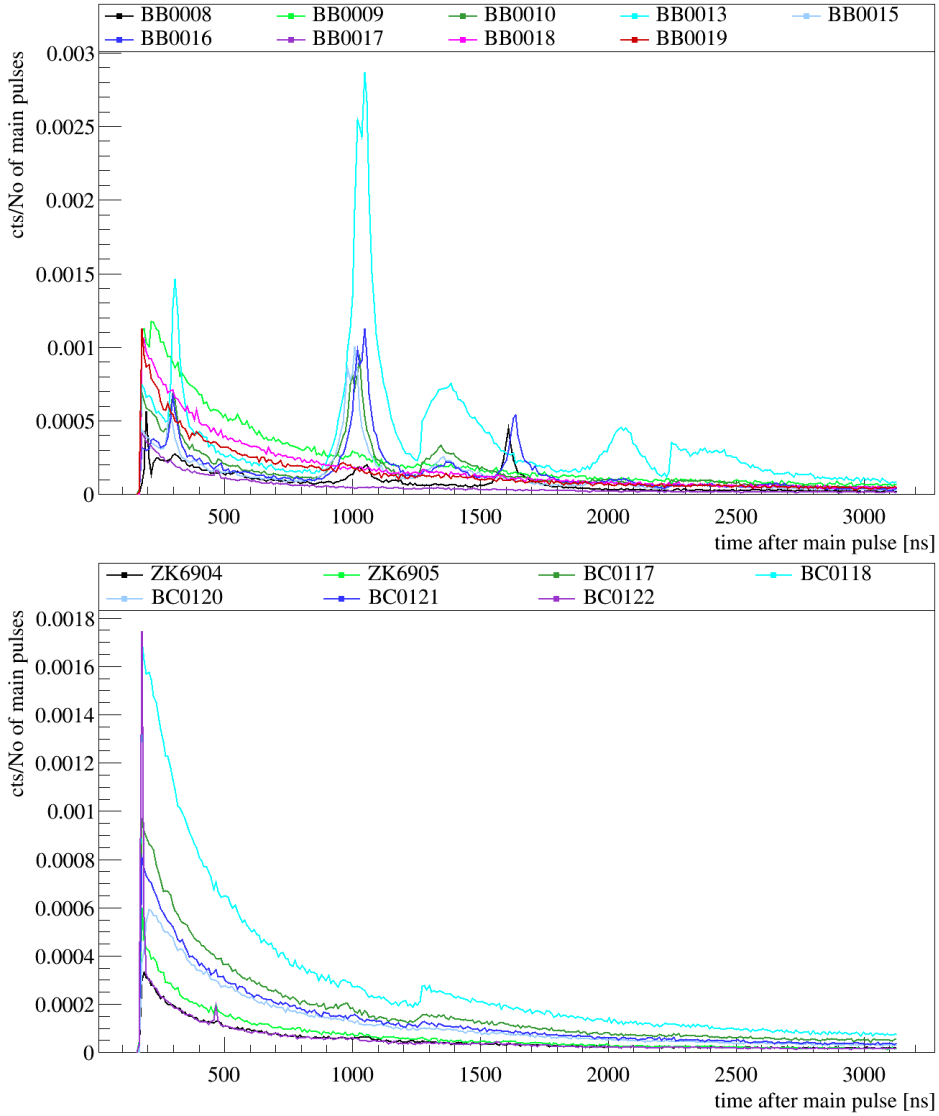

Figure 4.13: **Normalized afterpulse spectra of two different batches of PMTs.** Top: Batch 1. Bottom: Batch 4 (see text for a discussion).

probably due to H^+ for which the afterpulse time has been simulated to be (270 ± 10) ns. The peak at 1600 ns is compatible with simulations of Ar^+ molecules. The sharp steps which are visible in both plots of Fig. 4.13 at ≈ 1250 and ≈ 2250 ns are caused by the single hit limitation of the TDC. Events arriving at a later time in the analysis window are measured with a lower probability than events arriving at an earlier time. In some afterpulse spectra the steps remain even though a correction function is applied [57].

For comparison, the normalized afterpulse spectra of all PMTs from the fourth batch are depicted at the bottom of Fig. 4.13. These measurements were carried out before the PMTs were submersed for the first time into a cryogenic liquid. The continuous part of the spectrum is visible in all the PMTs but the peaks are not visible.

An increase of peaks would indicate tiny leaks in the PMT vacuum caused by

argon version of the PMT since the only difference of the two versions, according to the manufacturer, is the photocathode [77].

thermal stress to the PMTs during cool-down as long as the PMT was stored long enough at room temperature to exclude an increase caused by a change in the emanation rate. However, the current understanding is that the observed differences in the first and fourth afterpulse spectra are related to the atmosphere under which the manufacturer produces the PMT vacuum. This thesis is supported by the fact that the same behavior is observed if the second and fifth batch are compared (see Fig. D.3).

Since no LED and trigger electronics are installed in the GERDA light instrumentation, it is not possible to determine the afterpulse probability during the final operation of the PMTs. It can be stated that no excess above the triplet decay structure of LAr is observed (see Fig. 7.8 for an average waveform taken in the GERDA setup).

4.5 Summary

Eighteen PMTs of type R11065 from Hamamatsu Photonics have been ordered by MPIK. The qualification tests at MPIK revealed that some of these PMTs exhibit internal light production that can be detected by other PMTs.

During the tests of the first PMT batch, potential problems related to the cryogenic PMT test stand and the fact that the dielectric strength of liquid argon is much smaller than the one of gaseous and liquid nitrogen, respectively, were resolved. At that point, the manufacturer was contacted and from then on, in close cooperation with MPIK, different countermeasures were carried out to solve the light emission problems at cryogenic temperature of the R11065 PMT.

Since the probability of light emission was found to increase with higher bias voltage, the PMTs should be operated at the lowermost acceptable gain. The DarkSide collaboration who is operating R11065-10 PMTs in a liquid argon time projection chamber decided to develop cryogenic pre-amplifiers mounted directly after the voltage divider base. Therewith, they are able to operate the PMTs at a low gain of $4 \cdot 10^5$ while maintaining good P/V and without encountering the light emission problems of this PMT type [11].

This approach was not considered as an option for the PMTs that should be operated in the GERDA experiment due to stringent restrictions on the radioactivity budget. The curves in Fig. 4.12 show that the peak-to-valley and the relative resolution of the PMTs start to saturate at a gain of $(2-3)\cdot 10^6$. Therefore, all PMTs that were delivered to MPIK underwent long-term stability test measurements in liquid argon at a gain of $2 \cdot 10^6$. The bias voltage at a gain of $2 \cdot 10^6$ was defined as the operational voltage.

After testing 42 PMTs, which were delivered gradually in five batches of up to ten PMTs, eighteen PMTs passed this long-term tests. 24 PMTs were returned to the manufacturer, out of these 23 due to light emission problems and one because it had an insufficient gain at the maximally allowed voltage.

CHAPTER 5

MONTE CARLO SIMULATIONS FOR LAR SCINTILLATION VETO DESIGN

The goal of the liquid argon scintillation light veto (LAr veto) is to reach an as high as possible background suppression while keeping the self-induced background index as low as possible and in any case below the aspired background index (BI) of Phase II of the experiment, namely $10^{-3}\,\mathrm{cts}/(\mathrm{keV}\cdot\mathrm{kg}\cdot\mathrm{yr})$.

These quantities were accessed by means of Monte Carlo simulations including optical photon tracking. In Sec. 5.1 the optical photon tracking, together with the implemented optical properties are described. In addition, measurements of the triplet lifetime of LAr in GERDA and reflectivities of materials in the light instrumentation setup are elucidated. In Sec. 5.2, simulations that helped answering special design issues, such as the spacing between the Germanium detector strings, are presented. Ultimately, a compilation of the main Monte Carlo results found with the initial optical parameters and a description of the initial Geant4 geometry is given in Sec. 5.3.

5.1 Monte Carlo simulations with optical photons

All Monte Carlo simulations presented in this thesis are performed with MAGE, a MAjorana-GErda simulation framework. It is a Geant4-based simulation framework [13] which includes the geometry of the actual experiment, customized event generators, Geant4 physics lists and output formats. The user selects the experimental setup and output via macros [49].

5.1.1 Optical photon tracking

Prior to the Monte Carlo simulation campaign, which was supposed to give information about the veto capability of the different light readouts and the optimal design, MAGE had to be extended with an algorithm to efficiently track optical photons created by the LAr scintillation. The task of implementing the tracking routine and part of the optical properties has been undertaken by the GERDA group at TU Dresden.

In ultra-pure liquid argon a scintillation light yield of 40.000 photons per 1 MeV energy deposition is created (see Sec. 3.1 for liquid argon scintillation light properties). To save CPU time, it is appropriate to restrict the tracking of optical photons to events

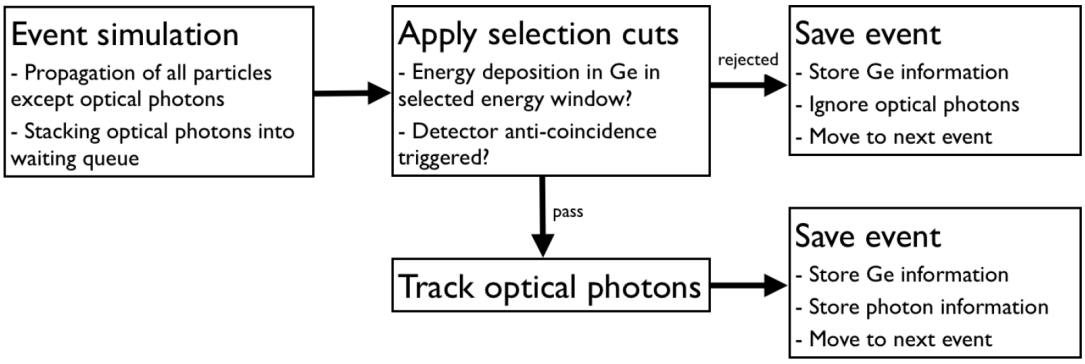

Figure 5.1: Flowchart of optical photon tracking routine. Figure taken from [103].

that fulfill certain requirements, as illustrated in Fig. 5.1. A typical requirement is that the events have to deposit energy in the Germanium detectors in the energy range that is used for background index calculation, namely $Q_{\beta\beta}\pm200\,\mathrm{keV}$. First, the optical photons are transferred to a waiting queue and processed only after the propagation of all other particles is finished and fulfilled the requirements. If the optical photons were propagated and registered by any sensitive surface, the photon hits are stored along with their wavelength, incident angle and a number which identifies the photosensor by which the photon was detected. All detection efficiencies are folded into the detection of photons by the individual photosensors, such that the number of photoelectrons obtained from these Monte Carlo simulations may be directly compared to the photoelectron distribution acquired by measurements with, e.g. calibration sources. The veto cut is set on one single photoelectron detected by either a SiPM or a PMT since the LArGe experiment had proven in the past that a LAr scintillation light veto in low radioactivity environments allows for such a low threshold.[1]

5.1.2 Optical properties

An implementation of optical properties is required by Geant4 in order to obtain reliable results from simulations including optical photons. Some optical properties could be measured, others are taken from the literature. The following paragraphs describe predominantly measurements carried out by MPIK that helped implementing some of the optical properties and summarizes briefly the remaining optical properties.

LAr properties

The scintillation light that should be tracked by these Monte Carlo simulations is created in the LAr volume of the GERDA experiment. In the Monte Carlo simulations the LAr emission spectrum is described by a Gaussian centered at 128 nm.

As explained in Sec. 3.1, the triplet lifetime of the LAr scintillation light strongly depends on the purity of the liquid argon while the fast component was assumed to be insensitive to such changes and was taken from [88]. Hence, the triplet lifetime had to be measured in the GERDA setup and accordingly implemented in MAGE. A small setup, depicted at the left of Fig. 5.2, was designed to perform this measurement. An

[1] The same was found to be true for the light instrumentation of the GERDA experiment during the LAr veto commissioning tests.

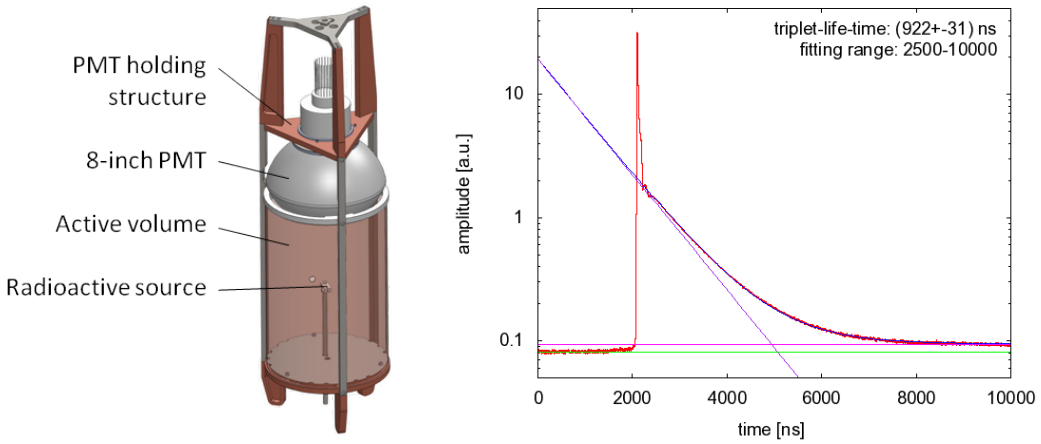

Figure 5.2: **Triplet lifetime measurement with R5912-02 8-inch PMT from Hamamatsu Photonics K.K. in Gerda.** Left: Schematic of the experimental setup. Right: Average waveform with triplet-lifetime fit [84].

8" PMT (R5912-02 from Hamamatsu Photonics K.K. [77]) was mounted in a holding structure which could be connected to the detector string insertion system of Phase I of the GERDA experiment. The photocathode of the PMT is open to a cylindrical volume of 12 l enclosed by a stainless steel foil. In the center of the volume a radioactive ^{228}Th source was mounted to enhance the statistics and allow for a short measurement time. The inner side of the stainless steel foil was lined with VM2000 coated with a wavelength shifter such that the scintillation light may be shifted and guided towards the photocathode of the PMT. An average waveform of the detected scintillation light has been extracted (right plot of Fig. 5.2) and a fit of the triplet component yielded $\tau_{\text{triplet}} = (922 \pm 31)$ ns.

The light yield of ultra-pure Argon which is 40.000 ph/MeV has been scaled down by the measured reduction of the triplet lifetime in the GERDA cryostat and is implemented as 28.120 ph/MeV.[2] The attenuation length of LAr for VUV light is largely unknown and set as an educated guess to 60 cm [92]. In contrast, optical photons exhibit an extremely long attenuation length in LAr. Hence, it is set to 1000 m. A dedicated measurement has been performed in the GERDA experiment to access the attenuation

property	GERDA LAr
emission spectrum	128 nm
triplet lifetime	922 ns
singlet lifetime	6 ns
yield ratio (singlet/triplet)	0.23
light yield	28120 ph/MeV
attenuation length XUV (< 200 nm)	60 cm
attenuation length optical (> 200 nm)	1000 m

Table 5.1: Optical properties of liquid argon in MAGE.

[2] Recent publications indicate that the assumed direct correlation between triplet lifetime and scintillation light yield may be to simplistic. It is found that, e.g., methane and nitrogen contaminations in liquid argon influence the prompt scintillation yield and break up the claimed proportionality [97, 96].

length of VUV photons [126]. However, at the time of writing this thesis, no conclusive result has been published. The Rayleigh scattering length of LAr depends also strongly on the wavelength ($\propto \lambda^{-4}$). At the emission wavelength of LAr it is $\approx 70\,\mathrm{cm}$ while it amounts to $\approx 300\,\mathrm{m}$ at the peak emission wavelength of TPB, the wavelength shifter in use [103]. The implemented values are compiled in Tab. 5.1.

Material reflectivities

The reflectivity of light at the boundary of LAr and a dielectric are calculated by Geant4 using Fresnel's formula if no reflectivity curve is assigned to the material. The refractive index of LAr n which enters in the calculation, is wavelength dependent $n = \sqrt{\epsilon(\lambda)}$ and the dielectric constant $\epsilon(\lambda)$ is calculated by using the empirical Bideau-Sellmeier formula [48]. The reflectivity of metals depends on the surface quality. In general, the

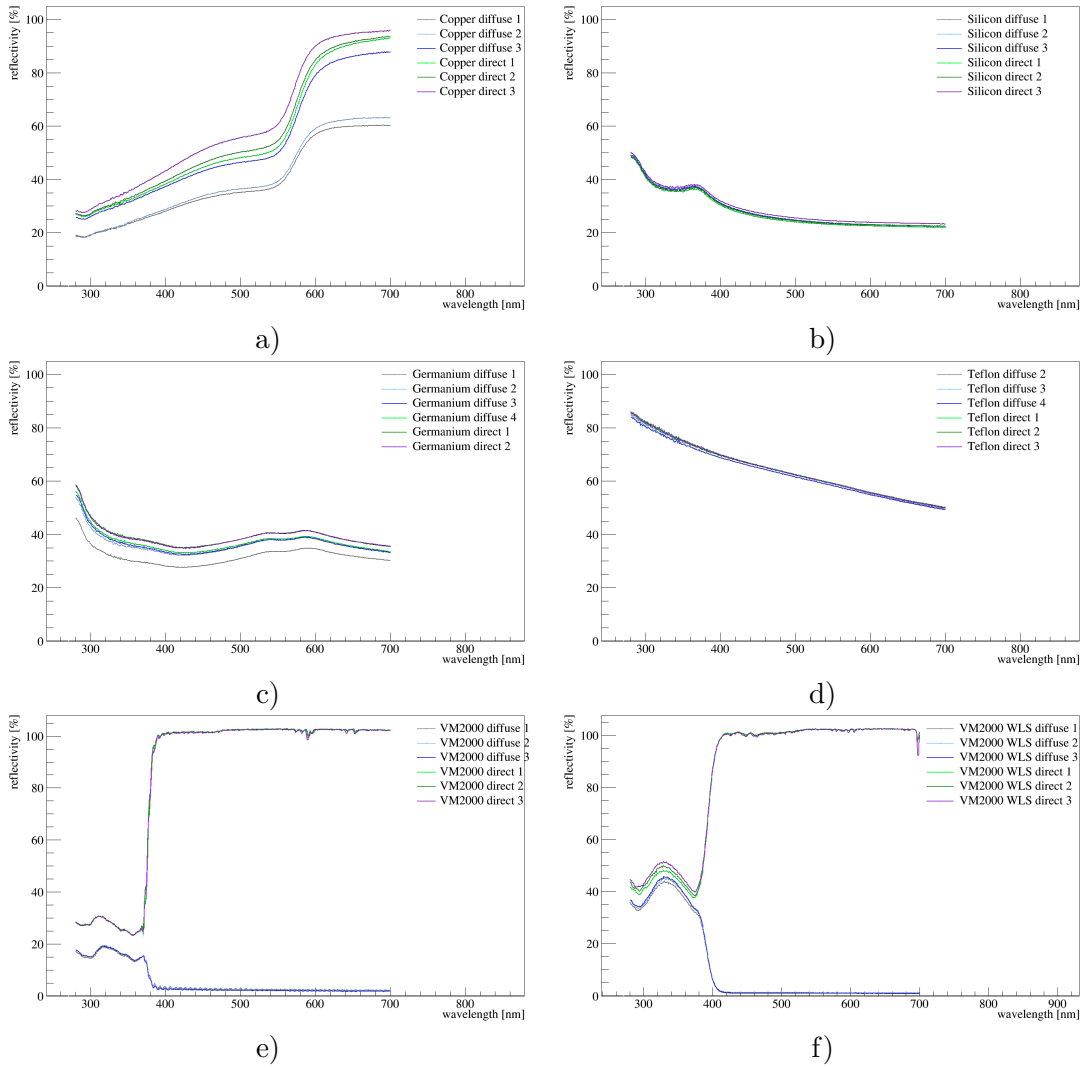

Figure 5.3: **Reflectivities of materials used in GERDA as measured by a reflectometer.** a) Copper. b) Silicon. c) Germanium. d) PTFE. e) VM2000 reflector foil. f) VM2000 reflector foil coated with wavelength shifter. The measurements labeled 'direct' include both the specular component of the light reflection and the diffuse reflection.

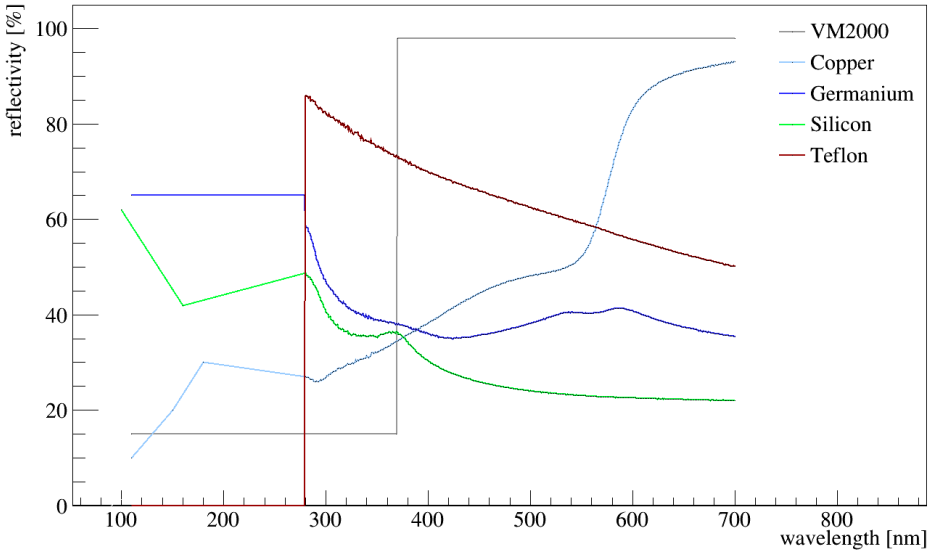

Figure 5.4: **Reflectivities of materials as implemented in MaGe.**

polishing has been set to 50% in this framework. The reflectivity of materials that are commonly used in the light instrumentation setup, such as copper, germanium, PTFE, silicon and VM2000 reflector foil haven been measured in a reflectometer (Cary 400 Conc, UV-visible spectrophotometer) in the wavelength range 300 nm to 700 nm. The diffuse and total (labeled 'direct' in the figure) reflectivity curves have each been measured at three different spots on the samples. The results are compiled in Fig. 5.3. The wavelength dependent reflectivity curves show that copper, silicon, germanium and PTFE (labeled 'Teflon' in the figures) are diffuse reflectors while pure VM2000 and coated with a wavelength shifting matrix composed of polystyrene and tetraphenylbutadiene is a specular reflector. Above a cut-off wavelength of 380 nm the reflectivity is almost 100%, while below it reflects less than 20% of the light. In MaGe an average curve is implemented for the reflectivity of optical photons at each of these materials.

The optical parameters, such as the thickness of the wavelength shifter (WLS) coating, the WLS efficiency and material reflectivities in the VUV region have been tuned using calibration source measurements from the LArGe facility [103]. The reflectivity curves that were, eventually, implemented in MaGe are depicted in Fig. 5.4. A description of the wavelength shifter properties may be found in [103], only the emission spectrum has been taken from the fluorimeter measurements of VM2000 coated with wavelength shifter as presented in Sec. 4.2.3.

The detection efficiency of the PMTs is given as the product of the wavelength dependent quantum efficiency and the collection efficiency. Hamamatsu Photonics K.K. provided with the first batch of R11065-10 PMTs a measurement of the quantum efficiency. The collection efficiency of this type of PMT is 95%. It was folded into the detection efficiency curve and accordingly implemented in MaGe.

The absorption and emission spectra of the scintillating fiber along with their attenuation length have been measured and implemented in MaGe. Moreover, the quantum

efficiency and sensitivity curve is known for the deployed SiPMs and also implemented in Geant4. Details of the properties of the scintillating fibers and SiPMs are given in [94].

5.2 Design optimizations

In an early phase of the LAr veto design simulations it was not yet decided if a LAr veto based only on PMTs or scintillating fibers coupled to SiPMs, or a combination of both (*hybrid design*) will be installed in the GERDA experiment. Consequently, two independent geometries – a fiber design and a PMT design – were implemented in MAGE in the beginning. Two of the early simulations of the PMT LAr veto design, helped answering design related questions.

The dimensions of the PMT design were the same as the dimensions of the initial hybrid design (see Sec. 5.3.1). The only difference was that the middle shroud did not consist of a fiber cylinder but a closed copper shroud lined with reflector foil, similar to the copper shrouds at the top and bottom of the cylinder of the hybrid design.

5.2.1 Compactness of the detector array

The radial distance of a central and the outer germanium detector strings influences the veto capability of a LAr scintillation light veto by either shadowing the light that is created inside the volume of the detector array or by allowing the light to be more easily guided to the next sensitive, or reflective and wavelength shifting surface. The two most extreme options were considered.

1. *dense packing:* the closest distance between the central and outer detector strings that is realizable is $r = 110\,\text{mm}$.

2. *loose packing:* the maximal radial distance which allows to keep a little safety margin to the cylinder of the light instrumentation, is $r = 146\,\text{mm}$.

For this kind of simple checks ^{226}Ra and ^{228}Th in the detector holders were frequently used. These simulations represent a proxy of close-by γ-background for which an efficient background rejection is envisaged (see Sec. 3.2 for a discussion of background that may be vetoed by a LAr scintillation light veto). Moreover, it was assumed that ^{226}Ra placed within the detector array is the most sensitive background component to such geometry changes.

	suppression factor in ROI	
	^{208}Tl in holder	^{214}Bi in holder
dense	55.6 ± 6.6	5.35 ± 0.06
loose	45.8 ± 3.9	4.33 ± 0.04

Table 5.2: Suppression factors in ROI for ^{208}Tl and ^{214}Bi placed in the BEGe detector holders in case of a dense and loose detector array packaging. The ROI is defined as $Q_{\beta\beta}\pm35\,\text{keV}$ in case of ^{214}Bi and $Q_{\beta\beta}\pm100\,\text{keV}$ in case of ^{208}Tl, respectively.

The background induced in the region of interest (ROI) from ^{226}Ra decays is predominantly caused by ^{214}Bi belonging to the decay chain and emitting a 2204 keV γ-ray

which undergoes Compton scattering. Therefore, each time a ^{226}Ra contamination is considered, only ^{214}Bi has been simulated. Since ^{214}Bi emits many γ-rays the energy spectrum around $Q_{\beta\beta}$ is not flat and a small window of $Q_{\beta\beta}\pm35\,\mathrm{keV}$ is considered to estimate the suppression factors at $Q_{\beta\beta}$. The suppression factor is defined as the ratio of total over not-vetoed events (see Eq. 6.2). In case of the ^{228}Th decay chain ^{208}Tl which induces background in the ROI by its 2615 keV γ-ray, is simulated. The energy region around $Q_{\beta\beta}$ is flat and, consequently, the suppression factors are calculated in a wider window of $Q_{\beta\beta}\pm100\,\mathrm{keV}$.

The dense packing of the detector array results in a suppression factor of $SF = 55.6 \pm 6.6$ and $SF = 5.35 \pm 0.06$ for ^{208}Tl and ^{214}Bi homogeneously distributed in the BEGe detector holders, respectively. In contrast, the loose packing yields only suppression factors of $SF = 45.8\pm3.9$ and $SF = 4.33\pm0.04$, respectively, and therewith approximately 20% below the ones of the dense packing. Therefore, it was decided to realize a dense packing of the germanium detector array in Phase II of the experiment.

The overall suppression capability of ^{208}Tl and ^{214}Bi induced backgrounds is discussed in, e.g., Sec. 5.3.2 and Sec. 7.2.

5.2.2 Number of PMTs

In order to get an impression of how much the veto efficiency depends on the actual number of PMTs and if there might be an optimal number of PMTs, 31 PMTs have been implemented in the MaGe geometry. Thereof, sixteen are placed at the bottom and fifteen at the top such that a cable chain might still be guided through the center of the top plate. In the off-line analysis a varying number of these PMTs was then turned on to provide a veto information.

Fig. 5.5 illustrates the suppression factor in dependence of the number of PMTs that are read out. First, the number of PMTs at the bottom was kept fixed (seven PMTs) and the number of PMTs placed at the top varies from three to fifteen. Only, in the case the maximal number of 31 PMTs are read out, sixteen PMTs are placed

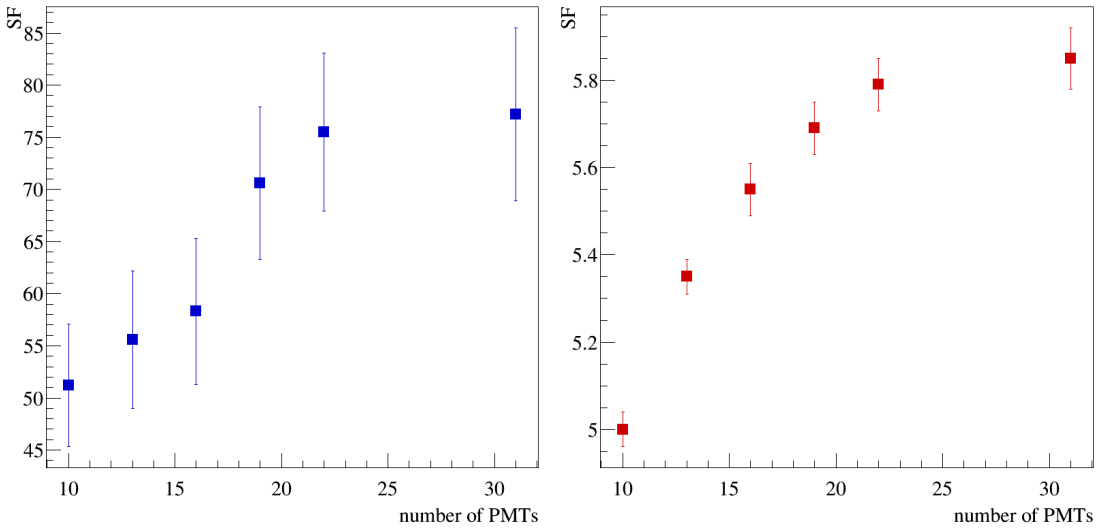

Figure 5.5: Suppression factor in dependence of the number of PMTs. Left: ^{208}Tl in the detector holders. Right: ^{214}Bi in the detector holders.

at the bottom. First, a rather steep increase is observed when augmenting the number of PMTs from ten to nineteen. In case of ^{208}Tl the suppression factor increases by approximately 50% whereas in case of ^{214}Bi the suppression factor increases by less than 20%. In both cases, the suppression factors seem to saturate when increasing the number of PMTs further.

At this moment, it was decided to implement less than twenty PMTs in the GERDA light instrumentation as the veto efficiency always has to be balanced against the self-induced background due to the internal radioactivity of the PMTs (few mBq level).

5.3 Predictions by initial Monte Carlo simulations

This section discusses the results that were obtained during a first simulation campaign of a *hybrid LAr veto design*. Both photomultiplier tubes and SiPMs connected to scintillating fibers are combined in this liquid argon scintillation light read-out system. The actual Geant4 geometry is described in Sec. 5.3.1. For a comparison to the final light instrumentation as it has been implemented in 2014 in the GERDA experiment the reader is referred to Sec. 6.1.

In particular, it was found during the LAr veto commissioning that the nominal optical parameters that were used for this first simulation campaign are not correct and subsequently cited suppression factors will not be reached in the GERDA experiment. However, since they give insight into the different decay topologies and relative veto suppression power, they are presented here.

5.3.1 Monte Carlo geometry of the initial simulation campaign

At the moment of implementing the first hybrid design in MAGE mostly geometrical restrictions were known (see Sec. 3.4). In addition, it was envisaged to deploy the BEGe detectors in pairs to reduce the mass of the detector holders per kilogram of enriched germanium.

Some key points that were relevant for the obtained suppression factors and the background index induced by the light instrumentation are listed in the following:

1. Dimensions of the instrumented volume are a cylinder with radius = 490 mm and height = 2100 mm.

2. In the middle, a scintillating fiber shroud is placed. It is implemented as a full cylinder (h = 900 mm) with a fully reflective surface at the bottom and a sensitive surface at the top.

3. Above and below the fiber cylinder, copper shrouds with = 600 mm height are placed. They are lined out with VM2000 reflector foil coated with wavelength shifter to enhance the light collection efficiency.

4. Six PMTs are mounted on a circle with r = 150 mm at the top. In total, seven PMTs are placed at the bottom of the instrumented volume. Thereof six are placed on a circle with r = 150 mm and one in the center of the support plate.

5. BEGe detectors are not yet implemented individually according to the dimensions of the Phase II detectors but approximated by an average BEGe (r = 36.0 mm,

$h = 32.5\,\text{mm}$). Each time two of these average BEGe detectors are placed as a detector pair with a gap of 5 mm between them in the Geant4 geometry.

6. Tentative Phase II holders are implemented which can be placed with the BEGe detector pairs. They consist of circular silicon plates with a hole in the center which are placed at the top and bottom of the pair. The silicon plates are connected by three copper rods.

7. Semi-coaxial detectors from Phase I can only be placed with the old Phase I holders.

8. No mini-shroud is placed around the germanium detector strings since the copper mini-shrouds used in Phase I of the experiment would deteriorate the LAr veto suppression. At this time, it was not yet clear which kind of mini-shroud will be deployed in Phase II of the experiment that allows to detect light which is created inside its volume.

9. Neither signal and high-voltage cables nor the front-end electronics of the germanium detectors are implemented.

10. The germanium detector array for the initial simulation campaign is composed of seven detector strings. Three thereof contain the semi-coaxial detectors from Phase I and the heaviest of these strings is placed in the center. In addition, four BEGe strings, each containing four BEGe detector pairs, are built-in.

5.3.2 Suppression factors and instrumentation-induced background

A series of Monte Carlo simulations of background contributions that were expected to be present and that might efficiently be vetoed have been performed (see Sec. 3.2). The results obtained with the full LAr veto systems and the subsystems, namely the SiPMs coupled to scintillating fibers, the top and bottom PMTs, and the full PMT array, are compiled in Tab. 5.3.

bg source	Suppression factor in ROI				
	LAr veto	SiPMs	PMT array	PMT top	PMT btm
^{208}Tl in holders	320 ± 34	320 ± 34	242 ± 23	123 ± 8	137 ± 10
^{214}Bi in holders	10.3 ± 0.3	10.2 ± 0.3	8.0 ± 0.2	5.1 ± 0.1	5.5 ± 0.1
^{214}Bi on det. surface	3.5 ± 0.1	3.5 ± 0.1	3.3 ± 0.1	2.9 ± 0.1	3.0 ± 0.1
^{214}Bi hom. in LAr	54.8 ± 7.9	54.8 ± 7.9	32.4 ± 3.7	15.8 ± 1.4	18.5 ± 1.7
^{42}K hom. in LAr	5.3 ± 0.6	–	–	–	–
^{208}Tl far away	112 ± 39	112 ± 39	93 ± 30	80 ± 24	40 ± 9

Table 5.3: Suppression factors in the ROI for important γ-backgrounds.

Two examples of close-by γ backgrounds are ^{208}Tl and ^{214}Bi in the bulk of the detector holders. The suppression factors reached by the full LAr veto system for this type of background source are $SF = 320 \pm 34$ and $SF = 10.3 \pm 0.3$, respectively. Both isotopes decay via a β^--decay. ^{208}Tl has a Q-value of 5001 keV while ^{214}Bi has a lower Q-value of only 3272 keV. Moreover, ^{208}Tl background in the region of interest is due to a 2615 keV γ-ray which is in 84.5% in coincidence with a 583 keV γ-ray. Consequently,

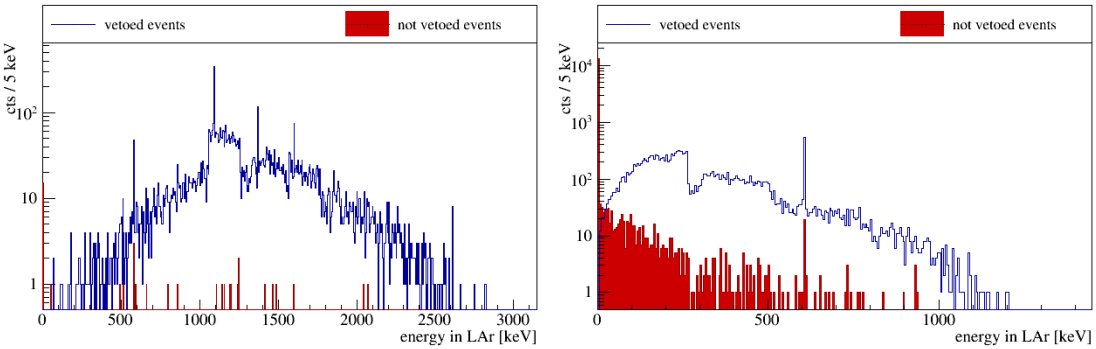

Figure 5.6: Energy distribution in LAr of vetoed and not vetoed events in the region of interest. Left: ^{208}Tl in the detector holders. Right: ^{214}Bi in the detector holders.

up to 1159 keV excess energy in form of γ-rays remain to trigger the LAr veto. The left plot of Fig. 5.6 illustrates the corresponding energy deposition in LAr for vetoed (blue) and not vetoed (red) events in the region of interest. At 1159 keV a sharp edge is visible in the energy distribution of the vetoed events. Moreover, at maximum 3000 keV are deposited in LAr. This reproduces, together with the energy deposition that is required in a germanium crystal, the Q-value of a ^{208}Tl decay. The fact that up to 3000 keV are detected in LAr means that part of the betas escape the thin silicon detector holder plates and help vetoing this type of background source and thus, contribute to the suppression factor.

The right plot of Fig. 5.6 shows the energy deposited in LAr in the case of a ^{214}Bi contamination in the silicon plates of the detector holders both for vetoed and not vetoed events. The lower Q-value of the decay results in an endpoint of the energy spectrum in LAr around 1200 keV. The sharp edge at 265 keV in the spectrum of the vetoed events represents the maximal excess energy of the 2204 keV γ-ray in the case 1939 keV are deposited in a germanium detector. Note that the region of interest was enlarged to $Q_{\beta\beta} \pm 100$ keV to enhance the statistics in this plot. As in the case of ^{208}Tl in the holders, it becomes clear that part of the suppression is due to betas which escape the holder bulk volume. But in general, the energy spectra show that much more events have only little or no energy deposition in the LAr and do not trigger the LAr veto.

The total suppression factor reached for a ^{208}Tl contamination placed far away from the germanium detector array amounts to only $SF = 112 \pm 39$. The reduced veto efficiency is a combination of the β-energy not being deposited inside the instrumented LAr volume and the 583 keV γ-ray which may also deposit all its energy outside the instrumented volume.

The suppression factor in the case of ^{214}Bi homogeneously distributed in LAr yields $SF = 54.8 \pm 7.9$. Since the β-decay happens directly in LAr it is most likely that all the β-energy is deposited in LAr and triggers the LAr veto. In contrast, ^{214}Bi on the germanium detector surface most likely loses energy in form of β's and γ's in the dead layer of the detectors and thus, results in a reduced veto efficiency with $SF = 3.5 \pm 0.1$.

^{42}K decays via β^- with an endpoint of 3.5 MeV and only with 17.8% probability a 1525 keV γ-ray is emitted. An energy deposition at $Q_{\beta\beta}$ is only possible if both the γ-ray and the beta deposit energy in the germanium detector. The beta will lose part of its energy in the dead layer such that relatively little energy may be deposited in LAr.

However, if it is homogeneously distributed in LAr, already little excess energy may be sufficient to trigger the LAr veto, resulting in a suppression factor of $SF = 5.3 \pm 0.6$.

In general, Tab. 5.3 shows that the Monte Carlo simulations predict the total suppression factors to be dominated by the scintillating fibers coupled to SiPMs, and the PMTs to veto only part of the same events. In Sec. 7.2 calibration source measurements with a pilot string and the LAr veto are described. In contrast to the Monte Carlo predictions, they reveal that the PMTs contribute significantly to the overall suppression factor.

Background related to the PMT light read-out

Based on the initial implementation in MaGe the background indices induced by PMT-related components of the light instrumentation have been calculated. The results for these components are compiled in Tab. 5.4.

background source	activity	BI [cts/(keV · kg · yr)]	
		after AC	after LAr veto
^{228}Th			
PMTs	$< 1.94\,\mathrm{mBq/PMT}$	$< (2.45 \pm 0.05) \cdot 10^{-4}$	$< (2.43 \pm 0.45) \cdot 10^{-6}$
Voltage dividers	$< 0.5\,\mathrm{mBq/VD}$	$< (6.30 \pm 0.12) \cdot 10^{-5}$	$< (6.27 \pm 0.12) \cdot 10^{-7}$
Cables	$< 14.4\,\mu\mathrm{Bq/m}$		
- along Cu shrouds		$< (1.62 \pm 0.02) \cdot 10^{-5}$	$< (5.99 \pm 0.41) \cdot 10^{-7}$
- along Fiber shroud		$< (2.27 \pm 0.01) \cdot 10^{-4}$	$< (6.42 \pm 0.02) \cdot 10^{-6}$
Cable plugs @ center shroud	$2\,\mu\mathrm{Bq/pin}$	$(1.47 \pm 0.02) \cdot 10^{-5}$	$(3.89 \pm 0.28) \cdot 10^{-8}$
Copper shrouds	$37\,\mu\mathrm{Bq/kg}$	$(8.59 \pm 0.11) \cdot 10^{-6}$	$(3.17 \pm 0.22) \cdot 10^{-7}$
reflector foil in shrouds	$0.07\,\mathrm{mBq/m^2}$	$(1.82 \pm 0.02) \cdot 10^{-5}$	$(6.72 \pm 0.46) \cdot 10^{-7}$
sum ^{228}Th backgrounds		$< (5.93 \pm 0.05) \cdot 10^{-4}$	$< (1.11 \pm 0.05) \cdot 10^{-5}$
^{226}Ra			
PMTs	$< 1.70\,\mathrm{mBq/PMT}$	$< (3.27 \pm 0.20) \cdot 10^{-5}$	$< (6.27 \pm 0.88) \cdot 10^{-6}$
Voltage dividers	$< 1.14\,\mathrm{mBq/VD}$	$< (2.19 \pm 0.14) \cdot 10^{-5}$	$< (4.21 \pm 0.59) \cdot 10^{-6}$
Cables	$< 11.2\,\mu\mathrm{Bq/m}$		
- along Cu shrouds		$< (2.14 \pm 0.04) \cdot 10^{-6}$	$< (2.73 \pm 0.15) \cdot 10^{-7}$
- along Fiber shroud		$< (3.66 \pm 0.04) \cdot 10^{-5}$	$< (5.27 \pm 0.21) \cdot 10^{-6}$
Cable plugs @ center shroud	$3\,\mu\mathrm{Bq/pin}$	$(5.42 \pm 0.03) \cdot 10^{-6}$	$(4.53 \pm 0.17) \cdot 10^{-7}$
Copper shrouds	$148\,\mu\mathrm{Bq/kg}$	$(5.65 \pm 0.11) \cdot 10^{-6}$	$(7.21 \pm 0.39) \cdot 10^{-7}$
reflector foil in shrouds	$0.15\,\mathrm{mBq/m^2}$	$(6.42 \pm 0.12) \cdot 10^{-6}$	$(8.19 \pm 0.44) \cdot 10^{-7}$
sum ^{226}Ra backgrounds		$< (1.11 \pm 0.02) \cdot 10^{-4}$	$< (1.80 \pm 0.11) \cdot 10^{-5}$

Table 5.4: Background index induced by PMT-related components of the LAr light instrumentation, as determined for the region of interest.

The background index in the region of interest after applying the detector detector anti-coincidence cut amounts to $BI = (5.93 \pm 0.05) \cdot 10^{-4}\,\mathrm{cts/(keV \cdot kg \cdot yr)}$ if only the ^{228}Th contaminations are considered and to $BI = (1.11 \pm 0.02) \cdot 10^{-4}\,\mathrm{cts/(keV \cdot kg \cdot yr)}$ if only the ^{226}Ra contaminations of the components are taken into account. The LAr veto reduces the background indices to $BI = (1.11 \pm 0.05) \cdot 10^{-5}\,\mathrm{cts/(keV \cdot kg \cdot yr)}$ and

$BI = (1.80 \pm 0.11) \cdot 10^{-5}\,\mathrm{cts}/(\mathrm{keV} \cdot \mathrm{kg} \cdot \mathrm{yr})$, respectively. As a consequence, one can conclude that the instrumentation induced background index of components related to the PMT light read out is well within the background budget of Phase II.

5.4 Summary

The Monte Carlo simulation framework MaGe has been successfully extended with optical photon tracking [103]. The required optical properties were measured whenever possible and taken from the literature if they could not be measured. The most influential parameter for the LAr veto efficiency are the light yield and the attenuation length of the VUV scintillation light. A dedicated setup was built to measure the attenuation length [126]. However, at the time of writing this thesis the result was not yet available to be implemented in the simulation framework.

Simulations with a LAr light instrumentation design based only on PMTs led to the decision to install a closely packed germanium detector array. Moreover, based on these early simulations it was decided to install ≤ 20 PMTs in the Gerda light instrumentation setup.

Simulations with a hybrid LAr light instrumentation in which the scintillation light is read out by PMTs and SiPMs coupled to scintillating fibers and a tentative Phase II germanium detector array were performed to evaluate the LAr veto suppression efficiency of different background components. They yielded, e.g., suppression factors of $SF = 320 \pm 34$ for ^{208}Tl in detector holders, $SF = 10.3 \pm 0.3$ for ^{214}Bi in holders and $SF = 5.3 \pm 0.6$ for ^{42}K homogeneously distributed in LAr.

In Sec. 7.3 a comparison of Monte Carlo predictions to LAr veto commissioning results obtained with radioactive calibration sources are presented. They reveal that the nominal optical parameters that were initially implemented in MaGe do not reproduce the measured suppression factors despite the fact that the Geant4 geometry has been updated and the lacking transparent mini-shrouds were implemented according to their final Phase II design.

CHAPTER 6
LAR VETO IN GERDA

The following section presents the light instrumentation of the LAr veto using both photomultiplier tubes and scintillating fibers connected to SiPMs which is employed during Phase II of the GERDA experiment. This includes a detailed description of the design along with the integration of the new detectors in the data acquisition system. Furthermore, the analysis chain of the light instrumentation detectors with focus on the PMTs is explained, including the extraction of photon hits from the acquired FADC traces and the subsequent mandatory steps to provide a veto flag.

6.1 Experimental setup

The design of the light instrumentation as it has been installed in the GERDA experiment in 2014 is shown in Fig. 6.1. It is a cylindrical setup with an instrumented volume of 2200 mm height and a diameter of 470 mm, surrounding the Germanium detector array.

It combines two light detection systems: 3" photomultiplier tubes of type R11065 from Hamamatsu and scintillating fibers connected to SiPMs in order to maximize long-term stability and veto performance.

Due to their internal radioactivity (few mBq level) and the PMT induced background index (see Sec. 4.2 and Sec. 5.3.2), the PMTs are placed far from the Germanium detector array at the top and bottom of the active LAr volume. The top plate, on which nine PMTs are mounted, is depicted in Fig. 6.1 b). The cable chain, containing all signal and high voltage cables for the deployed detectors, is running through a rectangular cut-out in the middle of the plate. The entire top module sits on a U-shaped support structure which is connected to the cable chain. In addition, three reniform holes are cut-out to guide through radioactive calibration sources. On the bottom plate, displayed in Fig. 6.1 c), seven PMTs in total are mounted.

To enhance the probability to detect scintillation light that is created in the vicinity of the Germanium detector array with the PMTs, the upper and lower copper shrouds are lined out with wavelength shifting reflector foil. Due to long-term stability issues of the wavelength shifting reflector foil used in the LArGe experiment, namely VM2000 coated with a solution of Tetraphenyl-butadiene (TPB) and polysterene dissolved in toluene, a new kind of reflector foil has been installed in the GERDA setup. This reflector

foil has been developed by the University of Zürich [135] and consists of Tetratex® [65], a diffuse reflecting PTFE fabric, dip-coated with Tetraphenyl-butadiene (TPB). It shifts the wavelength from 128 nm to the visible range with the maximum of the emission spectrum being at 430 nm [45]. At this emission wavelength, it reflects approximately 95% of the light [93].

In striking distance of the Germanium detector array, a shroud built-up of scintillating fibers coated with wavelength shifting TPB encloses the detector array. The cylindrical module has a height of 1 m and an outer diameter of 490 mm. The advantage

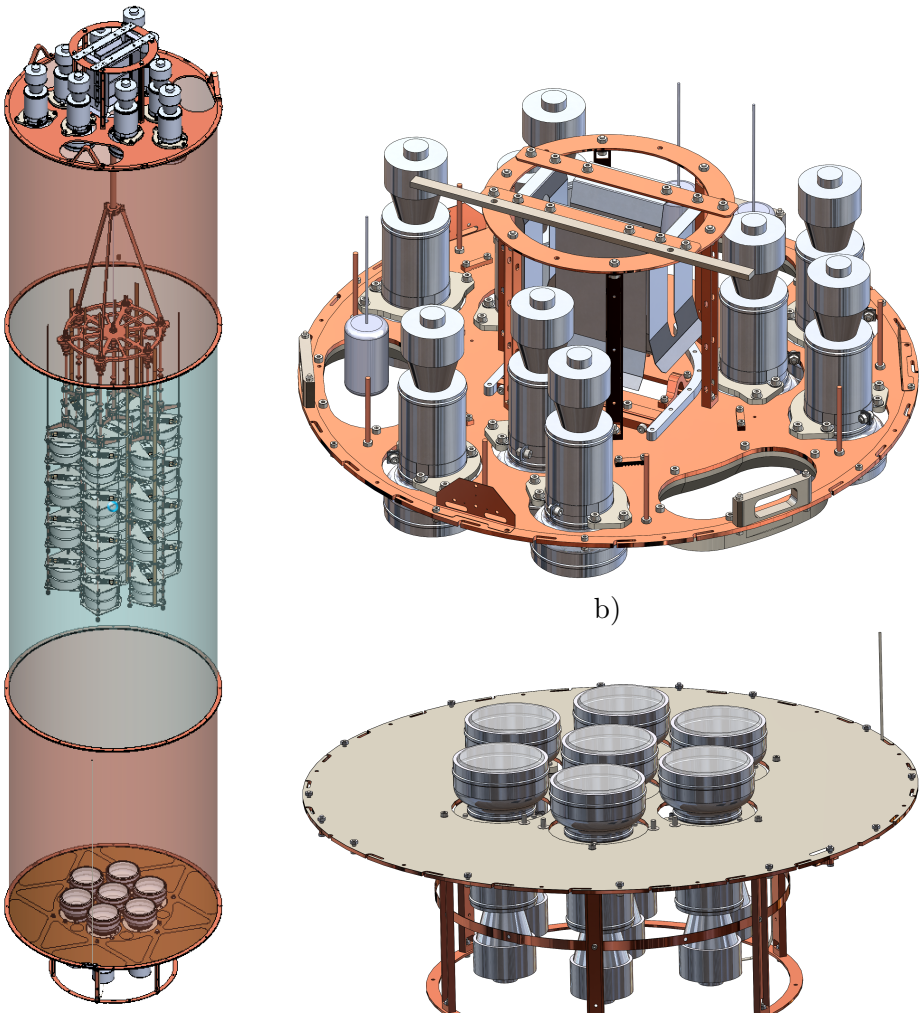

Figure 6.1: **a) Schematic drawing of the LAr veto design** which will be used during the Phase II of the GERDA experiment as anti-coincidence veto. The cylindrical volume surrounds the Germanium detector array. It is composed of two copper shrouds at the top and bottom lined out with wavelength shifting reflector foil and a central cylinder made out of scintillating fibers coated with wavelength shifter. Two copper plates equipped with photomultiplier tubes are placed at the top and bottom of the instrumented volume. These plates are depicted in b) and c).

of this fiber cylinder is that it is not lightproof to the outside. Therefore, scintillation light that is created by a background event outside the shroud depositing at the same time energy in one Germanium detector can still hit the fiber curtain and be detected by the SiPMs. Thus, it promises an enhanced background suppression efficiency. A short description of the setup and its components is given in Sec. 6.1.2.

Since the SiPMs, the Germanium detector cables and also the Front-End electronics of the Germanium detectors are placed above the detector array, a stronger contribution to the background index is expected in the top Germanium detectors. To counteract, the Germanium detector array is placed 150 mm deeper than the center of the LAr light instrumentation.

The design is made in a modular way in order to be able to take advantage of the total height of the lock system. The bottom plate together with the bottom copper shroud can stay inside the movable tube of the lock (see Fig. 3.7) and be slided away when the bottom and center shrouds are disconnected. The upper part of the light instrumentation setup can then be lifted up to the "parking position" and be fixed via three bolts. In this position, it is completely stored inside the upper lock tube. Because of a cable loop for the Germanium detector cables running inside the light instrumentation, the Germanium detector array can be lowered independently from the light instrumentation. This allows access to the Germanium detectors or the electronic interconnection plate.

Nylon mini-shroud

^{42}Ar with its progeny ^{42}K is a potentially high and dangerous background component. To reduce the amount of ^{42}K ions drifting towards the surface of the Germanium detectors, the concept of mini-shrouds surrounding the detector strings was adapted. In Phase I of the experiment, these mini-shrouds were made of 100 μm thick copper foil. Since copper prevents the propagation of scintillation light that is created in close vicinity of the Germanium detectors, a transparent mini-shroud was required for Phase II [105].

125 μm thick Nylon foil from the Borexino experiment [46] was chosen as material for the Phase II mini-shrouds because of its very low intrinsic radioactivity and high transparency for optical photons. To circumvent the absorption of photons with a wavelength below 300 nm [50] a wavelength shifter consisting of 30% TPB and 70% polystyrene is coated on the inner and outer Nylon surface.

Fig. 6.2 shows a prototype of such a mini-shroud illuminated by a UV lamp. The light is shifted to the optical range and the bright end of the cylinder indicates that light is guided trough the mini-shroud material.

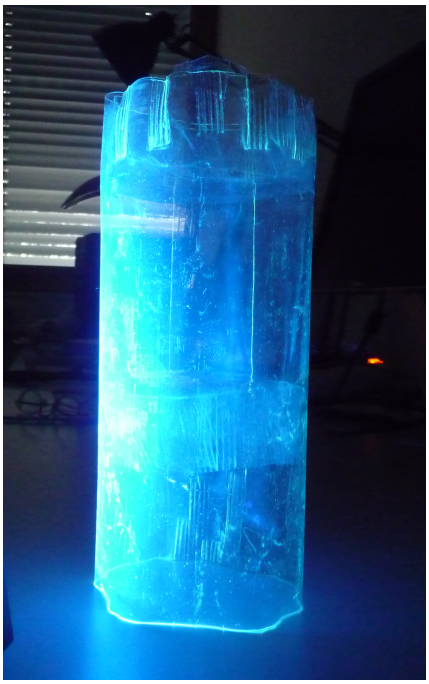

Figure 6.2: Nylon mini-shroud illuminated with an UV-lamp.

6.1.1 The PMT light read-out

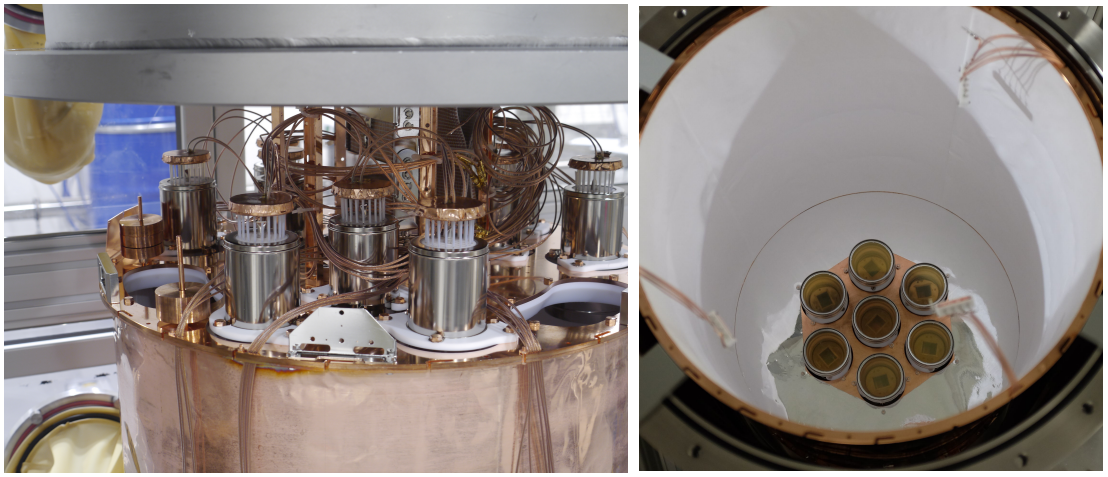

Figure 6.3: Pictures of top and bottom PMT modules in the lock of the GERDA cryostat.

A top view from the top PMT module which is mounted in the lock of the GERDA cryostat, is shown at the left part of Fig. 6.3. Nine PMTs are arranged in groups of three between holes for the radioactive sources. Each PMT is connected via PTFE holders to the copper support plate. Custom-made voltage dividers (see Sec. 4.2.2) are mounted to the PMT leeds and connected by low radioactivity coaxial cables (SAMI RG178) to the high voltage and signal cables which are all running through the cable chain.

A picture of the bottom PMT module together with the bottom copper shroud is shown at the right side of Fig. 6.3. This part of the instrumentation is already placed inside the movable lock tube and put by plastic holders in the mounting position. The photocathodes of all seven PMTs are facing the inner volume of the instrumentation. Six PMTs are mounted on a circle with a radius of 120 mm and the remaining one in the center of the copper support plate. To maximize the reflectivity, the outer ring of the support plate is covered with VM2000 coated with wavelength shifter. Furthermore, three bundles of cables with a connector at the end are running along the bottom shroud to provide the voltage dividers with high voltage and connect the signal read-out cables.

6.1.2 The SiPM light read-out

The left picture of Fig. 6.4 shows the fiber shroud connected to the top part of the instrumentation.

Multiclad scintillating fibers of type BCF-91A from Saint-Gobain have been installed. They have a square-shaped cross-section of 1 mm^2 size [94].

Bundles of nine fibers are always connected to one SiPM by means of optical cement. Six of these bundles are arranged in a module, depicted in the middle picture of Fig. 6.4. Each fiber is fixed diagonally in a copper holder (see right bottom picture of Fig. 6.4) which reduces the number of fibers needed to obtain full coverage of the cylinder surface by a factor of $\sqrt{2}$. To avoid mirrors or additional light detectors at the bottom of the module, the fibers are bent by 180° and built-in the adjoining module. As a

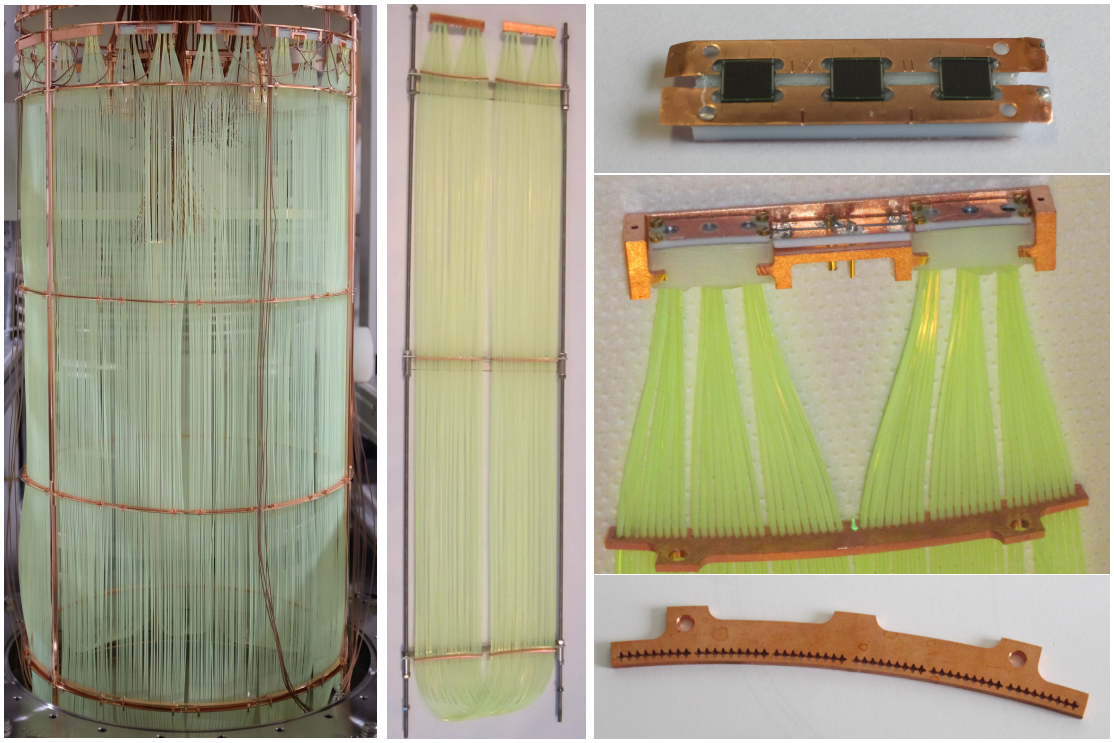

Figure 6.4: Pictures of full fiber shroud and its components. Left) Full fiber shroud. Middle) Two adjoining modules in a mounting frame. Right top) holding frame with three SiPMs. Right middle) top part of a fiber module. Right bottom) copper holder for 54 fibers.

consequence, all SiPMs are installed at the top of the module. The full fiber cylinder is realized by fifteen modules.

Also in order to detect scintillation light with a combination of scintillating fibers and SiPMs, the VUV scintillation light has to be shifted to the blue-visible range by using TPB as wavelength shifter (WLS). Fig. 6.5 shows the overlap of the absorption spectrum of the BCF-91A fibers and the emission of TPB. About 60% of the shifted light can be absorbed by the fibers. The coating is realized by evaporating TPB with

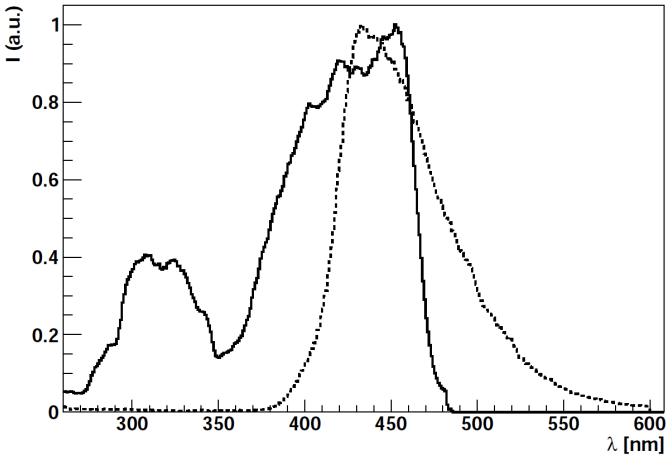

Figure 6.5: Absorption spectrum of BCF-91A fiber (solid line) and emission spectrum of TPB (dashed line). Figure taken from [94].

a thickness of 200 nm on the fiber inside a vacuum chamber.

The read-out is realized by 3 mm x 3 mm SiPMs with 50 μm pixel size (product code PM3550), purchased from Ketek GmbH in die. The packaging is custom-made by the group at TU München to meet the radioactivity requirements for material deployed in close vicinity of the Germanium detectors. The dark rate of SiPMs at liquid argon temperature is almost negligible, being a mandatory requirement for the deployment as read-out detectors of a scintillation light veto.

A description of tests done prior to the final construction of the fiber shroud and installation in the GERDA setup can be found in [136, 137].

6.2 Data acquisition

In Phase II, signals from three different detector types are recorded: Germanium detectors, LAr light detectors and light detectors of the muon veto system. Thereof, the Germanium detector and LAr light detector read-out is handled by the same trigger unit (called MPIC [9]).

1. **Germanium detectors** NIM modules from CAEN [52] placed in the electronic cabinet provide the high voltage bias for the Germanium detectors via 20 m long coaxial cables of type RG179. The Germanium detector signals are fed into a charge sensitive preamplifier (called CC3) which is placed in the argon, approximately 50 cm away from the detectors. The output is connected via a 20 m long coaxial cable (SAMI, 75 Ω) to a fast-analog-to-digital-converter (FADC) (SIS 3301, 14 bits, 100 MSamples/s). At the boundary of the cryostat, high-voltage filters are installed to reduce the noise on the germanium detector signals.

2. **LAr light instrumentation detectors**

   (a) **photomultiplier tubes** The high voltage for the PMTs is supplied via a HV multichannel system by CAEN [51] placed 30 m far away from the high voltage filters and feedthroughs connecting the LAr cryostat to the outside. Afterwards, 10 m of coaxial cables are running inside the cryostat to the PMT voltage dividers. The PMT signals are fed into a custom made shaper and then digitized by an FADC.

   (b) **silicon photomultipliers** The bias voltage of the SiPMs is provided by a custom made low voltage board placed in the electronics cabinet. The signal is AC decoupled and fed into a charge sensitive preamplifier (time constant 50 μs) [94]. The signal is then digitized by a FADC.

The data acquisition of the muon veto system is handled by a separate DAQ system. Both systems are synchronized by a common GPS pulse per second (PPS) signal. For further information the reader is solely referred to [9, 71].

6.2.1 Trigger schemes

Different trigger schemes are employed, depending on the type of data that should be acquired.

1. **physics data** In this case the trigger is set on the Germanium detectors. If one of the Germanium detectors finds a trigger all other Germanium detectors and the LAr light detectors are read out simultaneously. These are 160 μs long Germanium traces with 10 ns sampling, 80 μs long SiPM traces with a fourfold compression and 12 μs long uncompressed PMT traces.

2. **calibration data**: In this case, the difference between an exclusively Germanium detector calibration and a calibration including the LAr light detector channels has to be made.

   (a) **Germanium detector calibration** During the standard Germanium detector energy calibration only the triggered Germanium detectors are read out with 160 μs trace length and 40 ns sampling. An energy threshold of about 500 keV is set. Additionally 10 μs long high frequency traces are saved with 10 ns sampling around the rising edge of the signal (see Fig. 6.7). In the meantime, the PMTs are switched off due to the high source activity and thus, high signal rate and the resulting high amount of data.

   (b) **pcalib**: In this mode the trigger is set on the Germanium detectors and all Germanium and LAr detectors are read out simultaneously. The trigger threshold can be varied and was set to ≈ 500 keV during the commissioning measurements with a radioactive ^{228}Th and ^{226}Ra calibration source (see Sec. 7.2.1 and Sec. 7.2.2).
   Using this trigger mode allows to reach the best detector-detector anti-coincidence and therewith LAr veto performance.

   (c) **LAr calib**: Moreover, there is a mode that triggers on the LAr detectors themselves. If a calibration source is lowered during this calibration it is possible to get the energy spectrum with the LAr light detectors and to determine the photoelectron yield based on one or more characteristic peaks in this spectrum (see [94]).

6.2.2 PMT monitoring with the scaler

The easiest way to monitor the state of the photomultipliers of the LAr instrumentation during their operation in the GERDA experiment is to determine the rate of the PMTs continuously. For this purpose a custom-made multi channel scaler has been developed by K. Pelczar from the Jagiellonian University in Kraków, Poland, and installed in the electronics cabinet [117].

The scaler is composed of three different units, the analog front-end, the trigger and counter logic and the data server for the GERDA slow control. The analog front-end is responsible for signal conditioning and discrimination of physical events. Shaped negative PMT signals, fed in from the first output of the Genius shaper, are AC coupled to remove the baseline, inverted and then amplified by a factor 10. Each channel has a separate programmable digital-to-analog converter output that sets the threshold level in the way that the comparators to which the conditioned signal is passed trigger on single photoelectrons. These pulses are then registered by the trigger and counter logic. The data server and controller is realized on a single-board-computer (SBC). It provides the Ethernet interface for count rate read-out and programming. It reads out the count rates of the individual channels every 0.5 s from the FPGA module and

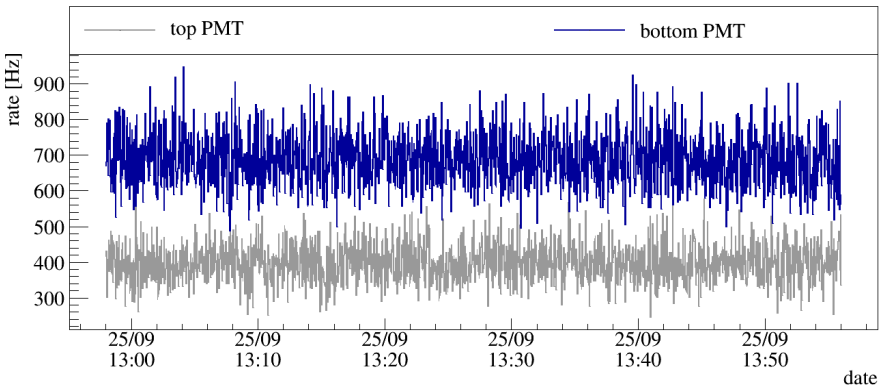

Figure 6.6: **PMT signal rates recorded with a custom-made scaler [117].**

stores the most recent values in the database. A more detailed description including an operator's manual can be found in reference [117].

6.3 Data analysis

Three signal traces are shown in Fig. 6.7 as examples. The trace of the Germanium detector that triggered the read-out is depicted on top. The middle plot shows one

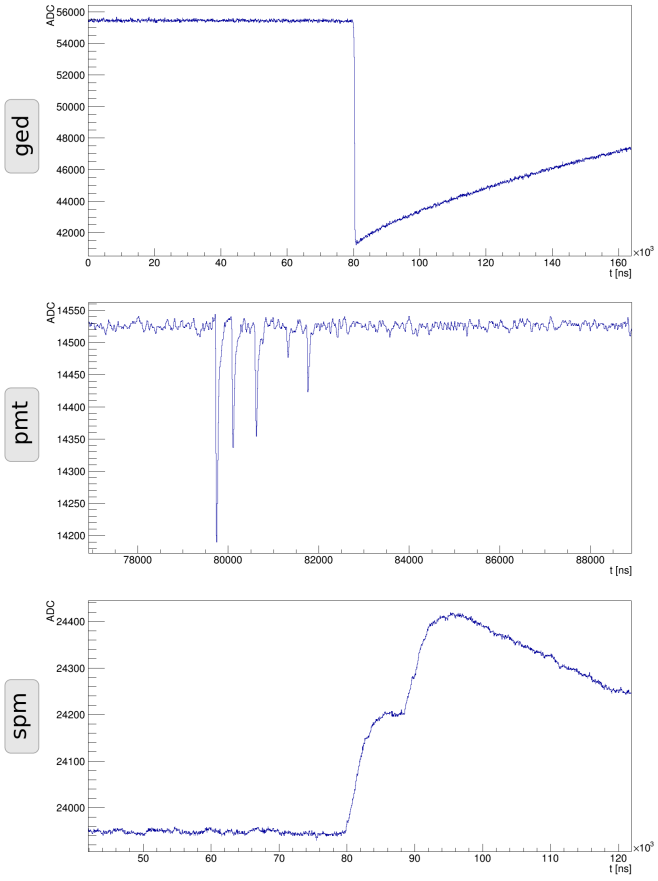

Figure 6.7: **Three typical signal traces of the different detector types recorded in GERDA Phase II.**
ged: The top trace shows the signal for the Germanium detector that triggered the read-out. The trigger is set in the middle of the 160 μs long trace.
pmt: In the middle, one of the corresponding PMT traces is shown. The trace is 12 μs long whereof approximately 3 μs are recorded prior to the Germanium trigger position. The fast component of the scintillation is followed by several smaller pulses representing the triplet component of the scintillation light.
spm: At the bottom one of the fifteen SiPM traces is depicted. The trigger position is set to the center of the trace.

of the corresponding PMT traces and the bottom plot one of the corresponding SiPM traces. Eventually, the information that has to be extracted from the traces is the calibrated energy deposited in the Germanium diode, a quality flag, the classification as signal or background event from the PSD analysis, a veto flag from the μ-veto and the veto flag from the LAr veto analysis.

This information can only be extracted stepwise from the data as they are partly dependent on each other. Therefore, the GERDA Phase II data will be saved in a tier structure, embedded in the software framework GELATIO, similar to the data organization in the Phase I of the experiment. At first, the raw data is saved in the so-called *tier0* files. The rootified version of the data is saved in *tier1* where at the same time the blinding of the region around $Q_{\beta\beta}$ is applied.

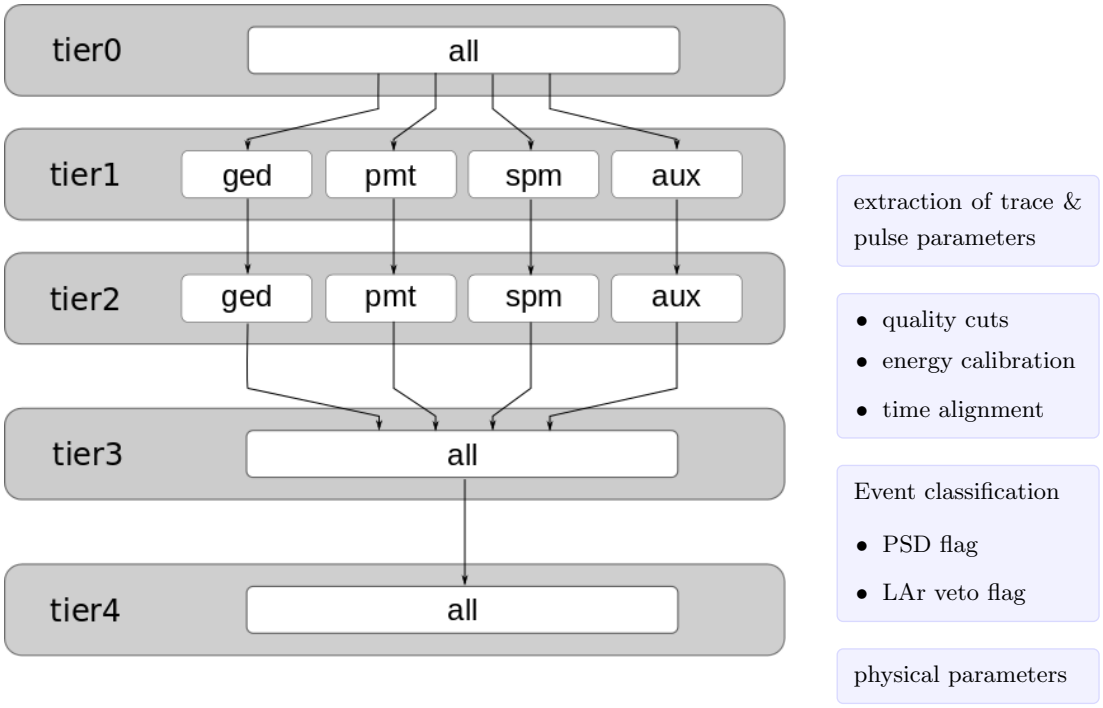

Figure 6.8: **Sketch of the GELATIO data tier structure.** The information is stored in five data tiers (tier0 - tier4) each being represented by a gray box. Tier0 contains the raw data. Tier1 is the rootified and blinded copy of the tier0 files except that the data is split into four different data streams - the Germanium data *ged*, the PMT data *pmt*, the SiPM data *spm* and the auxiliary data *aux*. Starting from tier1, during the conversion, information is extracted from each tier and the newly acquired information is saved in the next tier (shown in the light blue boxes which are placed in between the different tiers). During the conversion from tier1 to tier2, important parameters of the trace, e.g. the baseline and the baseline sigma, as well as from triggered pulses, like e.g. the trigger position, the energy,.. are extracted and stored in tier2. During the conversion from tier2 to tier3 the quality cuts for the Germanium signals are applied, the calibrated energy is determined by applying a calibration curve to the uncalibrated energy and the time alignment of the LAr light detectors is made relative to the first Germanium trigger position and then saved in one single tier3 stream. At this stage, the A/E analysis for the PSD of the BEGe detectors, the neural network analysis for the PSD of the coaxial Germanium detectors and the LAr veto analysis are carried out and the corresponding flags are saved in tier4.

During the conversion from *tier1* to *tier2* important information is extracted from the traces. In the case of the Germanium signals this is the baseline, baseline sigma, trigger position, uncalibrated energy as the output of a digital signal filter, rise time and also general information like the timestamp of the event. For the PMTs and SiPMs the baseline and its sigma are calculated, up to fifteen hits with trigger positions, corresponding signal amplitudes and charges are saved, along with the total number of triggers in the trace.

During the next step, the conversion from *tier2* to *tier3*, the Germanium detector quality cuts are applied, the energy calibration of all Germanium detectors and the calibration in photoelectrons of all light detectors is made. Furthermore, the trigger positions of the LAr light detectors are saved relative to the first Germanium trigger position.

At the level of *tier3* the pulse shape discrimination is performed on the Germanium detector signals, as well as the LAr veto analysis. The veto flags and additional information are saved at the *tier4* level and based on this information the $0\nu\beta\beta$ analysis is performed. More information about the tier structure is available in [15]. In the following sections the algorithms for the tier conversion of the PMTs (and if identical for the SiPMs) are explained in detail.

6.3.1 PMT hit reconstruction

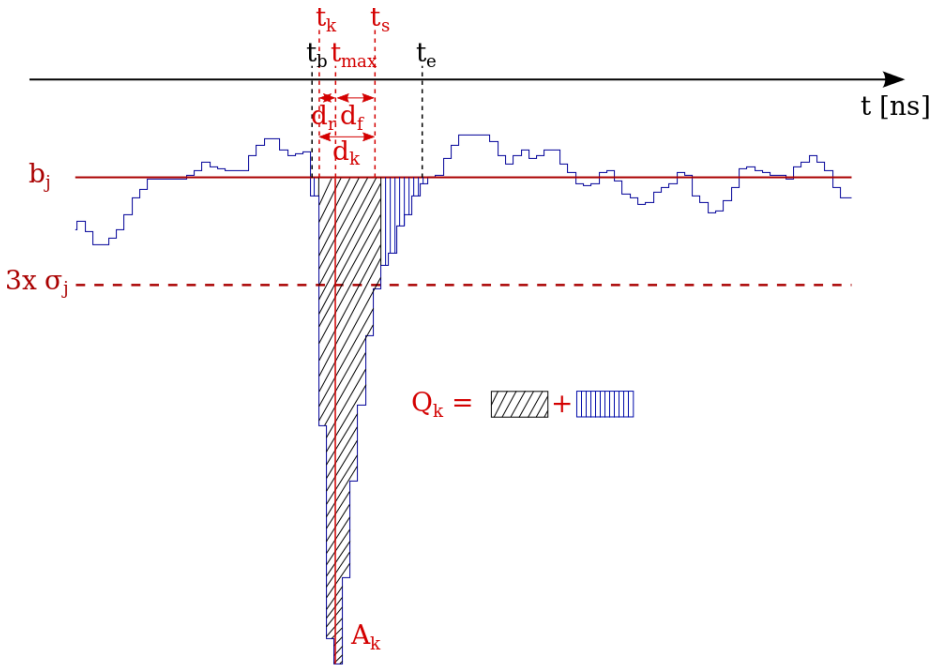

Figure 6.9: PMT pulse with trigger parameters.

To identify photon hits in PMT traces, several parameters are extracted from the FADC PMT traces. Fig. 6.10 shows a flowchart of the program utilized to extract these parameters. The program is implemented as a GELATIO module in the official data flow at the level of tier1 to tier2 conversion (see Fig. 6.8).

First, the baseline is determined using an iterative method which has been applied for the veto analysis in the LArGe experiment [82]. As a first step, the mean average

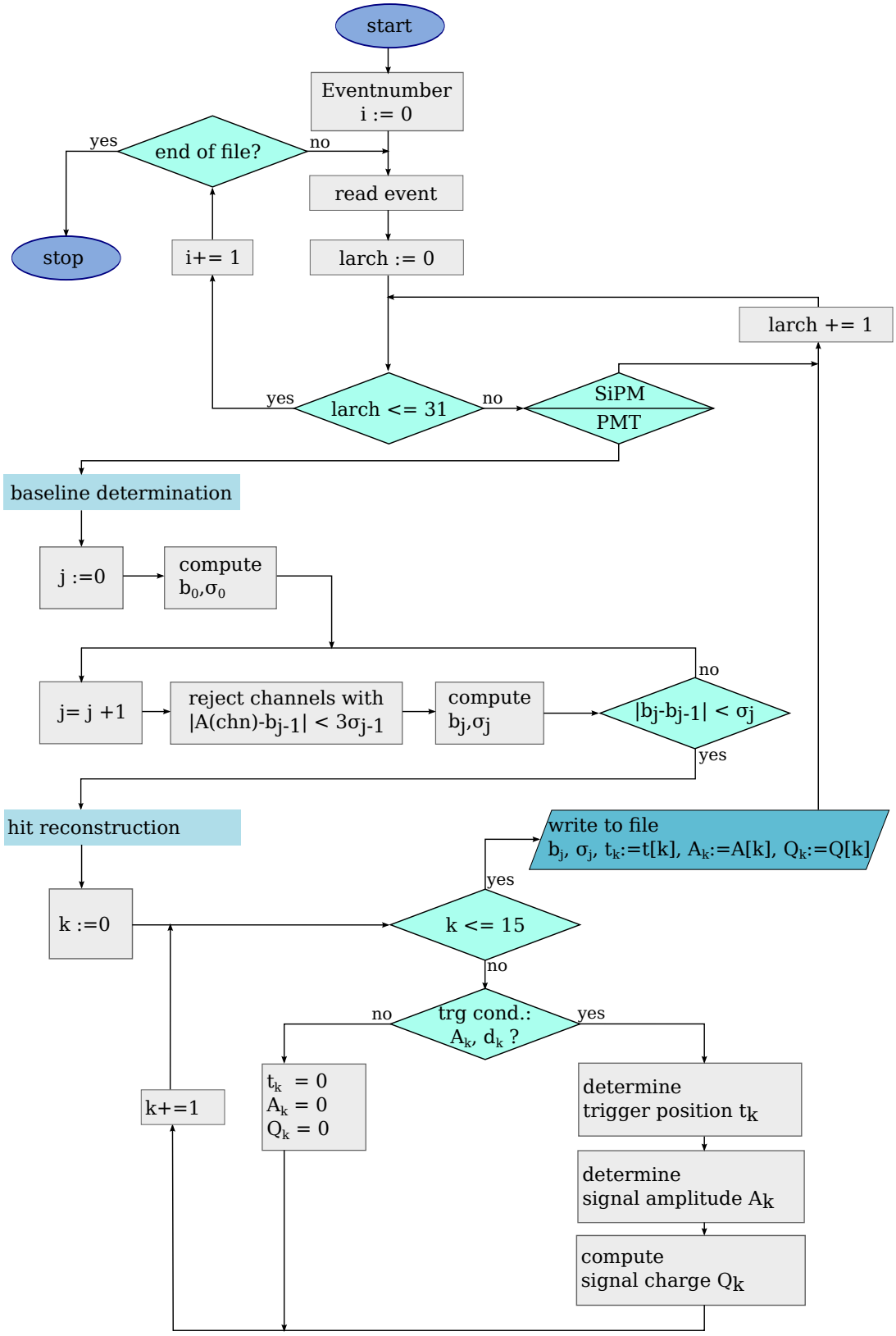

Figure 6.10: Flowchart of PMT hit info extraction.

b_0 and the baseline spread σ_0 of the event are calculated using all samples of the trace. Second, the samples whose amplitude A(S) is not within a window of $3\sigma_0$ around b_0 are discarded from the calculation of b_j and σ_j. This procedure is repeated in further iterations until the change of the baseline parameter $|b_j - b_{j-1}|$ is smaller than its uncertainty $\overline{\sigma_j}$, given as $\overline{\sigma_j} = \sigma_j/\sqrt{S-1}$.

Subsequently, a leading edge trigger with a threshold of $3\sigma_j$ is applied to identify up to fifteen hits in the PMT trace. In addition, the amplitude has to stay above the threshold for at least 40 ns to minimize the number of noise events saved as a hit. The time when the amplitude exceeds the level of $3\sigma_j$, denoted t_k in Fig. 6.9, is saved as trigger position (trigger0,... trigger15). To determine the amplitude and the charge of the hits, the baseline is subtracted from each sample. The maximal amplitude, denoted A_k in Fig. 6.9, within the region around the trigger exceeding the trigger threshold is saved as the amplitude of the hit (amplitude0, ... amplitude15). The charge Q_k of a hit is calculated by integrating the area below the pulse.

$$Q_k = \int_{t_b}^{t_e} A(S)dS \tag{6.1}$$

To account for the asymmetric pulse shape caused by the shaper in use, the integration window $[t_b, t_e]$ is enlarged compared to the window in which the amplitude exceeds the $3\sigma_j$ level $[t_k, t_s]$. As recognizable in Fig. 6.9 the pulses exhibit a fast rising edge with and a longer falling edge. As a consequence, two extra samples are added to the integration window on the left side and seven samples on the right side.

As discussed in Sec. 6.3.2, relatively long noise signals with small amplitude but consequently high charge are injected in some channels (see Fig. 6.11). To have the possibility to distinguish these hits from hits caused by single photons, two more variables are extracted from the pulses, namely the rise time d_r and the falling time d_f. They are defined as the time differences $|t_{max} - t_k|$ and $|t_{max} - t_s|$, respectively.

6.3.2 Quality cut for PMT signals

The top of Fig. 6.11 shows a 2D histogram of the amplitude of the pulses and their charge (see section 4.4) of a typical, well performing PMT, namely LAr channel 0 in run 51. A band can be identified for which the amplitude and charge are proportional to each other, following the expectations for normal PMT signals.

The dense band in region I is populated by single photoelectrons and it extends to signals with a higher amount of photoelectrons, thus higher amplitudes and charges. An example for a pulse from this region is shown in Fig. 6.12 a).

Events with single photoelectron amplitude but higher charge, marked as region II, are due to hits which happened in quick succession but which cannot be resolved within the pulse width of the PMT signals. In most cases, two maxima can be identified by eye but in GELATIO only one trigger with the maximal amplitude and the integral over both (unresolved) pulses is stored. An example of such an event together with the extracted pulse amplitude and the integral is depicted in Fig. 6.12 b).

Moreover, region III is populated with noise events of low amplitude and charge which fulfill the proportionality condition. An example of such a normal noise pulse is shown in Fig. 6.12 c).

The projection of either the amplitude or the charge in this region is normally referred to as the *(single) photoelectron spectrum*. As described in Sec. 4.4, the Gaussian

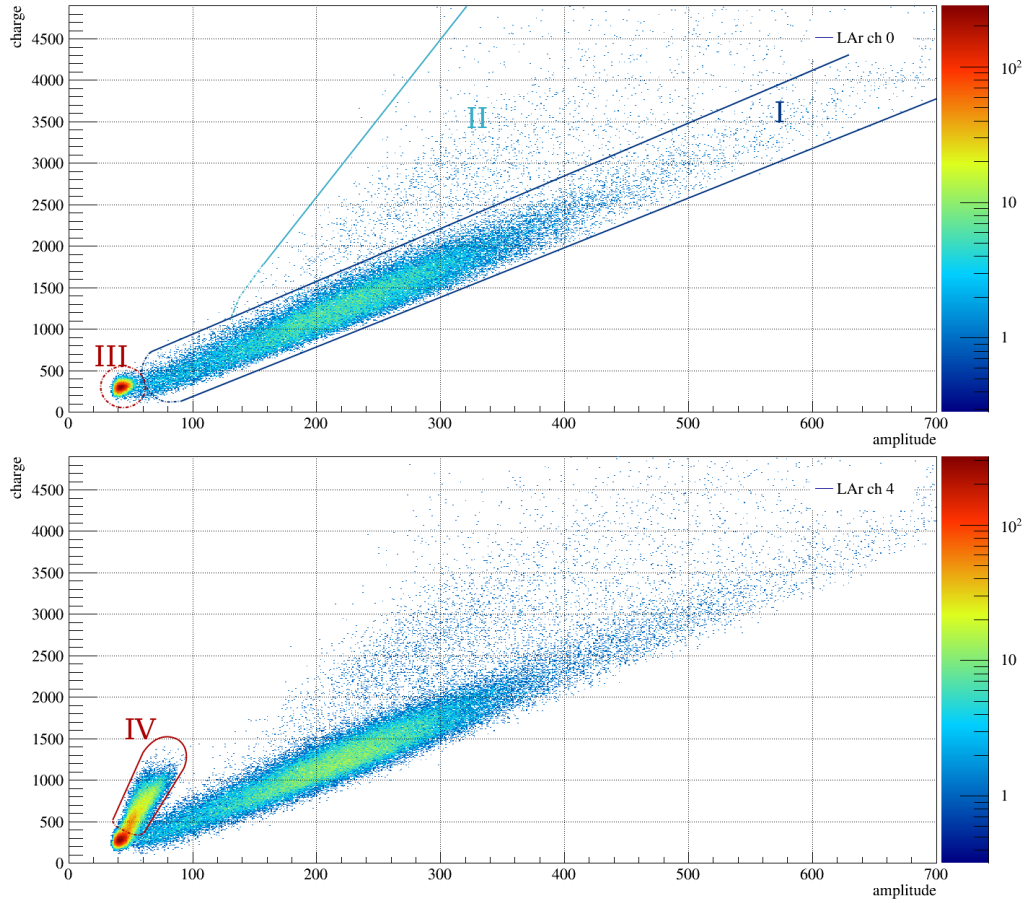

Figure 6.11: Amplitude against charge for PMT signals. Top: Distribution for a typical PMT. Indicated are three regions of different event classes: I) clean single photoelectron signals, II) overlapping pulses with single photoelectron amplitude, III) noise signals.
Bottom: Distribution of a noisy PMT. A forth event class, populated by noise signals of low amplitude but high charge is present.

distributed peak is used to calibrate the PMT pulses in photoelectrons. Additionally, the ratio of the peak height and the height in the valley between the noise component and the single photo electron peak is a measure for the signal-to-noise separation and therewith for the quality of the PMTs.

Several PMTs which have been installed in GERDA exhibit noise signals for which the charge of the pulse is not proportional to the amplitude (see Fig. 6.12 d) for such a noise pulse). An example for such a PMT - LAr channel 4 in run 51 - is shown in the bottom of Fig. 6.11 and marked as region IV.

In the corresponding single photoelectron spectra, depicted in Fig. 6.13, the peak-to-valley is significantly worse compared to LAr channel 0. No efficient cut has been found using the pulse duration and the pulse asymmetry. In the end, the most efficient and simple cut was found directly in the plane of charge over amplitude against the charge. Fig. 6.14 shows the event distribution at low amplitudes for the two PMTs under comparison together with the cut. Since baseline noise on the FADC channels should be symmetric, the distribution of triggers with inverse polarity is overlaid in Fig. 6.14 (red) and confirms that these events can be explained by baseline noise. For

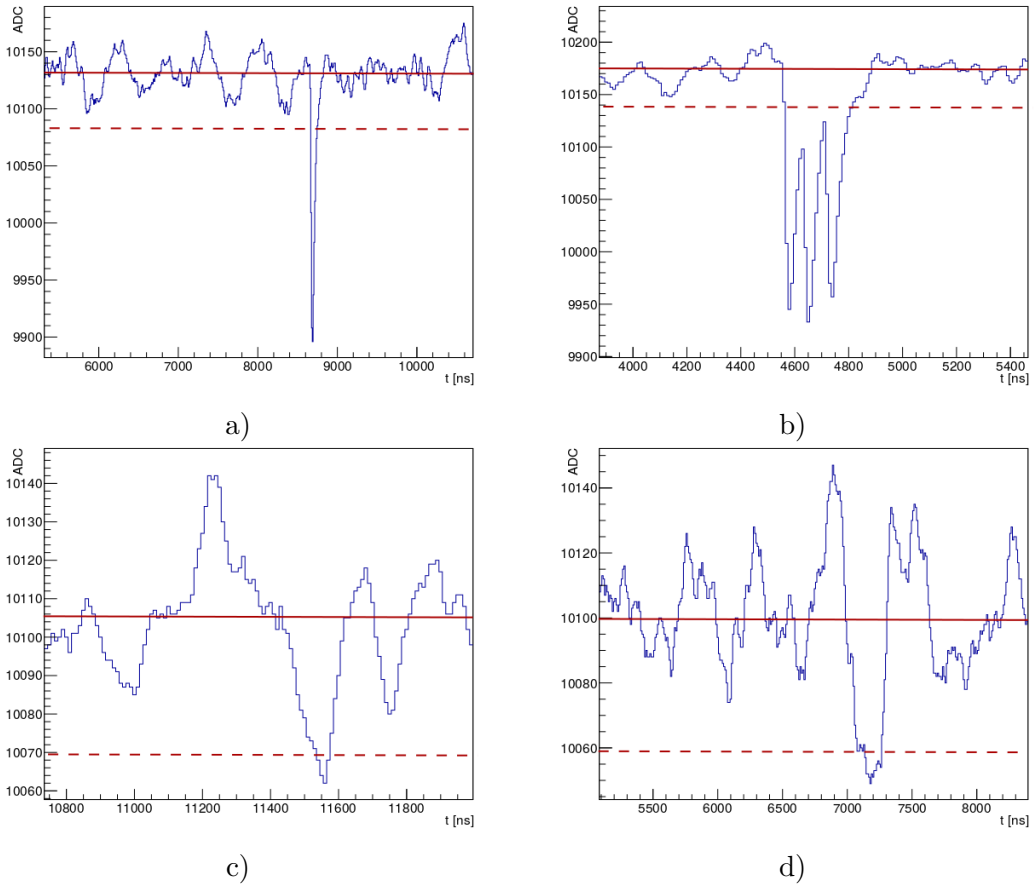

Figure 6.12: Event topology of different classes of PMT pulses. The red lines indicate the value for the baseline b_j and the trigger threshold which is set to $3 \cdot \sigma_j$. See text for further discussions.

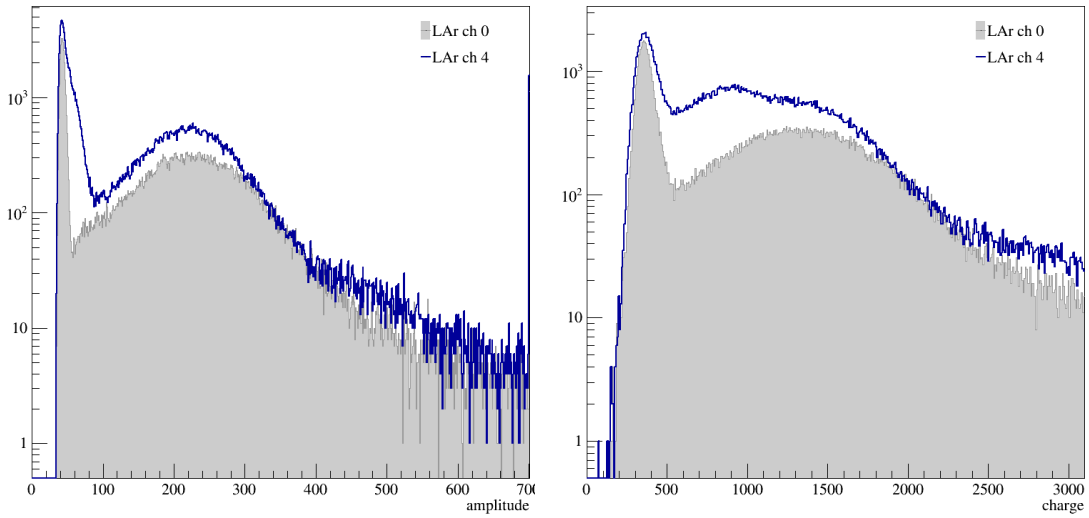

Figure 6.13: Single photoelectron spectra using the amplitude (left) and charge (right) of a reference PMT (gray) and a noisy PMT (blue).

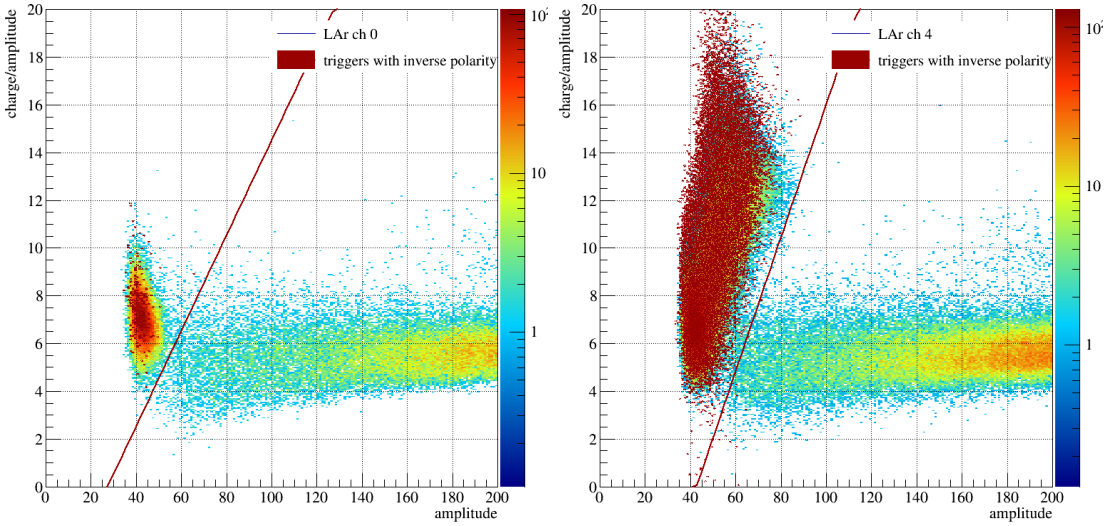

Figure 6.14: Amplitude against charge of hits with both polarities.

this specific PMT the peak-to-valley increases from 1.6 to 4.3.

Since no quality cut was foreseen for the LAr light detectors in the data conversion structure, it was not possible to have it implemented on the timescale of the first Phase II data release. As illustrated in Fig. 6.13 the single photoelectron distributions based on the amplitude of the signals show for some channels a much better peak-to-valley. Therefore, it was decided to export the calibrated amplitudes in photoelectrons to tier3 and to extract the veto flag based on the amplitude of the PMT signals.

6.3.3 PMT gain calibration

The next step in the data conversion and analysis chain is the gain calibration of all light detector channels in photoelectrons. At the same time, the trigger positions are converted into time differences relative to the first trigger found in a Germanium detector.

The calibration of the PMT signals in photoelectrons is carried out by fitting the photoelectron distributions with Gaussian peaks accounting for 1 p.e., 2 p.e., 3 p.e. and a noise pedestal. The procedure along with a more detailed discussion of the individual components of such a single photoelectron distribution has been explained in Sec. 4.4.5.

For the performance as anti-coincidence veto neither an absolute gain calibration nor the same gain in arbitrary units is mandatory. Important is the time stability of the gain calibration and in general, of the veto system (see Fig. 7.17) and the separation of single photoelectrons from noise. This is characterized by the peak-to-valley as elucidated in Sec. 4.4.6. Under the given noise conditions, a peak-to-valley of ≥ 3.5 is typically reached for the PMTs in the GERDA LAr veto system.

A similar gain calibration with slightly different functions is performed for the SiPM channels. Details can be found in [137].

6.3.4 Anti-coincidence veto algorithm

The veto efficiency of a scintillation light veto in GERDA is an interplay of suppression efficiency in a certain energy range and the veto acceptance.

The suppression factor is defined as

$$SF = \epsilon_{acc} \cdot \frac{N_0}{N_S} \tag{6.2}$$

where N_0 is the number of events before the veto is applied, N_S the number of remaining events and ϵ_{acc} the acceptance of the veto system. Latter gives a measure for events that are vetoed by random coincidences. In the GERDA setup this number is extracted by calculating the fraction of accepted pulser events.

$$\epsilon_{acc} = \frac{N_{a,pulser}}{N_{0,pulser}} \tag{6.3}$$

with $N_{a,pulser}$ the number of accepted pulser events after applying the LAr veto cut and $N_{0,pulser}$ the initial number of pulser events. Since the pulser signal is directly injected in the preamplifier of the Germanium detectors they have no physical origin. These signals can only be vetoed by: the intrinsic dark rate of the light detector channels, misidentified noise signals, afterpulses belonging to another physical signal in the light detectors, photons created by background that does not deposit energy in the Germanium detectors, such as ^{39}Ar. The veto acceptance can be cross-checked by calculating the survival fraction of single γ-lines, such as the full energy peak of ^{40}K (see Sec. 7.5.3). In this case, all the energy released in the decay is deposited in the Germanium detectors and no energy is left to be converted into scintillation light in the liquid argon.

Both the suppression factor and the veto acceptance depend on the veto window and the energy threshold, defining if a hit in one of the light detection channels gives a veto signal

For the first data release of Phase II , the individual thresholds and veto windows are set by hand. The overall veto flag is set if at least one photoelectron is found in any single light detector (see Sec. 7.5.2).

CHAPTER 7
LAR VETO PERFORMANCE IN GERDA

In December 2014, the integration test runs of the Phase II hardware started, including the LAr light instrumentation setup and a varying number of Germanium diodes.

In the first part of this chapter the achieved suppression factors during the LAr veto commissioning runs with two different calibration sources will be presented along with a measurement of the triplet lifetime of the LAr in the GERDA cryostat by the PMTs. The second part describes the analysis performed for the first six months of Phase II of the GERDA experiment with special focus on the performance of the LAr veto.

7.1 Operational light detectors

Tab. 7.1 shows the different runs that were performed during the integration and commissioning of the Phase II setup and the physics runs of the first six months of Phase II.

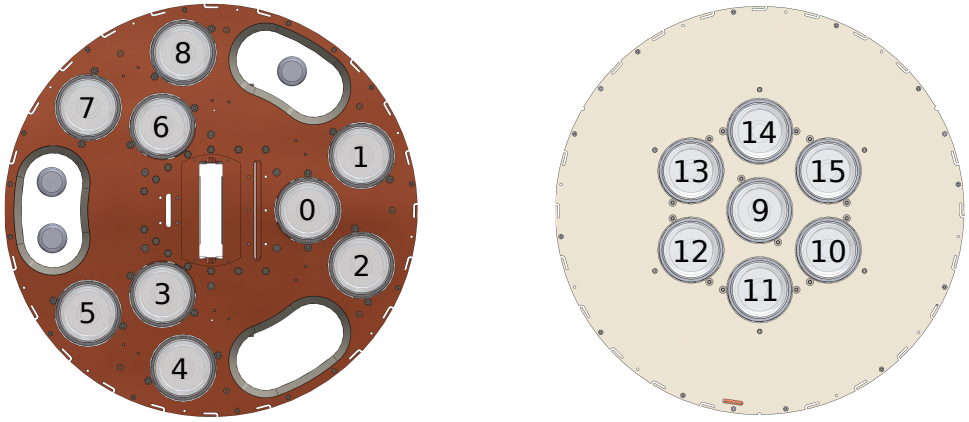

Figure 7.1: **PMT positioning in the GERDA setup.** Left: Scheme of the upper copper support plate for the PMT channels 0 - 8. Right: Drawing of the bottom support plate lined with reflector foil. Seven PMTs are mounted (PMT ch. 9 - 15). The numbers indicate the order in which the PMTs are connected to the FADC channels (often referred to as *LAr channel* in order to distinguish them from the Germanium detector FADC channels).

run	period		operational PMTs	operational SiPMs
INTEGRATION TESTS				
Jan15	I	2015/01/28 - 2015/02/21	16/16	7/15
20150417		2015/04/17 - 2015/04/20	15/16	7/15
Replacement of SiPMs				
LAR VETO COMMISSIONING				
20150430		2015/04/30 - 2015/05/23	13/16	15/15
20150528		2015/05/28 - 2015/06/15	13/16	15/15
Operations on PMTs				
20150715	II	2015/07/15	14/16	15/15
GERMANIUM COMMISSIONING				
50		2015/07/26 - 2015/09/07	14/16	15/15
Operations on PMTs				
51	III	2015/09/30 - 2015/10/29	16/16	15/15
52		2015/11/13 - 2015/12/08	16/16	15/15
PHASE II PHYSICS RUNS				
53 - 64		2015/12/20 - 2016/06/01	16/16	15/15

Table 7.1: Overview of PMT performance in GERDA integration and commissioning runs.

In the very beginning, half of the SiPMs were not working properly. These SiPMs were replaced mid of April by eight SiPMs with a higher fill factor. Since then all SiPMs could be used for analysis. Due to significantly higher suppression factors of these new type of SiPMs, the remaining eleven SiPMs were replaced iteratively (June 2015, September 2015).

The PMT channel ordering in the light instrumentation setup is shown in Fig. 7.1. Before the first operations on the PMTs mid of April 2015, three PMTs were not working. Two showed a huge afterpulse rate (LAr ch. 6, LAr ch. 14) and another PMT tripped due to light flashing (LAr ch. 15, see Sec. 4.4.3). The problematic PMTs have been replaced and three others have been interchanged to have supposedly stable working PMTs mounted at the top plate. Since two PMTs remained not operational (LAr ch. 6, LAr ch. 10), the PMT light readout system has been changed again in September 2015. This time two new PMTs have been installed, two PMT bases have been exchanged and one PMT was put on another channel. Since then all PMTs are operational. The assignment of the LAr channels (PMTs) to the PMT serial number is listed for all three periods in Tab. D.1.

7.2 LAr veto commissioning results

Finishing the Germanium detector integration tests in April 2015, the LAr veto commissioning took place in April and May 2015. In this section the focus is set on the commissioning test measurements that have been important to evaluate the LAr veto performance. First of all, these are two runs with two different calibration sources that have been used to evaluate the background suppression efficiency of the LAr veto and their comparison to Monte Carlo simulations.

energy window	suppression factor after				
	PMT top	PMT bottom	PMT	SiPM	LAr veto
ROI	5.22 ± 0.04	16.04 ± 0.25	31.40 ± 0.70	71.44 ± 2.51	98.08 ± 0.08
DEP	14.75 ± 0.12	738.46 ± 3.83	-610.3 ± 2.5	1808.52 ± 5.55	2663.96 ± 7.43
1.6 MeV FEP	1.01 ± 0.02	0.99 ± 0.02	0.99 ± 0.02	1.03 ± 0.02	1.03 ± 0.02
SEP	5.29 ± 0.04	15.24 ± 0.08	34.10 ± 0.14	93.45 ± 0.22	91.77 ± 0.19
2.6 MeV FEP	2.03 ± 0.01	2.84 ± 0.01	3.48 ± 0.01	4.96 ± 0.01	5.20 ± 0.01
pulser acc.	98.1 %	96.8 %	96.1 %	88.9 %	87.3 %

Table 7.2: Overview of suppression of different LAr veto sub-systems in different energy regions of ^{228}Th calibration spectrum, along with the pulser acceptance.

7.2.1 ^{228}Th calibration

In April and May a pilot Germanium detector string containing six enriched and two depleted BEGes was inserted together with the light instrumentation in the GERDA cryostat. During this time, six out of eight Germanium detectors were at operational voltage but one (91B) exhibited leakage current. This detector, together with the remaining two detectors (61C and 91C) which were not depleted, were used only for the detector-detector anti-coincidence cut in the subsequent analysis.

End of April 2015 a calibration measurement with a $\approx 1.5\,\mathrm{kBq}$ ^{228}Th calibration source from Phase I was performed while reading out the LAr scintillation light veto at the same time (pcalib). The calibration source was placed in source position S2 10 cm below the uppermost Germanium detector surface, in between Germanium detector 1/D and 91B. During this measurement, three out of 16 PMTs were not ramped up (see Tab. 7.1).

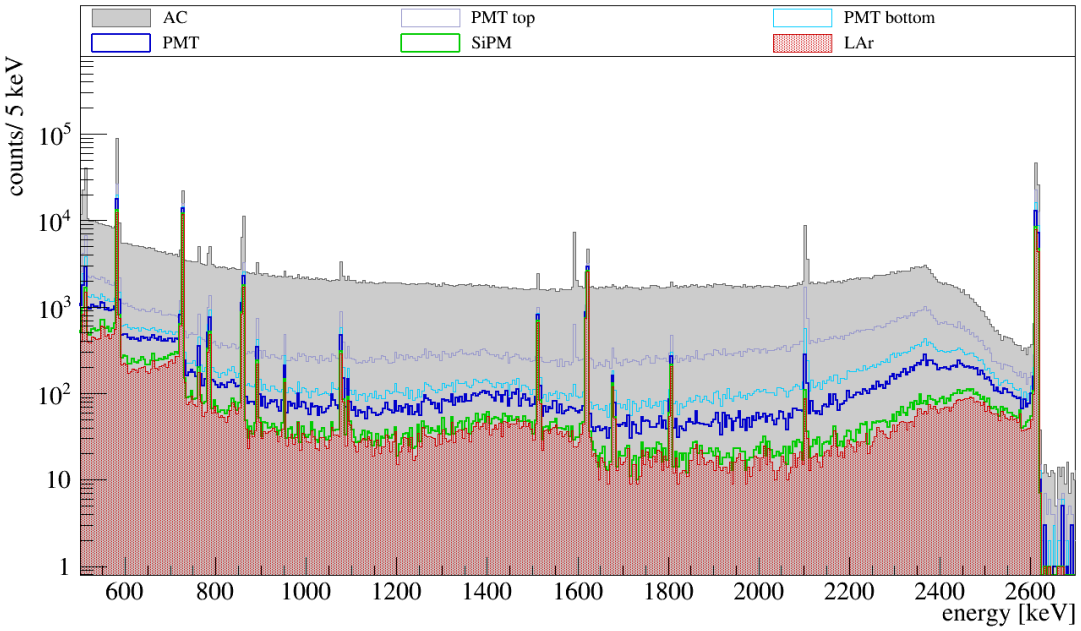

Figure 7.2: ^{228}Th calibration spectrum after anti-coincidence cut and after applying the LAr veto cuts of the different light readout systems individually.

The energy spectra of the five Ge detectors that could be used for analysis are depicted in Fig. 7.2. The gray histogram shows the energy spectrum after applying the detector-detector anti-coincidence cut. The anti-coincidence cut keeps 78.65% of the events in the region of $Q_{\beta\beta} \pm 100\,\mathrm{keV}$ ($\widehat{=}$ ROI), excluding a 20 keV wide window around the single escape peak of the 2615 keV γ-ray of ^{208}Tl. To compare the background rejection efficiency of the different light readout systems, namely the SiPMs and the PMTs, the open histograms show the energy spectra after applying the different anti-coincidence veto cuts. The filled red histogram illustrates the energy spectrum with the combined veto cut.

Tab. 7.2 summarizes the suppression factors SF, as defined in Eq. 6.2, of the different subsystems and their combination in different energy regions. In addition, the pulser acceptance which enters in the calculation of the SF is quoted. In the ROI, the top and bottom PMTs suppress the spectrum by a factor $SF = 5.22 \pm 0.04$ and $SF = 16.04 \pm 0.25$, respectively. Combined they reach a suppression of $SF = 31.40 \pm 0.70$. The SiPMs alone reach a suppression factor of $SF = 71.44 \pm 2.51$ and together with the PMTs the spectrum is suppressed by a factor $SF = 98.08 \pm 0.08$ in the region of interest. Also in the other listed energy regions, such as the DEP, SEP and FEP of the 2615 keV γ-ray of ^{208}Tl, this gradation of background rejection efficiency is confirmed. The top PMTs give the lowest suppression factor, followed by the bottom PMTs and finally the SiPMs. In contrast to early Monte Carlo simulations, the combined suppression by PMTs and SiPMs is higher than the suppression by the SiPMs alone (see Sec. 5.3 or Sec. 7.3). It is apparent that the combined suppression factor in the ROI, which is dominated by Compton scattered events, is approximately the sum of the suppression factors of the PMTs and the SiPMs. This means that the PMTs make up almost 30% of the suppression in the ROI. The full energy peak of ^{212}Bi is created by a single γ-ray. As expected the suppression factors of this peak are compatible with one for

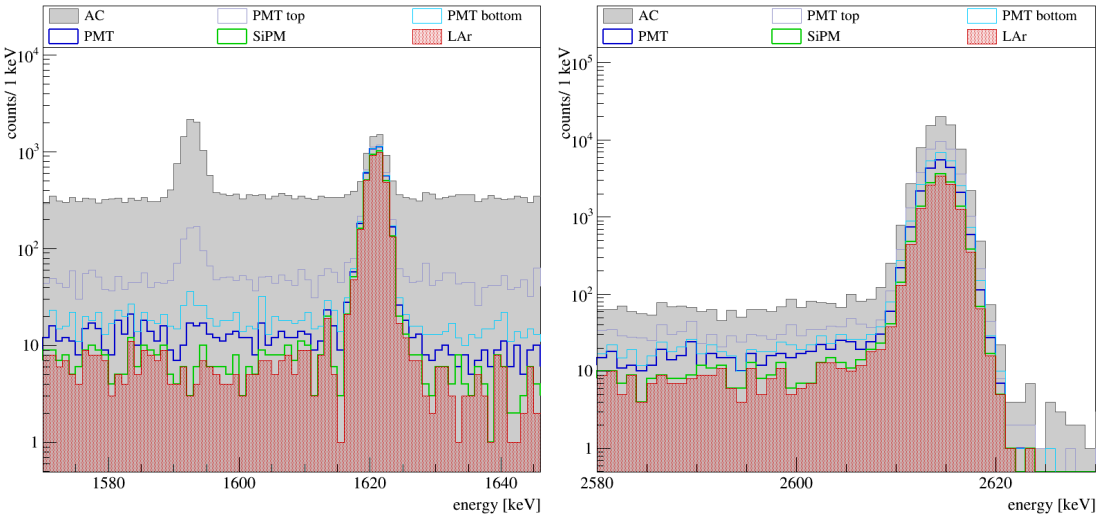

Figure 7.3: **Suppression of different peaks in the ^{228}Th calibration spectrum by the LAr veto subsystems.** Left: Double escape peak of ^{208}Tl at 1592 keV and full energy peak of ^{212}Bi at 1620 keV. Right: Full energy peak of ^{208}Tl at 2615 keV, which is to 84.5% accompanied by a 583 keV γ-ray.

all veto sub-systems. In contrast, the DEP is not visible anymore after applying the LAr veto since 1022 keV are available to trigger the LAr veto (illustrated at the left of Fig. 7.3). In case of the SEP, 511 keV still leave the germanium detector. Most likely, the energy is deposited close to the detectors and consequently, high suppression factors of $SF = 34.10 \pm 0.14$ and $SF = 93.45 \pm 00.22$ are reached by the PMTs and the SiPMs, respectively. The FEP at 2615 keV of ^{208}Tl is accompanied with 84.5% by a 583 keV γ-ray. However, it is more probable that this γ-ray leaves the instrumented volume without triggering the LAr veto which manifests itself in lower suppression factors.

The left plot of Fig. 7.4 shows the suppression factors of the individual light detectors in the region of interest of the sum energy spectrum of all operational BEGes. Breaking down the suppression in the ROI to the individual light detectors shows that the top PMTs reach the lowest suppression factors of $SF \approx 1.3$. The bottom PMTs yield suppression factors of $SF \approx 2.5$, which is compatible with the suppression factors of the SiPMs. Most of them are varying between $SF \approx 1.3$ and $SF \approx 2.7$. Only the ones in close proximity of the calibration source exhibit higher suppression factors around 3.5.

The right plot of Fig. 7.4 compares the suppression factors that are reached in the ROI for the energy spectra of the individual Germanium detectors by the different LAr light readout sub-systems. Germanium detector channel 0 corresponds to the uppermost detector and ch. 7 to the lowermost detector (see Fig. D.4). The bottom PMTs (gray-blue graph) exhibit a decrease of rejection power from $SF = 6.4 \pm 0.1$ to $SF = 4.0 \pm 0.2$ as lower the Germanium detector channel is placed in the detector string. In contrast, the suppression by the bottom PMTs (cyan graph) increases with the Germanium detector channel number from $SF = 13.1 \pm 0.3$ to $SF = 23.4 \pm 2.9$. The course of the suppression factors obtained with all PMTs (dark-blue) is almost constant over the whole detector string and around 30, except for the bottommost detector for which the suppression factor is $SF = 36.3 \pm 5.6$. Consequently, the decrease of rejection power of the top PMTs is more than compensated by the increase of rejection efficiency by the bottom PMTs. The SiPMs (green), which are placed above the uppermost Germanium detector, show a quite strong decrease in suppression efficiency from $SF =$

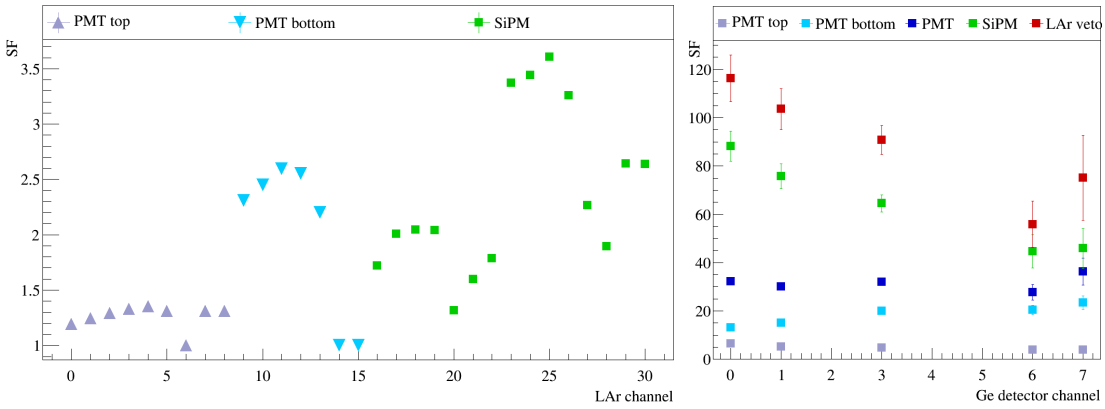

Figure 7.4: **Suppression factor distributions of ^{228}Th calibration source measurement**. Left: The suppression factors in the ROI of the sum energy spectrum are plotted for each LAr channel. Right: The suppression factors of the energy spectra of the individual Germanium detector channels are shown for the different LAr veto subsystems and their combination.

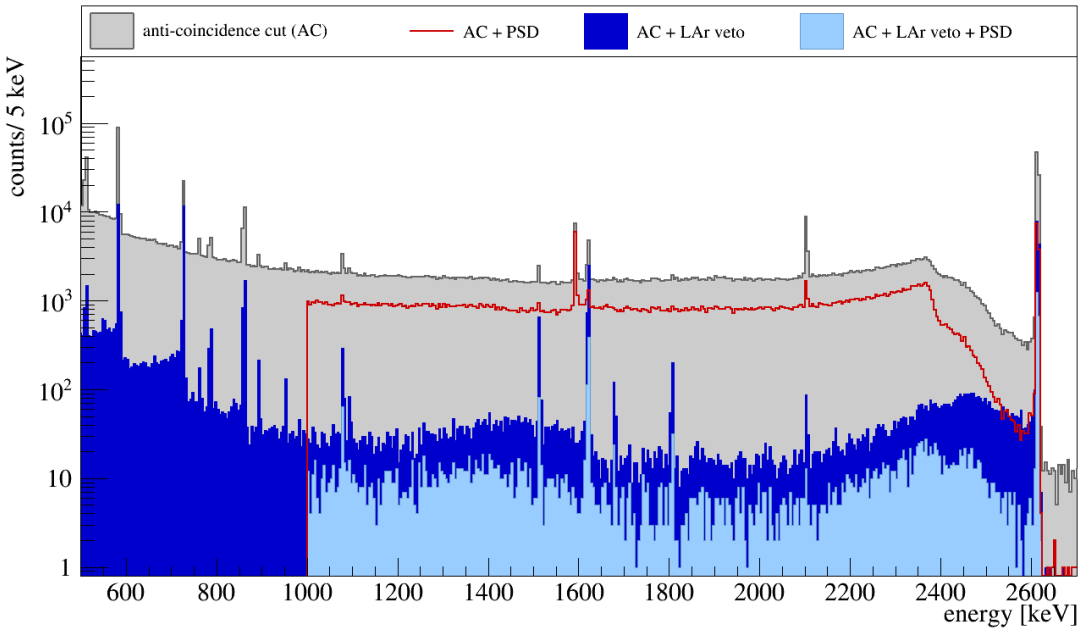

Figure 7.5: ^{228}Th calibration spectra after PSD and LAr veto cuts.

88.2 ± 6.3 in the uppermost BEGe to $SF = 44.2 \pm 6.8$ in the second lowest. A slightly higher suppression of $SF = 45.82 \pm 8.3$ is reached for the bottommost detector. The suppression efficiency of the whole LAr veto system is dominated by the rejection power of the SiPMs. Consequently, the same trend is visible when going down along the Germanium detector string. The highest suppression factor $SF = 116.3 \pm 9.6$ is obtained for the BEGe in channel 0, the lowest for ch. 6 $SF = 55.8 \pm 9.6$. Due to a stronger rejection power by the PMTs the overall suppression factor is $SF = 75.1 \pm 17.6$ for the bottommost detector.

Combining the LAr veto with pulse shape discrimination enhances the background suppression significantly. Fig. 7.5 shows the energy spectrum with the different background suppression techniques and their combination. Since only BEGe detectors are mounted in the pilot string the pulse shape discrimination is based on the A/E parameter (see Sec. 2.3.4). The cut is valid from 1000 keV on and set to the value that preserves 90% acceptance in the DEP [134]. The spectrum after this pulse shape discrimination cut and detector-detector anti-coincidence cut is depicted in red. In the ROI the energy spectrum is suppressed by a factor 2.1 ± 0.1. As discussed above, the LAr veto suppresses the ^{228}Th calibration spectrum by a factor 98.1 ± 0.1 (blue). The spectrum after applying PSD and LAr veto cut is depicted in cyan. In total, the spectrum is suppressed by a factor $SF = 360.9 \pm 28.9$. The fact that the total suppression factor is higher than the product of the individual suppression factors is discussed in Sec. 7.4.

Fig. 7.6 illustrates the different rejection principles of a scintillation light veto and a pulse shape discrimination technique. In case of γ-ray induced background, such as the ^{228}Th calibration data under consideration, pulse shape discrimination distinguishes single-site events from multi-site events. The DEP of ^{208}Tl, which is often used as a proxy for a single-site event class, is set to 90% acceptance. As discussed beforehand, the peak is highly suppressed by the LAr veto. In contrast, the FEP of ^{212}Bi is known

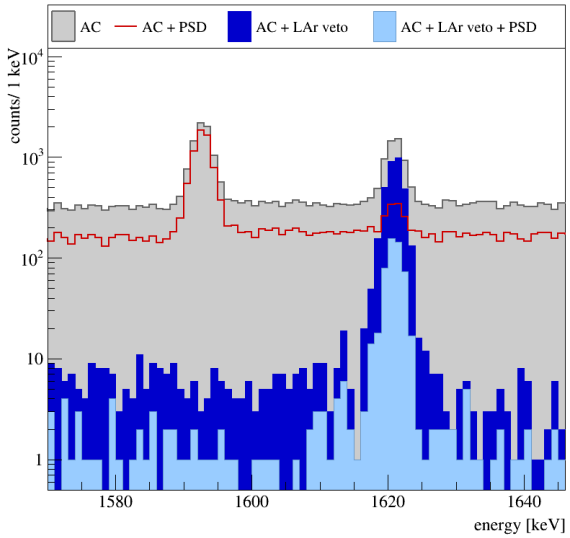

Figure 7.6: Energy spectra around the DEP of 2615 keV γ-ray after PSD and LAr veto.

to be populated by 92% of multi-site events and the suppression factor by PSD is determined to be $SF = 7.0 \pm 0.1$ [134]. The LAr veto preserves the peak since it is caused by a single γ-line. In future, these complementary features can be used to identify if a potentially emerging peak at $Q_{\beta\beta}$ is really due to $0\nu\beta\beta$-decay.

7.2.2 ^{226}Ra calibration

In May 2015 a ^{226}Ra calibration source measurement with the pilot string was performed. The LAr scintillation light detectors were read out at the same time to evaluate the background rejection efficiency for this kind of γ-ray background. Since no radioactive source was available which could have been placed in the Tantalum absorber of the Phase II source insertion system a custom made source holder together with a 1 kBq ^{226}Ra wire source was attached below the Tantalum absorber and lowered so far that the radioactive source was at the same height as the source during the ^{228}Th calibration

energy window	acc.	suppression factor after		
		LAr veto	PSD	LAr veto + PSD
^{228}Th calibration				
ROI		98.1 ± 4.1	2.1 ± 0.1	360.9 ± 28.9
DEP		2664.0 ± 7.4	1.1 ± 0.1	761.1 ± 0.8
1.6 MeV FEP	87.3 %	1.0 ± 0.1	7.0 ± 0.1	7.0 ± 0.1
SEP		91.8 ± 0.2	10.8 ± 0.1	675.8 ± 0.6
2.6 MeV FEP		5.2 ± 0.1	6.6 ± 0.1	33.1 ± 0.1
^{226}Ra calibration				
ROI	91.3 %	4.5 ± 0.1	3.6 ± 0.1	24.8 ± 1.8
2.2 MeV FEP		1.0 ± 0.1	8.0 ± 0.2	8.2 ± 0.2

Table 7.3: Overview of suppression factors in different energy ranges by LAr veto, PSD and their combination.

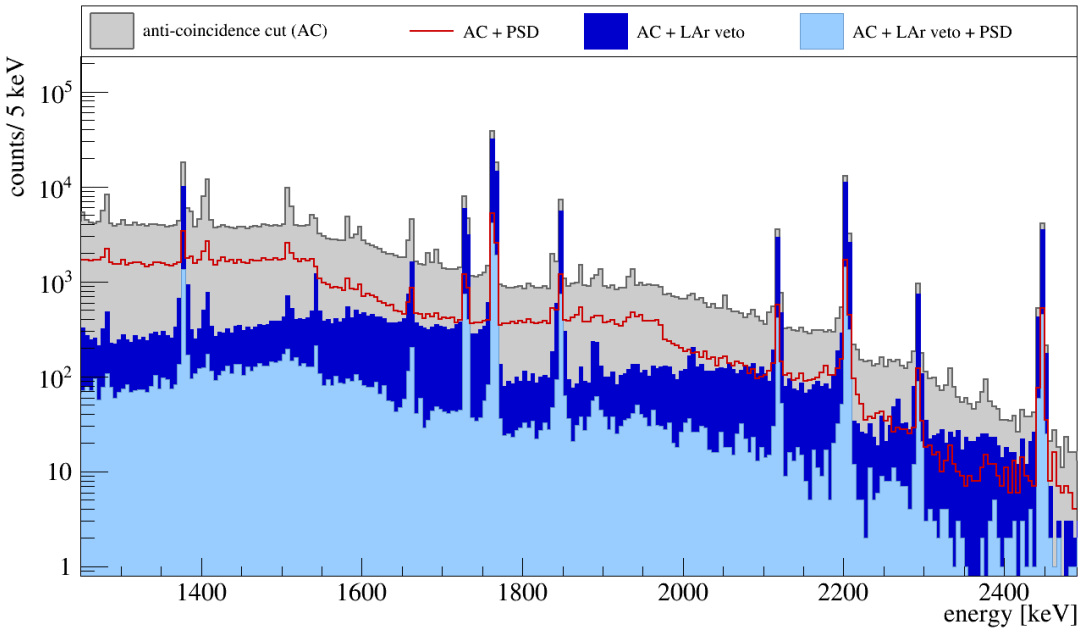

Figure 7.7: ^{226}Ra calibration spectra after PSD and LAr veto.

measurement (see Fig. D.4 for a sketch of the setup).

All FADC traces were read out for events that deposited at least 1 MeV in a single Germanium detector (pcalib). Fig. 7.7 shows the corresponding energy spectrum. 86.4 % of the events in the ROI survive the detector-detector anti-coincidence cut. For this calibration source measurement the ROI is defined as the energy window from 2023 keV to 2074 keV, excluding the full energy peak of ^{214}Bi at 2053 keV.

The PSD cuts were determined by accepting 90% of the DEP at 1592 keV in a dedicated ^{228}Th calibration spectrum. Subsequently, these cut values were applied to this calibration data in order to extract the energy spectrum of the ^{226}Ra after PSD (red). Pulse shape discrimination analysis suppresses the background in the ROI by a factor 3.6 ± 0.1.

The background rejection efficiency of each light detector follows the same trend as during the ^{228}Th calibration (see Sec. 7.2.1) and will not be discussed in detail for this source. Overall, the LAr veto reaches a much smaller suppression factor in the ROI of the ^{226}Ra energy spectrum (dark-blue), namely $SF = 4.1 \pm 0.1$, than in the case of ^{228}Th source. The pulser acceptance during this measurement was determined to be 91.3%. This difference is expected since the background in the ROI originates mainly from Compton-scattered 2204 keV γ-rays. Consequently, the excess energy that is able to create scintillation light in the LAr amounts to 181 keV at best. The fact that this γ-ray is not in coincidence with another γ-ray is confirmed by the suppression factors that are listed in Tab. 7.3. Combining LAr veto and PSD (light blue) increases the background rejection power in the ROI to $SF = 22.6 \pm 1.7$.

As indicated in Tab. 7.3 the 2.2 MeV FEP of ^{214}Bi is not vetoed by the LAr veto but by PSD. In total, a suppression factor of $SF = 8.2 \pm 0.1$ is reached.

By comparing the suppression factors that were reached for the ^{228}Th and ^{226}Ra calibration source measurements one can conclude that the LAr veto efficiency is strongly

dependent on the isotope and the excess energy that is available to trigger a LAr scintillation light veto. Furthermore, these suppression factors are only representative for the specific measurement itself since dead material, such as nearby detectors which are not operational and the absorber of the calibration source, can absorb energy that cannot be detected by the LAr veto.

7.2.3 LAr triplet lifetime

As elucidated in Sec. 3.1, the triplet lifetime gives a good measure for the purity of LAr. In ultra-pure liquid Argon it has been measured to be: $\tau = 1590 \pm 100\,\text{ns}$ [88].

The triplet lifetime of the liquid Argon in the GERDA cryostat can be extracted by averaging the waveforms that are acquired with the FADC for each PMT and fitting the slow exponential component, as depicted for one PMT in Fig. 7.8. On average, a triplet lifetime of $\tau = 971.7 \pm 30.2\,\text{ns}$ is measured.

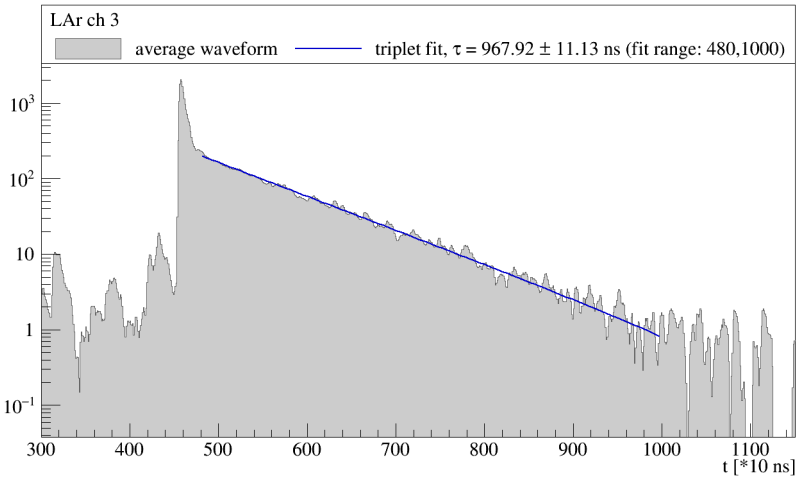

Figure 7.8: Average PMT waveform with triplet lifetime fit.

7.3 Comparison of Monte Carlo simulations with commissioning data

This section is based on the LAr veto commissioning data with a ^{228}Th and a ^{226}Ra calibration source (see Sec. 7.2.1 and Sec. 7.2.2). These calibration source measurements are used to compare the suppression factors and photoelectron yield predicted by the Monte Carlo simulations including photon tracking to the actually measured ones.

7.3.1 Updated Monte Carlo configuration

In contrast to the early Geant4 simulations (see Ch. 5) which where used to help answering design-related questions and evaluate the LAr veto capability of the hybrid LAr veto design and its sub-systems, these simulations have been performed after the LAr veto instrumentation and the full Phase II detector array have been inserted in the GERDA setup. Consequently, the final geometry of holders, cables, mini-shrouds,... was known and implemented in MAGE.

This led to the following modifications in the Geant4 geometry:

1. Radius of the shrouds of the light instrumentation has been changed from 490 mm to 470 mm.
2. Top and bottom PMT holding structures and therewith the PMT positions have been adapted to the final setup.
3. The material of the PMT holder plates changed from PTFE to copper.
4. BEGe detector pairs can now be composed of two individual BEGe detectors from the GERDA detector library. In the first simulations, they were composed of two identical but mirrored BEGe detectors with average dimensions.
5. Silicon detector holder plates are now implemented with their quasi-triangular shape and not as a circular plate.
6. Semi-coaxial detectors are now implemented with Phase II holders, similar to the BEGe detector holders but with only one silicon plate below the detector. In the first simulations, semi-coaxial detectors could only be placed with Phase II holders. As a result, a deteriorated veto efficiency was obtained in case of contaminations in the detector holders.
7. The distance between two detectors and two BEGe detector pairs can now be adapted to the real dimensions.
8. Signal and high-voltage cables which are running from the detectors to the pre-amplifiers were added along with the electronics plate which holds all the pre-amplifiers and cable connections to the cable chain.
9. In the first simulations, no mini-shrouds were implemented. Now, the final transparent Nylon mini-shrouds coated with wavelength shifter are implemented in MAGE [103].

One remaining difference between the Geant4 geometry and the real setup, is the reflector foil which is placed in the top and bottom copper shroud (see Sec. 6.1). Due to instabilities of the wavelength shifter coating of VM2000 found in LArGe (see Sec. 3.3) the a Tetratex® [65], a diffuse reflecting PTFE fabric, dip-coated with Tetraphenyl-butadiene (TPB) has been installed in the light instrumentation setup [135].

7.3.2 Comparison for different optical parameters

As mentioned before, three of eight BEGe detectors were not fully operational during these measurements. To be able to compare the results of the Monte Carlo simulations to data it is necessary to extract results from the data without using the problematic Ge detectors for detector anti-coincidence. Tab. 7.4 summarizes the suppression factors of the commissioning runs with a ^{228}Th and a ^{226}Ra calibration source in case only the five stable working detectors of the pilot string are used for detector anti-coincidence.

First, simulations of both calibration sources with the updated Geant4 geometry and the nominal optical parameters from Sec. 5.1.2 have been run. The results are compiled in Tab. 7.4. The energy spectra after detector anti-coincidence and after LAr veto of the data and the Monte Carlo simulations are compared in Fig. 7.9. In the

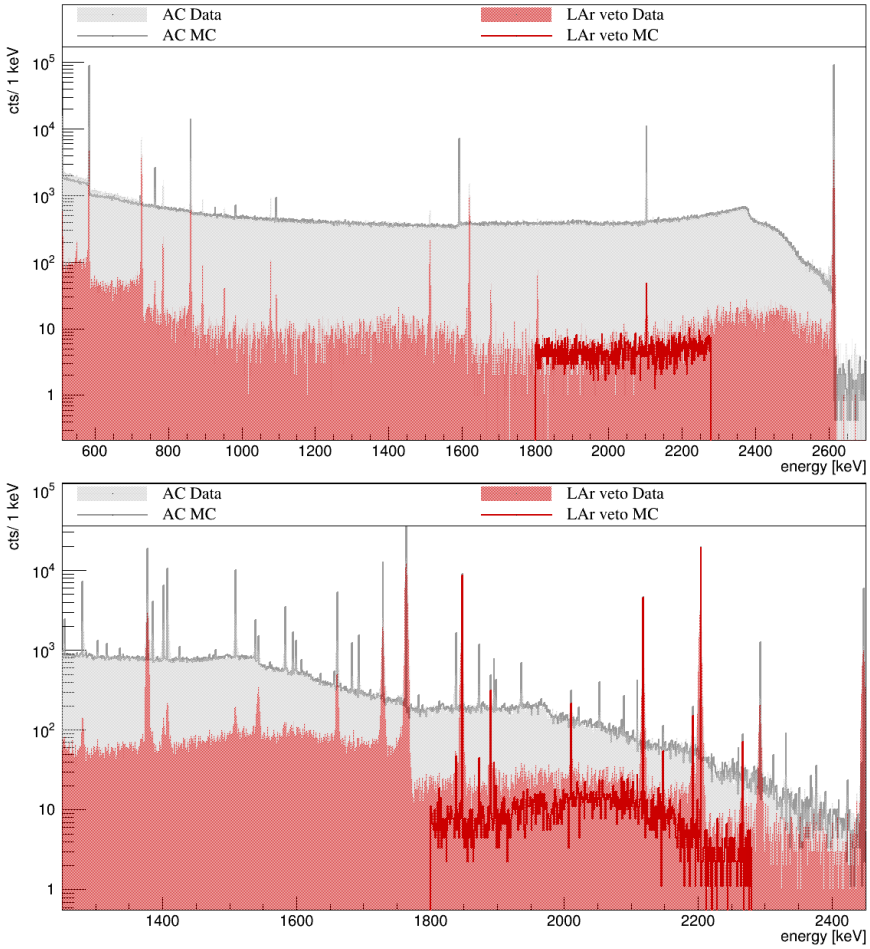

Figure 7.9: Energy spectra of calibration source measurements during LAr veto commissioning together with Monte Carlo simulation performed with nominal optical parameters. Top: ^{228}Th calibration source measurement. Bottom: ^{226}Ra calibration source measurement.

measured sum energy spectrum of the ^{228}Th calibration a suppression factor of 64.3±2.1 is reached by the whole LAr veto system, while the Monte Carlo simulation predicts 87.2 ± 2.1. In case of the ^{226}Ra calibration measurement the data yields a suppression factor of 4.0 ± 0.1 and the simulation a factor of 8.4 ± 0.5. It becomes obvious that the

	suppression factor in ROI					
	^{228}Th calibration			^{226}Ra calibration		
	data	nominal MC	tuned1	data	nominal MC	tuned1
top PMTs	4.8 ± 0.1	45.9 ± 0.8	15.7 ± 0.4	1.4 ± 0.1	4.5 ± 0.2	2.2 ± 0.1
btm. PMTs	13.6 ± 0.2	43.0 ± 0.8	12.3 ± 0.3	2.1 ± 0.1	4.5 ± 0.2	2.3 ± 0.1
all PMTs	24.2 ± 0.4	63.6 ± 1.3	32.0 ± 1.1	2.4 ± 0.1	6.3 ± 0.3	3.4 ± 0.2
SiPMs	50.6 ± 1.4	87.1 ± 2.1	71.5 ± 3.6	3.5 ± 0.1	8.3 ± 0.4	6.9 ± 0.5
LAr veto	64.3 ± 2.1	87.2 ± 2.1	74.1 ± 3.7	4.0 ± 0.1	8.4 ± 0.5	7.2 ± 0.5

Table 7.4: Comparison of suppression factors in ROI in data and Monte Carlo simulations for the whole detector string for ^{228}Th and ^{226}Ra calibration measurement.

suppression factors are over-estimated by the Monte Carlo simulations. The strongest deviation is observed in case the top PMTs are analyzed. The Monte Carlo simulations predict similar suppression factors as in case of the bottom PMTs but in reality a factor two to three difference is observed between the two read-out systems.

The first assumption for the overall deviation was that the photoelectron yield is significantly lower in the GERDA setup than assumed in the Monte Carlo simulations. The figures at the top of Fig. 7.10 show a comparison of the photoelectron yields measured in the ^{228}Th and ^{226}Ra calibration and obtained in the Monte Carlo simulations with the nominal optical parameters. The photoelectron yield of the bottom PMTs predicted by the Monte Carlo simulations is approximately over-estimated by a factor two, while it amounts even to a factor of three to four in case of the top PMTs and the SiPMs.

An effective scaling of the Monte Carlo has been introduced to tune the Monte Carlo simulations. As mentioned earlier the fiber shroud is implemented as a full cylinder with one readout channel at the top of the cylinder. In reality, the fiber shroud is

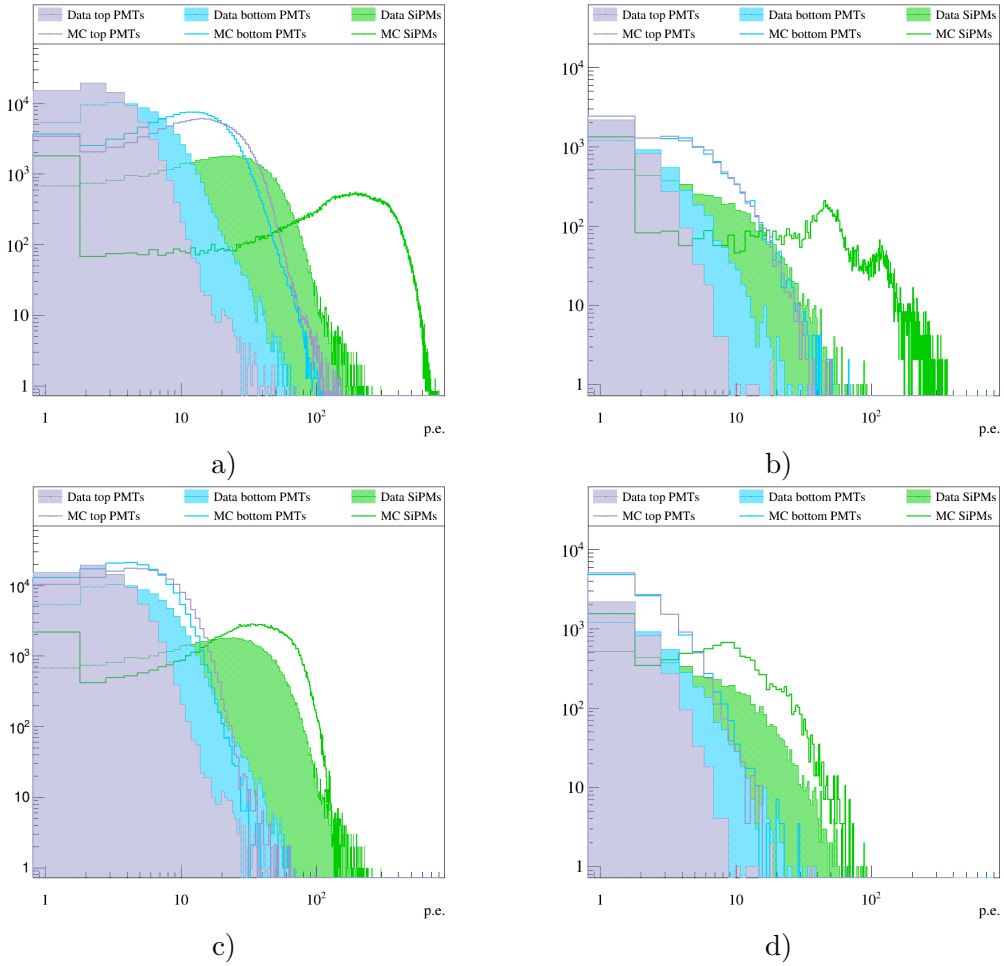

Figure 7.10: Comparison of photoelectron distribution in data and MC for ^{228}Th and ^{226}Ra calibration with nominal and tuned optical parameters. a) ^{228}Th calibration with nominal parameters. b) ^{226}Ra calibration with nominal parameters. c) ^{228}Th calibration with tuned parameters. d) ^{226}Ra calibration with tuned parameters.

composed of individual fibers assembled to a curtain. In this way the real coverage is in any case smaller than 100%. Since the fibers are put diagonal in their holders (see Sec. 6.1.2), a natural assumption would be that they turn in liquid argon such that only one side of the rectangle is directed to the center of the shroud, resulting in a coverage of 70%. In addition, the light yield was scaled down.

A first tuning was based solely on the ^{228}Th calibration source measurement and found a scaling factor of the SiPM efficiency of 0.6 and a scaling factor of the light yield of liquid argon of 0.3, corresponding to 8436 ph/MeV [103]. Meanwhile, the Geant4 geometry has been updated to better match the real Phase II geometry and furthermore, a ^{226}Ra calibration measurement is available to cross-check the tuning parameters. The suppression factors are compiled in Tab. 7.4 and the photoelectron distributions are shown at the bottom of Fig. 7.10. Neither the predicted suppression factors are in good agreement with the measured results, nor the shape of the photoelectron distribution is well described. In particular, the Monte Carlo predicts that almost the whole suppression is caused by the SiPMs detecting light while in the measured suppression factors the SiPMs and PMTs contribute both with a significant percentage to the total suppression factor.

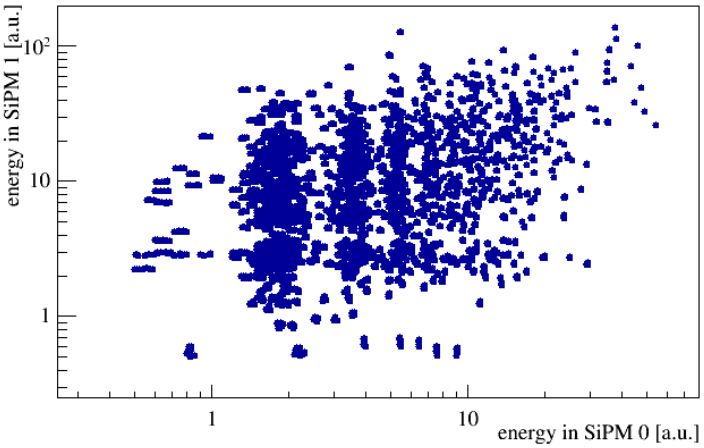

Figure 7.11: Light correlation in two SiPMs connected to the same fibers.

It is found that the fiber modules in which the fibers are running from a SiPM at the top through a loop at the bottom to another SiPM at the top (see Sec. 6.1.2) do not transmit the light as efficient as assumed through the curvature. As a result, no strong correlation between the two SiPMs connected to the same fibers is found (Fig. 7.11). In the reference Monte Carlo setup the bottom surface of the full cylinder is set to a 100% reflectivity, imitating the fiber connection at the bottom. To account for the reduced light correlation, this surface was set to be fully absorbing. Fig. 7.12 illustrates the suppression factors reached by the different LAr veto sub-systems as a factor of the applied scaling factor of the LAr light yield. The fiber coverage scale factor is fixed to 0.7. At the left the plot is shown for the ^{228}Th calibration source measurements and at the right the ^{226}Ra calibration measurement. In both cases the measured suppression factors are illustrated by dashed lines. The curves reveal that none of these combinations of scale factor for the fiber coverage and light yield reproduce the measured suppression factors.

In particular, these simulations predict that the SiPMs make up almost the total suppression factor. However, it may be possible to reproduce the relative contribution of the PMT light read-out by lowering the fiber efficiency. Moreover, the Monte Carlo

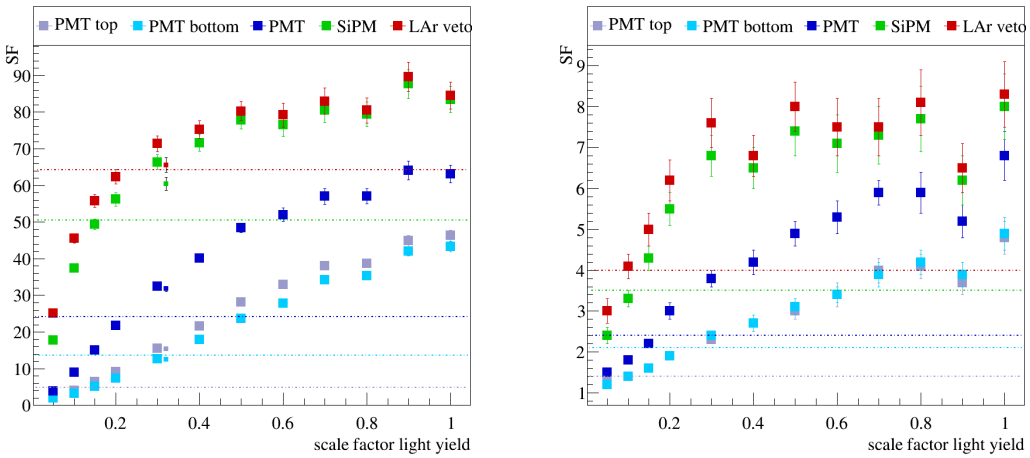

Figure 7.12: Comparison of photoelectron distribution in data and MC for ^{228}Th calibration with reference and tuned optical parameters.

simulations predict comparable suppression factors by the top and bottom PMTs. In reality, the veto efficiency of the top PMTs is reduced by a factor two to three. This difference might be explained by the fact that all germanium detector cables are running to the electronics plate above the detector array. In the simulation the cables are running up straight to the electronics plate while in reality they had to be placed as a loop. As a consequence, the shadowing of the top PMTs by the cables and electronics plate is probably not implemented as close to reality as it would be necessary.

At this point, it was decided to wait for the analysis of additional measurements with the full Phase II germanium detector array and with different radioactive calibration sources at several positions. By means of these measurements it may be possible to tune the optical parameters in a way that all available calibration source measurements and the Phase II physics spectrum after LAr veto are reproduced. Furthermore, the LAr attenuation length for VUV light has been measured by a dedicated setup. The result of this measurement is not yet validated at the time of writing this thesis but it may be available in future and provide independent input [126].

7.4 Study of the interplay of PSD and LAr scintillation veto

In Sec. 7.2.1 and Sec. 7.2.2 the combined background rejection efficiency of LAr veto and PSD was determined for calibration source measurements with a ^{228}Th and a ^{226}Ra source, as summarized in Tab. 7.5.

isotope	acc.	suppression factor			orthogonality ratio
		LAr veto	PSD	total	R
^{228}Th	87.32%	98.1 ± 4.1	2.1 ± 0.1	360.9 ± 28.9	1.75 ± 0.18
^{226}Ra	91.30%	4.1 ± 0.1	3.6 ± 0.1	22.6 ± 1.7	1.53 ± 0.13

Table 7.5: Orthogonality factors of calibration source measurements during commissioning tests.

It was ascertained that the combined suppression is stronger than the product of both suppression factors. This means that the probabilities to suppress a background event in the ROI by the LAr veto and by PSD are correlated. The orthogonality factor R is defined as

$$R = \frac{SF_{total}}{SF_{PSD} \cdot SF_{LArveto}} \tag{7.1}$$

where SF_{total} is the combined suppression factor, and SF_{PSD} and $SF_{\text{LAr veto}}$ are the individual ones. R provides an effective measure of the *over-orthogonality* of the suppression techniques [82].

To understand which mechanism and topology of the events is responsible for the over-orthogonality of PSD and LAr veto cut, Monte Carlo simulations with photon tracking of the ^{228}Th calibration source measurement are analyzed. To obtain the strongest signature, every Germanium detector contributes to the detector-detector anti-coincidence cut and in addition, the Monte Carlo simulation with the nominal optical parameters is used for this analysis.

The A/E value is emulated by the rms of the hit distribution in the active volume of the Germanium detector. It is defined as

$$rms = \sqrt{|center2_x - center_x^2| + |center2_y - center_y^2| + |center2_z - center_z^2|} \tag{7.2}$$

with

$$center_{x/y/z} = \sum_{j=0}^{j<\#\text{hits in detector}} \frac{Edep\_hit(j)}{E_{total}} \cdot Pos\_hit_{x/y/z}(j)$$

$$center2_{x/y/z} = \sum_{j=0}^{j<\#\text{hits in detector}} \frac{Edep\_hit(j)}{E_{total}} \cdot Pos\_hit^2_{x/y/z}(j)$$

The contributions of the individual hits j are weighted by the ratio of the energy deposition of the hit $Edep\_hit(j)$ to the total energy of the event E_{total}. Events with an rms < 1 mm are classified as single site events and events with an rms > 1 mm as MSE[1] (see [134] for a detailed description).

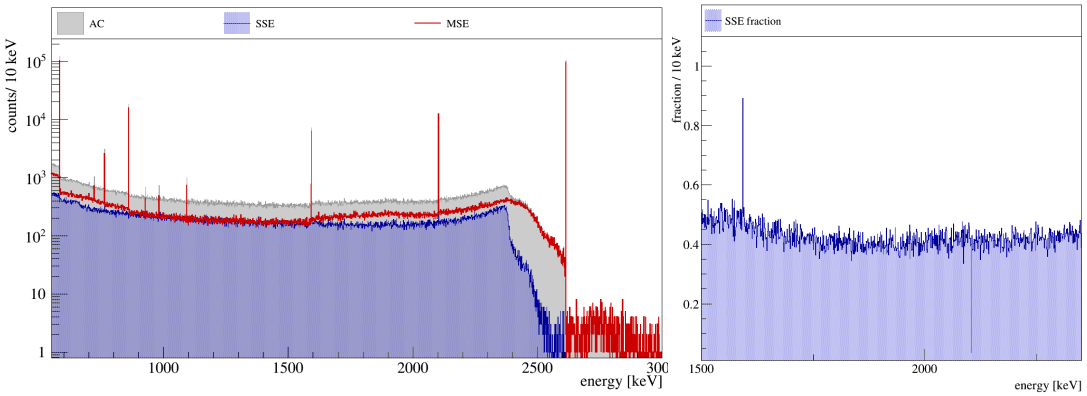

Figure 7.13: SSE and MSE contributions to ^{228}Th spectrum.

[1]This method classifies events which lie on a ring with the same radial distance and height from the p^+ contact as MSE. In contrast, A/E is only sensitive to differences in the drift time of charges and would classify such events as SSE.

The left figure of Fig. 7.13 shows the SSE (blue) and MSE (red) contributions to the spectrum together with the full simulated energy spectrum (gray). In the energy region in which the photon tracking was applied, namely from 1800 keV to 2280 keV ($\widehat{=}$ ROI in this section), approximately 40% of the events are single site events and survive the PSD cut, as illustrated in the right figure of Fig. 7.13. Hence, a suppression factor of $SF = (2.45 \pm 0.01)$ is reached by this cut.

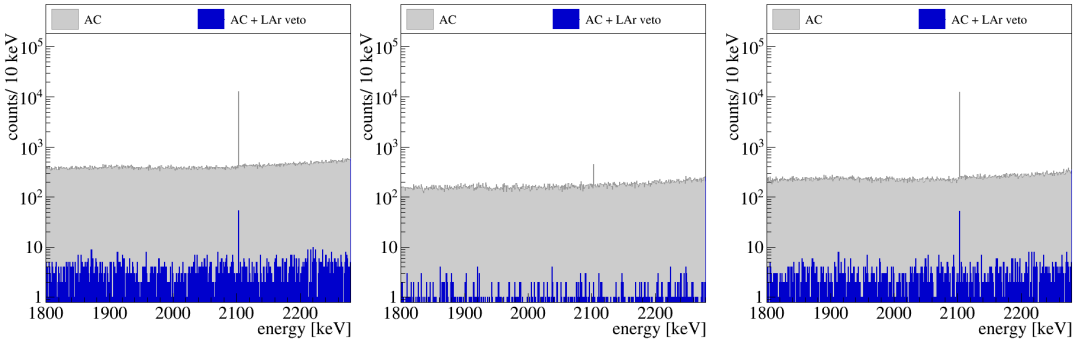

Figure 7.14: LAr veto efficiency on all events, SSE and MSE.

Fig. 7.14 shows the energy spectrum in the ROI before and after the LAr veto cut in case of all events (left), SSE (middle) and MSE (right). The suppression factor obtained for all events amounts to $SF = (129.8 \pm 3.2)$. It increases to $SF = (227.1 \pm 11.9)$ in case single site events are selected and decreases to $SF = (102.0 \pm 2.8)$ in case of multi site events. This leads to an orthogonality factor of $R = ((2.45 \pm 0.01) \cdot (227.1 \pm 11.9))/((2.45 \pm 0.01) \cdot (102.0 \pm 2.8)) = 2.23 \pm 0.13$. This is compatible with the measured orthogonality factor ($R = 1.75 \pm 0.18$) of this calibration source.

As the PSD cut preselects single site events the question is: „*What is special about single site events so that the LAr veto suppresses them more efficiently?* “

At this point it was already known that the effect of a stronger suppression of single site events is only observable if the detector-detector anti-coincidence cut is applied to the data. The original assumption was that more energy is deposited in „dead material“ close to the detector in case of multi site events. The top of Fig. 7.15 shows the energy deposited in the detector dead layer by single site events (blue) and multi site events (red) for events that are discriminated by the LAr veto (left) and for events that survive the cut (right). Over the whole spectrum the counts normalized to the number of single site and multi site events, respectively, are higher in case of multi site events. Consequently, the probability to have an energy deposition in the dead layer is 7.6% in case of a single site event and 14.6% in case of multi site events. This translates into a higher amount of multi site events that do not deposit energy in LAr and henceforth, in a reduced veto efficiency.

The question why the probability of having an interaction in the dead layer is higher in case of multi site events cannot be answered unambiguously with the information contained in the current Monte Carlo simulation. It would be necessary to save the interaction process that triggered the energy deposition, such as Compton scattering or photo-electric effect, in the Germanium detectors along with the trajectory information. This analysis is beyond the scope of this thesis. Nevertheless, the most probable explanation is that in case of single site events a 2.6 MeV γ-ray penetrates the germa-

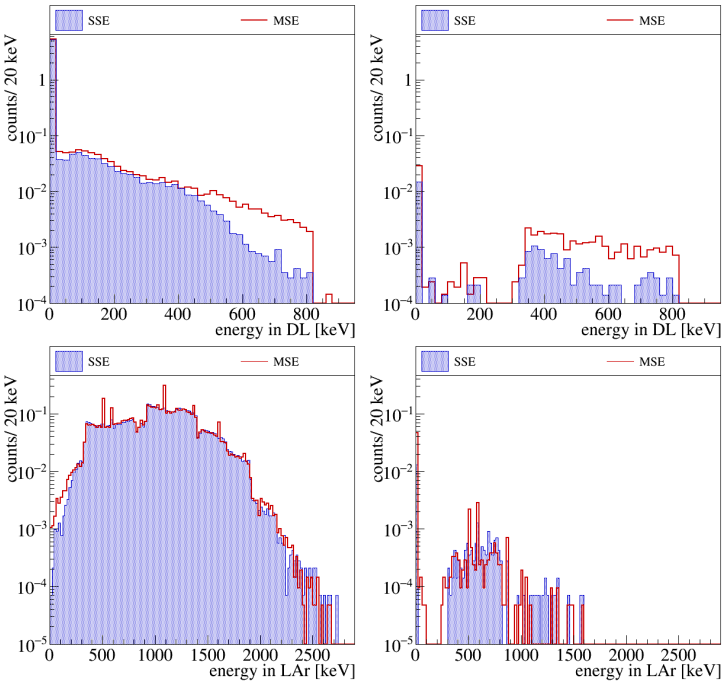

Figure 7.15: **Energy spectra in dead layer and in LAr for vetoed and not vetoed events.**
Top) The energy deposited in the detector dead layer of events vetoed by the LAr veto and classified as SSE (blue) and MSE (red) is shown at the left while the right figure shows the energy spectra of not vetoed events.
Bottom) The energy deposited in LAr is shown for the same topologies.

nium detector with its full energy. The Compton scattered γ-ray still has 600 keV after depositing ≈ 2 MeV in the crystal and an absorption length of 2.5 cm [129]. Thus, the probability of leaving the crystal without an additional interaction is quite high. In contrast, if a 2.6 MeV γ-ray interacts first in material close to the detector, i.e. depositing 500 keV, and ≈ 2 MeV in the active volume of the crystal the range of the resulting γ-ray is shortened to 0.3 cm. Hence, the probability to have again an energy deposition in the dead layer is increased.

7.5 First release of Phase II data

On December 23rd 2015 the data taking of Phase II started with the full Germanium detector array (sketched in Fig. D.5) and the LAr veto. Seven detector strings are immersed, containing 30 BEGe detectors, seven semi-coaxial Germanium detectors from Phase I and in addition, in the central string three natural Germanium detectors. For a more detailed description of the final Germanium detector configuration the reader is referred to [22].

This section describes the data set of the first data release of Phase II. First, it explains the technical work in order to extract the veto flags of the LAr veto instrumentation in coincidence with Germanium detector signals (see Sec. 7.5.1 and Sec. 7.5.2). Second, the acquired background spectrum after LAr veto and background indices are discussed for semi-coaxial and BEGe detectors.

7.5.1 Stability of PMTs in physics run

Fig. 7.16 shows the signal amplitude of one bottom PMT versus time over the whole time period of the first data release. At three moments modifications have been made that concerned the PMT gain and noise level during this period:

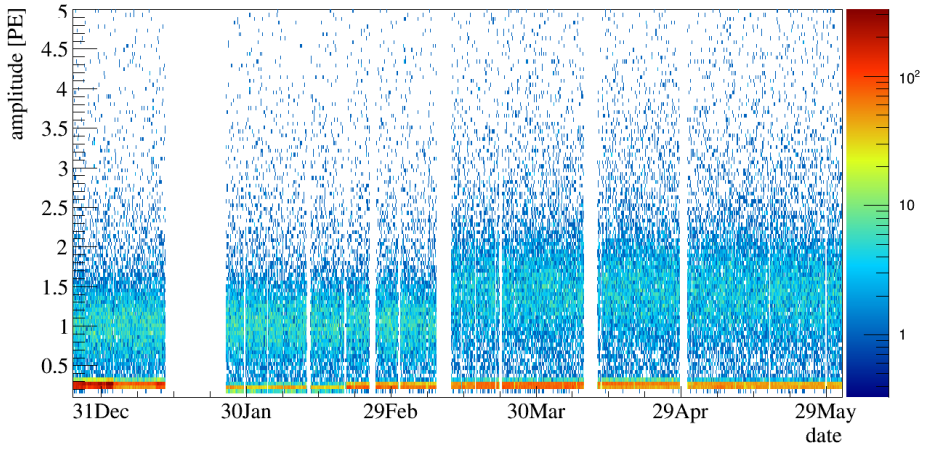

Figure 7.16: Amplitude versus time of one bottom PMT during Phase II dataset.

1. 13.01.2016 - 26.01.2016: At this time a campaign was conducted to reduce the noise on the Germanium detector channels. As part of this campaign the HV filters of the top PMTs were modified by putting an additional resistor to ground. This lead to a significant decrease of the gain of the top PMTs and two PMTs were not operational afterwards.

2. 19.02.2016: Modifications of the grounding scheme changed especially the noise level of the PMT on LAr ch. 6.

3. 10.03.2016: A gain calibration of all PMTs was performed using the FADC spectra. At the same time, connections at two top HV filters were resoldered which recovered the two PMTs which were not operational since the noise reduction campaign in January.

Accordingly to the modifications the data set is split in three time periods. Fig. 7.17 shows the single photoelectron position in ADC channels for a typical PMT in time bins of 5 days (red) and superimposed the single photoelectron position that has been extracted for the respective time periods (blue).

Since the relative deviation is at most 5% it was decided to use a single calibration in photoelectrons in the three different time periods.

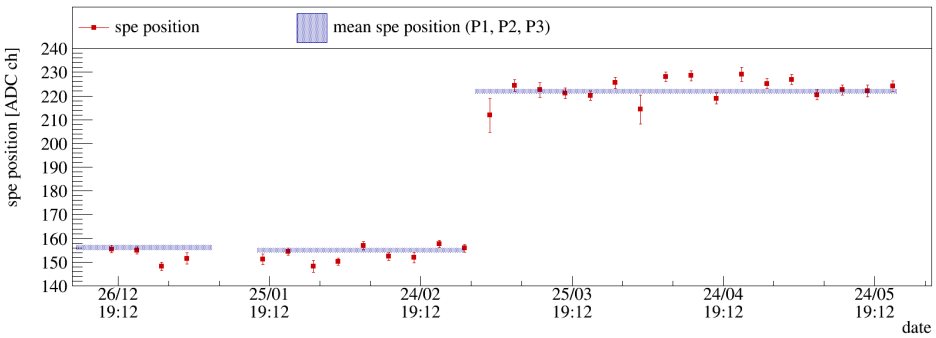

Figure 7.17: **SPE position during Phase II data set.** The variation of the SPE position of one typical PMT are displayed for time intervals of five days (red). Superimposed are the SPE positions that have been determined over the whole time of the calibration periods (blue).

7.5.2 Veto parameters

A calibrated single photoelectron spectrum of one typical PMT is shown in Fig. 7.18 (top). The veto threshold is set to the valley position of this distribution, as indicated in red. Veto thresholds of the PMTs vary between 0.25 and 0.50 photoelectrons, depending on the noise level, while the thresholds of the SiPMs are set between 0.4 and 0.8 photoelectrons.

The veto windows were set by plotting the trigger positions relative to the Germanium detector trigger position that initialized the read-out of the event. The distribution, depicted at the bottom of Fig. 7.18, peaks at 0 ns time difference and then follows the exponential decay due to the slow component of the scintillation light (see Sec. 7.2.3). The region that is not considered to provide a veto flag is hatched in red. Typical values are $[-800\,\text{ns}; 5200\,\text{ns}]$ for the PMTs and $[-100\,\text{ns}; 6000\,\text{ns}]$ for the SiPMs, respectively.

If one single trigger is found in one of the PMTs inside the veto window whose energy exceeds the veto threshold a veto flag is set for this LAr channel in *tier 4* (see Sec. 6.3). In the case of a SiPM channel the sum of the amplitudes in the veto window must exceed the veto threshold in order to provide a veto flag.

A global veto flag is set as soon as one single light detector provides a veto flag.

7.5.3 Physics spectrum after LAr veto

In the first data taking period an exposure of $10.845\,\text{kg}\cdot\text{yr}$ was collected with 35.6 kg of enriched detector mass. Thereof $5.826\,\text{kg}\cdot\text{yr}$ with the BEGes and $5.019\,\text{kg}\cdot\text{yr}$ with the enriched semi-coaxial detectors.

At a first glance, the same major background components are visible in the Phase II physics spectrum as in the Phase I spectrum (see Sec. 2.4.3).

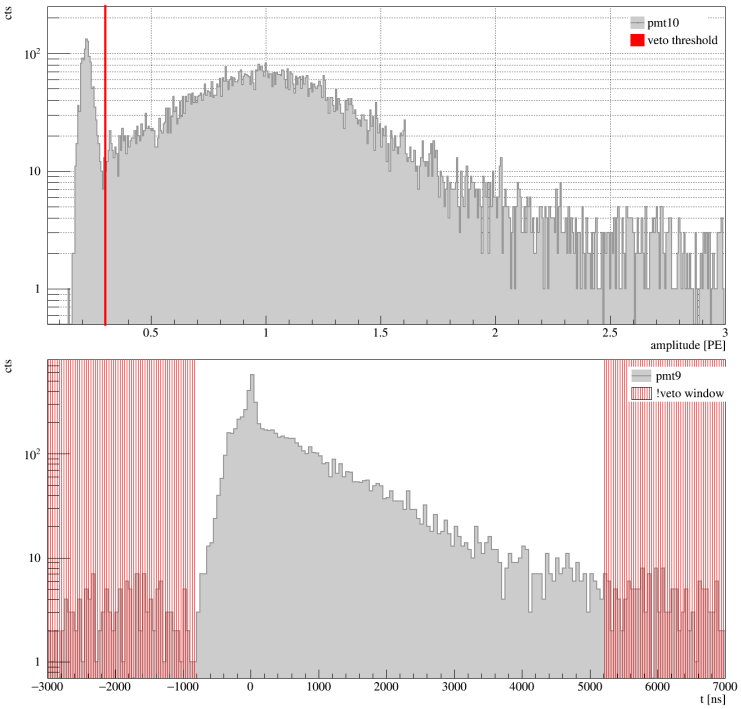

Figure 7.18: **Veto threshold and veto window of a typical PMT.** Top) The calibrated SPE spectrum is shown and the veto threshold is indicated by the red line. Bottom) The distribution of triggers in the PMT traces relative to the Germanium trigger position is illustrated for one PMT. The red hatched areas delimit the veto window.

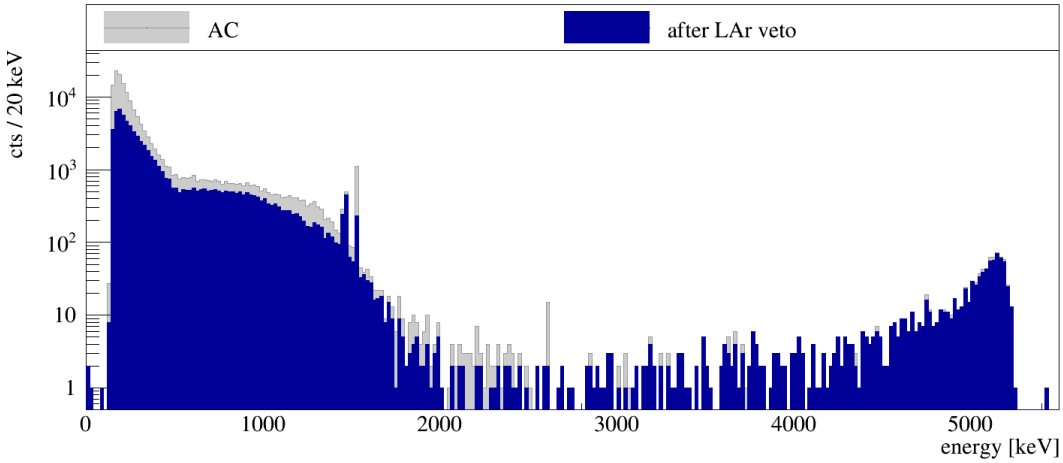

Figure 7.19: Background spectrum of Phase II dataset after AC and after applying AC and the LAr veto.

1. ^{39}Ar β-decay in the region below 565 keV.
2. $2\nu\beta\beta$ spectrum.
3. ^{40}K background which is identified via the FEP at 1460 keV.
4. ^{42}K decays via β-decay which is to 17.6 % accompanied by the 1525 keV γ-ray and thereby visible in the spectrum.
5. ^{228}Th can be identified by eye in the energy spectrum by the FEP of ^{208}Tl at 2615 keV.
6. degraded α decays which are responsible for events with an energy > 3.5 MeV.

In the following paragraphs, the suppression by the LAr veto is discussed in the different energy regions. An overview of the suppression factors is given in Tab. 7.6.

The pulser acceptance is determined to be $p_{acc} = 97.7\%$ and is in the following used to correct the suppression factors of several background components. This efficiency enters in the limit setting analysis of $0\nu\beta\beta$-decay.

	energy window	suppression factor after LAr veto	
		BEGe	coaxial
^{39}Ar	$180 - 380$ keV	2.83 ± 0.01	1.85 ± 0.01
^{40}K FEP	1460 keV $\pm 5\sigma$	1.00 ± 0.02	0.98 ± 0.03
^{42}K FEP	1525 keV $\pm 5\sigma$	4.93 ± 0.10	5.86 ± 0.10
α region	$3550 - 7000$ keV	1.04 ± 0.02	1.02 ± 0.01
ROI	$1930 - 2190$ keV	3.50 ± 0.10	1.58 ± 0.11

Table 7.6: Suppression factors of the LAr veto in different energy regions of the energy spectrum of the first data release.

^{39}Ar suppression

^{39}Ar is a cosmogenically produced isotope which is homogeneously distributed in LAr. It decays via β-decay and has an endpoint of 565 keV as illustrated in Fig. C.2. In this energy region the β-decay spectrum dominates the energy spectrum.

Given the actual statistics ^{39}Ar is the only background for which the suppression by the LAr veto can be discussed detectorwise. Fig. 7.20 shows the suppression factor of the LAr veto in the energy region from 180 keV − 380 keV for each Germanium detector individually. The different strings are color coded, the detector type is given in the caption and the detector ids increase from top to bottom. Three effects are clearly visible:

1. The suppression factors of the BEGe detectors are higher than the ones for the semi-coaxial detectors.

2. The veto efficiency of the central string (semi-coaxial natural GTF detectors) is not deteriorated compared to the other strings with semi-coaxial detectors.

3. The top and especially the bottommost detector of each detector string give the highest suppression factors of the string.

BEGe detectors have a flat p^+ contact in the center of one of the flat detector surfaces while for semi-coaxial detectors the p^+ is placed on an axial well. Scintillation light of ^{39}Ar decays which occur in the borehole is likely to be absorbed without triggering the LAr veto. In addition, the dead layer on the n^+ surface of semi-coaxial detectors is in average thicker than the one of BEGe detectors. This changes the spectral shape of the semi-coaxial detectors in the way that they have more events at higher energy and at the same time more energy is deposited in average in the dead layer, which is then not available to create scintillation light. Both effects decrease the probability

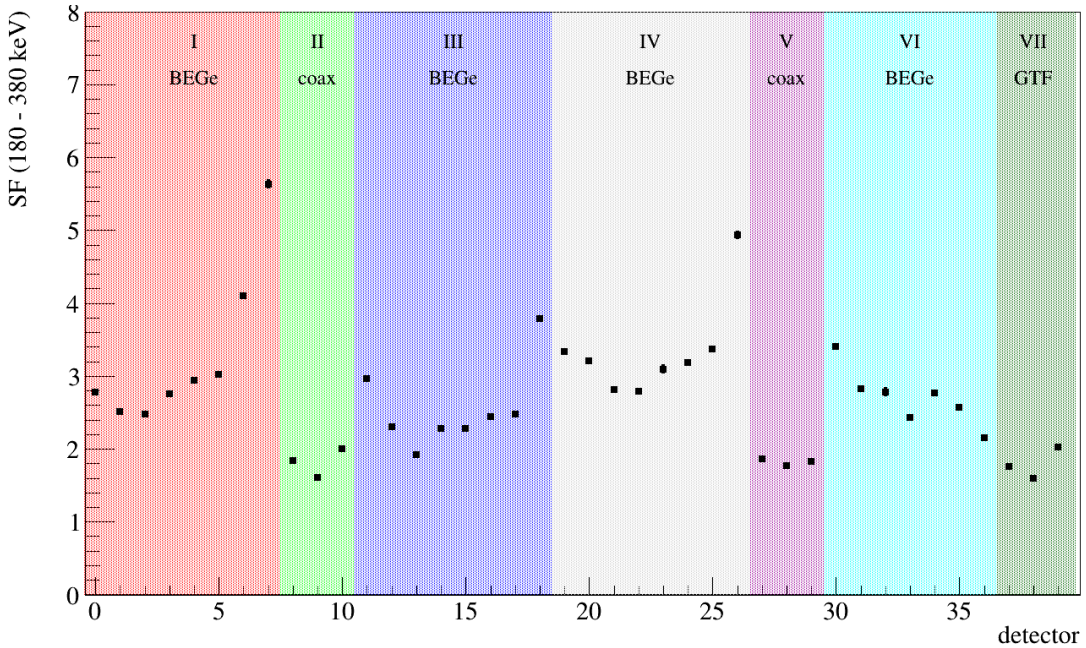

Figure 7.20: ^{39}Ar suppression by the LAr veto for the individual Germanium detectors.

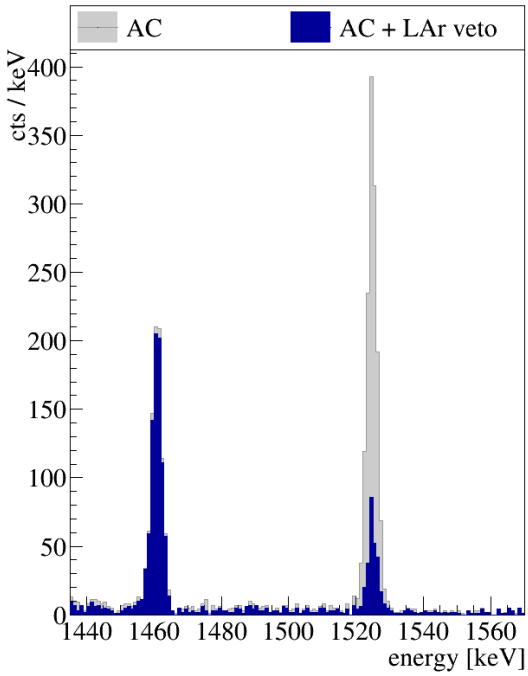

Figure 7.21: Suppression of ^{40}K and ^{42}K full energy peaks by the LAr veto.

that scintillation light is created and thus detected by the PMTs and SiPMs in case of ^{39}Ar decays in vicinity of semi-coaxial detectors. Hence, they support the observation of lower suppression factors in case of semi-coaxial Germanium detectors.

The central string is filled with semi-coaxial natural Germanium detectors. The average suppression factor for this detector string amounts to 1.85 ± 0.02 which is in perfect agreement with $SF = 1.85 \pm 0.01$ quoted for the enriched semi-coaxial detectors in Tab. 7.6. This result indicates that light which is created in the middle of the detector array does not suffer from shadowing.

Last, a strong increase of rejection power is found for the bottommost (and less pronounced for the topmost) detector of each string. These detectors have one additional surface which is not covered by other Germanium detectors but open to the instrumented LAr volume. Consequently, scintillation light which is created by an energy deposition below the bottommost detector is more likely to be detected by the bottom PMTs.

To summarize the observed differences in the suppression factors of the different detector types are most likely due to the detector geometry itself and not primarily to shadowing as supported by the suppression factor of the central GTF detector string in comparison to other semi-coaxial detector strings.

$2\nu\beta\beta$ spectrum

$2\nu\beta\beta$ events dominate the energy region from 600 keV − 1300 keV. The spectrum, the background decomposition and the suppression by the LAr veto along with a calculation of the half-life of $2\nu\beta\beta$-decay in ^{76}Ge are discussed in detail in Ch. 8.

^{40}K and ^{42}K suppression

^{40}K contaminations are expected in materials close to the detector array. It decays via electron-capture under emission of a 1460 keV γ-ray.

Since the γ-ray is not accompanied by any other radiation no suppression by the LAr veto apart from random coincidences is expected. Fig. 7.21 illustrates that the FEP is fully accepted. The corresponding suppression factors are determined to $SF = 1.00 \pm 0.02$ for the BEGe dataset and $SF = 0.98 \pm 0.03$ for the semi-coaxial dataset, respectively. This provides an independent cross-check of the veto acceptance, which is normally quoted as the acceptance of test pulser events.

^{42}Ar is naturally present in liquid argon and homogeneously distributed. In contrast, its ionized short lived decay isotope ^{42}K can drift due to electric fields near the Germanium detectors. ^{42}K decays via β-decay with an endpoint of 3.5 MeV and is to 17.6% accompanied by a 1525 keV γ-ray. This FEP represents the strongest γ-line in the background spectrum in Fig. 7.19.

Since a β-particle with up to 2 MeV energy is released at the same time a significant suppression of the peak is expected. The calculation yields a suppression factor of $SF = 4.93 \pm 0.10$ in case of the BEGe dataset and $SF = 5.86 \pm 0.10$ in the semi-coaxial dataset, respectively. The Compton background of this γ-ray is expected to be even stronger vetoed. An estimate of the suppression in the Compton region which is based on the energy dependent survival fraction of the LAr veto in a ^{228}Th calibration measurement is presented in Ch. 8.

Suppression in the α region

Background in the energy window above 3.5 MeV originates predominantly from α-decays. Since α-particles deposit their energy within a few μm only contaminations in the detector groove and on the p+ contact can create background in the Germanium detectors. Consequently, little to no energy is deposited in LAr which would create scintillation light. Nevertheless, events in this energy region are suppressed with a factor 1.04 ± 0.02 (BEGes) and 1.02 ± 0.01 (semi-coaxial), respectively.

Fig. 7.22 shows the normalized A/E value of events in the region above 2 MeV against their energy (open gray circles) for the BEGe dataset. Events that are vetoed by the LAr veto are marked in blue. The single-site band which identifies signal-like events is centered around 0 and is indicated by the shaded red area. In the energy region above 3.5 MeV all but one event are cut by the high A/E-cut. The remaining event has an energy of 3662 keV and a first visual inspection of the pulse shape points to the MSE character of the event [134]. This is supported by the A/E-value of 0.90 which is clearly below the single site band. The A/E value suggests that more than 3 MeV were deposited at one single interaction point in the BEGe detector. Therewith, all γ-rays from the natural decay chains are excluded.

To judge if the suppression of α-events is an artifact of the way the veto flags are extracted in this analysis or if the light instrumentation really detects light in coincidence with α-events, Tab. 7.7 categorizes the vetoed events of the BEGe and the semi-coaxial dataset in different veto classes. For comparison, 50 test pulses were also analyzed and put as a reference in the table. The assumption is that random coincidences arising from dark rate of the light detectors should only be vetoed by

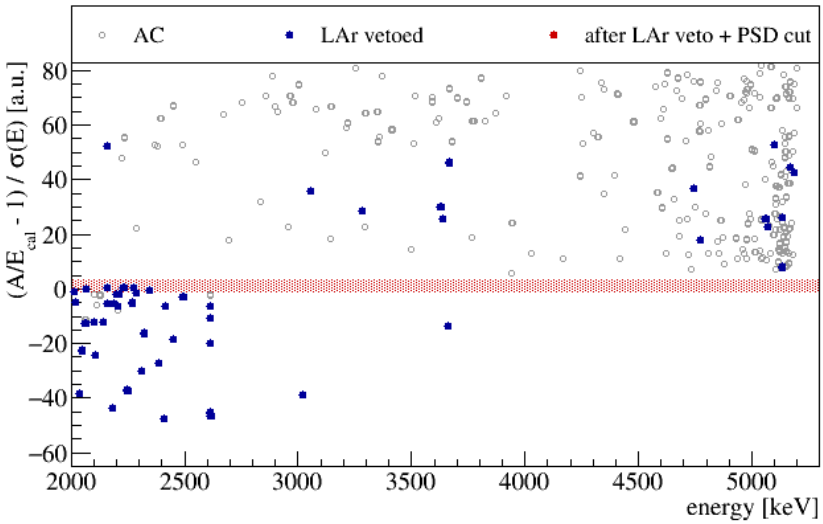

Figure 7.22: Normalized A/E against energy in α-region of BEGe dataset.

one light detector (ch) and one detected pulse (trigger $\widehat{=}$trg) with the energy of one photoelectron in the veto window. This is only true for $\approx 50\%$ of the vetoed test pulses. It appears that 18% are vetoed by one light detector and one trigger but with an energy of > 1.5 photoelectrons and another third of the events is vetoed by more than one trigger. This points to a physical origin of 50% of the random coincidences, such as ^{39}Ar β-decays in LAr which do not deposit energy in any Germanium detector. The pulser acceptance of 97.7% explains five to six out of fourteen vetoed events in the α-sample of the BEGe dataset and sixteen out of 29 events in the semi-coaxial, respectively. No definite explanation and classification of these distributions can be given at this moment. Further analysis including a larger test sample would be required.

The time distributions of α-events vetoed by the PMTs (filled blue) and the SiPMs (filled green) are plotted together with reference distributions (PMTs: open blue, SiPMs: open green) in Fig. 7.23. No deviation is observable between the distributions of α events and the distribution over the whole energy region. However, the

	α region (3550 keV - 7000 keV)		pulser events
	BEGe	coaxial	
# events	232	697	$50/(1-p_{acc})$
vetoed events	14	29	50
vetoed by			
1 ch. && 1 trg			
<1.5 pe	7	22	24
>1.5 pe	3	1	9
>1 ch.	1	0	0
>1 trg	2	5	17
>1 ch. && >1 trg	1	1	0

Table 7.7: Classification of vetoed events in α-region of BEGe and semi-coaxial dataset and for test pulses.

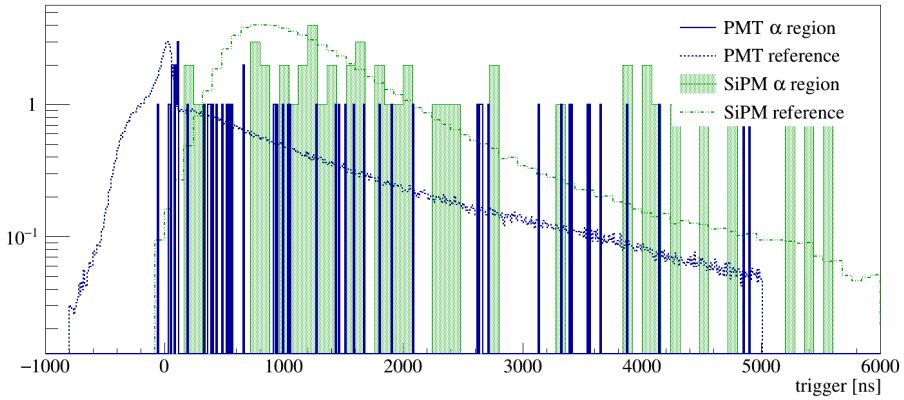

Figure 7.23: **Trigger distributions of α events** (filled lines) in LAr light detectors and as a reference events from the whole energy spectrum (dashed lines). Distribution in the PMTs (blue) and SiPMs (green) are plotted separately.

statistics are relatively poor.

Returning to the event at 3662 keV which is cut by the low A/E-cut: The event is marked in red in Tab. 7.7 due to its special character. In the BEGe dataset it is the only event which is vetoed by more than one light detector (12 light detectors fired) and for which several triggers are found at the same time. This fact together with the low A/E indicate that this event could be due to neutron capture in ^{40}Ar or ^{64}Cu and subsequent emission of high energetic γ-rays.

In the semi-coaxial dataset, one event at an energy of 4360 keV is found which has the same signature by means of the LAr light detectors and which is not vetoed by the μ-veto. Since the pulse shape of events in semi-coaxial detectors is more complicated and do not provide a clear distinction of MSE and α-events a further discussion of this event is omitted.

7.5.4 Background index after LAr veto

The background index at $Q_{\beta\beta}$ is a crucial parameter for the sensitivity of neutrinoless double beta decay experiments. The design goal of Phase II is to reach a BI of $10^{-3}\,\mathrm{cts}/(\mathrm{kg}\cdot\mathrm{keV}\cdot\mathrm{yr})$.

The background spectrum around $Q_{\beta\beta}$ is shown in Fig. 7.24 for the dataset of the BEGe (top) and for the semi-coaxial detectors (bottom), respectively. The open gray histogram is after the detector-detector anti-coincidence cut and the muon veto, the filled blue histogram shows events that survive also the LAr veto and in filled red the energy spectrum after AC, LAr veto and PSD is depicted.

The background indices are calculated in the energy window from 1930 keV to 2190 keV, discarding a 10 keV wide window around known γ-lines (^{208}Tl SEP at 2103 keV, ^{214}Bi FEP at 2119 keV) and around $Q_{\beta\beta}$ as indicated by the gray shaded areas.

The BEGe and the semi-coaxial dataset have similar exposures of 5.826 kg · yr and 5.019 kg · yr, respectively. They also exhibit a comparable number of counts after applying the AC and μ-veto cut, namely 19 in the BEGe and 21 in the semi-coaxial dataset, respectively. Consequently, the background indices in the background window are calculated to be $15.67^{+3.69}_{-3.19}\cdot 10^{-3}\,\mathrm{cts}/(\mathrm{kg}\cdot\mathrm{keV}\cdot\mathrm{yr})$ (BEGe) and $16.46^{+4.10}_{-3.51}\cdot 10^{-3}\,\mathrm{cts}/(\mathrm{kg}\cdot\mathrm{keV}\cdot\mathrm{yr})$ (coaxial).

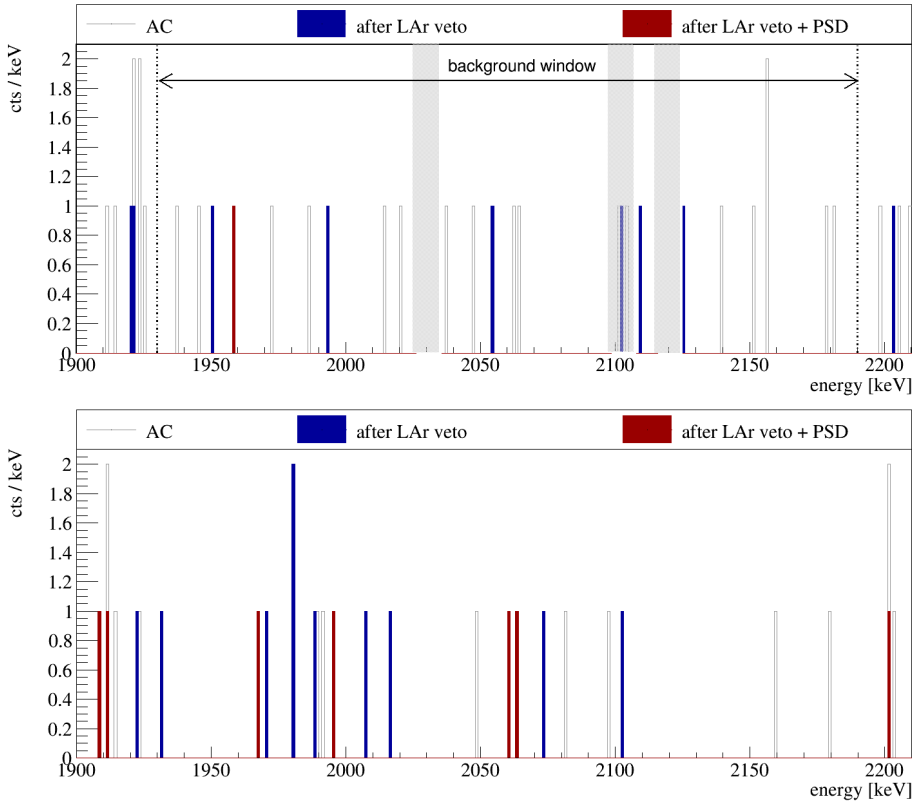

Figure 7.24: **Background spectrum around $Q_{\beta\beta}$.** The energy spectra after detector-detector anti-coincidence (AC) and μ-veto (open gray histogram), after LAr veto (filled blue) and after combining it with PSD (filled red) are illustrated for the BEGe (top) and the semi-coaxial (bottom) dataset. The region from 1930 keV − 2190 keV is taken into account to calculate the background indices. As indicated by the gray shaded areas 10 keV wide windows around known γ-lines (SEP at 2103 keV and a γ-line of ^{214}Bi at 2119 keV) and around $Q_{\beta\beta}$ are discarded.

The LAr veto suppresses the background of the BEGe dataset by a factor ≈ 3.5 which converts into a background index of

$$BI_{\text{LAr veto}}(\text{BEGe}) = 4.48^{+2.13}_{-1.61} \cdot 10^{-3}\,\text{cts}/(\text{kg} \cdot \text{keV} \cdot \text{yr}). \tag{7.3}$$

Whereas, the background level of the semi-coaxial dataset is only reduced by a factor ≈ 1.5, leading to $BI_{\text{LAr veto}}(\text{coaxial}) = 10.40^{+3.33}_{-2.75} \cdot 10^{-3}\,\text{cts}/(\text{kg} \cdot \text{keV} \cdot \text{yr})$.

Combining the LAr veto with pulse shape discrimination reduces the background further. In case of the BEGe dataset a PSD based on the A/E parameter is applied [134] which decreases in combination with the LAr the background index to

$$BI_{\text{LAr veto \& PSD}}(\text{BEGe}) = 0.75^{+1.13}_{-0.55} \cdot 10^{-3}\,\text{cts}/(\text{kg} \cdot \text{keV} \cdot \text{yr}). \tag{7.4}$$

Two neural networks are applied to the semi-coaxial dataset. The first one is identical to the one from Phase I [17] and supposed to separate SSE from MSE events. The second one is meant to discriminate α-events on the p^+ contact from $0\nu\beta\beta$ signal events. It accepts $\approx 10\%$ of the events in the energy region above > 3.5 keV while accepting $(93 \pm 1)\%$ of the events in the $2\nu\beta\beta$ region (1.0 MeV − 1.3 MeV) which serves

	exposure	BI $[10^{-3}\,\mathrm{cts}/(\mathrm{kg}\cdot\mathrm{keV}\cdot\mathrm{yr})]$ after		
	$[\mathrm{kg}\cdot\mathrm{yr}]$	AC + μ-veto	LAr veto	LAr veto + PSD
BEGe	5.826	$15.67^{+3.69}_{-3.19}$	$4.48^{+2.13}_{-1.61}$	$0.75^{+1.13}_{-0.55}$
coaxial	5.019	$16.46^{+4.10}_{-3.51}$	$10.40^{+3.33}_{-2.75}$	$3.47^{+2.09}_{-1.49}$

Table 7.8: Background indices of the BEGe and the semi-coaxial dataset of the first data release of Phase II after different cuts.

as a proxy of signal events [22]. Due to a less efficient PSD and a less pronounced over-orthogonality of the LAr veto and PSD in case of semi-coaxial Germanium detectors, the BI of the coaxial dataset is only reduced to $BI_{\text{LAr veto \& PSD}}(\text{coaxial}) = 3.47^{+2.09}_{-1.49} \cdot 10^{-3}\,\mathrm{cts}/(\mathrm{kg}\cdot\mathrm{keV}\cdot\mathrm{yr})$.

In summary, by combining LAr veto and PSD the goal of reaching a background index of $10^{-3}\,\mathrm{cts}/\mathrm{kg}\cdot\mathrm{keV}\cdot\mathrm{yr}$ in Phase II is achieved for the BEGe dataset.

7.6 Summary

As described in Ch. 6, the LAr veto has been successfully installed in the GERDA setup in December 2014. The first LAr veto commissioning runs with radioactive calibration sources (^{228}Th and ^{226}Ra) could prove that the LAr veto performs as expected. In the case of ^{228}Th, a suppression factor of $SF = 98.1 \pm 4.1$ could be reached by the LAr veto in the region of interest. In the case of ^{226}Ra, which deposits on average less energy in LAr if an energy deposition in one germanium detector around $Q_{\beta\beta}$ is detected, a suppression factor of 4.5 ± 0.1 was reached.

A first comparison of this data to Monte Carlo simulations with the nominal optical parameters from Sec. 5.1.2 revealed that a significantly higher photoelectron yield and thus, suppression factors were expected by the Monte Carlo simulations. The assumption was that the light yield in the GERDA LAr cryostat is smaller than expected. As explained in Ch. 5, a direct correlation between the LAr triplet lifetime and the light yield was assumed. The LAr triplet lifetime was cross-checked and yielded $\tau = 971.7 \pm 30.2\,\mathrm{ns}$, a value comparable to the previous measurement of 2012 (see Sec. 5.1.2). However, existing literature suggests that contaminations in LAr, such as methane and nitrogen, might also affect the fast component and thus that a direct scaling of the light yield with the triplet lifetime might not be correct [97, 96]. Moreover, the fiber coverage is overestimated in the Geant4 geometry since the shroud is implemented as a full cylinder of scintillating fiber material. It may be realistic to assume a coverage of 70%. As a consequence, it was tried to tune the Monte Carlo simulations based on the ^{228}Th calibration source measurement during the LAr veto commissioning by implementing two effective scaling factors accounting for a reduced light yield and fiber coverage [103]. This tuned Monte Carlo was cross-checked with the ^{226}Ra calibration source measurement. It was found that the tuned Monte Carlo gives better but not yet sufficient agreement. In particular, the Monte Carlo is not able to reproduce the contributions of the SiPMs and the PMTs to the total suppression factor. New measurements with the full Phase II germanium detector array and radioactive

calibration sources may help to solve this inconsistency.

A pulse shape analysis (PSD) was performed on the LAr veto commissioning data with radioactive calibration sources [134]. Combining both the LAr veto and the PSD cut yielded strongly increased suppression factors of $SF = 24.8 \pm 1.8$ (^{226}Ra) and $SF = 360.9 \pm 28.9$ (^{228}Th). These background rejection efficiencies are higher than they would be in the case the suppression of both methods were uncorrelated. With the help of Monte Carlo simulations of the ^{228}Th calibration source measurement, the following possible explanation could be found: The probability of an event depositing energy in the dead layer of a germanium detector is twice as high in the case of an event classified as background (multi-site event) by the pulse shape analysis than in the case of an accepted event (single site event). This energy is missing to trigger the LAr veto and results in a reduced background rejection efficiency in the case of multi-site events.

In December 2015, a full germanium detector array was installed in the GERDA experiment, containing 35.6 kg of enriched Germanium detector mass and three natural semi-coaxial detectors. The background spectra after six months of data taking allowed to address the background rejection efficiency on different background components which are visible in the spectrum. First, this is the β-decay spectrum of ^{39}Ar dominating the energy spectrum up to an energy of ≈ 550 keV. Since ^{39}Ar is homogeneously distributed in LAr, the same contribution and suppression factor by the LAr veto is expected for all germanium detectors. A difference in the suppression of ^{39}Ar events by the LAr veto is found for the BEGe detectors ($SF = 2.83 \pm 0.01$) and the semi-coaxial detectors ($SF = 1.85 \pm 0.01$). This difference can be explained by a thicker dead layer which absorbs more energy and the borehole which shadows light in the case of the semi-coaxial detectors. A comparison of the suppression factors of the natural germanium detectors placed in the central string and the enriched semi-coaxial detectors in the outer strings reveals no significant shadowing of light created in the center of the germanium detector array. The suppression of the ^{42}K FEP at 1525 keV yielded suppression factors of $SF \approx 5$ since the remaining β-energy is to a great extent deposited in LAr. In contrast, the 1460 keV γ-ray of ^{40}K which is emitted without further radiation is not suppressed at all and can serve to calculate the random coincidence rate which corresponds to the induced dead time.

After applying the LAr veto, 12 out of 19 events remain in the semi-coaxial dataset in the region of interest which corresponds to a suppression of $SF = 1.6 \pm 0.1$ and a background index of $BI = 10.40^{+3.33}_{-2.75} \cdot [10^{-3}\,\mathrm{cts}/(\mathrm{kg} \cdot \mathrm{keV} \cdot \mathrm{yr})]$. In the BEGe dataset, 6 out of 21 events remain in the region of interest, yielding a suppression factor of 3.5 ± 0.1 and a background index of $BI = 4.48^{+2.13}_{-1.61} \cdot [10^{-3}\,\mathrm{cts}/(\mathrm{kg} \cdot \mathrm{keV} \cdot \mathrm{yr})]$. In combination with PSD this background is further reduced to a level of $BI = 0.75^{+1.13}_{-0.55} \cdot [10^{-3}\,\mathrm{cts}/(\mathrm{kg} \cdot \mathrm{keV} \cdot \mathrm{yr})]$. Therewith, the aspired background index of Phase II is met in the case of the BEGe dataset, allowing to reach a $0\nu\beta\beta$-decay half-life sensitivity of 10^{26} yr with 100 kg $\cdot$ yr exposure .

CHAPTER 8

MEASUREMENT OF THE $2\nu\beta\beta$-DECAY HALF-LIFE OF ^{76}GE

In the past, the accuracy of the $2\nu\beta\beta$-decay half-life measurement relied strongly on the accuracy of the background model as the signal-to-background ratio was at best 4:1 [19] in the energy window of interest from 600 keV to 1300 keV. Fig. 8.1 shows the $2\nu\beta\beta$-decay dominated energy region of the BEGe dataset before and after LAr veto together with a simulated $2\nu\beta\beta$-spectrum assuming a half-life of $1.92 \cdot 10^{21}$ yr. It becomes obvious that the LAr veto provides an excellent tool to suppress background in this energy region, yielding a signal-to-background ratio of 30:1 (see Sec. 8.1.3). Consequently, the spectral shape of the simulated $2\nu\beta\beta$-decay is almost perfectly reproduced and a more accurate measurement of $T^{2\nu}_{1/2}$ of ^{76}Ge is made possible.

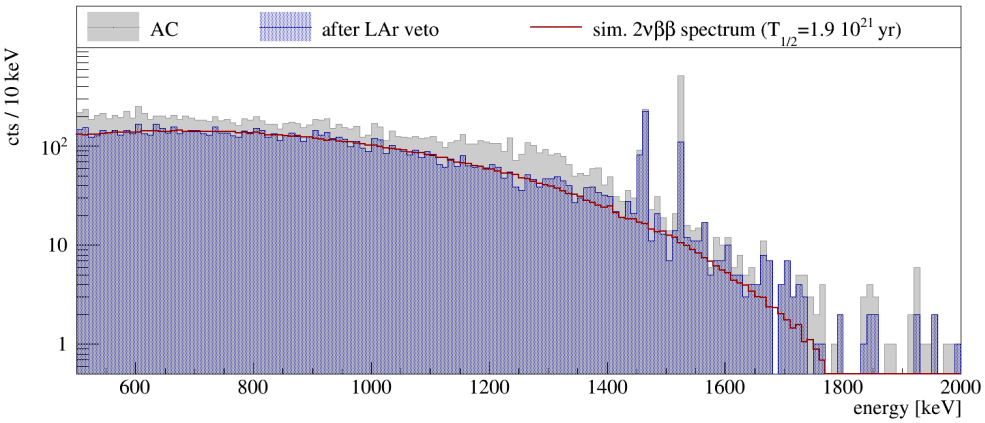

Figure 8.1: Energy spectrum of BEGe dataset before and after LAr veto together with a simulated $2\nu\beta\beta$ spectrum assuming a half-life of $1.92 \cdot 10^{21}$ yr.

In the first section the background decomposition in the energy window from 600 to 1300 keV is elucidated. This includes the description of the preliminary background model which has been developed on the energy spectrum before LAr veto and PSD [123]. Subsequently, the procedure of extracting energy spectra of the individual background components after LAr veto is discussed. By means of these energy spectra, the background decomposition after LAr veto is extracted and the number of $2\nu\beta\beta$ counts in the analysis window is calculated. Ultimately, the $2\nu\beta\beta$-decay half-life as measured

by each detector individually and by all BEGe and semi-coaxial detectors, respectively, is given, along with a discussion of systematic uncertainties.

8.1 Background decomposition in $2\nu\beta\beta$ energy region

The preliminary background model for the first six months of Phase II data is developed for the energy spectra of the semi-coaxial and BEGe detectors, respectively, after anti-coincidence cut [128]. Since the optical parameters of the Monte Carlo simulation including photon tracking have not yet been fully validated and some tension is still observed at the time of writing this thesis, no attempt was made to develop a background model based on the the energy spectra after LAr veto cut. For the purpose of extracting the $2\nu\beta\beta$-decay half-life a scaling of the background components based on the suppression measured with radioactive calibration sources – so-called „approximative" LAr veto – is performed and described in Sec. 8.1.2.

8.1.1 Predictions from background model

Fig. 8.2 illustrates the measured energy spectra before LAr veto and PSD of the BEGe and semi-coaxial detectors, respectively, in gray. The preliminary background model which has been developed on these energy spectra is given in black and the individual background components are color-coded. The fit range was set to $580 - 5300\,\mathrm{keV}$.

The most prominent components in the energy spectra, such as ^{40}K, ^{42}K and the α-region, have been already discussed in Sec. 7.5.3 along with the rejection efficiency by the LAr veto. Based on screening measurements of the material deployed in close vicinity of the Germanium detector array, the background components that are considered by the background model are all close-by sources: (1) ^{40}K on the nylon mini-shroud, (2) ^{42}K homogeneously distributed in LAr, (3) ^{228}Th in the detector holders, (4) ^{228}Ac in the detector holders, (5) ^{226}Ra in the cables and (6) on the p^+ contact of the Germanium detectors, and (7) the α-model as developed for the Phase I dataset [18].

In the following measurement of the $2\nu\beta\beta$-decay half-life an analysis window from 600 keV to 1300 keV is utilized. Therewith, the fraction of $2\nu\beta\beta$ events is the largest while ^{40}K and ^{42}K, which are expected to be easy to scale, dominate the background

	BEGe dataset		semi-coaxial dataset	
bg	counts	contribution [%]	counts	contribution [%]
data	10595		8986	
model	10519.0		8937.5	
$2\nu\beta\beta$	7497.4	71.3	6588.24	73.7
^{40}K mini-shroud	712.8	6.8	481.6	5.4
^{42}K hom LAr	1932.4	18.4	1575.2	17.6
^{228}Th holder	23.2	0.2	13.9	0.2
^{228}Ac holder	179.3	1.7	173.0	1.9
^{226}Ra cables	126.9	1.2	93.1	1.1
^{226}Ra p^+	32.7	0.3	–	–
α model	14.3	0.1	12.5	0.1

Table 8.1: Itemization of the background contributions in the 600 to 1300 keV energy region of the BEGe and the semi-coaxial dataset. The $2\nu\beta\beta$ half-life entered as a free parameter in the background model fit and were determined as $1.94 \cdot 10^{21}$ yr and $1.84 \cdot 10^{21}$ yr, respectively.

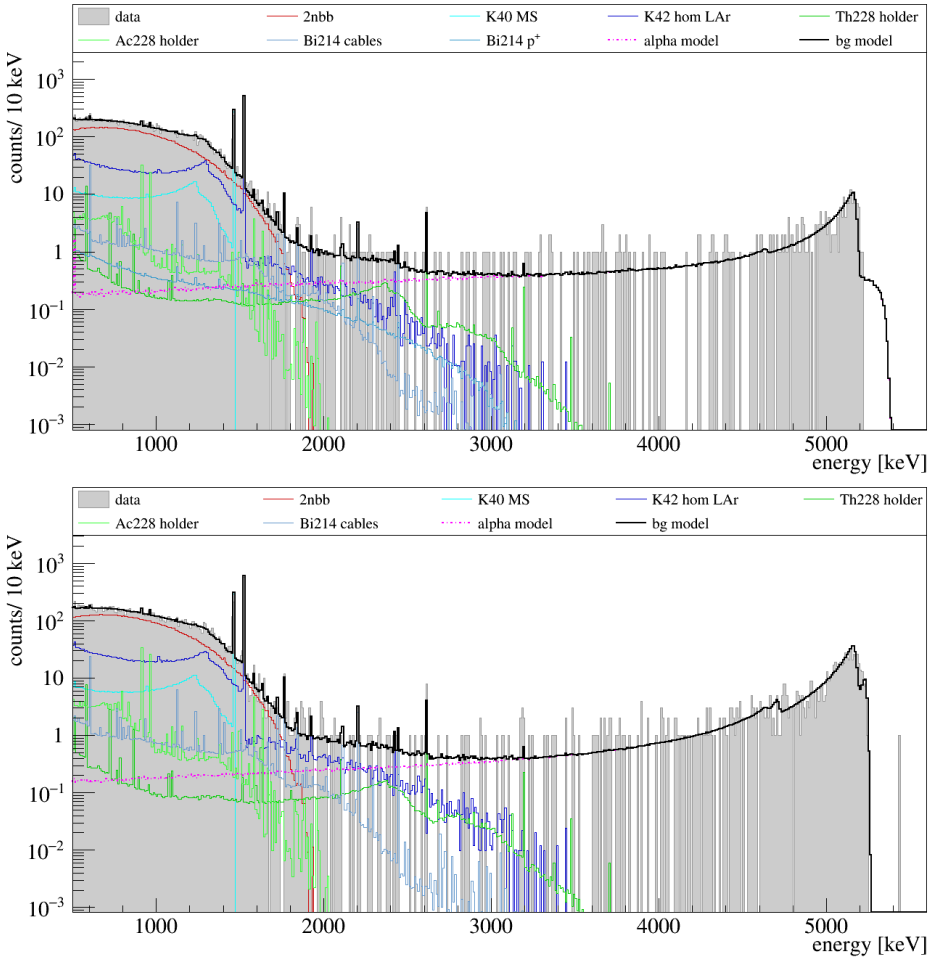

Figure 8.2: **Energy spectra of the first six month of Phase II data with preliminary background model.** Top: BEGe dataset. Bottom: Semi-coaxial dataset.

contributions. In the BEGe dataset 71% of the events are attributed to $2\nu\beta\beta$-decays and 74% in the semi-coaxial dataset, respectively (see Tab. 8.1). This corresponds to a signal-to-background ratio of $\approx$ 3:1, being comparable to the one reached in Phase I of the experiment: 4:1 [19]. The strongest background contributions in the analysis window are due to ^{42}K decays homogeneously distributed in LAr (18.4% in the BEGe dataset and 17.6% in the semi-coaxial dataset) and ^{40}K in the mini-shroud (6.8% in the BEGe dataset and 5.4% in the semi-coaxial dataset). All other contributions together make at most 4% of the background counts.

8.1.2 Background spectra after LAr veto

As explained in Sec. 7.3, the Monte Carlo simulations with optical photon tracking are not yet fully validated. Thus, another procedure was adapted to extract the energy spectra of the different background components after LAr veto.

Fig. 8.3 is based on the energy spectra taken with a ^{226}Ra calibration source during the LAr veto commissioning, as shown in Fig. 7.7. The energy spectrum after detector-detector anti-coincidence has been scaled binwise to one (gray histogram in Fig. 8.3).

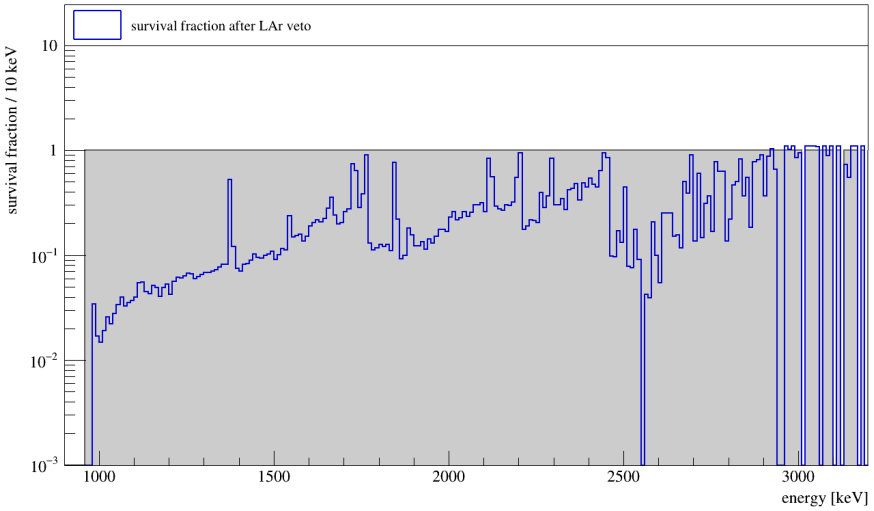

Figure 8.3: Energy dependent survival efficiency of ^{226}Ra after the LAr veto.

The same scaling procedure has been applied to the energy spectrum after LAr veto, depicted in blue in Fig. 8.3. Eventually, this corresponds to the energy dependent survival efficiency of the LAr veto system in the case of ^{226}Ra background.

The procedure has been applied to the energy spectra that were taken with a ^{228}Th calibration source and the complete Phase II germanium detector array. In Fig. 8.4 the spectrum after anti-coincidence has been scaled to one (gray) and the energy dependent survival efficiency is plotted in blue. In addition, the survival efficiency normalized to the suppression of the 2.6 MeV γ-line is depicted in red.

Mathematically, these operations correspond to the following equation

$$\text{Survival Eff}_i = pdf_i^{\text{LAr veto}} \otimes (1/pdf_i^{\text{AC}}) \otimes SF_{\text{reference peak}}, \tag{8.1}$$

where i stands for the i-th bin, *pdf* is the collection of all bins in the histogram after anti-coincidence or LAr veto, respectively, $\otimes$ denotes the binwise multiplication and $SF_{\text{reference peak}}$ is the suppression factor of the reference peak reached by the LAr veto. In the case of the blue-colored survival efficiencies, the scaling with the suppression of the reference peak is omitted, while the suppression of the 2.6 MeV γ-peak has been used to obtain the red curve in Fig. 8.4.

These energy dependent survival efficiencies are then used to reproduce the LAr veto rejection efficiency for some special background components. Subsequently, the procedure that has been applied to every component of the background model is explained in order to obtain the energy spectra after the „hand-made“ LAr veto. Solely, the scaling with the LAr veto acceptance $p_{acc} = 0.977$ (see Sec. 7.5.3) which reduces all components in the same manner, is applied but not mentioned anymore:

1. *$2\nu\beta\beta$ decays*: $2\nu\beta\beta$ decays are most likely single site events in the germanium detectors. Solely, in case a Bremsstrahlung γ-ray deposits energy in LAr, a $2\nu\beta\beta$ event may be rejected by the LAr veto. This has been taken into account by suppressing events which deposit more than 100 keV in LAr. By applying such a cut 0.6% of $2\nu\beta\beta$ decays are suppressed by the LAr veto in the BEGe and semi-coaxial dataset ($\epsilon_{SF} = 0.994$).

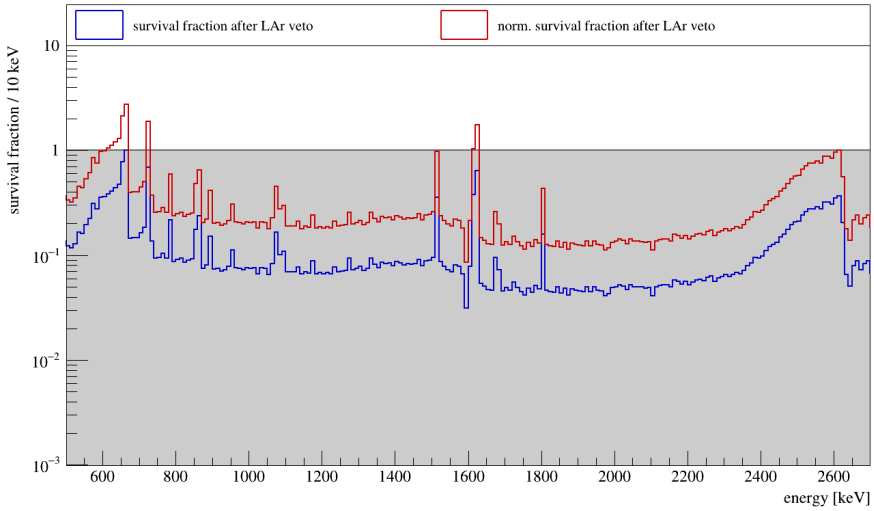

Figure 8.4: Energy dependent survival efficiency of ^{228}Th after the LAr veto.

2. *α decays*: not suppressed since they are local detector surface events (see Sec. 7.5.3 for a detailed discussion of the LAr veto suppression efficiency in the α region).

3. *^{226}Ra in cables/ on p^+ contact*: simulated histogram is scaled by the survival efficiencies of each bin in the ^{226}Ra calibration source measurement as shown in Fig. 8.3.

4. *^{228}Th in holders*: simulated histogram is directly scaled with the blue survival efficiency curve depicted in Fig. 8.4.

5. *^{228}Ac in holders*: since no ^{228}Ac calibration source measurement was available, a cut with an energy threshold of 100 keV in LAr, representing the best knowledge of the energy threshold of the LAr veto, has been applied to the simulated spectrum.

The decay topologies of ^{40}K and ^{42}K are discussed in Sec. 7.5.3. In both cases, the Compton background from a single γ-ray dominates their energy spectrum in the 600 to 1300 keV analysis window. This may be compared to the high energy part of a ^{228}Th calibration spectrum in which the energy spectrum from $\approx$ 1600 keV to the 2615 keV full energy γ-peak of ^{208}Tl is dominated by its Compton continuum. The 2615 keV γ-ray is emitted during a β^--decay with an endpoint of 5.0 MeV and is to 84.5% accompanied by a 583 keV γ-ray. Consequently, the 2615 keV FEP and the Compton region below the peak are each suppressed by a constant factor which is determined by the β- and γ-ray energy released in LAr, if 2615 keV are detected in a germanium detector. In addition, x keV of the 2615 keV γ-ray energy may be deposited in LAr if $(2615 - x)$ keV are released in a Germanium detector. The additional energy in LAr enhances the rejection power by the LAr veto and this additional energy dependent survival efficiency is given by the normalized red curve in Fig. 8.4. One can assume that the suppression efficiency below a single γ-peak, such as the FEP's of ^{40}K and ^{42}K, are in good approximation described by the normalized survival efficiency.

6. *^{40}K in mini-shroud*: The energy dependent normalized survival efficiency below the 2.6 MeV γ-peak of the ^{228}Th has been utilized to reproduce the part of the

energy spectrum from the 1460 keV FEP down to 580 keV after LAr veto. γ-lines which occur in the calibration source spectrum (SEP at 2103 keV, FEP at 1806 keV) are omitted by ignoring a 10 keV wide energy window around the peak and scaling by the survival efficiency of the bin which lies 15 keV above the respective γ-peak.

7. ^{42}K *homogeneously distributed in LAr*: In principle, the same procedure as for the ^{40}K simulated background has been adapted to the spectrum. The scaling is applied from the FEP at 1525 keV down to 580 keV. In contrast to ^{40}K, the γ-ray is emitted during a β^--decay of the isotope with an end-point energy of 3.5 MeV. As a result, the remaining β-energy can trigger the LAr veto and suppresses the peak by a factor of ≈ 5 (see Sec. 7.5.3). The suppression of the γ-peak has to be multiplied with the total survival efficiency in Eq. 8.1 and would be written as $\otimes SF_{\text{peak}}$ in Eq. 8.1.

8.1.3 Decomposition after LAr veto

The result of the approximative background model after LAr veto is illustrated in Fig. 8.5. The energy spectra after applying the anti-coincidence cut and LAr veto (gray) are drawn together with the individual background components (colored) and the derived background model (black) for the BEGe dataset (left) and the semi-coaxial dataset (right), respectively. A good agreement between data and the approximative background model after LAr veto is obtained over the entire energy spectrum.

The background contributions after applying the approximative LAr veto scaling are listed in Tab. 8.2 for the BEGe and the semi-coaxial dataset, respectively. After LAr veto, 96.5% of the events in the BEGe dataset are attributed to $2\nu\beta\beta$-decays and 96.8% in the semi-coaxial dataset, respectively.

Both in the energy spectra in Fig. 8.5 and in Tab. 8.2 it becomes obvious that the model predicts more events in the analysis window than observed in the measured energy spectra. As a consequence of the better signal-to-background separation, it gets clear that the $2\nu\beta\beta$ counts are overestimated by the current GERDA background model

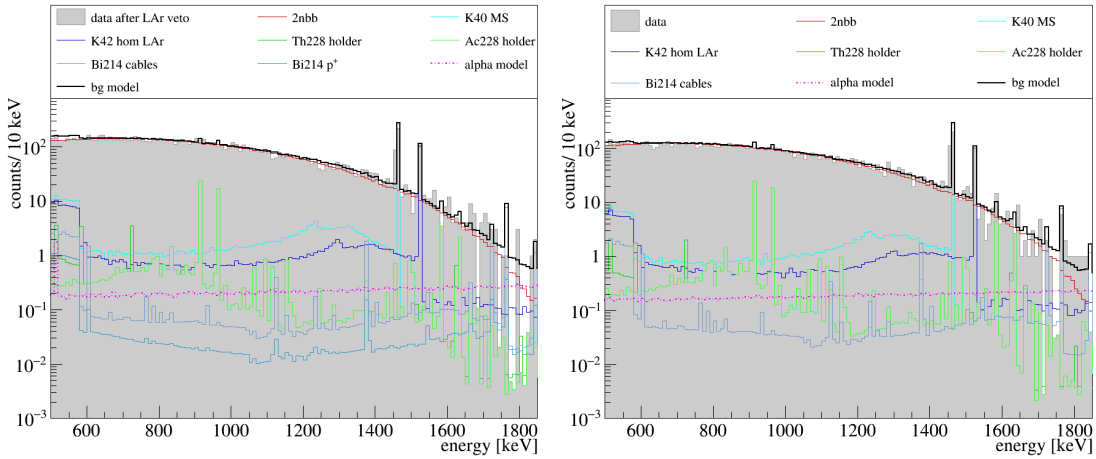

Figure 8.5: **Energy spectra after LAr veto with an approximative background model.** Left: BEGe dataset. Right: Semi-coaxial dataset.

bg	BEGe dataset cts	BEGe dataset contribution [%]	semi-coaxial dataset cts	semi-coaxial dataset contribution [%]
data	7425		6381	
model	7545.3		6613.6	
$2\nu\beta\beta$	7277.0	96.5	6400.9	96.8
^{40}K mini-shroud	115.6	1.5	84.4	1.3
^{42}K hom LAr	57.4	0.8	42.0	0.6
^{228}Th holder	7.0	0.1	3.9	0.1
^{228}Ac holder	65.9	0.9	65.8	1.0
^{226}Ra cables	6.0	0.1	4.4	0.1
^{226}Ra p^+	1.5	0.0	–	–
α model	14.0	0.2	12.2	0.2

Table 8.2: The background contributions after LAr veto in the 600 to 1300 keV energy region of the BEGe and the semi-coaxial dataset and their relative contributions to the model.

after anti-coincidence [128]. Consequently, the latter is expected to measure a longer half-life.

8.2 Two-neutrino double-beta decay half-life $T^{2\nu}_{1/2}$ of ^{76}Ge

The half-life of $2\nu\beta\beta$-decay is calculated from the number of observed $2\nu\beta\beta$ events $N_{2\nu\beta\beta}$ in an analysis window AW as

$$T^{2\nu\beta\beta}_{1/2} = \frac{ln(2)\cdot N_A \cdot \epsilon_{LAr}}{N_{2\nu\beta\beta}\cdot m_{A,76}} \cdot \sum_{i=0}^{N_{det}} M_i \cdot T_i \cdot f_{76,i} \cdot \epsilon_{SF,i} \cdot \underbrace{[f_{AV,i}\cdot\epsilon_{AV,i} + (1-f_{AV,i})\epsilon_{DL,i}]}_{:=\epsilon_{2\nu\beta\beta,i}} \cdot f_{AW,i}, \quad (8.2)$$

where

N_A	$= 6.022140857\cdot 10^{23}$ /mol, Avogadro's number,
M	detector mass [g],
T	detector livetime [yr],
$N_{2\nu\beta\beta}$	number of measured counts from $2\nu\beta\beta$ in analysis window,
ϵ_{LAr}	$= 0.977$, LAr veto acceptance,
f_{AW}	fraction of $2\nu\beta\beta$ events in analysis window,
$m_{A,76}$	$= 75.6$ g/mol,
f_{76}	enrichment fraction,
$\epsilon_{SF,i}$	survival efficiency of $2\nu\beta\beta$ events after LAr veto,
$\epsilon_{2\nu\beta\beta}$	fraction of $2\nu\beta\beta$ events fully contained in active volume,
f_{AV}	active volume fraction,
ϵ_{AV}	fraction of $2\nu\beta\beta$ events generated and detected in active volume,
ϵ_{DL}	fraction of $2\nu\beta\beta$ events generated in dead layer and detected in active volume,
i	the i-th detector channel.

The parameters for the detector mass M_{76}, the active mass fraction f_{AV}, the enrichment fraction f_{76}, $\epsilon_{2\nu\beta\beta}$, f_{AW} and the livetime T of each detector are listed in Tab. D.2. The number of $2\nu\beta\beta$ events is calculated by subtracting the number of predicted

detector	surv. frac. LAr veto [%]	total cts	bg cts	$2\nu\beta\beta$ cts	$T^{2\nu}_{1/2}$ [10^{21} yr]	dev in σ (stat)	exp. $2\nu\beta\beta$ cts (central $T^{2\nu}_{1/2}$)
BEGe	70.0 ± 0.4	7425	263.2	7161.8	1.98 ± 0.02		
GD32A	70.9 ± 2.9	180	4.8	175.2	2.26 ± 0.17	1.67	200.1
GD32B	66.5 ± 2.6	220	6.8	213.2	2.13 ± 0.14	1.02	229.0
GD32C	75.2 ± 2.1	334	7.3	326.7	1.95 ± 0.11	−0.33	320.9
GD32D	81.4 ± 2.4	219	7.1	211.9	1.89 ± 0.13	−0.68	202.5
GD35A	70.3 ± 2.1	325	14.1	310.9	2.19 ± 0.12	1.71	343.9
GD35B	68.1 ± 2.1	326	11.5	314.5	2.10 ± 0.12	1.00	333.1
GD35C	58.3 ± 2.3	257	14.4	242.6	2.26 ± 0.14	1.91	276.0
GD61A	75.4 ± 2.1	304	12.1	291.9	1.93 ± 0.11	−0.44	284.7
GD61B	65.8 ± 2.2	296	9.7	286.3	1.96 ± 0.11	−0.19	283.2
GD61C	74.3 ± 2.5	234	7.8	226.2	2.03 ± 0.13	0.35	231.5
GD76B	72.6 ± 3.0	164	4.4	159.6	2.00 ± 0.16	0.12	161.1
GD76C	71.3 ± 1.9	404	17.7	386.3	1.84 ± 0.09	−1.50	359.2
GD79B	77.5 ± 2.7	183	8.6	174.4	1.62 ± 0.12	−2.99	142.5
GD79C	76.6 ± 3.1	146	6.2	139.8	1.80 ± 0.15	−1.24	126.7
GD89A	77.3 ± 2.3	259	9.9	249.1	1.82 ± 0.11	−1.41	228.9
GD89B	70.8 ± 2.4	248	9.1	238.9	1.93 ± 0.12	−0.46	232.1
GD89C	76.4 ± 2.4	244	9.8	234.2	2.18 ± 0.14	1.41	257.7
GD89D	71.8 ± 2.5	234	5.1	228.9	1.95 ± 0.13	−0.27	225.0
GD91A	56.8 ± 2.2	297	13.9	283.1	1.94 ± 0.11	−0.39	276.8
GD91C	67.8 ± 2.5	230	7.4	222.6	2.16 ± 0.14	1.25	242.6
GD91D	75.5 ± 2.2	292	9.0	283.0	1.83 ± 0.11	−1.38	261.8
GD00A	61.2 ± 2.5	226	10.4	215.6	2.00 ± 0.13	0.14	217.7
GD00B	75.2 ± 2.3	274	7.4	266.6	1.82 ± 0.11	−1.46	244.9
GD00C	72.9 ± 2.1	315	12.0	303.0	2.02 ± 0.11	0.35	309.0
GD00D	74.7 ± 1.9	396	13.8	382.2	1.86 ± 0.09	−1.28	358.9
GD02A	56.0 ± 2.5	227	8.8	218.2	2.20 ± 0.15	1.48	242.1
GD02B	71.8 ± 2.2	300	9.8	290.2	1.87 ± 0.11	−1.02	274.1
GD02C	66.8 ± 2.3	291	11.2	279.8	2.11 ± 0.12	1.02	297.7
coaxial	71.0 ± 0.5	6381	205.3	6175.7	1.92 ± 0.02		
ANG1	70.9 ± 1.8	455	12.7	442.3	1.74 ± 0.08	−2.16	390.5
ANG2	67.1 ± 1.2	1100	41.9	1058.1	1.90 ± 0.06	−0.21	1022.7
ANG3	70.9 ± 1.2	1073	34.4	1038.6	1.99 ± 0.06	1.19	1048.4
ANG4	73.2 ± 1.2	1066	31.7	1034.3	2.01 ± 0.06	1.53	1055.5
ANG5	65.1 ± 1.2	960	36.9	923.1	1.99 ± 0.06	1.15	932.6
RG1	75.6 ± 1.3	821	22.8	798.2	1.97 ± 0.07	0.82	799.4
RG2	77.2 ± 1.2	906	24.6	881.4	1.69 ± 0.06	−3.96	757.6

Table 8.3: **Measured $T^{2\nu}_{1/2}$ of BEGe and semi-coaxial dataset and of each detector.** Listed are the total, background and $2\nu\beta\beta$ counts per dataset (detector), along with the calculated $T^{2\nu}_{1/2}$ values. The deviation of the measured half-life by a single germanium detector to the central $T^{2\nu}_{1/2}$ value and the expected number of $2\nu\beta\beta$ events if the detector would have measured the central value is computed. Furthermore, the measured survival fraction after applying the LAr veto is quoted for each detector and the sum datasets.

background events in the analysis window from the measured events.

If the complete BEGe and semi-coaxial dataset, respectively, are considered, the counts attributed to background are subtracted from the total counts using the numbers and relative contributions f given in Tab. 8.2.

The contribution of ^{40}K and ^{42}K may vary by a factor of four in the single germanium detectors depending on the detector position. In general, it is found that the top and bottom detectors show the highest contributions [31]. This has been corrected for by scaling the ^{40}K and ^{42}K contributions to the measured peak counts of each detector before applying the LAr veto. The contributions of ^{228}Th, ^{228}Ac holder and ^{226}Ra are not expected to be strongly dependent on the detector position and are taken from Tab. 8.1. Subsequently, the approximate LAr veto has been applied to the background spectra of a single detector and the relative background contributions in the analysis window are calculated. These contributions are subtracted from the events in the measured energy spectrum and the number of $2\nu\beta\beta$ counts per detector is extracted. The attributed number of total, $2\nu\beta\beta$ and background counts are compiled in Tab. 8.3. An unprecedented signal-background-ratio of 27:1 and 30:1 are reached in the case of the BEGe and the semi-coaxial dataset, respectively.

With the help of the numbers in Tab. 8.3 and Tab. D.2, $T^{2\nu\beta\beta}_{1/2}$ is calculated for the BEGe and semi-coaxial dataset and for each single detector (see Tab. 8.3). The BEGe dataset leads to the following mean value

$$T^{2\nu\beta\beta}_{1/2}(BEGe) = (1.98 \pm 0.02\ (\text{stat})) \cdot 10^{21}\,\text{yr} \tag{8.3}$$

and the semi-coaxial dataset

$$T^{2\nu\beta\beta}_{1/2}(Coax) = (1.92 \pm 0.02\ (\text{stat})) \cdot 10^{21}\,\text{yr} \tag{8.4}$$

The half-life measured by the BEGe and the semi-coaxial dataset differ by 2.1σ of the combined statistical uncertainty. This observation will be discussed in the context of systematical uncertainties (see Sec. 8.2.1).

The measured half-lifes are compiled in Fig. 8.6. The central $T^{2\nu}_{1/2}$ values of the BEGe (blue) and the semi-coaxial (red) dataset are illustrated by the horizontal lines, along with their statistical uncertainty (gray bands). The values measured by the individual detectors are drawn against their detector channel number (BEGes in blue and semi-coaxial detectors in red). The small error bars indicate the statistical uncertainty only. For a detailed discussion of the systematic errors see Sec. 8.2.1.

Due to the relatively small BEGe mass (i.e. 670 g), the statistical uncertainty of a single detector varies between 5% and 8%. Therewith only one out of 28 detectors yields a deviation from the central value at the level of 3σ, while all the other detectors deviate by less than 2σ. However, only twelve detectors lie within the 1σ range. From a Gaussian distribution one would expect nineteen detectors within $\pm 1\sigma$. This observation may indicate that a homogeneous suppression assumed by the approximative LAr veto does not reproduce the measured suppression in each detector position, as discussed in Sec. 8.2.1.

The semi-coaxial detectors have, in average, four times the mass of a BEGe detector. The statistical uncertainty is $< 4\%$ (excluding ANG1 which has only a mass of 958 g). The half-life measured by six out of seven semi-coaxial detectors deviates by less than 3σ from the central value. RG2 measures $(1.70 \pm 0.06) \cdot 10^{21}$ yr which corresponds to a deviation of 3.97σ if only the statistical uncertainty is considered. This should only

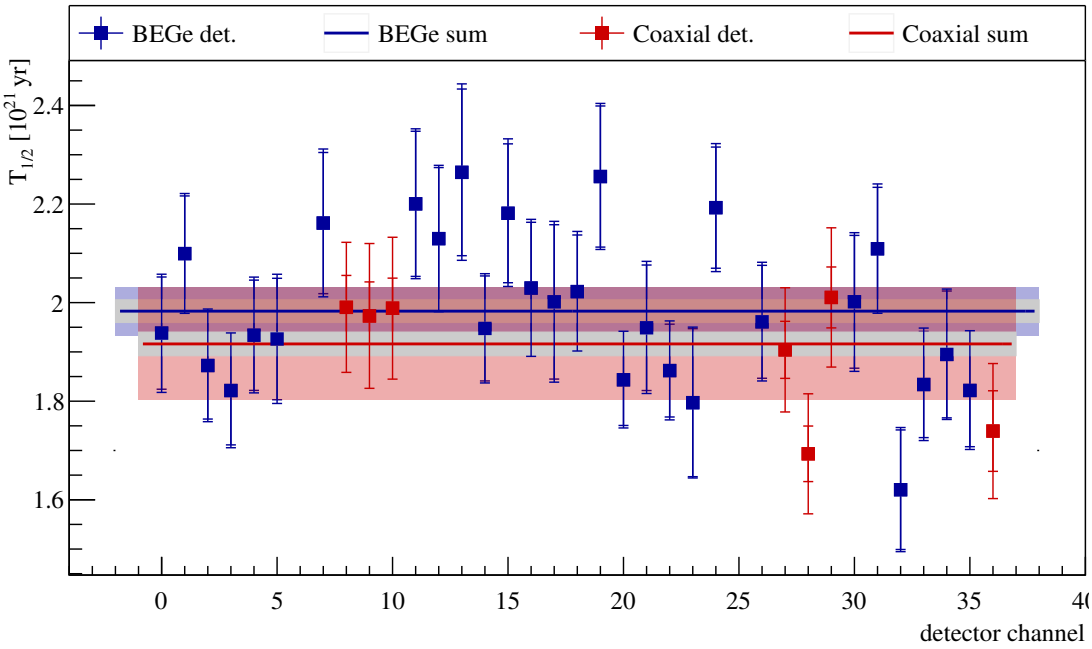

Figure 8.6: $2\nu\beta\beta$-decay half-life of individual Germanium detectors, together with the average value of the BEGe and semi-coaxial dataset, respectively. In the case of the single detector measurements the smaller uncertainty represents the statistical uncertainty and the bigger error bar the statistical and uncorrelated systematic uncertainty. The gray error band of the sum datasets is statistical and the colored bands indicate the total uncertainty.

happen in one out of 10.000 cases. The measurement by this detector is rediscussed when systematic uncertainties are taken into account (see Sec. 8.2.1).

8.2.1 Systematic uncertainties

Several uncertainties and simplifications of the analysis method and of the parameters that enter in the calculation of the $2\nu\beta\beta$-decay half-life contribute to the systematic uncertainty. This includes: (1) the approximative LAr veto, (2) the background modeling after anti-coincidence cut and (3) the uncertainties on the active masses of the germanium detectors which are expected to dominate.

In the following, the main uncertainties are discussed and an attempt is made to provide systematic errors. However, it has to be noted that at some indicated points, the approach is simplified and should be revised in the future.

LAr veto suppression

The measured LAr veto survival fraction for all detector channels is drawn in Fig. 8.7. It varies between 58% and 81%. For each string it can be observed that the LAr veto reaches the strongest suppression for the topmost detectors and the LAr veto suppression is the least for the detectors placed in the middle of a string (see Fig. D.5 for a sketch of the detector array and detector channel numbers).

To great extent, this behavior is reproduced by the individual scaling on the counts of the ^{40}K and ^{42}K FEP in the energy spectrum of each detector. However, the LAr veto suppression efficiency is assumed to be homogeneous, independent on the germanium

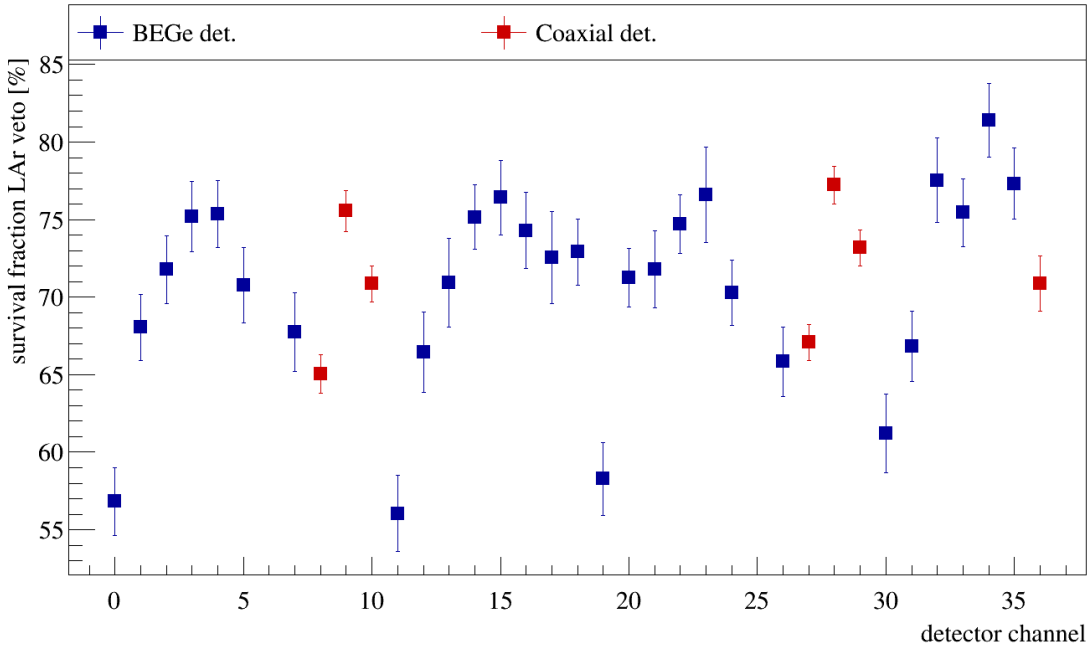

Figure 8.7: Survival fraction after LAr veto in energy window from 600 keV to 1300 keV.

detector position. Thus, this scaling does take not into account that the suppression factors measured by the top detectors are higher because of a stronger veto efficiency by the SiPMs. This fact has been discussed for the LAr commissioning run with a ^{228}Th calibration source (Sec. 7.2.1). The statistics of the calibration source measurement of the full array did not allow to use the survival efficiency histograms (compare Fig. 8.4) measured by each single detector. Moreover, the energy dependent survival efficiency of a ^{228}Th calibration source measurement does not fully imitate the suppression that is reached in case of ^{40}K, ^{42}K and ^{228}Th placed in different positions and materials than the calibration source.

The systematic uncertainty which is induced by this approach has been evaluated in a threefold way: (1) The uncertainty on the suppression of the ^{40}K, ^{42}K and ^{228}Th background components and their impact on the $2\nu\beta\beta$-decay half-life measurement has been determined by using a survival efficiency histogram from the LAr commissioning run. The suppression factors that were reached were approximately twice as high as in case of the measurement with the full detector array. As a result, a systematic uncertainty of $\sigma_{\text{LAr veto}} = 0.02 \cdot 10^{21}$ yr for the BEGe and the semi-coaxial dataset has been calculated. (2) The ^{228}Ac background component had been scaled down by applying a cut on the energy deposition in LAr of 100 keV. To deduce the systematic uncertainty induced by a more or less efficient LAr veto cut, this threshold has been varied by a factor two. The associated systematic uncertainty is calculated to $\sigma_{\text{LAr veto, Ac228}} = 0.01 \cdot 10^{21}$ yr. (3) Since the same cut has been applied to the $2\nu\beta\beta$ energy spectra, the energy threshold has been equally varied by a factor two. This approach results in a systematic uncertainty on the measured half-life of $\sigma_{\text{SF},2\nu\beta\beta} = 0.01 \cdot 10^{21}$ yr.

Active mass determination of germanium detectors

Uncorrelated and correlated uncertainties have been assigned to the active masses of the BEGe detectors accounting for uncertainties in Monte Carlo physics processes, γ-ray source, detector and cryostat, data collection and analysis methods [107]. However, since the correlated uncertainties are small in comparison to the uncorrelated ones, they are, for simplicity, added in quadrature and treated as uncorrelated uncertainty in the following discussion.

The uncertainties on the active volume of the germanium detectors lead to a systematic uncertainty of $\sigma_{AV} = 0.04 \cdot 10^{21}$ yr in the case of the BEGe dataset and $\sigma_{AV} = 0.11 \cdot 10^{21}$ yr in the case of the semi-coaxial dataset. This corresponds to uncertainties below 2.0% and $\approx 5.7\%$ in the measurement of the $2\nu\beta\beta$-decay half-life by the BEGe and semi-coaxial detectors, respectively. The numbers reflect the enormous effort that has been put in the characterization of the new Phase II BEGe detectors, providing a more accurate measurement of the active volume [107].

Adding the uncertainty on the active mass of RG2 ($\approx 6\%$) in quadrature to the statistical uncertainty, the measured half-life of this detector deviates only by 2.1σ from the central $T^{2\nu}_{1/2}$ value. Consequently, no significant tension between the detector measurement and the measurement by the complete semi-coaxial dataset is observed.

Background model

The background model developed on the datasets after anti-coincidence takes only close-by sources into account [128]. Obviously, the statistics after six month of data taking of a ultra-low background experiment, such as GERDA do not allow to disentangle contributions of the same isotope placed close-by or medium far away from the Germanium detector array.

In the case of the strongest background contributors in the $2\nu\beta\beta$ analysis window, ^{40}K and ^{42}K, the fit is strongly constraint by the counts in the FEP's. In the background model only ^{40}K in the mini-shroud is included, although a contribution from ^{40}K in the fibers is expected from screening measurements. The difference of the peak-to-Compton ratio of these two background components impacts the measurement of the half-life by attributing more or less events to $2\nu\beta\beta$-decays in the analysis window.

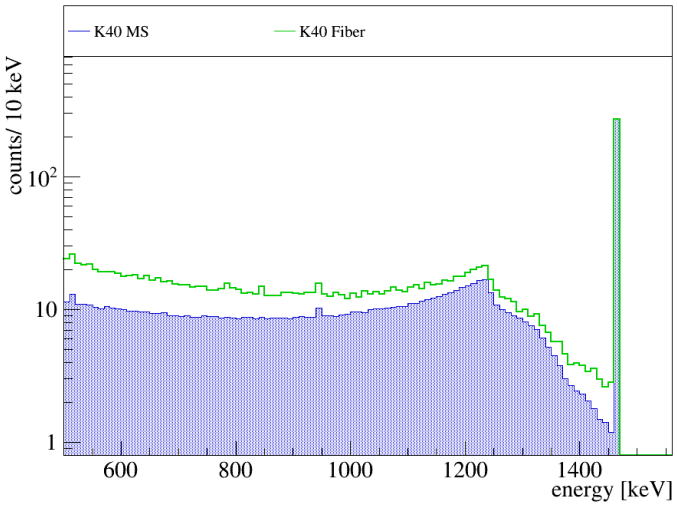

Figure 8.8: Energy spectra induced by ^{40}K in the mini-shrouds (blue) and in the fibers (green) in the BEGe detectors. The spectra are normalized to the same number of counts in the FEP.

For the BEGe dataset the peak-to-Compton ratio in the energy range from 600 to 1300 keV of ^{40}K in the mini-shroud was calculated to 1.0000 : 0.0075. The energy spectra of ^{40}K in the mini-shrouds and in the fibers are depicted in Fig. 8.8. The peak-to-Compton ratio for the fibers is determined to 1.0000 : 0.0109. Assuming the most extreme case of having the whole background arising from the fibers and not the mini-shrouds would assign 45 and 38 less counts as $2\nu\beta\beta$-events in the 600 to 1300 keV energy window of the BEGe and semi-coaxial dataset, respectively. The associated uncertainty is $< 0.5\%$.

8.2.2 Results

The induced systematic uncertainties by this approach of measuring $T^{2\nu\beta\beta}_{1/2}$ with the help of the energy spectra after LAr veto have been discussed in Sec. 8.2.1. Therewith, the half-life measured by the BEGe and the semi-coaxial dataset with an exposure of 5.826 kg · yr and 5.019 kg · yr, respectively, are extracted with an unprecedented accuracy as

$$T^{2\nu\beta\beta}_{1/2}\ (\text{BEGe}) = (1.98 \pm 0.02\ (\text{stat}) \pm 0.05\ (\text{syst})) \cdot 10^{21}\,\text{yr}, \tag{8.5}$$

$$T^{2\nu\beta\beta}_{1/2}\ (\text{coaxial}) = (1.92 \pm 0.02\ (\text{stat}) \pm 0.11\ (\text{syst})) \cdot 10^{21}\,\text{yr}. \tag{8.6}$$

The systematic uncertainty is dominated by the uncertainty of the active volume determination. The uncertainty on the active volume fraction amounts to $\sigma_{\text{AV,coax}} = 0.11 \cdot 10^{21}$ yr in the semi-coaxial dataset. In contrast, it is reduced to $\sigma_{\text{AV,BEGe}} = 0.04 \cdot 10^{21}$ yr in the case of the BEGe detectors which underwent a careful characterization campaign after their production in 2011-2012 [107].

The other contributions to the systematic uncertainty are based on the uncertainty induced by both the approximative scaling of the energy spectra after LAr veto of the individual background components and the background model which only accounts for close-by background sources. The uncertainties related to the LAr veto have been split in three contributions as discussed in Sec. 8.2.1. If these four systematic uncertainties are added in quadrature they amount, in total, to $0.03 \cdot 10^{21} yr$ in case of the BEGe and of the semi-coaxial dataset.

One may claim to observe a systematic shift in the half-lifes measured by the BEGe ($T^{2\nu}_{1/2} = 1.98 \cdot 10^{21}$ yr) and the semi-coaxial dataset ($T^{2\nu}_{1/2} = 1.92 \cdot 10^{21}$ yr). At the one hand, the deviation of the value measured by RG2 from the central value may still indicate a wrong determination of its active mass or just on unlucky over-fluctuation of the measured $2\nu\beta\beta$ counts. However, the difference of 757.6 expected and 881.4 measured $2\nu\beta\beta$ counts is quite high. If RG2 would not be taken into account the half-life measured by the semi-coaxial dataset would shift to a higher value of $T^{2\nu}_{1/2} = (1.95 \pm 0.03(stat)) \cdot 10^{21}$ yr. On the other hand, the central value of the BEGe dataset may be shifted from the actual $2\nu\beta\beta$-decay half-life. Prior to the mounting of all germanium detectors in the Phase II setup and inserting them in the LAr cryostat, the germanium detectors were stored for 2-3 years at room temperature. From literature, it was known that the dead layer increases, in average, by 0.1 mm/yr within the first years under such conditions and starts then saturating. In case of the semi-coaxial detectors which were produced in the 1990s, it is assumed that the dead layer does not grow anymore. The storage under warm conditions of the newly produced BEGe detectors has been taken into account by assuming a growth of 0.1 mm/yr and thus, a decrease

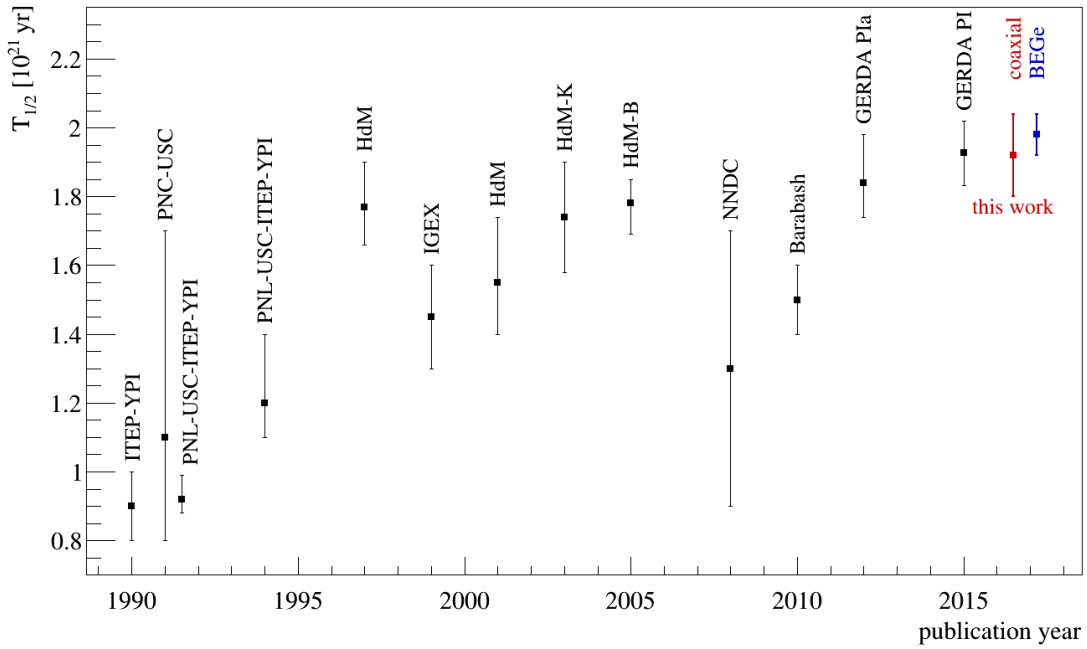

Figure 8.9: **Comparison of $2\nu\beta\beta$ half-life result to former experiments.** $2\nu\beta\beta$ half-lifes measured by different experiments and with different statistics along with the new results determined for the BEGe (blue) and semi-coaxial (red) dataset separately. The values are taken from [19] and [8] and references therein.

of the active mass fractions. It may be that the increase within the first year of storing germanium detectors under warm conditions is significantly stronger [107]. Hence, the active masses of the BEGe detectors would in reality be smaller than the ones that are taken into account by the GERDA collaboration and consequently, a systematic shift to higher $2\nu\beta\beta$-decay half-lifes may be induced.

Fig. 8.9 shows the $2\nu\beta\beta$-decay half-life of ^{76}Ge measured by different experiments within the last three decades. Over the course of time and with increasing signal-to-background ratio, the measured half-life shifted to higher values. The measurement with the currently best accuracy was based on a dataset with $17.9\,\mathrm{kg}\cdot\mathrm{yr}$ exposure. It was published by the GERDA collaboration in 2015 and yielded $T^{2\nu}_{1/2} = (1.926 \pm 0.094)\,10^{21}\,\mathrm{yr}$ at 90% confidence level [19]. This analysis (see Eq. 8.6) is based on two datasets, each only exhibiting an exposure of $5.826\,\mathrm{kg}\cdot\mathrm{yr}$ and $5.019\,\mathrm{kg}\cdot\mathrm{yr}$, respectively. Due to an unprecedented signal-to-background ratio of 27:1 and 30:1, respectively, reached in the analysis window after LAr veto, the total uncertainty could be reduced to 3% in the BEGe dataset and amounts to 6% in the semi-coaxial dataset, respectively.

Despite approximations and simplifications of the approximative background model after LAr veto, one does not expect a significant change of the obtained signal-to-background ratio of 30:1. So, also future analyses might not shift significantly the obtained $T^{2\nu}_{1/2}$ values but describe in more detail the uncertainty budget.

CHAPTER 9

CONCLUSION & OUTLOOK

This thesis was carried out within the GERDA experiment searching for neutrinoless double beta decay of ^{76}Ge. The existence of this second order transition process is predicted by several extensions of the Standard Model of particle physics and would prove lepton number violation by two units. GERDA operates bare germanium semiconductor detectors, enriched in the $\beta\beta$ isotope ^{76}Ge, in liquid argon. An integral part of the detection potential of such rare process searching experiments is the background level induced by external and internal radioactivity. In Phase II, a background index better than $10^{-3}\,\mathrm{cts}/(\mathrm{kg}\cdot\mathrm{keV}\cdot\mathrm{yr})$ in the region of interest around the $Q_{\beta\beta}$-value of ^{76}Ge at 2039 keV is aspired. Thorough selection of radiopure materials, reduction of materials close to the germanium detectors and the deployment of detectors which exhibit an enhanced pulse shape discrimination efficiency alone, do not allow to reduce the background to this level.

However, the detection of liquid argon scintillation light in coincidence with germanium detector signals makes it possible. This thesis focused on the implementation and characterization of such a scintillation light anti-coincidence veto (LAr veto) in the upgraded GERDA Phase II experiment.

In a first part, the LAr veto capability for different background sources was accessed by means of extensive Monte Carlo simulations including the full tracking of optical photons. The redundancy of two scintillation light readout systems, namely cryogenic photomultiplier tubes and silicon photomultipliers connected to scintillating fibers, was decided for to ensure a stable performance over several years. In parallel, 3" photomultiplier tubes (PMTs) were characterized and tested for their stability during long-term operation in liquid argon at MPIK, Heidelberg. In this context, internal light emission of several cryogenic PMTs was discovered at the ceramic stem and at the last dynodes. In close cooperation with the manufacturer, different countermeasures were adopted to the PMT design and materials in order to prevent such (micro-)discharges. The long-term tests had proven that this type of PMTs can be operated at a gain of $2\cdot10^6$, while maintaining good performance parameters, such as a peak-to-valley ratio of $\gtrsim 3$. In the end, 42 PMTs of different batches from the same manufacturer were tested to obtain a selection of 18 PMTs that were qualified to be operated in GERDA.

The hybrid LAr scintillation light instrumentation has been successfully installed in the GERDA Phase II experiment. The first commissioning tests with calibration sources were used to evaluate the background rejection efficiency of external γ-rays by the LAr veto. This external background in the region around $Q_{\beta\beta}$ is suppressed by a factor of $SF = 98.1 \pm 0.1$ and $SF = 4.1 \pm 0.1$ in the ^{228}Th an ^{226}Ra calibration source measurement, respectively. As expected, the suppression factor by which a LAr veto suppresses background in a certain energy region depends strongly on the excess energy that may be released in LAr. Moreover, any material that absorbs part of the energy without being read out, such as not operational germanium detectors in the LAr veto commissioning tests, reduces the background rejection power of the LAr veto.

With this knowledge, it was possible to answer to the question why the combination of the LAr veto with a Germanium detector pulse shape analysis results in a stronger background rejection than the product of both efficiencies: The suppression factors in the ^{228}Th calibration source measurement augmented to $SF = 361 \pm 29$ and to $SF = 23 \pm 2$ in the ^{226}Ra calibration, respectively. By analyzing the spacial distribution of the events in the germanium detectors of a Monte Carlo simulation of the ^{228}Th calibration, the pulse shape discrimination cut was reproduced and combined with the LAr veto predicted by tracking the optical photons. Germanium detector pulse shape discrimination preserves events that interact at one single site in the active volume of the Germanium detector. It is found that for such a topology the probability to deposit part of the excess energy in the dead layer of germanium detectors is reduced by a factor of two in comparison to events interacting at least two times within the active volume. Consequently, the percentage of events that do not deposit any energy in LAr is higher in case of multi-site events, resulting in a less efficient background rejection.

The calibration source measurements which were carried out during the LAr veto commissioning allowed for the first time to compare results from the LAr veto of the GERDA experiment to predictions from Monte Carlo simulations. It became apparent that the Monte Carlo predictions using the nominal optical parameters overestimate both the suppression factor and in particular the photoelectron distribution. First trials of tuning the Monte Carlo results by using two effective scaling factors accounting for a reduced fiber coverage and liquid argon light yield resulted in better but not sufficient agreement. Additional measurements with radioactive calibration sources at different positions were carried out in summer 2016 and may eventually help to find effective optical parameters which reproduce the measured results.

In December 2015, Phase II of the GERDA experiment started with an increased germanium detector array containing 35.6 kg of ^{76}Ge enriched germanium semiconductor diodes and the novel LAr veto. The first data allowed to analyze the LAr veto performance on different background components. The suppression by the LAr veto in the low energy region dominated by the β-spectrum of ^{39}Ar was measured for each germanium detector individually and revealed as expected a small shadowing of scintillation light created in close vicinity to the central detector string. Its suppression factors vary between $SF = 1.63 \pm 0.04$ and $SF = 2.07 \pm 0.03$ and are comparable to suppression factor reached for other semi-coaxial germanium detectors placed in an outer string.

Around $Q_{\beta\beta}$ the background of the semi-coaxial detectors is suppressed by a factor of $SF = 1.6 \pm 0.1$ while the suppression factor of the BEGe dataset amounts to

	exposure	BI [10^{-3} cts/(kg · keV · yr)] after		
	[kg · yr]	AC + μ-veto	LAr veto	LAr veto + PSD
BEGe	5.826	$15.7^{+3.7}_{-3.2}$	$4.5^{+2.1}_{-1.6}$	$0.7^{+1.1}_{-0.5}$
coaxial	5.019	$16.5^{+4.1}_{-3.5}$	$10.4^{+3.3}_{-2.7}$	$3.5^{+2.1}_{-1.5}$

$SF = 3.5 \pm 0.1$. In comparison with the ^{228}Th calibration source measurement, the background rejection efficiency is strongly reduced. It may be explained by the background composition around $Q_{\beta\beta}$ which reveals significant contributions from α-decays on the detector surface and β induced backgrounds such as ^{42}K homogeneously distributed in LAr. By means of the LAr veto in combination with pulse shape discrimination (PSD) the background index of the BEGe dataset is reduced to $0.7^{+1.1}_{-0.5} \cdot 10^{-3}$ cts/(kg · keV · yr). Thus, the Phase II goal is reached in the case of the new BEGe detectors. Based on this background index, the sensitivity of the GERDA Phase II experiment for an exposure of 100 kg · yr will be $T^{0\nu\beta\beta}_{1/2} < 10^{26}$ yr.

Compton background from ^{42}K is the strongest background contribution in the $2\nu\beta\beta$-decay dominated energy region of the first Phase II data. Pulse shape discrimination reduces this background only by a factor of approximately five, however, this strongly depends on the ratio of beta to γ-ray induced background counts in this energy region.

An estimate of the LAr veto rejection efficiency based on calibration source measurements predicts a reduction of the background in the 600 to 1300 keV window by a factor of ≈ 35. Therewith the signal-to-background ratio improves from 3:1 to an unprecedented ratio of 30:1. This allowed an almost background-free determination of the $2\nu\beta\beta$-decay half-life by a simple counting method. The half-life measurement by the BEGe dataset yielded

$$T^{2\nu\beta\beta}_{1/2} = (1.98 \pm 0.02\ (\text{stat}) \pm 0.05\ (\text{syst})) \cdot 10^{21}\ \text{yr}$$

and the semi-coaxial dataset

$$T^{2\nu\beta\beta}_{1/2} = (1.92 \pm 0.02\ (\text{stat}) \pm 0.11\ (\text{syst})) \cdot 10^{21}\ \text{yr}.$$

based on an exposure of only 5.826 kg · yr and 5.019 kg · yr, respectively, but with a reduced systematic uncertainty in comparison to earlier measurements [19].

A deviation of the mean $2\nu\beta\beta$-decay half-life values measured by the BEGe and the semi-coaxial dataset is observed. It may be that a slightly wrong determination of the active volume fraction of one of the semi-coaxial germanium detectors (RG2) shifts the half-life measured by the semi-coaxial dataset to a shorter $2\nu\beta\beta$-decay half-life. At the other hand, it is possible that the reduction of the active mass fraction of all BEGe detectors due to their storage at room temperature during 2-3 years prior to the installation in the GERDA cryostat has been underestimated and shifted the measured half-life to an systematically longer value of $T^{2\nu}_{1/2}$. These systematic uncertainties have not been taken into account in the quoted systematic uncertainties.

Over the course of time and with an increasing signal-to-background ratio a shift to higher $2\nu\beta\beta$-decay half-lifes has been observed, such that the first measurements

deviate by more than 5σ from this measurement. Despite approximations and simplifications in the utilized analysis method, one does not expect a significant change of the obtained signal-to-background ratio of 30:1 of the GERDA Phase II setup and therewith, of the measured $2\nu\beta\beta$-decay half-life. One may claim that a lower signal-to-background ratio in earlier measurements resulted in a systematic shift of the $2\nu\beta\beta$-decay half-life measurements.

The first six months of the GERDA Phase II experiment were able to prove that the background in the region of interest could be reduced to the aspired level of $10^{-3}\,\mathrm{cts}/(\mathrm{kg}\cdot\mathrm{keV}\cdot\mathrm{yr})$, allowing to measure over the entire run time in the background-free regime. This was made possible by combining semiconductor properties such as excellent energy resolution and an efficient pulse shape discrimination technique with a novel LAr scintillation light veto. This improvement means a significant step towards the next generation Germanium detector experiments performing rare-event searches at an extremely low background level with several hundred kilograms of enriched detector mass. As a consequence, many next generation germanium experiments take up the idea of implementing an active scintillation light veto and reducing the mass of *dead* material close to the germanium detectors.

As an example, the GERDA cryostat fits up to 200 kg of Germanium detector mass arranged in several strings. If the background in the region of interest can be further reduced by a factor of five, such a future experiment would stay background-free until reaching an exposure of $1000\,\mathrm{kg}\cdot\mathrm{yr}$ and thus, reaching a half-life sensitivity of $10^{27}\,\mathrm{yr}$.

To conclude, one convincing aspect of a $0\nu\beta\beta$-experiment using germanium semiconductors is the possibility of distinguishing a potential $0\nu\beta\beta$ signal from a nuclear transition peak by both the pulse shape discrimination preserving at $\sim 90\%$ probability signal-like events and in case of an unknown nuclear transition a potential signature in the LAr.

APPENDIX A

MY CONTRIBUTION

Ch. 4 concerns the cryogenic 3" inch PMTs that were purchased by MPIK for a light instrumentation in the GERDA experiment. The cryogenic test stand was designed and constructed by M. Heisel, and later operated in cooperation with him. The long-term tests and the PMT characterization were mainly carried out by me, but he was available for exchanging ideas over the whole time of the long-term tests. The measurement series for the delayed build-up of the PMT signal rates were performed by me, while the subsequent analysis was done by M. Heisel. The measurements at room temperature that I carried out and analysed could use existing infrastructure in the dark room test stand at MPIK.

The extension of the Monte Carlo simulation framework MAGE with optical photon tracking, the implementation of the light instrumentation designs and the Monte Carlo simulations (Ch. 5) were a common effort of the "LAr light instrumentation task group", mainly involving seven people. My main task was the implementation of a light instrumentation using only PMTs – the *PMT LAr veto design* – in MAGE. This included reflectivity measurements of commonly used materials such as PTFE, copper, silicon, germanium and VM2000 reflector foil – with and without a wavelength shifting coating. Moreover, the emission spectrum of the wavelength shifter was measured and used to optimize the thickness of the wavelength shifter coating. In a second step, the design itself was implemented along with the wavelength dependent detection efficiency of the PMTs. Simulations of common background sources and this type of LAr veto design helped answering design related questions and could be compared to a *Fiber LAr veto* implemented by colleagues from TU Munich. The PMT LAr veto design was later modified to the *hybrid LAr veto design* by replacing a central copper cylinder by a fiber shroud. This task has been undertaken by colleagues from TU Munich and TU Dresden. Simulations of the hybrid design were split between the three institutes to share the huge amount of CPU time that Monte Carlo simulations with optical photon tracking require. The instrumentation induced background index has to be low in comparison to the profit acquired by the background suppression through the light instrumentation. I ran and evaluated the Monte Carlo simulations to estimate the background index caused by PMT-related components of such a light instrumentation.

The installation and integration of the hybrid design in the GERDA experiment was a common effort of the groups responsible for the sub-systems (see Ch. 6), namely TU

Munich and MPIK. This splitting of PMT and SiPM related tasks was kept in the following. I was responsible for the development and implementation of the algorithms to identify hits and extract important parameters from the FADC traces of the PMT channels. In this context, I could re-use an efficient algorithm to determine the baseline of the trace which was already developed for the analysis of the PMT signals in the LArGe experiment. Moreover, I was involved in the implementation of the algorithm to set a veto flag in coincidence with the germanium detector signals, which included the calibration of the PMT signals in photoelectrons and the definition of veto thresholds and windows.

During the first LAr veto integration and commissioning tests, I was actively involved in the data taking (Ch. 7). As indicated above, the analysis of the LAr veto data containing both SiPM and PMT channels happened always in cooperation with the responsible persons for the light read-out by SiPMs. Therefore, the main results represent a common effort. However, the presented analysis was performed on my own. For the first time, I tried to find an explanation of the over-orthogonality of the PSD analysis and the LAr veto. This analysis uses common data from the LAr commissioning test runs and a Monte Carlo simulation that I had performed. The results of the first six months of GERDA Phase II data taking with the LAr veto are based on common GERDA data. In the course of this data taking I was responsible for the extraction of the parameters of the PMT signals and the definition of veto flags for the PMT channels.

The measurement of the $2\nu\beta\beta$-decay half-life presented in Ch. 8 is based on the energy spectra acquired during the first six months of Phase II data taking. I resorted to an existing background model of the energy spectra after detector-detector anti-coincidence to develop my own background model after LAr veto. Therewith, I computed the $2\nu\beta\beta$-decay half-life and estimated the systematic uncertainties.

APPENDIX B

NATURAL DECAY CHAINS

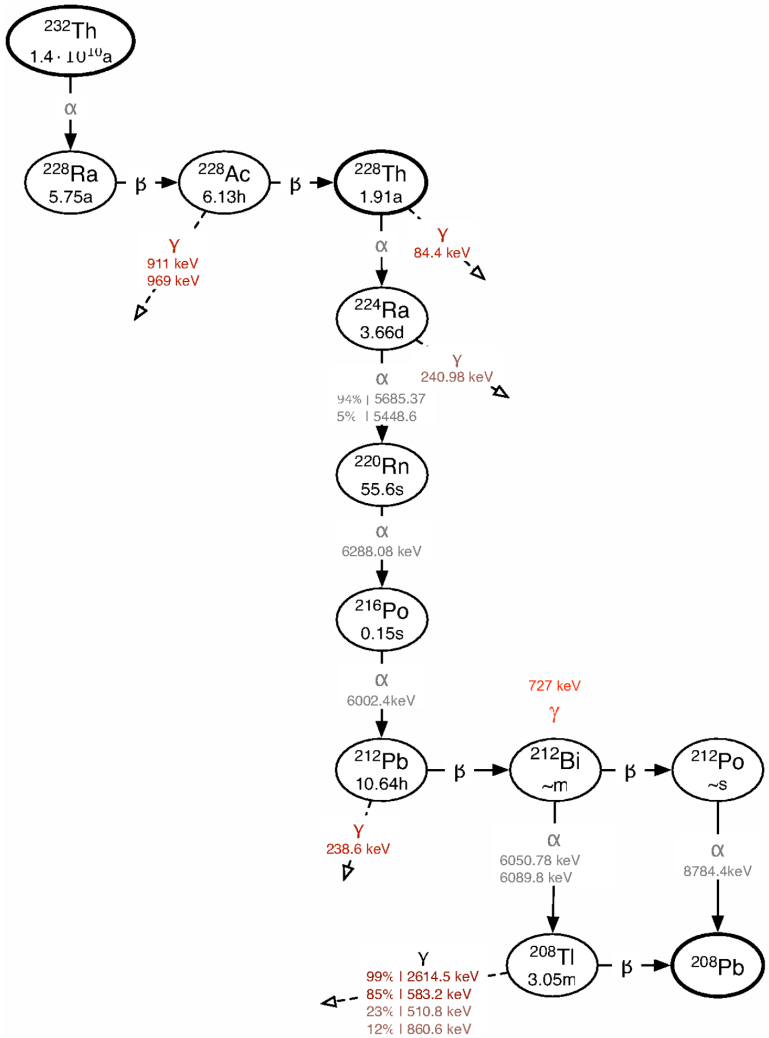

Figure B.1: Natural ^{232}Th decay chain. Background relevant gamma lines are displayed in red colour [69].

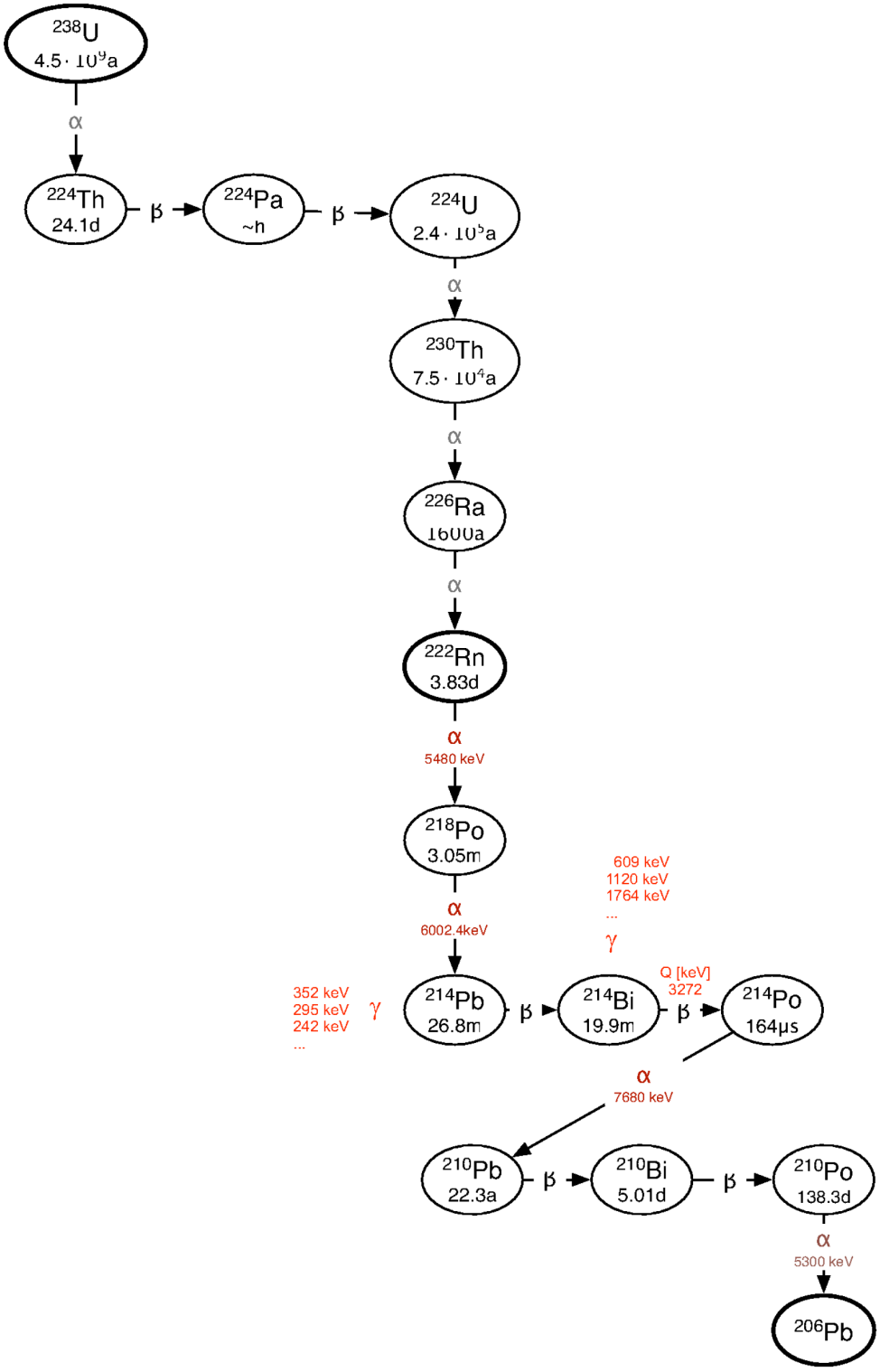

Figure B.2: The natural ^{238}U decay chain. Background relevant gamma lines are displayed in red colour [69].

APPENDIX C

RADIOACTIVE DECAY SCHEMES

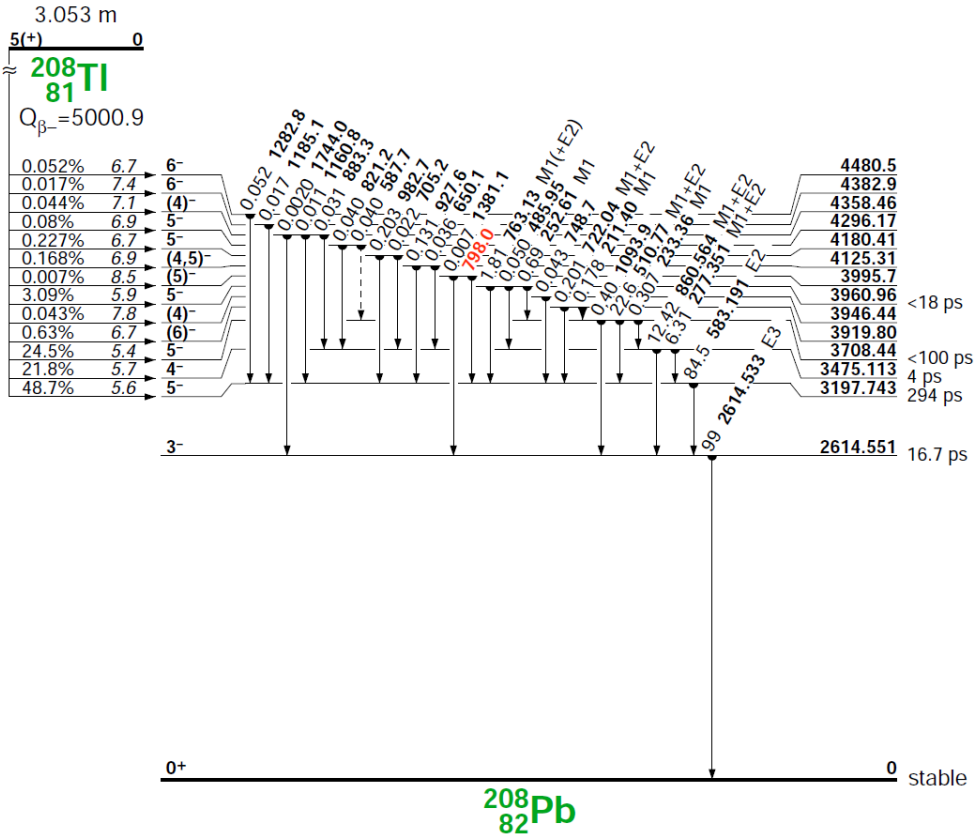

Figure C.1: Decay scheme of ^{208}Tl [69].

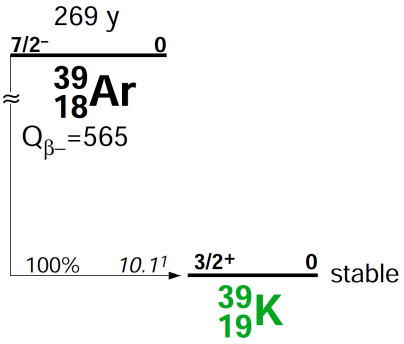

Figure C.2: Decay scheme of ^{39}Ar [69].

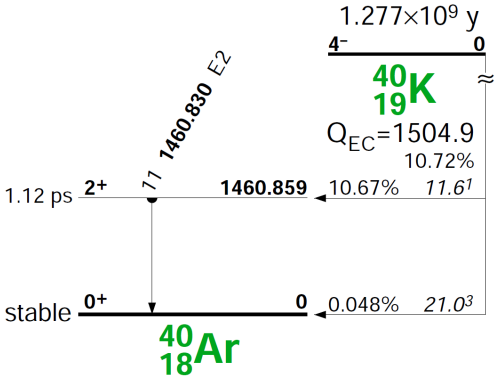

Figure C.3: Decay scheme of ^{40}K [69].

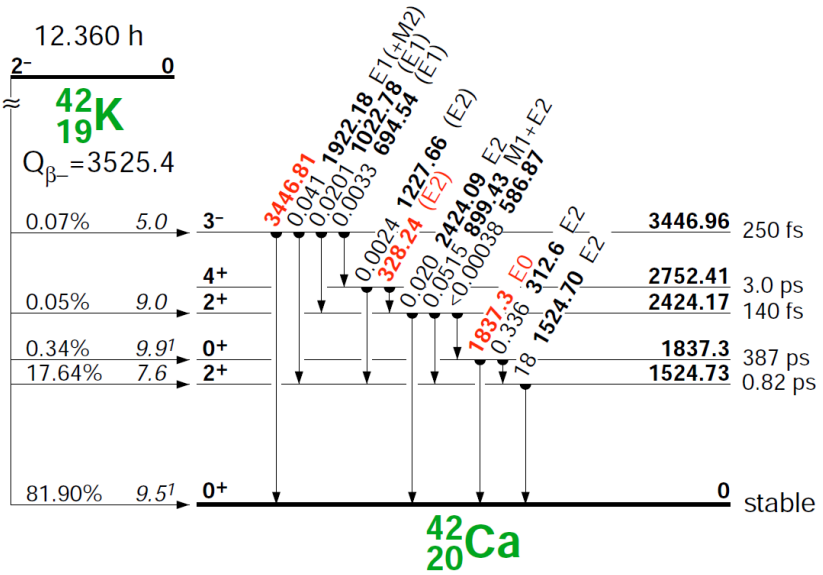

Figure C.4: Decay scheme of ^{42}K [69].

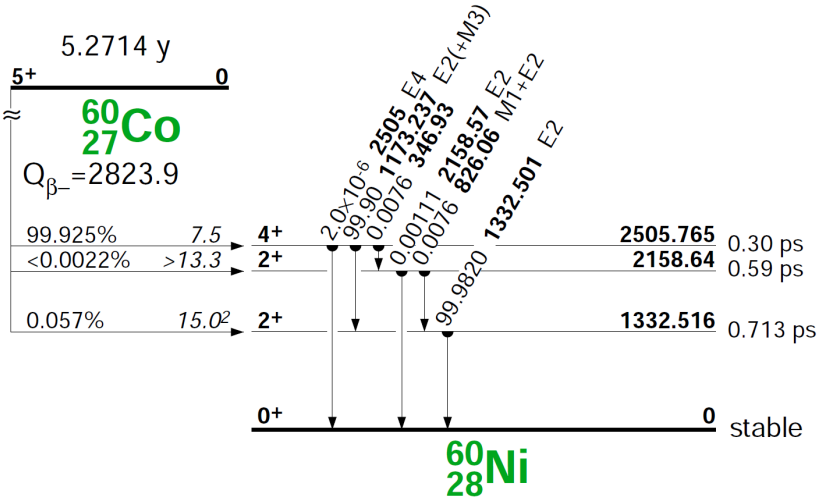

Figure C.5: Decay scheme of ^{60}Co [69].

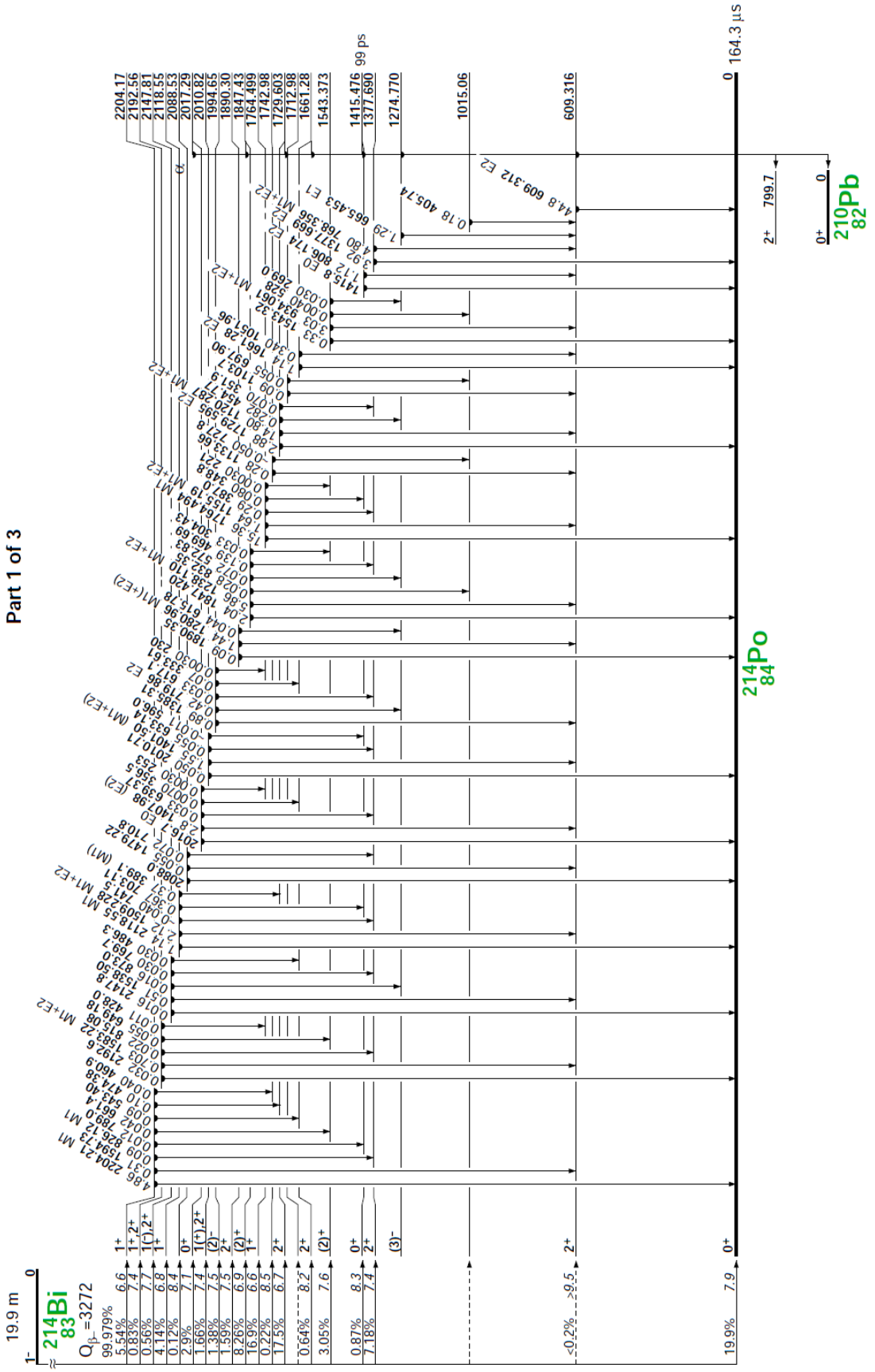

Figure C.6: Decay scheme of ^{214}Bi, part 1 of 3 [69].

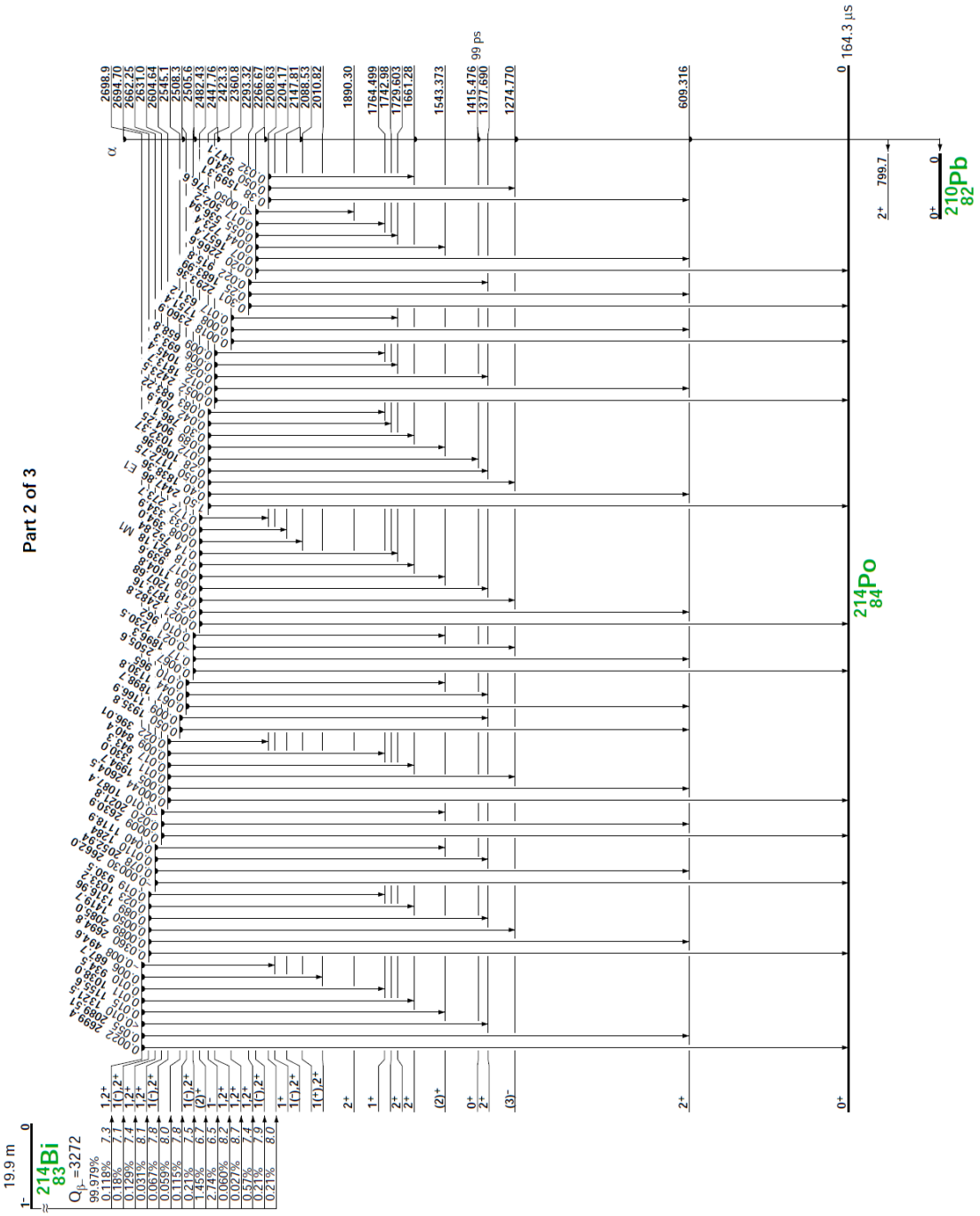

Figure C.7: Decay scheme of ^{214}Bi, part 2 of 3 [69].

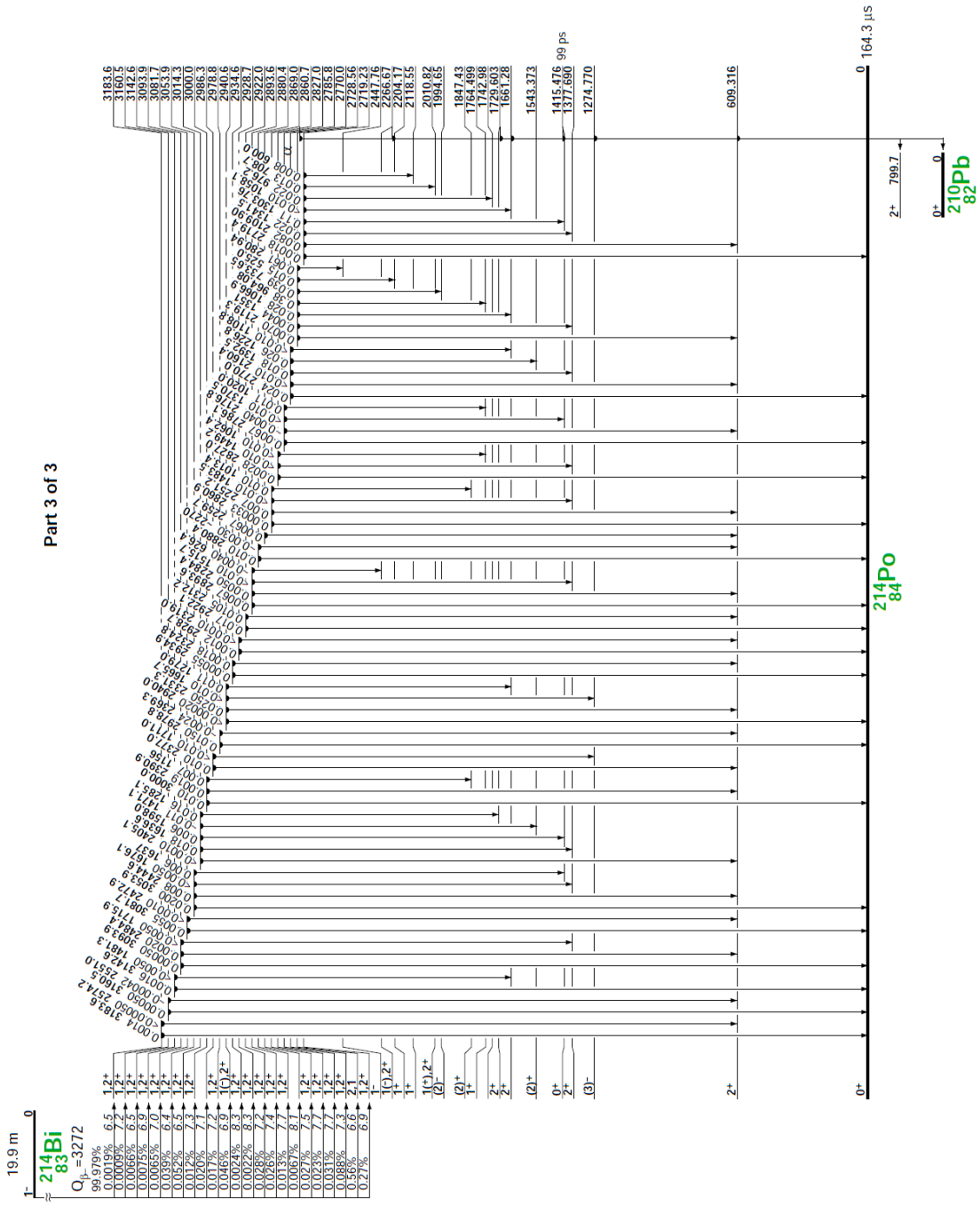

Figure C.8: Decay scheme of ^{214}Bi, part 3 of 3 [69].

APPENDIX D

DIAGRAMS AND TABLES

D.1 3” R11065 PMTs

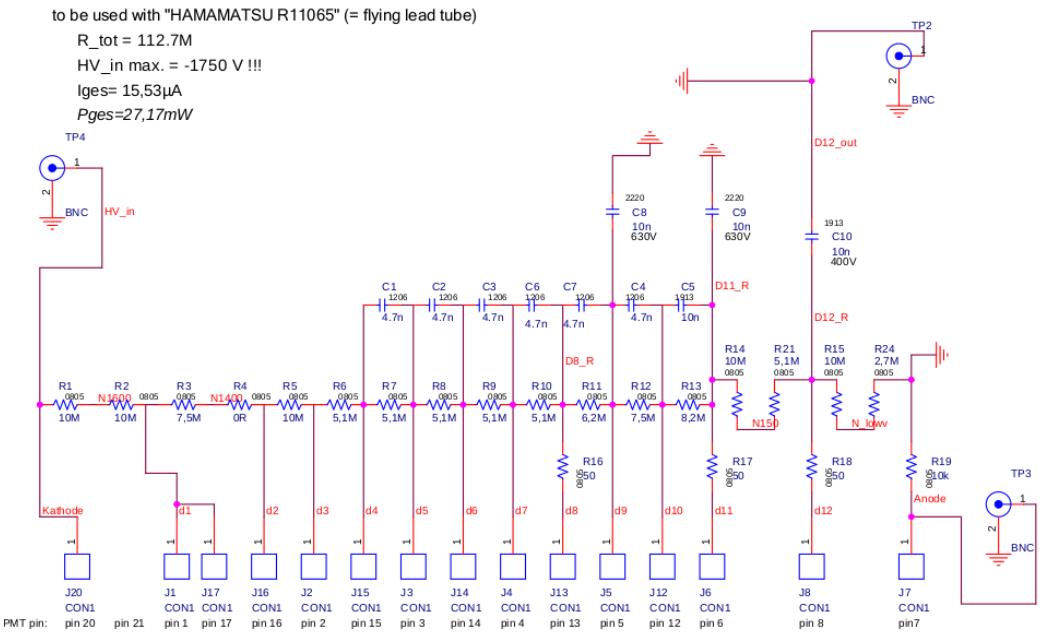

Figure D.1: Circuit diagram of the custom-made voltage divider for Hamamatsu PMTs of type R11065.

Delayed signal rate

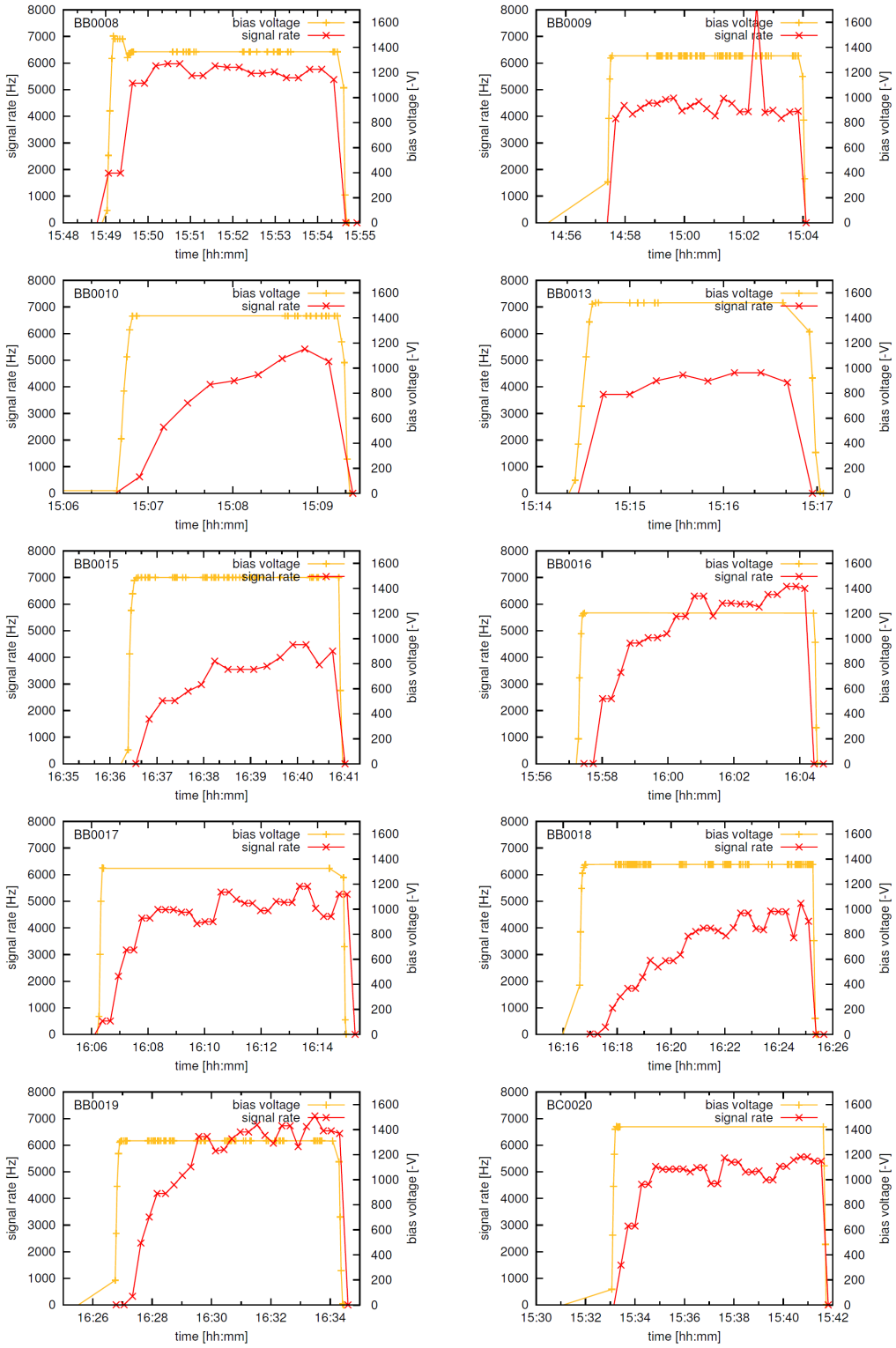

Figure D.2: Delayed signal build-up measured with ten PMTs from first and second batch. Figure taken from [85].

Afterpulse spectra

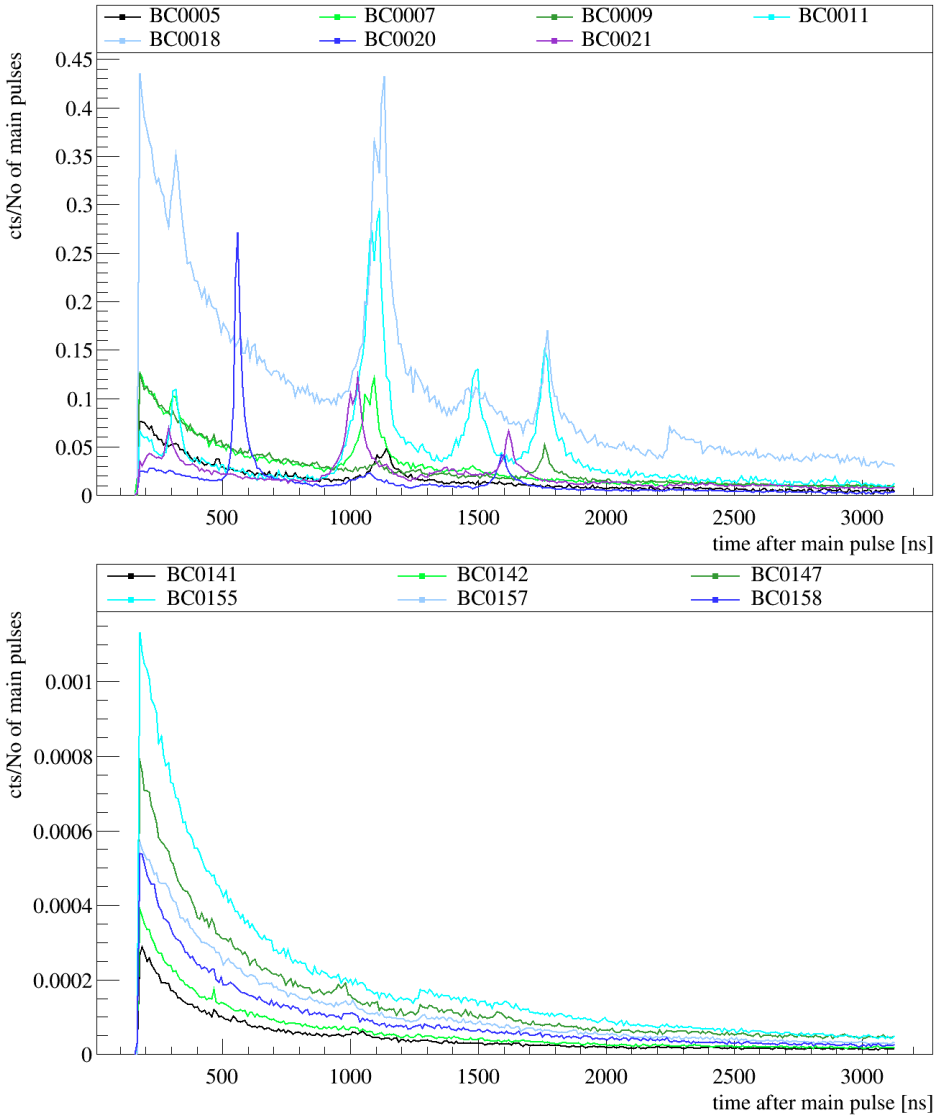

Figure D.3: Afterpulse spectra of PMT batch 2 and batch 5.

Modifications on PMT light read-out in GERDA

After installing the light instrumentation in the GERDA experiment there were two modifications on the PMT light read-out. At these moments, not operational PMTs or damaged voltage divider bases were exchanged. Some PMTs changed only their positions in the PMT array from the top to the bottom and vice versa to have the most reliable PMTs placed at the top plate. This has been done since changes at the top PMT plate require much more work and the PMTs at the top plate are not accessible at all if a germanium detector array is installed.

- Period I: 2015/01/28 - 2015/06/15
- Period II: 2015/07/15 - 2015/09/07
- Period III: 2015/09/30 - 2016/11/01

Tab. D.1 gives the assignment of the LAr channel number ($\widehat{=}$DAQ channel) and the serial number (S/N) of the installed PMT along with an indication if the PMT was operational . In the first period the PMTs were installed on the DAQ channels 16-31. Since then the PMTs are connected to the channels 0 to 15.

LAr channel	period I		period II		period III	
	S/N	comment	S/N	comment	S/N	comment
0 (16)	ZK6853		ZK6853		ZK6853	
1 (17)	BC0086		BC0086		BC0086	
2 (18)	BC0089		BC0089		BC0089	
3 (19)	BC0092		BC0092		BC0092	
4 (20)	BC0093		BC0093		BC0093	
5 (21)	BC0094		ZK6904		ZK6904	new VD
6 (22)	ZK6905	x, afterpulses	BC0120		ZK7720	
7 (23)	BC0117		BC0117		BC0117	
8 (24)	BC0122		BC0122		BC0122	
9 (25)	ZK6904		BC0084		BC0084	
10 (26)	BC0120		BC0139		BC0139	new VD
11 (27)	BC0141		BC0141		BC0141	
12 (28)	BC0142		BC0142	x	BC0120	
13 (29)	BC0147		BC0147		BC0147	
14 (30)	BC0155	x	BC0094		BC0094	
15 (31)	BC0158	x	BB0019	x	ZK7717	

Table D.1: Assignment of PMT serial numbers to LAr channel during operation in GERDA .

D.2 LAr veto commissioning test setup with radioactive calibration sources

The LAr veto commissioning tests in April and May 2015 were performed with the same pilot string setup and two different radioactive calibration sources. The configuration of the ^{228}Th calibration measurement is illustrated at the left side of Fig. D.4 while the ^{226}Ra calibration measurement is depicted at the right. The Germanium detector ordering in the pilot string was the same during both measurements and the detector string was surrounded by a Nylon mini-shroud.

Three out of eight germanium detectors were not fully operational

1. GD91B
2. GD61C
3. GD91C

During the ^{228}Th calibration source measurement in April, these three detectors could at least be used in anti-coincidence mode. In May (^{226}Ra calibration), only GD61C and GD91C could be used for the detector-detector anti-coincidence cut. Both calibration sources were lowered to the same position: 100 mm below the uppermost germanium

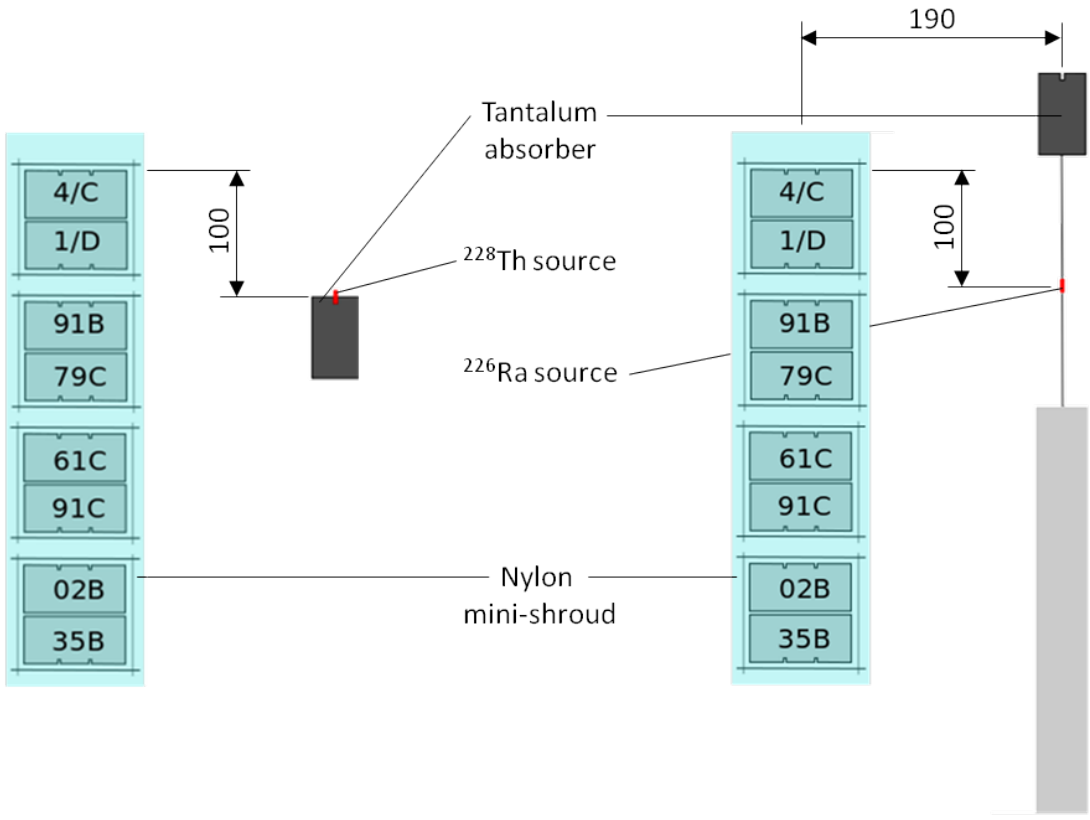

Figure D.4: **Pilot string with ^{228}Th and ^{226}Ra calibration sources.** Left: Detector string with ^{228}Th calibration source inserted in position S2 of the source insertion system and lowered to 7560 mm. Right: Detector string with ^{226}Ra calibration source inserted in position S2 of the source insertion system and lowered to 7560 mm.

detector surface and with a radial distance of 190 mm. The ^{228}Th calibration source (red cylinder at the left of Fig. D.4) was a Phase I calibration source and was directly mounted into the Tantalum absorber of the source insertion system. The ^{226}Ra calibration source was a wire source and had to be mounted below the Tantalum absorber (red cylinder at the right). The wire of the ^{226}Ra source was stored in the gray cylinder.

D.3 Phase II setup

In December 2015, a full germanium detector array containing 35.6 kg of enriched detector mass and three natural semi-coaxial detectors (GTFxx), was inserted in the GERDA cryostat and Phase II of the experiment started. Fig. D.5 illustrates the detector ordering within the strings. From the cross-sections one can differentiate semi-coaxial and BEGe detectors. The blue colored detectors were passivated and the yellow detectors were not passivated.

The assignment of the detector names and positions to the DAQ channel number is given in Tab. D.2. Furthermore, the table gives important detector parameters of the first Phase II data release as they were used for the $T^{2\nu\beta\beta}_{1/2}$ measurement in Ch. 8.

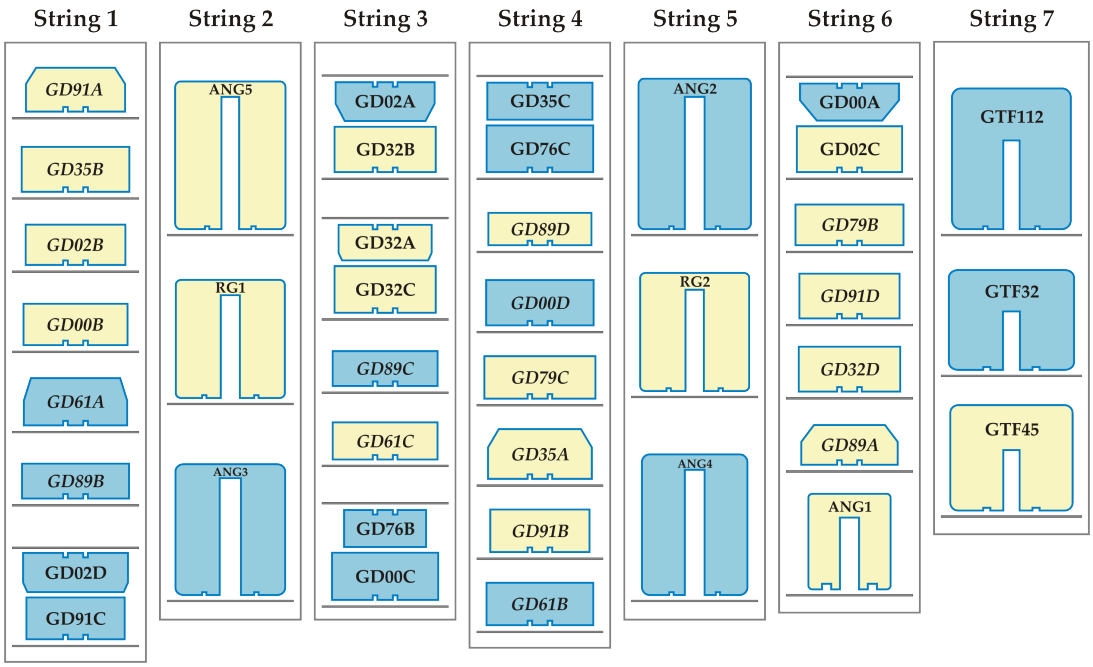

Figure D.5: **Scheme of the Phase II detector array.** Cross sections through the detector center are shown together with the detector names and the holder plates for all seven strings. The color coding distinguishes passivated detectors (blue) from non passivated (yellow) detectors. The assignment of the detectorname and therewith position to the DAQ chanel number can be found in Tab. D.2. Figure done by K. Gusev.

DAQ ch.	det. name	det. mass [g]	active mass [g]	f_{76}	livetime [d]	$\epsilon_{2\nu\beta\beta}$
0	GD91A	627	557	0.877	130.67	0.898236
1	GD35B	810	740	0.877	130.67	0.922058
2	GD02B	625	553	0.877	114.96	0.892824
3	GD00B	697	613	0.877	114.96	0.888489
4	GD61A	731	652	0.877	130.67	0.899440
5	GD89B	620	533	0.877	111.97	0.868013
6	GD02D	662	552	0.877	–	0.843133
7	GD91C	627	556	0.877	57.91	0.896432
8	ANG5	2746	2281	0.856	108.49	0.850311
9	RG1	2110	1908	0.855	111.97	0.914006
10	ANG3	2391	2070	0.883	130.67	0.881205
11	GD02A	545	488	0.877	130.67	0.904982
12	GD32B	716	632	0.877	105.16	0.890951
13	GD32A	458	404	0.877	130.67	0.890478
14	GD32C	743	665	0.877	111.97	0.901999
15	GD89C	595	520	0.877	108.49	0.883285
16	GD61C	634	562	0.877	127.19	0.896248
17	GD76B	384	326	0.877	81.09	0.856830
18	GD00C	815	727	0.877	130.67	0.900309
19	GD35C	634	572	0.877	111.97	0.911339
20	GD76C	824	723	0.877	130.67	0.885608
21	GD89D	526	454	0.877	130.67	0.872945
22	GD00D	813	723	0.877	130.67	0.896972
23	GD79C	812	713	0.877	127.19	0.885965
24	GD35A	768	693	0.877	130.67	0.908978
25	GD91B	650	578	0.877	–	0.896808
26	GD61B	751	666	0.877	95.42	0.896601
27	ANG2	2833	2468	0.866	108.99	0.885468
28	RG2	2166	1800	0.855	111.97	0.849545
29	ANG4	2372	2136	0.863	130.67	0.911625
30	GD00A	496	439	0.877	130.67	0.895125
31	GD02C	788	700	0.877	111.97	0.895513
32	GD79B	736	648	0.877	118.43	0.888784
33	GD91D	693	615	0.877	46.79	0.896089
34	GD32D	720	657	0.877	130.67	0.920990
35	GD89A	524	462	0.877	114.96	0.889999
36	ANG1	958	795	0.859	130.67	0.848716

Table D.2: Parameters for $T_{1/2}^{2\nu\beta\beta}$ calculation. Detector mass, active mass and f_{76} taken from [107], livetime from [114] and $\epsilon_{2\nu\beta\beta}$ from [127].

ACKNOWLEDGEMENTS

To put forward this thesis would not have been possible without the support of many people. All of them I want to thank here.

First of all, I thank my advisor, Prof. Manfred Lindner, for the opportunity to write this thesis in his research group, for his continuous support, for creating such excellent working conditions and the chance to be visible in the science community.
I would like to thank Prof. Norbert Herrmann for agreeing to become one of the thesis referees.

I thank Mark Heisel for introducing me into the topic of an active veto using LAr scintillation light. In particular, he shared his expertise about cryogenic PMTs with me.
In this context, I would like to thank many people at the Max-Planck Institut für Kernphysik who helped solving little and bigger problems during the everyday work with the PMTs. To name some of them: Klaus Jaenner and Jonas Westermann for their help with the voltage divider base production, Michael Reissfelder who helped me several times inserting PMTs in the test stand, Benjamin Gramlich for his experience with the spectrophotometers at MPIK, Herbert Strecker, Reinhard Hofacker, and many more...
I would like to thank the Xenon PMT group for the possibility to use the dark room test stand, for the introduction to the setup and especially for enlightening conversations.
For the good times spend together, I would like to thank my former office mate Patrick Otto Ludl. Apart from discussions about physics he lightened up my every-day's office life with some little and sometimes funny stories. He was a great support whenever needed. To pass over from the past to the presence, I would like to thank my current office mate, Guillaume Eurin, who is always available for discussions.
For countless discussions about everything between work and the sense of life during our lunch and coffee breaks I want to thank my colleagues at MPIK from the GERDA and Xenon collaboration: Andrea Kirsch, Werner Maneschg, Stefan Brünner, Constanze Hasterok, Sebastian Lindemann, Janina Hakenmüller, and many more. My personal thanks go to Vici who was such a fellow sufferer. I spend all the last week-ends together with her at the institute despite I would have preferred to pass time together with a good bottle of red wine.

I would like to acknowledge all the members of GERDA for good collaboration and the entertaining social dinners at the meetings. I would like to mention some colleagues whom I owe special thanks: Karl-Tasso Knoepfle for disputing questionable conclusions with his years of experience and for his effort during the design and installation phase of the light instrumentation, Matteo Agostini for his help with all the GERDA software packages, Luciano Pandola for his expertise about Monte Carlo simulations and for replying so quickly to my mails, and Janina Hakenmüller for providing me simulated energy spectra for the $T^{2\nu}_{1/2}$-analysis. Christoph Wiesinger who was my counterpart on the SiPM light read-out side was always a good collaborator, supported me and provided helpful hints. I wish to give my special thanks to Bernhard Schwingenheuer who continuously supported me and shared some of his broad expertise. During the last months he gave decisive input for the progress of this thesis.

Many thanks go to everyone who helped with proof reading of my thesis, among them Werner Maneschg, Teresa Marrodan and Bernhard Schwingenheuer.
I thank Anja Berneiser and Britta Schwarz for their help with bothersome paperwork and cheerfulness.

Ich möchte meinen Eltern und Geschwistern für ihre Unterstützung und Fürsorge danken. Vor allem meine Mutter hat immer ein offenes Ohr für meine Probleme und lässt mich den Fokus auf wichtiges lenken.
Ich möchte meiner verstorbenen Großmutter danken, die immer ein Vorbild für mich war. Sie hat mich gelehrt und mir vorgelebt, was Nächstenliebe bedeutet und wie wichtig Familienzusammenhalt ist.
Zum Schluss möchte ich Christian danken, der mich auch in stressigen Zeiten erträgt, mir mit seiner Zuneigung Kraft gibt und es auf magische Weise immer wieder schafft, dass ich mich beruhige und abschalten kann.

BIBLIOGRAPHY

[1] C. E. Aalseth et al.: *Neutrinoless double-β decay of ^{76}Ge: First results from the International Germanium Experiment (IGEX) with six isotopically enriched detectors*, Phys. Rev. C **59**, 2108, (1999).

[2] C. E. Aalseth et al. [IGEX] : *THE IGEX ^{76}Ge NEUTRINOLESS DOUBLE-BETA DECAY EXPERIMENT: PROSPECTS FOR NEXT GENERATION EXPERIMENTS*, Phys. Rev. D **65**, 092007, (2002).

[3] C. E. Aalseth et al. [Majorana collaboration]: *An R & D project towards a tonne-scale germanium neutrinoless double-beta decay search*, AIP Conf.Proc. **1182**, 88-91, (2009).

[4] J. N. Abdurashitov et al. [SAGE Collaboration]: *Results from SAGE (The Russian-American gallium solar neutrino experiment)*, Phys. Lett. B 328, 234-248, (1994).

[5] Y. Abe et al. [Double Chooz Collaboration]: *Indication of Reactor $\bar{\nu}_e$ Disappearance in the Double Chooz Experiment*, Phys. Rev. Lett. **108**, 131801, 2012.

[6] R. Acciarri et al. [WArP Collaboration]: *Effects of Nitrogen contamination in liquid Argon*, arXiv:0804.1217v1 [nucl-ex], 2008.

[7] R. Acciarri et al. [WArP Collaboration]: *Oxygen contamination in liquid Argon: combined effects on ionization electron charge and scintillation light*, JINST **5**, P05003, 2010.

[8] M. Agostini et al. [GERDA collaboration]: *Measurement of the half-life of the two-neutrino double beta decay of ^{76}Ge with the GERDA experiment*, J. Phys. G: Nucl. Part. Phys. **40**, (2013) 035110.

[9] K.-H. Ackermann et al. [GERDA collaboration]: *The GERDA experiment for the search of $0\nu\beta\beta$ decay in ^{76}Ge*, Eur. Phys. J. C (2013) 73.

[10] P. A. R. Ade [Planck Collaboration]: *Planck 2013 results. XVI. Cosmological parameters*, Astronomy & Astrophysics, Volume 571, (2013).

[11] P. Agnes et al. [DarkSide Collaboration]: *First Results from the DarkSide-50 Dark Matter Experiment at Laboratori Nazionali del Gran Sasso*, arxiv:1410.0653v3 [astro-ph], 2014.

[12] P. Agnes et al. [DarkSide Collaboration]: *The Electronics and Data Acquisition System of the DarkSide Dark Matter Search*, arXiv:1412.2969v2 [astro-ph], 2014.

[13] S. Agostinelli et al. [Geant4 collaboration]: *Geant4 – a simulation toolkit*, Nucl.Instrum.Meth. A506 (2003) 250-303.

[14] M. Agostini, L. Pandola, P. Zavarise and O. Volynets: *GELATIO: a general framework for modular digital analysis of high-purity Ge detector signals*, JINST 6, (2011) P08013.

[15] M. Agostini, L. Pandola and P. Zavarise: *Off-line data processing and analysis for the* GERDA *experiment*, J. Phys. Conf. Ser. 368, (2012) 012047.

[16] M. Agostini et al. [GERDA collaboration]: *Results on Neutrinoless Double-β Decay of ^{76}Ge from Phase I of the* GERDA *Experiment*, Phys. Rev. Lett 111 (2013) 122503.

[17] M. Agostini et al. [GERDA collaboration]: *Pulse shape discrimination for GERDA Phase I data*, Eur. Phys. J. C 73, 2583, 2013.

[18] M. Agostini et al. [GERDA collaboration]: *The background in the $0\nu\beta\beta$ experiment* GERDA, Eur. Phys. J. C 74 (2014) 2764.

[19] M. Agostini et al. [GERDA collaboration]: *Results on $\beta\beta$ decay with emission of two neutrinos or Majorons in ^{76}Ge from* GERDA *Phase I*, Eur. Phys. J. C **75** (2015) 416.

[20] M. Agostini et al. [GERDA collaboration]: *$2\nu\beta\beta$ decay of ^{76}Ge into excited states with* GERDA *Phase I*, J. Phys. G: Nucl. Part. Phys. **42** (2015) 115201.

[21] M. Agostini, M. Barnabe-Heider, D. Budjas, C. Cattadori, A. Gangapshev, K. Gusev, M. Heisel, M. Junker, A. Klimenko, A. Lubashevskiy, K. Pelczar, S. Schönert, A Smolnikov, and G Zuzel: *LArGe – Active background suppression using argon scintillation for the* GERDA *$0\nu\beta\beta$-experiment*, arXiv:1501.05762v1, 2015.

[22] M. Agostini et al. [GERDA collaboration]: *Background free search for neutrinoless double beta decay with* GERDA *Phase II*, Nature, to be published.

[23] Q.R. Ahmad et al. [SNO collaboration]: *Direct Evidence for Neutrino Flavor Transformation from Neutral-Current Interactions in the Sudbury Neutrino Obersvatory*, Phys. Rev. Lett. 89, No. 1, 011301, 2002.

[24] J. K. Ahn et al. [RENO collaboration]: *Observation of Reactor Electron Antineutrinos Disappearance in the RENO Experiment*, Phys. Rev. Lett. **108**, 191802, 2012.

[25] J. B. Albert et al. [EXO-200 collaboration]: *Search for Majorana neutrinos with the first two years of EXO-200 data*, Nature **510**, 229â€“234, (2014).

[26] C. Alduino et al. [Cuore collaboration]: *Measurement of the Two-Neutrino Double Beta Decay Half-life of ^{130}Te with the CUORE-0 Experiment*, arXiv:1609.01666v1 [nucl-ex], 2016.

[27] The ALEPH, DELPHI, L3, OPAL, SLD Collaborations and the LEP Electroweak Working Group and the SLD electroweak, heavy flavour groups : *Precision Electroweak Measurements on the Z Resonance*, Phys. Rept. 427, 257-454, 2006.

[28] K. Alfonso et al. [CUORE collaboration]: *Search for Neutrinoless Double-Beta Decay of ^{130}Te with CUORE-0*, arxiv:1504.02454v2 [nucl-ex], (2015).

[29] C. Amsler, V. Boccone, A. Buchler, R. Chandrasekharan, C. Regenfus, et al.: *Luminescence quenching of the triplet excimer state by air traces in gaseous argon*, JINST **3** (2008) P02001, [arXiv:0708.2621].

[30] F. P. An et al. [Daya Bay Collaboration]: *Observation of Electron-Antineutrino Disappearance at Daya Bay*, Phys. Rev. Lett. **108**, 171803, 2012.

[31] V. d'Andrea: internal note, 2016.

[32] P. Anselmann et al. [GALLEX Collaboration]: *Solar neutrinos observed by GALLEX at Gran Sasso*, Phys.Lett. B 285, 376-389, (1992).

[33] E. Aprile et al. [XENON collaboration]: *Lowering the radioactivity of the photomultiplier tubes for the XENON1T dark matter experiment*, Eur. Phys. J. C75 (2015) 11, 546.

[34] C. Arnaboldi et al. [NEMO-3 collaboration]: *New Limit on the Neutrinoless $\beta\beta$ Decay of ^{130}Te*, Phys. Rev. Lett. **95**, 142501, (2005).

[35] R. Arnold et al. [NEMO collaboration]: *Result of the search for neutrinoless double-β decay in ^{100}Mo with the NEMO-3 experiment*, arXiv:1506.05825v4 [hep-ex], 2015.

[36] R. Arnold et al. [NEMO collaboration]: *Measurement of the $2\nu\beta\beta$ decay half-life of ^{150}Nd and a search for $0\nu\beta\beta$ decay processes with the full exposure from the NEMO-3 detector*, arXiv:1606.08494v1 [hep-ex], 2016.

[37] R. Arnold et al. [NEMO collaboration]: *Measurement of the double-beta decay half-life and search for the neutrinoless double-beta decay of ^{48}Ca with the NEMO-3 detector*, arXiv:1604.01710v3 [hep-ex], 2016.

[38] J. Argyriades et al. [NEMO-3 collaboration]: *Measurement of the two neutrino double beta decay half-life of Zr-96 with the NEMO-3 detector*, Nucl. Phys. A **847** 168 - 179, (2010).

[39] K. Asakura [KamLAND-Zen collaboration]: *Results from KamLAND-Zen*, arXiv:1409.0077 [physics.ins-det], 2014.

[40] J.N. Bahcall and M. H. Pinsonneault: *Solar models with helium and heavy-element diffusion.*, Reviews of Moderns Physics, Vol. 67, No. 4, 1995.

[41] A. S. Barabash and V. B. Brudanin: *Investigation of double-beta decay with the NEMO-3 detector*, Phys. At. Nucl. **74**, 312â€“317, 2011.

[42] J. Barea, J. Kotila and F. Iachello: *Nuclear matrix elements for double-β decay*, Phys. Rev. C, **87**, 014315, 2013.

[43] P. Barrow, L. Baudis, D. Cichon, M. Danisch, D. Franco, F. Kaether, A. Kish, M. Lindner, T. Marrodán Undagoitia, D. Mayani, L. Rauch, Y. Wei, J. Wulf : *Qualification Tests of the R11410-21 Photomultiplier Tubes for the XENON1T Detector*, arxiv:1609.01654v1 [astro-ph.IM], 2016.

[44] C. Bauer et al.: *Qualification Tests of 474 Photomultiplier Tubes for the Inner Detector of the Double Chooz Experiment*, JINST, 6:P06008, 2011.

[45] L. Baudis, G. Benato, R. Dressler, F. Piastra, I. Usoltsev and M. Walter: *Enhancement of light yield and stability of radio-pure tetraphenyl-butadiene based coatings for VUV light detection in cryogenic environments*, JINST 10 (2015) P09009.

[46] J. Benziger et al.: *The nylon scintillator containment vessels for the Borexino solar neutrino experiment*, Nucl. Instrum. Meth. A 582, 509-534, 2007.

[47] J. Beringer et al. (Particle Data Group): *Review of Particle Physics*, Phys. Rev. D, 86, 010001, 2012.

[48] A. Bideau-Mehu, Y. Guern, R. Abjean, A. Johannin-Gilles: *Measurement of refractive indices of neon, argon, krypton and xenon in the* $253.7 - 140.4\,\mathrm{nm}$ *wavelength range. Dispersion relations and estimated oscillator strengths of the resonance lines*, J. Quant. Spectrosc. Rad. Transfer 25, 395-402, 1981.

[49] M. Boswell et al.: *MaGe – a Geant4-based Monte Carlo Application Framework for Low-background Germanium Experiments*, arXiv:1011.3827v1 [nucl-ex], 2010.

[50] L. Cadonati: *The Borexino Solar Neutrino Experiment and its Scintillator Containment Vessel*, PhD thesis, Princeton University, 2001.

[51] SY1527 Universal Multichannel Power Supply System, CAEN S.p.A., Viareggio

[52] N1471H, 4ch Power Supply, CAEN S.p.A., Viareggio

[53] Canberra Industries Inc., 107 Union Valley Rd, Oak Ridge, TN, USA.
`http://www.canberra.com/`

[54] Canberra Semiconductor N.V., Lammerdries 25, 2250 Olen, Belgium.
`http://www.canberra.com/`

[55] M. Carvalho and G. Klein: *Alpha-particle induced scintillation in dense gaseous argon: emission spectra and temporal behaviour of its ionic component*, Nuclear Instruments and Methods 178 (1980), no. 23 469-475.

[56] J. Chadwick: *Über das β-Strahlenspektrum von $ThB + C$*, Verh. d. deutschen Phys. Ges., 16, 383, 1914.

[57] D. Cichon: *Examining Hamamatsu R11410-21 photomultipliers for XENON1T at room and liquid xenon temperatures*, bachelor thesis, Universität Heidelberg, 2013.

[58] C. L. Cowan Jr. et al.: *Detection of the free neutrino: a confirmation*, Science, Volume 124, pp. 103-104, (1956).

[59] O. Cremonesi and M. Pavan: *Challenges in double beta decay*, Adv. High Energ. Phys. 2014, 4, pp. 1-40, arXiv:1310.4692v2 [physics.inst-det], (2014).

[60] F. A. Danevich, et al.: *Search for double beta decay of* ^{116}Cd *with enriched* $^{116}CdWO_4$ *crystal scintillators (Aurora experiment)*, arXiv:1601.05578v1 [nucl-ex].

[61] R. Davis Jr., D. S. Harmer and K. C. Hoffman: *Search for Neutrinos from the Sun*, Phys. Rev. Lett. 20, 1205, (1968).

[62] R. Davis Jr.: *A Review of Measurements of the Solar Neutrino Flux and their Variation*, Nuclear Physics B (Proc. Suppl.) 48, 284-298 (1996).

[63] T. Doke, H. Crawford, A. Hitachi, J. Kikuchi, P. Lindstrom et al.: *Let Dependence of Scintillation Yields in Liquid Argon*, Nuclear Instrum. Meth. **A 269**, 291 - 296, 1988.

[64] T. Doke, A. Hitachi, et.al.: *Absolute Scintillation Yields in Liquid Argon and Xenon for Various Particles*, Jpn. J. Appl. Phys. Vol. 41 pp.1538-1545, 2002.

[65] Donaldson Company Inc., 1400 West 94th Street, Bloomington, Minnesota, U.S.A.

[66] M. Duerr, M. Lindner and A. Merle: *On the quantitative impact of the Schechter-Valle theorem*, JHEP, **1106**, 091, 2011.

[67] M. Duerr: *Phenomenological Aspects of Theories for Baryon and Lepton Number Violation*, PhD thesis, Universität Heidelberg, 2013.

[68] K. Eguchi et al. [KamLAND Collaboration]: *First Results from KamLAND: Evidence for Reactor Antineutrino Disappearance*, Phys. Rev. Lett. **90**, 021802, 2003.

[69] R. B. Firestone, V. S. Shirley, C. M. Baglin, S. F. Chu, and J. Zipkin: *Table of Isotopes*, Wiley & Sons, New York, 8th edition (1996).

[70] D. V. Forero, M. Tortola and J. W. F. Valle: *Neutrino oscillations refitted*, Phys. Rev. D 90, 093006, (2014).

[71] K. Freund, R. Falkenstein, P. Grabmayr, A. Hegai, J. Jochum, M. Knapp, B. Lubsandorzhiev, F. Ritter, C. Schmitt, A.-K. Schütz, E. Shevchik, M. Shirchenko, D. Zinatulina: *The performance of the Muon Veto of the* GERDA *experiment*, Eur. Phys. J. C 76, 298, 2016.

[72] S. Fukuda et al. [Super-Kamiokande Collaboration]: *Solar* ^8B *and hep Neutrino Measurements from 1258 Days of Super-Kamiokande Data*, Phys. Rev. Lett. 86, 5651, (2001).

[73] A. Gando et al. [KamLAND-Zen Collaboration]: *Search for Majorana Neutrinos Near the Inverted Mass Hierarchy Region with KamLAND-Zen*, Phys. Rev. Lett **117**, 082503, 2016.

[74] C. Giunti and C. W. Kim: *Fundamentals of Neutrino Physics and Astrophysics*, Oxford University Press, 2007.

[75] M. Goldhaber, L. Grodzins and A. W. Sunyar: *Helicity of Neutrinos*, Phys. Rev. 109, 1015, (1958).

[76] J. J. Gomez-Cadenas et al.: *Phenomenology of neutrinoless double beta decay*, PoS GSSI14 **004**, arXiv:1502.00581 [hep-ex], (2015).

[77] Hamamatsu Photonics K.K., 325-6, Sunayama-cho, Naka-ku, Hamamatsu City, Shizuoka Pref., 430-8587, Japan.

[78] Hamamatsu Photonics K.K., Datasheet 3" R11065 photomultiplier tube.

[79] Hamamatsu Photonics K.K.: *Photomultiplier Tubes, Basics and Applications*, Photomultiplier Handbook, Third Edition, 2006.

[80] J. Haser, F. Kaether, C. Langbrandtner, M. Lindner, S. Lucht, S. Roth, M. Schumann, A. Stahl, A. Stüken, C. Wiebusch: *Afterpulse Measurements of R7081 Photomultipliers for the Double Chooz Experiment*, arXiv:1301.2508v1 [physics.ins-det], 2013.

[81] T. Heindl, T. Dandl, M. Hofmann, R. Krücken, L. Oberauer, et al.: *The scintillation of liquid argon*, Europhys.Lett. 91 (2010) 62002.

[82] M. Heisel: *LArGe - A liquid argon scintillation veto for* GERDA, PhD thesis, Universität Heidelberg, 2011.

[83] M. Heisel: private communication, 2012.

[84] M. Heisel: analysis performed by M. Heisel, 2012.

[85] M. Heisel, M. Lindner, A. Wegmann: *Time delay of PMT response after ramping of Hamamatsu photomultiplier tubes R11065-10/20 in liquid argon*, Memo to Hamamatsu Photonics K.K., 2013.

[86] G. Heusser: *Low-Radioactivity background techniques*, Annu. Rev. Nucl. Part. Sci. **45**, 543, (1995).

[87] K. S. Hirata et al.: *Observation of ^8B solar neutrinos in the Kamiokande-II detector*, Phys. Rev. Lett. 63, 16, (1989).

[88] A. Hitachi, T. Takahashi, N. Funayama, K. Masuda, J. Kikuchi, et al.: *Effect of ionization density on the time dependence of luminescence from liquid argon and xenon*, Phys.Rev. B27 (1983) 5279â€“5285.

[89] A. Hitachi, T. Doke, A. Mozumder: *Luminescence quenching in liquid argon under charged-particle impact: Relative scintillation yield at different linear energy transfers*, Phys Rev B, Vol. 46 No. 18 p. 11463, 1992.

[90] O. Host, O. Lhaav, F. B. Abdalla and K. Eitel : *Forecasting neutrino masses from combining* KATRIN *and the CMB observations: Frequentist and Bayesian analyses*, Phys. Rev D 76 (2007) 113005.

[91] Y. Hotta (Hamamatsu Photonics K.K.): *Latest developments in PMTs for low temperature operation*, talk at the DM2014 conference on February 28, 2014.

[92] N. Ishida, et al.: *Attenuation length measurements of scintillation light in liquid rare gases and their mixtures using an improved reflection suppresser*, Nucl. Instr. and Meth. in Phys. A, 384(2-3), 380-386, 1997.

[93] M. Janecek: *Reflectivity spectra for commonly used reflectors*, IEEE 4710 TRANSACTIONS ON NUCLEAR SCIENCE, vol. 59, 2012.

[94] J. Janicsko Csathy, S. Schönert, and Ch. Wiesinger: *Optical fiber read-out for liquid argon scintillation light*, GSTR-16-501, internal GERDA report, 2016.

[95] Joint Stock Company "Production Association Electrochemical Plant", Pervaya Promyshlennaya 1, 663690 Zelenogorsk, Russia.
`http://www.ecp.ru/eng/`

[96] B.J.P. Jones et al.: *A measurement of the absorption of liquid argon scintillation light by dissolved nitrogen at the part-per-million level*, arxiv:1306.4605v2 [physics.inst-det], 2013.

[97] B.J.P. Jones et al.: *The effects of dissolved methane upon liquid argon scintillation light*, arxiv:1308.3658v2 [physics.inst-det], 2014.

[98] A. Kirsch: *Search for the neutrinoless double β-decay in* GERDA *PhaseI using a Pulse Shape Discrimination technique*, PhD thesis, Universität Heidelberg, 2014.

[99] H.V. Klapdor-Kleingrothaus et al. [HdM collaboration]: *Latest Results from the Heidelberg-Moscow Double-Beta-Decay Experiment*, Eur. Phys. J. A **12**, 147, (2001).

[100] H.V. Klapdor-Kleingrothaus et al.: *Search for neutrinoless double beta decay with enriched ^{76}Ge in Gran Sasso 1990-2003*, Phys. Lett B **586**, 198, (2004).

[101] H.V. Klapdor-Kleingrothaus, I. V. Krivosheina: *The evidence for the observation of $0\nu\beta\beta$ decay: The identification of $0\nu\beta\beta$ events from the full spectra*, Mod. Phys. Lett. A **21** (2006) 1547-1566.

[102] G. F. Knoll: *Radiation Detection and Measurements*, Wiley, New York, (1989).

[103] B. Lehnert: *Search for $2\nu\beta\beta$ Excited State Transitions and HPGe Characterization for Surface Events in* GERDA *Phase II*, PhD thesis, TU Dresden, (2016).

[104] V. M. Lobashev: *The search for the neutrino mass by direct method in the tritium β-decay and perspectives of study it in the project* KATRIN, Nucl. Phys. A, 719, 153c-160c, (2003).

[105] A. Lubashevskiy et al.: *Nylon mini-shroud coated with wavelengh shifter for the* GERDA *Phase II detectors array*, GSTR-15-504, internal GERDA report, 2015.

[106] Z. Maki, M. Nakagawa and S. Sakata: *Remarks on the Unified Model of Elementary Particles*, Prog. Theor. Phys. 28, 870, (1962).

[107] W. Maneschg, R. Falkenstein, B. Lehnert, K. Von Sturm, E. Andreotti, A. Garfagnini: *Full Charge Collection Depth and Active Volume of GERDA Phase II BEGe detectors*, GSTR-16-002, internal GERDA report, 2016.

[108] J. Menendez et al. : *Disassembling the Nuclear Matrix Elements of the Neutrinoless beta beta Decay*, Nucl. Phys. A, **818**, 139-151, 2009.

[109] J. Menendez et al.: *Neutrinoless Double Beta Decay: The Nuclear Matrix Elements Revisited*, J. Phys. Conf. Ser., **312**, 072005, 2011.

[110] S. P. Mikheyev and A. Yu. Smirnov: *Resonance enhancement of oscillations in matter and solar neutrino spectroscopy*, Sov. J. Nucl. Phys. 42, 913, (1985).

[111] P. Minkowski: $\mu \to e\gamma$ *at a rate of one out of* 10^9 *muon decays?*, Phys. Lett. **B67**, 421, 1977.

[112] K.A. Olive et al. (Particle Data Group): Chin. Phys. C, 38, 090001 (2014).

[113] H. Päs and W. Rodejohann: *Neutrinoless Double Beta Decay*, New J.Phys. **17**, 11, 115010, (2015).

[114] L. Pandola: private communication, 2016.

[115] W. Pauli: *Dear radioactive ladies and gentlemen*, Phys. Today 31N9 (1978) 27.

[116] P. Peiffer: *Liquid argon as active shielding and coolant for bare germanium detectors: A novel background suppression method for the* GERDA $0\nu\beta\beta$ *experiment*, PhD thesis, Universität Heidelberg, 2007.

[117] K. Pelczar and G. Zuzel : *Scaler for the LAr instrumentation PMTs*, GSTR-15-002, internal GERDA report, 2015.

[118] PPM Pure Metals GmbH, Am Bahnhof 1, 38685 Langelsheim, Germany. `http://www.ppmpuremetals.de/`

[119] P. K. Rath et al.: *Uncertainties in nuclear transition matrix elements for neutrinoless* $\beta\beta$ *decay within the projected-Hartree-Fock-Bogoliubov model*, Phys. Rev. C, **82**, 064310, 2010.

[120] W. Rodejohann: *Neutrinoless Double Beta Decay and Particle Physics*, Int. J. Mod. Phys. E, 20, 1833, 2011.

[121] W. Rodejohann: *Neutrinoless double-beta decay and neutrino physics*, J. Phys. G: Nucl. Part. Phys. **39**, 124008, (2012).

[122] J. Schechter and J. W. F. Valle: *Neutrinoless double-*β *decay in* $SU(2) \times U(1)$ *theories*, Phys. Rev. D **25** (1982) 2951.

[123] A.-K. Schütz: *tba*, PhD thesis, Universität Tübingen, 2017, to be published.

[124] B. Schwingenheuer: *Status and prospects of searches for neutrinoless double beta decay*, Ann. Physik (Berlin) 525 (2013) 269.

[125] F. Simkovic, V. Rodin, A. Faessler and P. Vogel: *$0\nu\beta\beta$and $2\nu\beta\beta$nuclear matrix elements, quasiparticle random-phase approximation, and isospin symmetry restoration*, Phys. Rev. C **87**, 045501, 2013.

[126] B. Schneider: *Development of a setup for an in-situ measurement of the light attenuation of liquid argon for the* GERDA *experiment*, diploma thesis, Technische Universität Dresden, 2014.

[127] A.-K. Schütz: private communication, 2016.

[128] A.-K. Schütz: *Background modeling Phase II*, GERDA Meeting, Ringberg, June 2016.

[129] E. Storm et al.: *Photon cross sections from 0.001 to* 100 MeV *for elements 1 through 100*, University of California, Los Alamos, New Mexico, 1967.

[130] J. Suhonen and O. Civitarese: *Review of the properties of the $0\nu\beta^-\beta^-$ nuclear matrix elements*, J. Phys. G **39**, 124005, 2012.

[131] M. Suzuki: *Recombination luminescence from ionization tracks produced by alpha particles in high pressure argon, krypton and xenon gases*, Nuclear Instruments and Methods in Physics Research 215 (1983), no. 12 345 â€“ 356.

[132] S. Umehara et al.: *Neutrinoless double-β decay of ^{48}Ca studied by CaF_2(Eu) scintillators*, Phys. Rev. C **78**, 058501, 2008.

[133] N. López Vaquero, T. R. Rodríguez, and J. L. Egido: *Shape and Pairing Fluctuation Effects on Neutrinoless Double Beta Decay Nuclear Matrix Elements*, Phys. Rev. Lett. **111**, 142501, 2013.

[134] V. Wagner: *Pulse Shape Analysis for the* GERDA *Experiment to Set a New Limit on the Half-life of $0\nu\beta\beta$ Decay of ^{76}Ge*, PhD thesis, Universität Heidelberg, 2017.

[135] M. Walter: *Background reduction techniques for the* GERDA *experiment*, PhD thesis, Universität Zürich, 2015.

[136] C. Wiesinger: *The TUM liquid argon test stand: Commissioning and characterization of a low background test stand for background suppression studies in the frame of the GERDA ($0\nu\beta\beta$)-experiment*, master thesis, Technische Universität München, 2014.

[137] C. Wiesinger: *tba*, PhD thesis, Technische Universität München, to be published.

[138] L. Wolfenstein: Neutrino oscillations in matter, Phys. Rev. D 17, 2369, (1978).

[139] C. S. Wu, E. Ambler, R. W. Hayward, D. D. Hoppes and R. P. Hudson: *Experimental Test of Parity Conservation in Beta Decay*, Phys. Rev. 105, 1413, (1957).